

Diss. ETH No. 25043

ENTROPIC LATTICE BOLTZMANN METHOD FOR COMPLEX FLOWS

A thesis submitted to attain the degree of
DOCTOR OF SCIENCES of ETH ZURICH
(Dr. sc. ETH Zurich)

presented by

Benedikt Dorschner

Master of Science in Mechanical Engineering,
ETH Zurich

born on February 3rd, 1989
citizen of Karlsruhe, Germany

accepted on the recommendation of

Prof. Dr. I. V. Karlin, examiner

Prof. Dr. G. Haller, co-examiner

Dr. S. S. Chikatamarla, co-examiner

Prof. Dr. S. Succi, co-examiner

2018

Benedikt Dorschner
bdorschn@alumni.ethz.ch

To my family

Acknowledgements

This thesis could not have been achieved without the help of many people to whom I would like to express my sincere gratitude.

First and foremost, I would like to thank my PhD advisor Prof. Dr. Ilya Karlin, who gave me the opportunity to join his group and conduct my doctoral thesis in such an exciting field. Your broad and profound knowledge has fueled many exciting and inspiring discussions. Thank you for your guidance and continuous support throughout the entire thesis and for always believing in me.

My deepest gratitude goes to Dr. Shyam Chikatamarla for his support, many insightful discussions and invaluable contributions. Without his help and expertise, the realization of this thesis would not have been possible. Thank you.

I would like to thank Prof. Dr. Sauro Succi and Prof. Dr. George Haller for agreeing to be part of the thesis committee. I am grateful for their valuable feedbacks on this thesis.

I am indebted to my colleagues Fabian Bösch, Nicolò Frapolli and Ali Mazloomi Moqqadam for their help and discussions. It was fun and productive working with you. I closely worked with Fabian Bösch on the development of numerical codes and we had many insightful on- and off-topic discussions. I wish to also thank Nicolò Frapolli for his contributions and the time spent together in the same office.

I thank Giovanni Di Ilio, who came to visit our group and collaborated with me on unstructured lattice Boltzmann methods. The collaboration with you was always joyful and productive.

I wish to thank all my colleagues in the Aerothermochemistry and Combustion Systems Laboratory (LAV) and particularly the head of the LAV, Prof. Konstantinos Boulouchos, for giving me the opportunity to work in such a pleasant environment.

Finally, I am grateful to my family and friends, who have endured and supported me during the ups and downs of this thesis.

The thesis was conducted at the Laboratory of Aerothermochemistry and Combustion Systems (LAV), in the computational kinetics group, at the Swiss Federal Institute of Technology of Zurich (ETHZ), Switzerland. The financial support of the ETH research grant ETH-32-14-2 is gratefully acknowledged. The computational resources at the Swiss National Super

Computing Center CSCS were provided under the grants s492, s630 and s800.

Zürich, February 2018

Benedikt Dorschner

Abstract

The lattice Boltzmann method is a promising approach to computational physics, which is based on the solid footing of kinetic theory and has shown success in various regimes of fluid dynamics including turbulence, multi-phase, thermal or compressible flows, among others.

While the original single-relaxation time lattice Bhatnagar-Gross-Krook model made the first connection to fluid dynamics, it suffers from fatal stability issues and thus was limited to resolved low Reynolds number flows. However, recent advances are starting to break these limits.

Various attempts to overcome this issue have been proposed. Notable is the entropic lattice Boltzmann method (ELBM), which introduced a discrete-time analog of Boltzmann's H-Theorem into the LBM framework, yielding a parameter-free and non-linearly stable scheme. Recently, this concept has been extended to the class of so-called multi-relaxation time models (MRT). The main idea of MRT models is to exploit the high dimensional kinetic space in order to increase stability without effecting hydrodynamics. However, prior to notion of a discrete H-function, the relaxation times were problem-dependent tuning constants. On the other hand, in entropic MRT models this ambiguity was resolved by maximizing the entropy of the post-collision state. The benefit of entropic MRT is that in contrast to ELBM the viscosity is not fluctuating but imposed with its nominal value. Recent studies have shown extraordinary stability properties without sacrificing accuracy.

While the stability problems of LBM have been resolved in the bulk flow by entropic LB models, complex simulations of engineering relevance have remained a challenge due to the lack of a consistent description of complex geometries, grid refinement strategies and extension to multi-physics problems such as fluid-structure interaction. In this thesis, the necessary numerical tools for the simulation of such complex flows are developed in a consistent and unique manner, compatible with the entropic paradigm.

After reviewing the general lattice Boltzmann method and its entropic version, consistent, second-order boundary conditions for complex, moving and deforming geometries are developed and validated. Subsequently, appropriate grid refinement strategies are developed for entropic LB methods, which, despite the extraordinary efficiency of LBM, are instrumental for realistic simulations at reasonable computational costs. First, a multi-domain grid refinement method is developed for incompressible flows and subsequently extended to thermal and compressible flow problems. Thorough validation and analysis of the entropic stabilizer is conducted, showing excellent results for challenging problems. In addition, an unstructured LBM based on a semi-Lagrangian approach is developed and its performance assessed for turbulent wall-bounded flows.

Equipped with these tools, accurate LB simulations of the complex flow in engine-geometries became feasible for the first time, while significantly reducing the computational costs compared to direct numerical simulations. Here, particular attention is paid on studying the models behavior in under-resolved simulations. Further investigations in the realm of transition to turbulence as well as biolocomotion show viability in terms of stability, accuracy and efficiency of the proposed scheme.

Finally, a novel fluid-structure interaction scheme is developed on the basis of the previously introduced methodology. Robustness of the scheme is shown by challenging simulations and extension to fluid-structure interaction for multiphase flows.

These ingredients significantly extend the range of applicability on several fronts and provide a simple, unified scheme for multi-physics simulations ranging from turbulence and fluid-structure interaction to thermal and multiphase flows.

Zusammenfassung

Die lattice Boltzmann Methode (LBM) ist ein vielversprechender Ansatz der rechnergestützten Physik, welcher auf der kinetischen Gastheorie basiert und erfolgreich auf verschiedenste Gebiete der Fluidodynamik angewandt wurde. Hierzu gehören unter anderem turbulente Strömungen, Mehrphasensysteme sowie thermische und kompressible Strömungen.

Obwohl das klassische, einfach-relaxierende lattice Bhatnagar-Gross-Krook Modell den ersten Bezug zur Fluidodynamik herstellen konnte, war es von fatalen numerischen Instabilitäten geprägt und somit auf Strömungen niedriger Reynolds-Zahl beschränkt. Jedoch fangen die Fortschritte der jüngsten Zeit an diese Limits zu brechen.

Dahingehend wurden viele Versuche unternommen. Nennenswert ist die entropische lattice Boltzmann Methode (ELBM), welche durch die Wiedereinführungen eines zeitdiskreten H-Theorems ein parameterfreies und nichtlinear stabiles Modell darstellt. Kürzlich wurde das entropische Konzept auf multi-relaxations Modelle (MRT) erweitert. Die Idee von MRT Modellen ist es, den hoch-dimensionalen kinetischen Raum auszunutzen um an numerischer Stabilität zu gewinnen, ohne die Hydrodynamik zu beeinflussen. Jedoch wurden vor der Einführung der diskreten H-Funktion die verschiedenen Relaxationsparameter problemabhängig eingestellt. Im Gegensatz dazu löst der entropische Ansatz diese Mehrdeutigkeit und bestimmt die Relaxationsparameter durch die Maximierung der Entropie des Postkollisionszustandes. Der Vorteile des entropischen MRT Modells zur einparameterigen ELBM besteht darin, dass dieses Verfahren zu keiner fluktuierende Viskosität führt, sondern die nominale Viskosität forciert. Jüngste Studien belegen der entropischen MRT Methode außergewöhnliche Stabilitätscharakteristiken ohne die Genauigkeit zu beeinflussen.

Während die intrinsischen Stabilitätsprobleme der LBM mit der Entwicklung von entropischen Modellen gelöst wurde, waren komplexe Simulationen von technischer Relevanz nicht möglich, da eine konsistente Behand-

lung von nicht-trivialen Geometrien, Netzverfeinerungsalgorithmen sowie die Erweiterung zu multiphysikalischen Problemen wie beispielsweise die Fluid-Struktur-Interaktion nicht existierten. Die Lösung dieser Probleme, welche Simulationen von komplexen Strömungen erlaubt und konsistent ist mit entropischen Modellen, ist Gegenstand dieser Dissertation.

Nach einem Überblick der lattice Boltzmann Methode und deren entropischen Erweiterungen, werden konsistente Randbedingungen für komplexe, bewegte und deformierbare Körper entwickelt und validiert. Nachfolgend werden geeignete Gitterverfeinerungsstrategien für entropische LBMs entwickelt, welche trotz der außergewöhnlichen Effizienz unerlässlich sind für realistische Simulationen. Zunächst wird eine neue multi-domain Gitterverfeinerungsstrategie für inkompressible, thermische und kompressible Strömungen entwickelt. Sorgfältige Validierung und Analyse des entropischen Stabilisators werden durchgeführt und zeigen gute Ergebnisse für anspruchsvolle Probleme in der Fluidodynamik. Zusätzlich wurde ein LB Modell für unstrukturierte Gittern basierend auf dem Semi-Lagrangian Ansatz entwickelt und deren Leistungsfähigkeit für turbulente Wandströmungen unter Beweis gestellt.

Mit diesen Neuentwicklungen wurden akkurate LB Simulationen von komplexen Strömungen in Motorgeometrien ermöglicht, wobei die benötigte Rechenzeit im Vergleich zu Direkten Numerischen Simulationen (DNS) signifikant reduziert wurde. Besonderer Augenmerk wurde auch auf das Verhalten der Modelle im Falle von Unterauflösung gelegt. Des Weiteren wurden die Modelle verwendet um den Übergang zu Turbulenz sowie Biolo-komotion zu studieren. Die Resultate unterstreichen die Leistungsfähigkeit der neuen Modelle bezüglich Stabilität, Präzision und Effizienz.

Abschließend wird eine neue Methode zur Simulation von Fluid-Struktur-Interaktionen entwickelt. Die Robustheit der Methode wird für verschiedene, herausfordernde Probleme gezeigt und erweitert um Fluid-Struktur-Interaktionen in Mehrphasenströmungen zu berechnen.

Die Resultate dieser Dissertation erweitern den Anwendungsbereich von LB Methoden an vielen Fronten und bieten somit ein einfaches und universales Schema für die Simulation von multiphysikalischen Problemen, welche von Turbulenz und Fluid-Struktur-Interaktionen zu thermischen und mehrphasigen Strömungen reichen.

Contents

Abstract	v
Zusammenfassung	vii
1 Introduction	1
1.1 Motivation	1
1.2 Outline of the thesis	5
2 The lattice Boltzmann method	7
2.1 The Boltzmann equation	7
2.1.1 Properties of the Boltzmann equation	9
2.1.2 Bhatnagar-Gross-Krook model	11
2.1.3 Kinetic algorithms	12
2.2 The lattice Boltzmann method	12
2.3 The Entropic lattice Boltzmann method	16
2.4 Entropic multi-relaxation time lattice Boltzmann method .	18
2.5 Conclusion	20
3 Complex and moving geometries	23
3.1 Introduction	23
3.2 Grad boundary condition	29
3.3 Validation	32
3.3.1 Order of accuracy	32
3.3.2 Sedimenting sphere	33
4 Grid refinement strategies	37
4.1 Introduction	37
4.2 Multi-domain grid refinement	37
4.2.1 Multi-domain coupling	38

4.2.2	Extensions to thermal and compressible lattice Boltzmann models	43
4.2.3	Numerical validation	51
4.3	Unstructured meshes	66
4.3.1	Semi-Lagrangian LBM	68
4.3.2	Validation and convergence study	71
4.3.3	Flow past a circular cylinder at $Re = 3900$	72
4.4	Conclusion	78
5	Flow in engine-like geometries	81
5.1	Introduction	81
5.2	Model validation for simple flows	85
5.2.1	Turbulent flow in a pipe	90
5.3	Valve/piston assembly	92
5.3.1	Numerical setup	93
5.3.2	Velocity field	95
5.3.3	Cyclic variability	102
5.4	Concluding remarks	104
6	Transitional flows	107
6.1	Introduction	107
6.2	Flow separation and transition to turbulence	112
6.2.1	Transitional flow past SD7003 airfoil	112
6.2.2	Flow in a low-pressure turbine passage	121
6.3	Concluding remarks	129
7	Biocomotion	133
7.1	Introduction	133
7.2	Plunging Airfoil	134
7.3	Anguilliform Swimmer	138
7.4	Outlook and possible extensions	144
7.4.1	Flapping flight	144
7.4.2	Interaction of multiple swimmers	147
7.5	Conclusion	149
8	Fluid-structure interaction	151
8.1	Introduction	151

8.2	Numerical approaches	153
8.2.1	Structural modeling	153
8.2.2	Fluid-structure coupling	157
8.3	Numerical results	159
8.3.1	Validation	159
8.3.2	Extensions to fluid-structure interaction in multiphase flow	166
8.4	Concluding remarks	173
9	Conclusions and outlook	175
9.1	Results	175
9.2	Limitations	177
9.3	Future research	178
	Appendix	181
A.1	Moment representation of the populations	181
	List of Tables	185
	List of Figures	186
	References	193
	Curriculum Vitae	235

Chapter 1

Introduction

1.1 Motivation

The dynamics of fluid flow is one of the most fascinating and beautiful subjects in physics. Its complexity arises from a variety and possibly co-existent phenomena spanning a vast range of temporal and spatial event scales. Its implications are omnipresent in science and engineering, ranging from the dynamics of stellar systems or accretion disks to industrial applications such as the optimization of internal combustion engines or the design of live-lasting artificial heart valves.

Despite its importance and focus of tremendous research effort, the theoretical understanding of the evolution of fluid flow is embarrassingly incomplete. Fluid motion is governed by a set of nonlinear partial differential equations, the so-called Navier-Stokes equations. These equations can only be solved analytically for the simplest cases and general solutions to the Navier-Stokes equations (NSE) remain one of the greatest unsolved problems in physics. The problem becomes particularly challenging for low-dissipative systems, i.e. turbulent flows, where complex and chaotic fluid motion arises from the nonlinearity of the Navier-Stokes equations, exhibiting a vast range of time and length scales, which eludes analytical description. Thus, studying turbulent flows requires advanced experimental or numerical tools.

While having provided invaluable insight for various fundamental prob-

lems, limitations in terms of accuracy, accessibility, cost and flexibility are inherent to experimental approaches. On the other hand, the continuing increase of computational power by developments of novel hardware and numerical methods make computer simulations an indispensable tool to advance the field of fluid mechanics.

However, even on the largest supercomputers available today, the level of complexity required for realistic engineering relevant applications remains an open challenge for state-of-the-art numerical solvers.

This is particular pronounced when various effects originating from, e.g., turbulence, complex geometries, thermal effects, multiple fluid phases or combinations thereof need to be taken into account for predictive simulations. Direct numerical simulations (DNS) are the most reliable approach and are based on a direct discretization of the NSE, which resolves all pertinent scales of the flow field. However, given the large range of scales in turbulent flows, this approach becomes prohibitively expensive and is thus limited to moderate Reynolds number flows. Remedy was sought in turbulence models, which reduce the computational requirements by coarse-graining the governing equation using either filtering or averaging operations. The affect of the under-resolved, small scales is modeled and projected onto the larger scales. Various models for different regimes have been deduced and range from introducing an eddy-viscosity to modeling an entire probability density function. However, the underlying modeling assumptions restrict the range applicability and typically rely on problem-dependent tuning of modeling parameters (see also chapter 5 for a discussion in the context of engine-flows).

The challenges for numerical methods become even more severe for wall-bounded turbulence, which is induced by complex, possibly moving or deforming geometries. Sophisticated and computationally expensive meshing strategies are required to ensure accuracy and hence puts yet another limit on the attainable level of complexity. Geometrically flexible methods such as immersed-boundary methods prevent these issues but are only recently starting to explore the turbulent flow regime. (see also chapter 3).

In contrast to traditional computational fluid dynamics (CFD), a different approach was initiated in [133–135] and developed in what is today known as the lattice Boltzmann method (LBM). Since then, the LBM has matured into a promising approach to computational fluid dynamics (CFD)

with applications in various regimes, ranging from incompressible turbulence, multiphase, thermal and compressible flows up to micro-flows and relativistic hydrodynamics [5, 54, 99, 102, 157, 229, 237, 326, 339]. In contrast to conventional numerical methods, the lattice Boltzmann method has its roots in kinetic theory and describes the flow field in terms of discretized particle distribution functions (populations) $f_i(\mathbf{x}, t)$ associated with discrete velocities $\mathbf{c}_i, i = 1, \dots, Q$, designed to recover the macroscopic Navier-Stokes equations in the hydrodynamic limit (see, e.g., [133–135, 325]). By organizing the discrete velocities into a regular lattice, the LBM reduces to a simple and highly efficient stream-and-collide algorithm with exact propagation and local nonlinearity, which is implemented by the collision operator.

The first realization, which made a practical connection of LBM to fluid dynamics was the well known lattice Bhatnagar-Gross-Krook (LBGK) model. The LBGK model remains popular due to its simplicity and numerical efficiency. Despite these attractive properties, the LBM was not competitive for long due to the lack of numerical stability and accurate boundary conditions in the simulation of high Reynolds number flows. This promoted the development of various models intended to resolve this issue, including explicit turbulence models in LBM formulation, crystallographic, regularized, cumulant as well as multiple-relaxation time (MRT) lattice Boltzmann models among others (see, e.g., [54, 67, 113, 158, 192, 252]). On the other hand, the entropic lattice Boltzmann method (ELBM) features nonlinear stability by introduction of a discrete entropy function H as the determining factor of the relaxation. In contrast to LBGK, the ELBM chooses the relaxation parameter of the collision adaptively at each point in space and time to locally ensure the discrete-time H-theorem. The macroscopic effect of choosing the relaxation parameter in this manner results in a locally varying, effective viscosity, which can be larger or smaller than the nominal one, leading to local enhancement or smoothing of the flow field [156]. This originates from the fact that, in ELBM, the same relaxation is equivalently imposed on all moments of the populations beyond the locally conserved quantities. It is important to stress that the relaxation parameter is not arbitrarily chosen but rather dictated by the physics of the flow, in accordance with the second law of thermodynamics. However, for resolved simulations where the populations remain close to the equilibrium state,

the ELBM recovers the LBGK model with its nominal viscosity [154]. An extension of the entropy concept was recently proposed in [157], where the viscosity may be kept at its nominal value by considering multiple relaxation times (KBC models). Recent studies in [40] have shown outstanding numerical stability for high Reynolds number flows while accuracy was not sacrificed. Furthermore, the role of the entropic stabilizer was investigated and quantified for periodic turbulence [40]. While this thesis mainly focuses on incompressible, isothermal flows, the concept of entropy-based LB methods is universal and has successfully been extended to various regimes, including thermal, compressible, multiphase as well as multi-component mixtures. Due to its advantages and universality, we only consider entropic LBM and in particular its multi-relaxation version in the scope of this thesis.

While stability issues in the bulk flow have been resolved by using entropy-based LBM, the simulation of engineering relevant applications involving wall-bounded turbulence, complex, moving and deforming geometries has remained challenging for LBM. Hence, enabling the numerical simulation of such complex flows is the main motivation of this thesis.

To that end, various strategies are developed. First, a novel treatment of complex, moving geometries is proposed, which exhibits second-order accuracy, is consistent with entropy-based LBM and provides reliable results even in severely under-resolved turbulent simulations. Furthermore, the classical LBM is bound to uniform, Cartesian meshes, which severely restrict the attainable level of complexity at reasonable computational costs. Thus, novel grid refinement strategies, which are consistent with entropy-based LBM are proposed. The combination of both enables predictive simulations of complex flows and we study the models behavior for both resolved and under-resolved simulations for engineering applications such as flows in engine-like geometries and transitional flows over airfoils and turbine blades. With these encouraging results, the scheme was further extended towards deforming geometries and fluid-structure interaction including nonlinear elasticity effects. Viability of the approach is demonstrated for canonical benchmark cases as well as in the realm of biocomotion and multiphase flows. Thus, the developments of this thesis are aiming towards establishing entropic LBM as a predictive tool for complex, multi-physics applications, relevant to science and engineering.

1.2 Outline of the thesis

The thesis is organized as follows:

- Chapter 2 : The fundamental principles of kinetic theory and statistical mechanics are reviewed. Starting from the Boltzmann equation and its properties, the construction of the classical lattice Boltzmann model is presented. Subsequently, based on a discrete H -function, the entropic lattice Boltzmann method along with its extension to multiple relaxation times is discussed in detail.
- Chapter 3 : In this chapter, we describe the implementation of complex, moving and deforming geometries within the lattice Boltzmann method. An overview of common methods such as immersed boundary methods and Cartesian grid methods along with their respective advantages or disadvantages is provided. Finally, a novel boundary treatment, the so-called Grad boundary condition is introduced, which exhibits second-order accuracy, is robust and consistent with entropy-based lattice Boltzmann models. The scheme is validated for the simple two-way coupled benchmark of a sedimenting sphere.
- Chapter 4 : To enable simulations of engineering relevant complexity, grid refinement strategies are indispensable. In this chapter, we consider multi-domain block refinement as well as LBM on unstructured grids. We start by introducing a novel block-refinement strategies, consistent with the entropy-based LBM and provide thorough validation for various challenging set-ups. Finally, we review recent advances for unstructured grids in LBM, and extend the so-called semi-Lagrangian LBM to entropic LBM and wall-bounded flows.
- Chapter 5 : The first engineering application, mimicking the flow in a simplified internal combustion engine, is presented. Before considering the final application in its full complexity, a thorough investigation of both resolved and under-resolved simulations of periodic and the turbulent pipe flow is reported . After these analyses, we consider a valve/piston arrangement, which allows us to probe the interaction between small and large scale flow structure in various distinct flow features. Detailed comparison to high-order DNS and

experiments for resolved and under-resolved simulation suggests encouraging accuracy and robustness of the proposed scheme.

- Chapter 6 : Transition to turbulence is both fascinating and of great relevance for the performance of many engineering applications. In this chapter, the laminar separation bubble over the *SD7003* airfoil as well as the turbine blade *T106* airfoil blade is studied in detail. We analyze its geometrical properties, its transient behavior as well as its sensitivity to free stream turbulence.
- Chapter 7 : In this chapter, we wander into the realm of bio-fluid-mechanics and consider flows relevant to animal locomotion with particular focus on flapping flight and undulatory fish locomotion. Thorough validation for a plunging airfoil in the transitional regime and a self-propelled anguilliform swimmer is presented. Finally, extensions and preliminary simulations of flapping flight and multiple anguilliform swimmers are discussed.
- Chapter 8 : A novel fluid-structure interaction scheme is proposed. Using a partitioned approach, the fluid domain is solved by the entropic multi-relaxation time model and the structural part by an appropriate FEM discretization. Apart from thorough validation, the scheme is extended to multiphase flows, where robustness is shown by the simulation of the droplet impact and elastic, superhydrophobic surfaces.
- Chapter 9 : In the last chapter of this thesis, a brief summary, concluding remarks and possible directions for future research are provided.

Chapter 2

The lattice Boltzmann method

In this chapter, we outline the construction of lattice Boltzmann models. Starting from the fundamental principles of kinetic theory and statistical mechanics, the Boltzmann equation and its pertinent properties are discussed. From that basis, the classical lattice Boltzmann method is introduced. Finally, the entropic lattice Boltzmann method and its extension to multiple relaxation times is discussed in detail.

2.1 The Boltzmann equation

The Boltzmann kinetic equation, first derived by the Austrian mathematician Ludwig Boltzmann in 1872, describes the dynamics of moderately rarefied gas by the evolution of the one-particle distribution function $f(\mathbf{c}, \mathbf{x}, t)$, where \mathbf{c} and \mathbf{x} denote the particle velocity and location in physical space, respectively. The distribution function $f(\mathbf{c}, \mathbf{x}, t)$ defines the probability density of finding a particle at time t within the phase-space volume $dV = d^3\mathbf{c}d^3\mathbf{x}$ and the number of particles dN contained in dV at time t is given by $dN = f(\mathbf{c}, \mathbf{x}, t)d^3\mathbf{c}d^3\mathbf{x}$. The dynamics of the particle is governed by an advection or free flight and the collision process. Based on the assumption of rarefaction, it is justified to only consider binary collisions. In its original version, the Boltzmann equation was derived for hard spheres and is expected to hold in the Grad-Boltzmann limit [119] for which $N \rightarrow \infty$ hard spheres with diameter $d \rightarrow 0$, occupy a volume

$Nd^3 \rightarrow 0$ and have a total collision cross section $Nd^2 \sim \text{const.}$. Under these circumstances, the evolution of $f(\mathbf{c}, \mathbf{x}, t)$ can be expressed as

$$\partial_t f + c_\alpha \partial_\alpha + g_\alpha \partial_{c_\alpha} f = \mathcal{Q}(f, f), \quad (2.1)$$

where g_α denotes an external force per unit mass acting on the particle and the collision integral is given by $\mathcal{Q}(f, f)$. The second and third term indicate the net change of the particle in dV by advection and acceleration, respectively.

The collision integral on the right hand side of Eq. (2.1) accounts for the effect of collisions of the particles on the distribution function. Put differently, the collision operator describes the change of the particle number dN in dV through binary collisions. For a quantification it is instructive to express the collision integral as a balance equation of an in- and outflux of the phase-space volume element dV as $\mathcal{Q}(f, f) = Q_{\text{in}} - Q_{\text{out}}$. The number of collisions during dt causing an in- or outflux is given by $dN_{\text{in/out}} = Q_{\text{in/out}} dV dt$.

While the influx corresponds to a collision of two particles with initial velocities $\{\mathbf{c}', \mathbf{c}'_1\}$ and post-collision velocities $\{\mathbf{c}, \mathbf{c}_1\}$, the outflux is given by a collision of type $\{\mathbf{c}, \mathbf{c}_1\} \rightarrow \{\mathbf{c}', \mathbf{c}'_1\}$.

Assuming binary collisions with two uncorrelated particles, i.e. molecular chaos, makes the quantification of the collision integral tractable and the number of colliding pairs for the outflux is given by $dN_{\mathbf{c}, \mathbf{c}_1} = dN dN_1$, where $dN_1 = f(\mathbf{c}_1, \mathbf{x}, t) d^3 \mathbf{c}_1 dV_c$ and $dV_c = |\mathbf{c} - \mathbf{c}_1| \Theta d\Omega$ is the collision volume for the classical scattering problem with the differential cross section Θ and the solid angle $d\Omega$. Note that for a central force interaction between molecules, the differential cross section solely depends on the deflection angle, which can be derived through classical mechanics for a given interaction potential. In the simple case of hard elastic spheres with diameter d , geometrical considerations yield a differential cross section of $\Theta = d^2/4$. The number of colliding pairs is given by $dN_{\mathbf{c}, \mathbf{c}_1} = [f(\mathbf{c}, \mathbf{x}, t) f(\mathbf{c}_1, \mathbf{x}, t) |\mathbf{c} - \mathbf{c}_1| \Theta d\Omega] d^3 \mathbf{c} d^3 \mathbf{x} dt$ and the rate of loss or outflux is thus obtained by integration over \mathbf{c}_1 and $d\Omega$, yielding

$$Q_{\text{out}}(\mathbf{c}, \mathbf{x}, t) = \int \int f(\mathbf{c}, \mathbf{x}, t) f(\mathbf{c}_1, \mathbf{x}, t) |\mathbf{c} - \mathbf{c}_1| \Theta d\Omega d^3 \mathbf{c}_1 \quad (2.2)$$

Using analog reasoning and the irreversibility of mechanical motion, a similar expression can be obtained for the influx. This yields the collision

integral as

$$\mathcal{Q}(f, f) = \int \int [f(\mathbf{c}', \mathbf{x}, t)f(\mathbf{c}'_1, \mathbf{x}, t) - f(\mathbf{c}, \mathbf{x}, t)f(\mathbf{c}_1, \mathbf{x}, t)] |\mathbf{c} - \mathbf{c}_1| \Theta d\Omega d^3\mathbf{c}_1. \quad (2.3)$$

It is mentioned that due to the point particle approximation, the collision integral is local in physical space and only non-local in velocity space.

A detailed discussion and derivation of the Boltzmann equation can be found in [51, 52, 116, 118, 119] among others.

2.1.1 Properties of the Boltzmann equation

Below, a non-exhaustive list of the most important properties of the Boltzmann equation and the collision operator is presented.

2.1.1.1 Moments

The hydrodynamic fields such as density ρ , momentum density $\rho\mathbf{u}$ and the energy density ρE can be obtained by the low order moments of the distribution function as

$$\rho(\mathbf{x}, t) = \int f(\mathbf{x}, \mathbf{c}, t) d\mathbf{c}, \quad (2.4)$$

$$\rho\mathbf{u}(\mathbf{x}, t) = \int \mathbf{c} f(\mathbf{x}, \mathbf{c}, t) d\mathbf{c}, \quad (2.5)$$

$$\rho E(\mathbf{x}, t) = \rho(u^2 + Dk_B T/m) = \int \mathbf{c}^2 f(\mathbf{x}, \mathbf{c}, t) d\mathbf{c}, \quad (2.6)$$

where D , k_B , T and m denote the dimensionality, the Boltzmann constant, the temperature and the particle mass, respectively.

2.1.1.2 Conservation laws

The conservation of the number of particles, momentum and energy is a consequence of the elastic collision and implies

$$\int \mathcal{Q}(f, f) (\chi + \boldsymbol{\zeta} \cdot \mathbf{c} + \lambda c^2) d\mathbf{c} = 0, \quad (2.7)$$

where χ , $\boldsymbol{\zeta}$ and λ are arbitrary constants. Hence, the local changes in time of the hydrodynamic fields are a consequence of a spatial redistribution in space of the probability functions.

2.1.1.3 Vanishing collision integral

For a vanishing collision integral $\mathcal{Q}(f, f) = 0$, the detailed balance

$$f(\mathbf{c}, \mathbf{x}, t)f(\mathbf{c}_1, \mathbf{x}, t) = f(\mathbf{c}', \mathbf{x}, t)f(\mathbf{c}'_1, \mathbf{x}, t) \quad (2.8)$$

holds for almost all velocities.

For the class of functions of the form

$$f = \exp(\chi + \boldsymbol{\zeta} \cdot \mathbf{c} + \lambda \mathbf{c}^2), \quad (2.9)$$

the collision integral vanishes and parametrization on the locally conserved quantities, namely, density, momentum and energy yields the well known Maxwell distribution function

$$f^{\text{eq}}(\mathbf{c}, \rho, \mathbf{u}, T) = \rho \left(\frac{m}{2\pi k_B T} \right)^{D/2} \exp\left(-\frac{m(\mathbf{c} - \mathbf{u})^2}{2k_B T} \right). \quad (2.10)$$

2.1.1.4 Local entropy production

Assuming the integral exists, the local entropy production inequality

$$\sigma(\mathbf{x}, t) = -k_B \int \mathcal{Q}(f, f) \ln f d\mathbf{c} \geq 0, \quad (2.11)$$

holds for any distribution function. Note that the entropy production $\sigma(\mathbf{x}, t)$ vanishes at the point of $\mathcal{Q}(f, f) = 0$, which includes the local Maxwellian as given by Eq. (2.10). Thus, the collision relaxes the distribution function f towards the local Maxwellian.

2.1.1.5 H -theorem

The H -theorem provides a quantitative measure of macroscopic irreversibility through the H -function, which is defined as

$$H(f) = \int f \ln f d\mathbf{c}. \quad (2.12)$$

The local, space-independent H -theorem postulates that the rate of change of H is proportional to the entropy production as

$$\frac{dH}{dt} = -\frac{1}{k_B} \sigma. \quad (2.13)$$

This implies the relaxation of the distribution functions towards the unique global Maxwell distribution function and the monotonic decay of the H -function. As a consequence, the local Maxwellian is the minimum of the H -function subject to fixed, locally conserved hydrodynamic fields.

In case of space-dependence, the local entropy density is defined as

$$S(\mathbf{x}, t) = -k_B H(\mathbf{x}, t), \quad (2.14)$$

which obeys its balance equation

$$\partial_t S(\mathbf{x}, t) + \partial_\alpha J_\alpha(\mathbf{x}, t) = \sigma(\mathbf{x}, t), \quad (2.15)$$

where $\mathbf{J}_s = -k_B \int \mathbf{c} f \ln f d\mathbf{c}$ is the entropy flux. Note that the contribution of \mathbf{J}_s to the total entropy $S_{\text{tot}} = \int S d\mathbf{x}$ vanishes for suitable boundary conditions (e.g., specular reflection), which yields the global H-Theorem $\partial_t S(\mathbf{x}, t) = \sigma_{\text{tot}}$ with $\sigma_{\text{tot}} = \int \sigma d\mathbf{x}$. For generalized boundary conditions, the entropy flux is non-zero and requires a modification of the H-theorem (see, e.g., [50]).

2.1.2 Bhatnagar-Gross-Krook model

The Boltzmann equation is an integro-differential equation and its non-linearity poses significant challenges. This promoted the development of various approximative solution strategies and kinetic models for the collision integral. Arguably the most prominent and widely used model, which obeys the properties of the Boltzmann collision integral is the Bhatnagar-Gross-Krook (BGK) model [24]. The approximate collision integral reads

$$\mathcal{Q}_{BGK} = \frac{1}{\tau} (f^{\text{eq}}(\mathbf{c}, \rho(f), \mathbf{u}(f), T(f)) - f), \quad (2.16)$$

where τ is the characteristic time for relaxation towards the local Maxwellian, i.e. relaxation time, which is of same order of magnitude than the time between particle collisions. Note that despite a significant simplification compared to the Boltzmann collision integral, the BGK approximation remains nonlinear as it is a nonlinear function of the lower order moments, namely density, momentum and energy. In contrast, the Boltzmann collision integral is nonlinear in the distribution function itself. Other models of the collision integral include generalized BGK models to incorporate quasi-equilibrium states [117] or Fokker-Planck models [198].

2.1.3 Kinetic algorithms

Given the tremendous complexity of the five dimensional collision integral, the solution of the Boltzmann equation requires sophisticated numerical procedures. In general, one can distinguish statistical and deterministic approaches to evaluate the collision term.

While statistical methods like Direct Simulation Monte-Carlo (DSMC) [29] are well suited for high Knudsen and Mach number flows, the large computational cost and slow convergence renders their application impractical in the continuum limit.

On the other hand, deterministic models that rely on velocity space discretization made the first connection to Navier-Stokes hydrodynamics. In particular, it was the development of the lattice-gas (LG) model [104], which reproduced Navier-Stokes with embarrassingly simple discrete kinetic equations. The LG is consistent with the H -theorem and the equilibria maximize the Fermi-Dirac entropy. However, the lack of Galilean invariance and large statistical noise precluded any serious hydrodynamic applications. By pre-averaging of the LG via a Boltzmann formulation, this issue was resolved and subsequent improvements lead to the lattice Boltzmann method [55, 56, 133, 134, 174, 235, 281], which made simulations of hydrodynamics feasible.

In the following, the lattice Boltzmann method and its entropic versions are presented.

2.2 The lattice Boltzmann method

As previously mentioned in section 2.1, the lattice Boltzmann method belongs to the class of discrete velocity models. Thus, let us introduce a set of discrete velocity vectors $\mathbf{c}_i, i = 1, \dots, Q$ and the corresponding discrete particle distribution function, so-called populations, $f_i(\mathbf{x}, t)$. In the following, unless stated otherwise, the summation over the index i is understood to be in the range of $i = 1, \dots, Q$. Except for the population index i , Einstein's summation convention is applied for repeated subscript indices. To derive the lattice Boltzmann equation, let us start with the velocity-discrete Boltzmann equation for the population f_i , which reads as

$$\partial_t f_i + c_{i,\alpha} \partial_\alpha f_i = \mathcal{Q}_i, \quad (2.17)$$

where \mathcal{Q}_i denotes the velocity discrete collision operator. For the discretization in time Eq. (2.17) is integrated along its characteristics $\mathbf{x} + \mathbf{c}_i \delta t s$ and $t + \delta t s$ for $s \in [0, 1]$ with the time step δt . The collision operator is evaluated using the trapezoidal rule, which eventually yields the second-order, implicit equation

$$f_i(\mathbf{x} + \mathbf{c}_i \delta t, t + \delta t) - f_i(\mathbf{x}, t) = \frac{\delta t}{2} [\mathcal{Q}_i(f(\mathbf{x}, t)) + \mathcal{Q}_i(f(\mathbf{x} + \mathbf{c}_i \delta t, t + \delta t))] + \mathcal{O}(\delta t^3) \quad (2.18)$$

For practical purpose, it is crucial to obtain an explicit scheme from the implicit Eq. (2.18). This can be achieved by a variable transformation of the form

$$f_i \rightarrow g_i = f_i - \frac{\delta t}{2} \mathcal{Q}_i(f), \quad (2.19)$$

for which the locally conserved quantities are equivalent and $g_i^{\text{eq}} = f_i^{\text{eq}}$. As we will see in the following section, various proposals for different LB models only differ in the choice of the collision operator. The classical LBM employs a velocity discrete version of the BGK collision model of Eq. (2.16), which we will use in the following to demonstrate the general construction of LBM. The discrete BGK collision reads

$$\mathcal{Q}_{i,BGK} = -\frac{1}{\tau} (f_i - f^{\text{eq}}). \quad (2.20)$$

Imposing the variable transform for the BGK collision yields

$$\mathcal{Q}_{i,BGK}(g) = \left(1 + \frac{\delta t}{2\tau}\right) \mathcal{Q}_{i,BGK}(f). \quad (2.21)$$

Thus, Eq. (2.18) can be expressed in terms of g as

$$g_i(\mathbf{x} + \mathbf{c}_i \delta t, t + \delta t) = g_i(\mathbf{x}, t) + \left(\frac{2\delta t}{2\tau + \delta t}\right) [g_i^{\text{eq}}(\mathbf{x}, t) - g_i(\mathbf{x}, t)] \quad (2.22)$$

or in a more conventional manner, the fully discrete lattice BGK (LBGK) model reads

$$g_i(\mathbf{x} + \mathbf{c}_i \delta t, t + \delta t) = g_i(\mathbf{x}, t) + \omega (g_i^{\text{eq}} - g_i), \quad (2.23)$$

where the left-hand side represents the stream operator, which advects the populations along \mathbf{c}_i and the right hand side the collision for which $\omega =$

\mathbf{c}_i	W_i
(0, 0, 0)	8/27
(±1, 0, 0), (0, ±1, 0), (0, 0, ±1)	2/27
(±1, ±1, 0), (±1, 0, ±1), (0, ±1, ±1)	1/54
(±1, ±1, ±1)	1/216

Table 2.1: $D3Q27$ lattice.

$\frac{2\delta t}{2\tau + \delta t} = \alpha\beta$ with $\alpha = 2$. Note that despite equivalent local conservation and equilibria of g and f , the functions g are strictly speaking not populations as they can become negative. In the following, we will not distinguish the two and adopt standard notation by renaming g to f . For further discussions on the construction of LBM and its link to kinetic theory the reader is referred to [38, 162].

For a complete LB algorithm, the velocity set and the equilibrium population remain to be specified. In the classical LBM for incompressible flows, the velocity set or lattice can be constructed by the quadrature points of the third-order, D -dimensional Gauss-Hermite quadrature and their corresponding weight W_i [8, 314]. Thus in one dimension, we have a velocity set $\{0, \pm 1\}$ with the corresponding weights $\{2/3, 1/6\}$. This corresponds to the so-called $D1Q3$ lattice, where D and Q indicate the number of dimensions and velocity vectors, respectively. In higher dimensions, such as the $D2Q9$ or $D3Q27$ lattice, the discrete velocity vectors can be constructed by tensor products of the $D1Q3$ lattice and the weights can be obtained by multiplying weights associated with each component direction. In particular, the three dimensional $D3Q27$ lattice, which, unless stated otherwise, is used for all simulations in the remainder of this thesis, is given in table 2.1.

Finally, in classical LBM, the equilibrium distribution function can be obtained by a truncated expansion of the Maxwell-Boltzmann distribution on the nodes of the third order Gauss-Hermite quadrature. The quadratic approximation reads

$$f_i^{\text{eq}} = \rho W_i \left(1 + \frac{u_\alpha c_{i,\alpha}}{T_0} + \frac{u_\alpha u_\beta (c_{i,\alpha} c_{i,\beta} - T_0 \delta_{\alpha\beta})}{2T_0^2} \right), \quad (2.24)$$

where the lattice specific reference temperature T_0 is related to the speed of sound c_s by $T_0 = c_s^2 = 1/3$ for the $D3Q27$. Note that alternative ways

to construct suitable lattices and equilibria have been developed in the context of the entropic lattice Boltzmann method, which is reviewed in section 2.3 [6, 62].

In the hydrodynamic limit (see, e.g. [325]), the LBGK model recovers the Navier-Stokes equations with a kinematic shear viscosity of

$$\nu = c_s^2 \delta t \left(\frac{1}{2\beta} - \frac{1}{2} \right). \quad (2.25)$$

These ingredients complete the classical lattice Boltzmann scheme. For the numerical evaluation of Eq. (2.23), one typically sets $\delta t = 1$ and splits Eq. (2.23) streaming and collision steps as follows:

- Streaming:

$$f_i(\mathbf{x}, t) \rightarrow f_i(\mathbf{x} + \mathbf{c}_i, t) \quad (2.26)$$

- Collision of the post-advection populations $f_i^*(\mathbf{x}, t)$:

$$f_i^*(\mathbf{x}, t) \rightarrow f_i^*(\mathbf{x}, t) + \omega (f_i^{\text{eq}} - f_i^*(\mathbf{x}, t)). \quad (2.27)$$

By exploiting the lattice with spacing c and assigning grid points to the lattice nodes, it follows that if \mathbf{x} is a grid point then $\mathbf{x} \pm \mathbf{c}_i \delta t$ is a grid point as well for $\delta t = 1$. Thus, propagation of the population is exact for a Cartesian grid of spacing c .

Note that the collision step can be regarded as a over-relaxation of the population. To elaborate, let us rewrite Eq. (2.23) as

$$f_i(\mathbf{x} + \mathbf{c}_i, t + 1) = f_i' = (1 - \beta) f_i(\mathbf{x}, t) + \beta f_i^{\text{mirr}}(\mathbf{x}, t), \quad (2.28)$$

where the streaming is accounted for by the left-hand side and the post-collision state f_i' is represented on the right-hand side by a convex linear combination between the population $f_i(\mathbf{x}, t)$ and the maximally over-relaxed mirror state $f_i^{\text{mirr}}(\mathbf{x}, t)$. Thus, for an initial state f_i^{init} , the fully discrete kinetic equation given by Eq. (2.28), relaxes the population vector beyond the equilibrium state for $\beta > 1/2$. This is termed over-relaxation and its magnitude is determined by the relaxation parameter $\beta \in [0, 1]$, which is related to viscosity by Eq. (2.25) and by the maximally over-relaxed mirror state. Note that all lattice Boltzmann models differ only in the realization of the mirror state and the LBGK model defines it as

$$f_i^{\text{mirr}}(\mathbf{x}, t) = 2f_i^{\text{eq}} - f_i. \quad (2.29)$$

The LBGK model remains a popular choice due to its simplicity and efficiency. However, as stated above, severe stability problems limit its usage to resolved, low Reynolds number flows. A remedy was found in entropic lattice Boltzmann models, which will be reviewed in the following.

2.3 The Entropic lattice Boltzmann method

The entropic lattice Boltzmann method (ELBM) [6, 32, 153, 161, 164, 327] differs from the LBGK model by the fact that it restores the second law of thermodynamics, i.e. the H -theorem, which was lost during the discretization process. To that end, a discrete version of the H -function [6, 164] was introduced and reads

$$H(f) = \sum_i f_i \ln \left(\frac{f_i}{W_i} \right). \quad (2.30)$$

The equilibrium can now be defined as the minimum of the discrete H -function Eq. (2.30) subject to the constraints of local conservation laws for mass, momentum and energy:

$$\min \left\{ H(f) = \sum_i f_i \ln \left(\frac{f_i}{W_i} \right) \right\}, \quad \text{s.t.} \quad \sum_i \{1, \mathbf{c}_i, c_i^2\} f_i = \{\rho, \rho \mathbf{u}, 2\rho E\}. \quad (2.31)$$

In the isothermal case, energy conservation is usually neglected. On the $D1Q3$ lattice and its higher dimensional extensions an analytical solution to the minimization problem exists [6] and reads

$$f_i^{\text{eq}} = \rho W_i \prod_{\alpha=1}^D \left(2 - \sqrt{1 + 3u_\alpha^2} \right) \left(\frac{2u_\alpha + \sqrt{1 + 3u_\alpha^2}}{1 - u_\alpha} \right)^{c_{i\alpha}}. \quad (2.32)$$

Note that the expansion of the equilibrium in Eq. (2.32) to second order is identical to the polynomial expression Eq. (2.24) used in the standard LBM.

Having defined the equilibrium through the notion of a discrete H -function, we proceed with the entropic time-stepping to restore the discrete-time analog of the H -theorem for which the total entropy $\hat{H}(t) = \sum_{\mathbf{x}} H(f(\mathbf{x}, t))$ is not increasing in time. To that end, the mirror state is defined as

$$f_i^{\text{mirr}} = f_i + \alpha(f_i^{\text{eq}} - f_i) \quad (2.33)$$

where the over-relaxation parameter α is given by the positive root of the entropy condition

$$H(f + \alpha(f^{\text{eq}} - f)) = H(f). \quad (2.34)$$

The entropy condition equates the entropy levels of the mirror and its pre-collision value f . Due to the convexity of $H(f)$, the entropy condition ensures over-relaxation with $\alpha > 1$ and $H(f(\beta)) < H(f)$ if the non-trivial solution α exists. Therefore, the production of entropy is only due to the parameter $\beta \in [0, 1]$, which is related to viscosity. For a sufficient grid resolution, the populations stay close to the local equilibrium and the maximal over-relaxation is automatically computed as $\alpha = 2$ [161]. This implies that for resolved simulations the ELBM results in the LBGK model, which recovers the Navier-Stokes equation with the viscosity as defined by Eq. (2.25). However, in under-resolved simulations, the entropic estimate α may result values smaller and larger than two. The macroscopic effect of choosing the over-relaxation parameter adaptively can be interpreted as a fluctuating effective viscosity

$$\nu_{\text{eff}} = c_s^2 \left(\frac{1}{\alpha\beta} - \frac{1}{2} \right). \quad (2.35)$$

While for $\alpha < 2$ the apparent, local viscosity is greater than the nominal one and thus tends to smoothen the flow field, lattice sites where $\alpha > 2$ have a lower effective viscosity, which corresponds to an enhancement of the local flow field.

A few comments regarding the practical realization of ELBM are in order. The roots of the nonlinear function Eq. (2.34) are computed numerically in every time step and at every grid point using a Newton-Raphson (NR) scheme with a tolerance of 10^{-5} for convergence of α . In practice, the NR scheme takes on average 3 to 4 iteration to converge. When the NR scheme does not find a solution in 15 iterations, we use the LBGK over-relaxation $\alpha = 2$.

To conclude, the adherence of the ELBM to the second law of thermodynamics prevents fatal instabilities and yields a parameter-free, locally adaptive and nonlinearly stable numerical scheme.

For further discussions and applications of ELBM, the reader is referred to [9–11, 61, 63, 159, 160, 163, 165].

2.4 Entropic multi-relaxation time lattice Boltzmann method

The LB models presented so far belong to the class of single-relaxation time models. However, one possible extension is to consider multiple relaxation parameters. These so-called multi-relaxation time (MRT) models exploit the fact that the dimensionality of the kinetic system is typically much larger than required to recover the Navier-Stokes equation in the hydrodynamic limit. Thus, the non-hydrodynamic, higher-order moments can be relaxed independently with the aim to increase stability. At which rate these moments are relaxed is a priori not clear and for long was chosen by flow dependent fine tuning [112, 187]. This ambiguity was resolved in the work [157] by extending the concept of the entropic LBM to multiple relaxation times, termed entropic multi-relaxation time lattice Boltzmann or KBC (Karlin-Bösch-Chikatamarla) method. At variance with the ELBM as presented above, the introduction of multiple relaxation times allows the KBC model to avoid a fluctuating viscosity and keep it at its nominal value while retaining stability.

In the following, we will outline the construction of the KBC model. Let us recall that the set of natural moments of the $D3Q27$ -lattice is given by

$$\rho M_{pqr} = \sum_i f_i c_{ix}^p c_{iy}^q c_{iz}^r \quad p, q, r \in \{0, 1, 2\}, \quad (2.36)$$

yielding the conservation laws as the first $1 + D$ moments and the pressure tensor $\mathbf{\Pi}$ as the second-order moments. Higher-order moments lack a direct physical interpretation in the athermal case. The moment system of Eq. (2.36) can be written in matrix notation as

$$\rho \mathbf{M} = \mathbf{C} \mathbf{f}, \quad (2.37)$$

where \mathbf{C} is the coefficient matrix and \mathbf{M} the corresponding moments according to Eq. (2.36). By inverting the matrix \mathbf{C} , the population can be expressed in terms of its moments by

$$\mathbf{f} = \rho \mathbf{C}^{-1} \mathbf{M}. \quad (2.38)$$

Thus, the moment representation spans a basis in which a population can equivalently be expressed (see Appendix A.1 for the explicit expressions on

the $D3Q27$ lattice). Note that the moment basis is not unique and, e.g., a central moment basis can be applied analogously [40]. However, in the scope of this thesis, only the natural moment basis was employed. Thus, in the collision step, by applying the moment transform to the lattice Boltzmann equation allows for individual moments to be relaxed at different rates. To complete the advection, the populations are again obtained by Eq. (2.38). This is the main idea of most multi-relaxation time models.

For the KBC model, the moment representation is used to decompose the population f_i into three parts as

$$f_i = k_i + s_i + h_i, \quad (2.39)$$

where k_i indicates the kinematic part and depends only on the conserved quantities. The shear part is denoted by s_i and necessarily includes the deviatoric stress tensor $\mathbf{\Pi}' = \mathbf{\Pi} - D^{-1}Tr(\mathbf{\Pi})\mathbf{I}$. Further non-conserved moments may however be included in s_i , yielding a family of KBC models. The higher-order moments correspond to h_i , which contains all remaining moments that are not included in k_i or s_i . Using this decomposition, the mirror state can be expressed as

$$f_i^{\text{mirr}} = k_i + (2s_i^{\text{eq}} - s_i) + ((1 - \gamma)h_i + \gamma h_i^{\text{eq}}), \quad (2.40)$$

where s_i^{eq} and h_i^{eq} indicate s_i and h_i evaluated at equilibrium and the parameter γ is the relaxation rate of the higher-order moments. Note that due to the fixed over-relaxation of the stresses, any specification of γ recovers the Navier-Stokes equation with the shear viscosity as given by Eq. (2.25) and the special case of $\gamma = 2$ results in the LBGK model.

In this thesis, we choose the shear part s_i to only include the mandatory deviatoric stress $\mathbf{\Pi}'$ and lump all other moments in h_i (see, e.g., Ref. [40] for a thorough study of various KBC-realizations), yielding the macroscopic equations as obtained through the standard Chapman-Enskog analysis as

$$\partial_t \rho = -\nabla \cdot (\rho \mathbf{u}), \quad (2.41)$$

$$\begin{aligned} \partial_t \mathbf{u} = & -\mathbf{u} \cdot \nabla \mathbf{u} - \rho^{-1} \nabla p + \\ & \rho^{-1} \nabla \cdot [\nu \rho (\nabla \mathbf{u} + \nabla \mathbf{u}^\dagger - 2D^{-1} \mathbf{I} \nabla \cdot \mathbf{u})] + 2D^{-1} \rho^{-1} \nabla [\xi \rho \nabla \cdot \mathbf{u}], \end{aligned} \quad (2.42)$$

where the pressure is given by $p = c_s^2 \rho$. It is important to notice that the bulk viscosity for the present KBC model (only the deviatoric stress tensor

is included in s_i) is related to the parameter γ as

$$\xi = c_s^2 \left(\frac{1}{\gamma\beta} - \frac{1}{2} \right). \quad (2.43)$$

This is not the case if the shear part s_i additionally includes $\text{Tr}(\mathbf{\Pi})$, which leads to $\xi = \nu$. The main idea of KBC lies now in the specification of γ , which is not tuned as in various other MRT models but rather computed locally in every time step and at every grid point by minimizing the discrete entropy function (see Eq. (2.30)) of the post-collision state f'_i . Carrying out the optimization leads to the following condition for γ ,

$$\sum_i \Delta h_i \ln \left[1 + \frac{(1 - \beta\gamma)\Delta h_i - (2\beta - 1)\Delta s_i}{f_i^{\text{eq}}} \right] = 0, \quad (2.44)$$

where $\Delta s_i = s_i - s_i^{\text{eq}}$ and $\Delta h_i = h_i - h_i^{\text{eq}}$ denote the deviations from equilibrium. By introducing the entropic scalar product as $\langle X|Y \rangle = \sum_i (X_i Y_i / f_i^{\text{eq}})$ and an expansion of Eq. (2.44) to the first non-vanishing order of $\Delta s_i / f_i^{\text{eq}}$ and $\Delta h_i / f_i^{\text{eq}}$, an analytic approximation for the relaxation parameter γ may be found as

$$\gamma = \frac{1}{\beta} - \left(2 - \frac{1}{\beta} \right) \frac{\langle \Delta s | \Delta h \rangle}{\langle \Delta h | \Delta h \rangle}. \quad (2.45)$$

Compared to numerically solving Eq. (2.44), the approximation as given in Eq. (2.45) has proven to be sufficient for all tested cases. For further discussions on the KBC model, the reader is referred to [39, 40].

2.5 Conclusion

To summarize, in this chapter we have introduced and reviewed the lattice Boltzmann method. We started with the fundamentals of kinetic theory and statistical mechanics, derived the Boltzmann equation and discussed some of its properties and approximative solution strategies.

From these basic ingredients and as a stepping stone for more advanced models, the construction of the classical LBGK model was outlined. While the LBGK remains popular due to its simplicity and extraordinary efficiency, more sophisticated models are needed for complex flows such as turbulence. To that end, the class of entropic LBM was introduced. First

its single-relaxation time formulation and subsequently its extension to multiple relaxation times, which retains the local viscosity at its nominal value.

Unless stated otherwise, we employ the KBC model as presented above in the remainder of this thesis. Having a good model for the bulk flow, we proceed by a discussion of how to incorporate complex, moving geometries into the framework of KBC.

Chapter 3

Complex and moving geometries

3.1 Introduction

Flows induced by complex, moving and deforming geometries bear many intriguing phenomena, which directly impact science and engineering ranging from industrial applications for the optimization of internal combustion engines, turbines and energy harvesting devices to investigations regarding the propulsion mechanisms of animals and robotic devices among many others (see, e.g., [142, 166, 199, 200, 306]).

Besides the valuable insight from experimental studies, light may be shed on these complex mechanisms through numerical simulations. However, for reliable and predictive simulations, accuracy, robustness and efficiency of the underlying numerical treatment is crucial.

Generally speaking, one can distinguish between body-conforming or body-fitted and non-conforming methods for the simulation of such flows. Most conventional methods are based on body-fitted grids for which the computational mesh conforms to the moving and deforming geometry. While the main advantage is that the desired boundary conditions can easily be imposed, the generation of the moving meshes for complex geometries are computationally expensive and require sophisticated procedures to avoid severe mesh distortion to preserve accuracy [130, 251, 338, 340]. This issue is particularly relevant for flexible geometries undergoing large, unprescribed deformations as discussed for fluid-interaction problems in chapter

8. The predominant approach for body-fitted methods is the arbitrary Lagrangian-Eulerian formulation (ALE) [1, 137] but others such as space-time finite element methods [337, 338] have also shown success.

On the other hand, to avoid expensive (re-)meshing procedures, viable alternatives were found in non-conforming methods. Its most prominent representative is the immersed boundary method (IBM), which was first introduced by Peskin [274] for the simulation of blood flow in the human heart. An additional advantage of these methods is that they allow the use of Cartesian meshes for which extraordinary robust and efficient numerical solvers exist.

In the scope of this thesis, both a realization of a body-fitted approach, as well as a non-conforming approach have been developed for the KBC model. The topic unstructured meshes within the realm of LBM is still a very active area of research without a clear superior approach. Notable is the recent development of the so-called semi-Lagrangian off-lattice Boltzmann method (SLLBM) as proposed in [177], which was extended to the KBC model and wall-bounded flows in the scope of this thesis (see chapter 4). However, due to its advantages (see above and chapter 4), the main focus of this thesis was on non-conforming methods.

In the context of LBM and non-conforming methods, one can again distinguish between Cartesian and immersed boundary methods, which we will briefly review below.

Immersed boundary methods The IBM solves the governing Navier-Stokes equations on a fixed, underlying Eulerian grid, while fluid-structure interfaces are described by immersed Lagrangian surface structures. Their effect on the flow field, i.e. the coupling between the fixed Eulerian and the Lagrangian surface mesh is accounted for by introducing fictitious body forces, which are distributed among the neighboring Eulerian grid points using a smoothed approximation of the Dirac delta function.

Since the original IBM [274], which was developed for deformable, elastic structures, various derivatives, adopting different methods of computing the body forces have been developed and extended its capabilities to handle more general cases such as stationary or moving rigid bodies (see, e.g., [140, 242, 276, 320] for recent reviews).

The treatment of the boundary force is the central issue in IBM and can

be imposed either explicitly or implicitly. Conventional explicit methods include penalty methods [275], direct forcing methods [89, 94] and momentum exchange methods [256].

A common issue of explicit schemes is that the no-slip condition is not satisfied to sufficient accuracy, which may lead to spurious behavior such as streamlines penetrating the solid object.

On the other hand a remedy was sought in implicit methods, where the boundary force is obtained by solving a linear system either directly or by iterative procedures. Notable suggestions for implicit schemes in the realm of LBM include the implicit velocity correction scheme as proposed and applied in, e.g., [316, 369–372]. Further, in [330] an iterative procedure was employed to satisfy the no-slip condition more accurately. The proposed scheme was then extended to higher order of accuracy in [329] and has shown promising results for the simulation of a butterfly-like wing-body model in [331].

However, as pointed out by a number of studies [124, 185, 329], while the velocity obtained by IBM is continuous across the boundary, its gradients exhibit a discontinuity on the boundary, which eventually degrades the order of accuracy of IBM. Thus, the majority of IB schemes are first- or less than second-order accurate.

Therefore, IBM is widely perceived to lose its benefits (no re-meshing and efficient flow solvers on a fixed grid) for high Reynolds number flows. This promoted further developments of higher-order accurate schemes and adaptive grid refinement techniques [121, 209, 298, 313, 329, 353]. However, particularly in the context of LBM, the simulation of three-dimensional turbulence remains a challenge for IBM.

Another issue to be considered within IBM is related to the fact that the fluid domain spans the entire computational domain, i.e. also within the solid object. Thus the fluid inside the solid is also affected by the body forces. While the flow field outside the solid might not be affected by the internal fluid, the computation of the force and torque are altered if obtained by standard procedures, i.e. negative sum of the body forces. This so-called internal mass effect was investigated by a few studies [95, 315, 330, 336, 352], suggesting that the error in the force evaluation is already significant for relatively low Reynolds number flows and requires suitable rigid body approximations (see, e.g., [330] for a comparative study

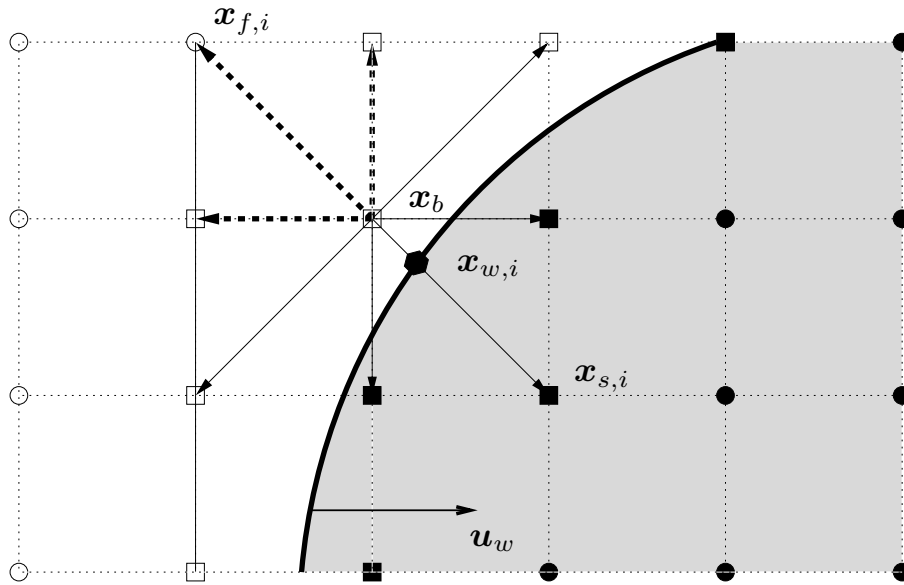


Figure 3.1: The unknown populations at the boundary node \mathbf{x}_b are represented by the dashed arrows. \bullet : Solid nodes. \circ : Fluid nodes. \blacksquare : Solid boundary nodes. \square : Fluid boundary nodes.

of various approximations).

However, due to its simple implementation and extraordinary flexibility the IBM remains the common choice for low Reynolds number flow simulations involving complex, moving geometries.

Cartesian grid methods In the context of Cartesian grid methods, various boundary conditions for flat, curved and moving wall boundaries can be found in the lattice Boltzmann literature. In contrast to IBM, it is not by exertion of a body force that the no-slip wall boundary condition is imposed. The general situation at the boundary is depicted in figure 3.1. In order to complete the streaming step in the LB algorithm, the set of populations \bar{D} advected from a solid node \mathbf{x}_s to a fluid boundary node \mathbf{x}_b are unknown and require to be specified in accordance with the desired boundary conditions. Thus, the problem of imposing boundary conditions reduces to finding a good approximation for these *missing* populations. The difficulty lies in the fact that while the macroscopic variables are readily obtained from the populations the reverse procedure is less obvious. While various propositions exist in the literature (see, e.g., [193, 254] for comparisons and reviews), only a few have shown to stable and accurate and thus limited for long to resolved and moderate Reynolds number

flows.

For its simplicity the most popular no-slip wall boundary condition in the context of Cartesian grid methods is undoubtedly the so-called bounce-back boundary condition. The bounce-back boundary condition replaces the missing population with the population associated the velocity pointing in the opposite direction, i.e. the incoming populations are reflected at the boundary. For flat walls various other boundary conditions have been proposed [146, 191, 319, 398] and are reviewed in [193].

For curved boundaries, most commonly interpolation or extrapolation schemes are applied to particle distribution to incorporate the exact boundary location and compensate the crude staircase approximation of the geometry by the underlying uniformly spaced grid of the LBM. (see, e.g. [43, 97, 122, 186, 236, 395] and for reviews [193, 254]). A popular representative of such kind is the interpolated bounce-back boundary condition (IBB) as presented in the article of [186]. In this context, an extension to moving boundaries was proposed by introducing a force expressed in terms of the populations in order to account for the momentum exerted from the boundary onto the fluid. However, due to the highly fluctuant nature of the populations, interpolation or extrapolation schemes are prone to numerical instabilities. Thus, despite the fact that stability issues in the bulk flow were overcome by introduction of a discretized entropy function, the simulation of complex engineering applications remained unfeasible for long due to a lack of accurate kinetic boundary conditions in resolved and under-resolved simulations. In particular, spurious discontinuities or shocks, which are triggered at the boundary and propagate into the bulk have been observed for the simulation of wall-bounded turbulence [189, 322]). This issue partially solved for stationary walls by the so-called Tamm-Mott-Smith (TMS) boundary condition as proposed by [59]. Furthermore, an interesting realization of the bounce-back for curved geometries can be found for a recent, so-called crystallographic LBM, in [252]. However, a universal approach for generic, moving wall boundaries, which is consistent with entropy-based LBM has not been developed.

To that end, a novel boundary condition capable of handling complex and moving geometries is proposed. Similar in spirit to immersed boundary methods, an analog of Grad's approximation for the populations was em-

ployed and used to prescribe the momentum transfer from the solid to the fluid. The idea of the scheme is to impose the boundary condition not directly on the populations itself but in terms of the inherently smoother macroscopic quantities such as density and momentum. Due to its evaluation on the Cartesian grid the common issues arising from the computation and distribution of the body force in the context of IBM are eliminated. Thus, the stability issues are resolved, while exhibiting second-order accuracy and consistency with entropy-based LBM [76]. Universality of the scheme was demonstrated by its extensions to multi-speed lattices and multiphase flows (see [103] and chapter 8, respectively).

For comparison, state-of-the-art IBM according to [330] was implemented in collaboration with Sebastien Röcken, who conducted his Bachelor thesis under my supervision. We found that the iterative procedure to improve the accuracy of the no-slip condition converges and works effectively. Further, IBM is trivially implemented and for a given resolution more efficient compared to the Grad boundary condition as there is no need to compute boundary intersection points (see $\mathbf{x}_{w,i}$ in figure 3.1). As also found in [329], the order of convergence is consistently below two and for classical benchmarks such as the flow past a two-dimensional cylinder, the resolution requirements are much more stringent, i.e. double the resolution compared to the Grad boundary condition is needed for convergent results. This implies an increase of computational cost of a factor of 8 and 16 in two and three dimensions (including time scaling), respectively. This is further confirmed by a comparative study of IBB as a Cartesian grid method and IBM (albeit using the outdated, original IBM) in [272], which highlights the superiority of Cartesian grid methods in terms of accuracy and consequently efficiency in the LB context. Furthermore, regarding stability properties, the IBM exhibits fatal instabilities at $Re \approx 1300$ for the flow past a two-dimensional circular cylinder and the LBGK model. For comparison, using LBGK, the IBB scheme becomes unstable at $Re \approx 200$, while the Grad boundary condition remains stable until $Re \approx 2200$.

The remainder of this chapter is structured as follows. First, the Grad boundary condition for moving and deforming objects is introduced in section 3.2. Validation and assessment of accuracy is subsequently presented in section 3.3.

3.2 Grad boundary condition

We aim at extending the capabilities of KBC models to an accurate implementation of moving and deforming objects. Thus, the boundary conditions as detailed in [76] are briefly summarized.

As mentioned above, in order to complete the streaming step in the LB algorithm, the set of populations \bar{D} advected from a solid node \mathbf{x}_s to a fluid boundary node \mathbf{x}_b are unknown and require to be specified in accordance with the desired boundary conditions (see also figure 3.1). Here, we propose to approximate these *missing* populations by an analog of Grad's moment approximation for the distribution functions. Originally, Grad's moment approximation stems from a truncated expansion in the Hermite velocity polynomials around the local Maxwellian. This results in a parametrization of the distribution in terms of relevant moments, where not only locally conserved but also other pertinent moments may be taken into account. It is worth noting that this is consistent with the notion of maximum entropy as used in bulk flow for the KBC model as the Grad distribution may analogously be derived using maximum entropy or quasi-equilibrium considerations as discussed in [116]. In the athermal case it suffices to include the locally conserved quantities along with the pressure tensor $\mathbf{\Pi}$. Explicitly, the Grad distribution with those contributions reads

$$f_i^*(\rho, \mathbf{u}, \mathbf{\Pi}) = W_i \left[\rho + \frac{\rho}{c_s^2} \mathbf{c}_i \cdot \mathbf{u} + \frac{1}{2c_s^4} (\mathbf{\Pi} - \rho c_s^2 \mathbf{I}) : (\mathbf{c}_i \otimes \mathbf{c}_i - c_s^2 \mathbf{I}) \right], \quad (3.1)$$

where the pressure tensor is approximated as

$$\mathbf{\Pi} = \mathbf{\Pi}^{\text{eq}} + \mathbf{\Pi}^{\text{neq}}, \quad (3.2)$$

with

$$\mathbf{\Pi}^{\text{eq}} = \rho c_s^2 \mathbf{I} + \rho \mathbf{u} \otimes \mathbf{u}, \quad (3.3)$$

$$\mathbf{\Pi}^{\text{neq}} = -\frac{\rho c_s^2}{2\beta} (\nabla \mathbf{u} + \nabla \mathbf{u}^\dagger). \quad (3.4)$$

The full specification of Grad's distribution requires the density ρ , the velocity \mathbf{u} and the pressure tensor to be prescribed. For this purpose, the

concept of target values is introduced. The momentum exerted by the object is accounted for by specifying an appropriate target velocity \mathbf{u}_{tgt} at \mathbf{x}_b , which may be obtained by an interpolation involving the wall velocity $\mathbf{u}_{w,i} = \mathbf{u}(\mathbf{x}_{w,i}, t)$ at the intersection point $\mathbf{x}_{w,i}$ with the object along the velocity vector \mathbf{c}_i and the velocities $\mathbf{u}_{f,i} = \mathbf{u}(\mathbf{x}_{f,i}, t)$ at the adjacent fluid nodes $\mathbf{x}_{f,i} = \mathbf{x}_b + \mathbf{c}_i \delta_t$ for $i \in \bar{D}$. Using an averaged linear interpolation for the target velocity yields

$$\mathbf{u}_{\text{tgt}} = \frac{1}{n_{\bar{D}}} \sum_{i \in \bar{D}} \frac{q_i \mathbf{u}_{f,i} + \mathbf{u}_{w,i}}{1 + q_i}, \quad (3.5)$$

where $n_{\bar{D}}$ is the number of unknown populations and $q_i = \|\mathbf{x}_b - \mathbf{x}_{w,i}\| / \|\mathbf{c}_i\|$. The target density on the other hand has two contributions corresponding to the static and the dynamic part as

$$\rho_{\text{tgt}} = \rho_{\text{stat}} + \rho_{\text{dyn}} \quad (3.6)$$

with

$$\rho_{\text{stat}} = \sum_{i \in \bar{D}} f_i^{\text{bb}} + \sum_{i \notin \bar{D}} f_i, \quad (3.7)$$

$$\rho_{\text{dyn}} = \sum_{i \in \bar{D}} 2W_i \rho_b \frac{\mathbf{c}_i \cdot \mathbf{u}_{w,i}}{c_s^2}, \quad (3.8)$$

where the static part ρ_{stat} is the implied density if one were to use the bounce-back boundary condition to ensure no mass flux through the boundary. The reflected population f_i^{bb} is defined as $f_i^{\text{bb}} = \tilde{f}_i$, where \tilde{f}_i is associated with the velocity vector $\tilde{\mathbf{c}}_i = -\mathbf{c}_i$. The dynamic part ρ_{dyn} accounts for the density alteration caused by the mass displacement by the moving body and $\rho_b = \rho(\mathbf{x}_b, t)$ denotes the post-collision density at the boundary node. The dynamic density may be derived by introducing a forcing term F_i , which is necessary for the displacement. The mass and momentum conservation $\sum_{i=1}^Q F_i = 0$ and $\sum_{i=1}^Q \mathbf{c}_i F_i = \rho_b \mathbf{u}_w$ directly lead to

$$F_i = 2W_i \rho_b \frac{\mathbf{c}_i \cdot \mathbf{u}_w}{c_s^2} \quad (3.9)$$

for the $D3Q27$ -lattice, where the summation over all unknown populations in \bar{D} yields the implied change in density for moving objects.

Finally, the pressure tensor is prescribed by computing $\nabla \mathbf{u}$ using a finite difference scheme and the velocity values from the previous time step and

evaluating Eqs. (3.3)-(3.4). The boundary condition is therefore not local anymore but accesses additional information from the neighboring cells in order to compute the velocity gradients. As shown by [193], this additional information is crucial in terms of accuracy. In particular, the velocity gradient along the x -axis and similarly for the y - and z -coordinate may be approximated as

$$\left. \frac{\partial \mathbf{u}}{\partial x} \right|_{x=x_b} = \frac{\mathbf{u}(\mathbf{x}_f) - \mathbf{u}(\mathbf{x}_w)}{x_f - x_w}, \quad (3.10)$$

where x_w, x_f denote the location of the wall intersection and the next fluid node (w.r.t. the boundary node \mathbf{x}_b) along the x -axis.

Another aspect to be considered for moving objects is the reinitialization or refill of the lattice sites, which are uncovered as the objects passes by. For such nodes, we again employ the Grad distribution as given in Eq. (3.1) with the wall velocity and a local density average, which has shown to exhibit reasonably small pressure oscillations (see also [335]). The pressure tensor is evaluated in the same manner as for the boundary conditions.

This boundary condition constitutes the action of the object onto the fluid. On the other hand, for two-way coupled simulations, the feedback exerted from the fluid onto the object is accounted for by solving Newton's equations of motion and will be detailed in the corresponding set-ups.

A few comments on the practical implementation are in order. For three dimensional geometries, the fluid-solid interface is described by a triangular surface mesh. The intersection locations $\mathbf{x}_{w,i}$ are computed by a signed distance field using angle-weighted pseudo-normals [13] in combination with a watertight ray-triangle intersection algorithm according to [332] and various sanity checks to ensure consistency. In addition, standard accelerator structures and SIMD vectorization are used to improve performance. For deforming geometries, the wall velocity $\mathbf{u}_{w,i}$ at the intersection location is non-uniform and time-dependent. The (prescribed or computed) velocities are stored at the locations of the triangle vertices and a barycentric interpolation is used to obtain the velocity $\mathbf{u}_{w,i}$ at the intersection location.

We proceed with selected validation studies of the proposed scheme.

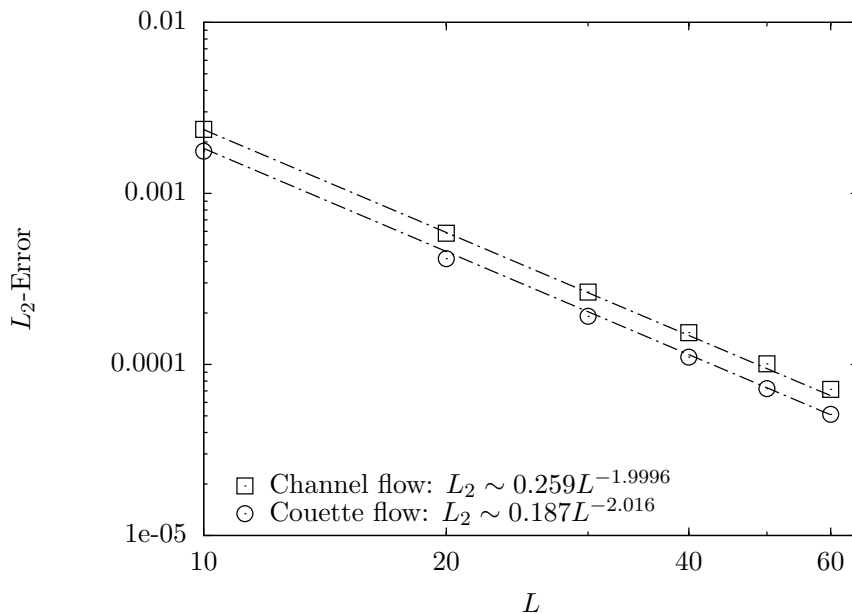


Figure 3.2: Scaling of L_2 error for the simulation of channel flow and Couette flow at $Re = 100$.

3.3 Validation

In this section, the order of accuracy of the Grad boundary condition is assessed and a validation for the sedimenting three-dimensional sphere is presented. Note that further validations and benchmarks in two dimensions including flow past a stationary and oscillating cylinder, a sedimenting particle as well as a flapping wing can be found in [76]. For brevity, we avoid presenting all validation studies and mention that unless stated otherwise, all simulations in this thesis are computed using the Grad boundary condition. This includes thorough validation of one- and two-way coupled laminar and turbulent flow simulations for moving as well as deforming geometries as presented in the following chapters.

3.3.1 Order of accuracy

It is important to note that the proposed boundary condition does not impose the desired values of the macroscopic quantities exactly at the boundary (since only the missing populations are replaced). Hence, we need to investigate the effect of boundary condition on the macroscopic quantities at the wall thoroughly. To this end, we simulate a channel flow to measure

the velocity slip at the wall and the order of convergence of the boundary condition. Figure 3.2 shows the scaling of L_2 error of velocity with respect to the grid size for the simulation of channel flow (driven by body force) for a Reynolds number of $Re = 100$. As expected, second order convergence is clearly seen in this plot. The velocity slip at the wall was measured to be around 10^{-5} to 10^{-7} (depending of the grid resolution) in lattice units which is small compared to the flow velocity typically of the order of 10^{-2} (lattice units), hence this does not affect the flow field far away and close to the wall. To further investigate the order of convergence also for a non-stationary case involving moving walls, we consider the time evolution of the Couette flow for which the bottom plate moves with a constant velocity \mathbf{u}_w whereas the plate on top is at rest. Initially, the velocity is set to zero everywhere except on the top boundary. The L_2 error is computed for the initial transient phase till steady state is reached by comparison to its analytical solution (see, e.g., [250]). As it is apparent from figure 3.2, the proposed boundary condition recovers a second order of accuracy also for non-stationary walls. Furthermore, excellent agreement was found for the evaluation of drag and lift forces at the wall and are presented in the next section.

3.3.2 Sedimenting sphere

We validate the proposed scheme for three-dimensional, two-way coupled simulations and consider the classical benchmark of a settling particle under gravity. For this purpose, we conduct two simulations. In the first simulation, we keep the sphere stationary and impose a mean flow in order to validate and compute the drag coefficient and the recirculation length for a Reynolds number of $Re = u_\infty D_s / \nu = 100$. The sphere is resolved with $D_s = 30$ grid points and the characteristic velocity $u_\infty = 0.01$ is given

Table 3.1: Flow past a sphere at $Re = 100$.

Contribution	C_d	L/D_s
[147]	1.1	0.88
[85]	1.098	0.87
present	1.1	0.86

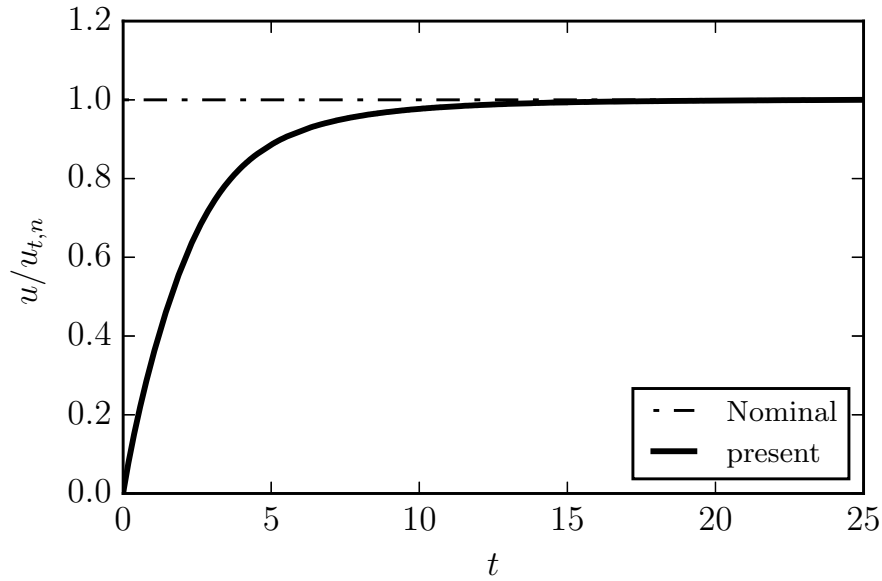


Figure 3.3: Temporal velocity evolution of a sedimenting sphere.

by the mean flow velocity. After the initial transient, the drag coefficient C_d and the recirculation length L are measured and the results are listed in table 3.1 along with literature values. With a good agreement to all reference data, we perform a second simulation for which there is no mean flow velocity but instead the sphere is settling under gravity. When released in a quiescent fluid with density ρ_f , the sphere with density ρ_s accelerates towards its terminal settling velocity u_t , where the gravitational force $F_g = \pi D_s^3 \rho_s g / 6$ is balanced by the buoyancy force $F_b = \pi D_s^3 \rho_f g / 6$ and the drag force $F_d = \rho_f u^2 \pi D_s^2 C_d / 8$. Establishing the force balance relates the density ratio to the terminal velocity as

$$\frac{\rho_s}{\rho_f} = 1 + \frac{3u_t^2 C_d}{4D_s g}. \quad (3.11)$$

In this two-way coupled simulation, the feedback from the fluid onto the sphere is prescribed by Newton's equations for the particle motion as

$$\dot{\mathbf{x}}_s = \mathbf{u}_s, \quad (3.12)$$

$$\ddot{\mathbf{x}}_s = \frac{\mathbf{F}}{m_s} + \left(1 - \frac{\rho_f}{\rho_s}\right) \mathbf{g}, \quad (3.13)$$

$$(3.14)$$

Table 3.2: Terminal settling velocity for a sedimenting sphere at $Re = 100$.

Contribution	$u_t/u_{t,n}$
[166]	1.006
[202]	1.005
present	1.0003

which is solved by an Euler integration and the force \mathbf{F} is computed via the Galilean invariant momentum exchange method (see [361]). The evolution of the settling velocity is shown in figure 3.3 for an imposed drag coefficient from the stationary simulation and a nominal settling velocity of $u_{t,n} = 0.01$. After the initial acceleration, a terminal velocity of $u_t = 0.0100033$ is reached at $t = t_{lb}u_{t,n}/D = 25$ non-dimensional time units, which corresponds to less than 0.033% error (see also table 3.2 for comparison with literature values). Thus, Galilean invariance is established between the stationary and the moving case and therefore validates the basic two-way coupling algorithm.

Chapter 4

Grid refinement strategies

4.1 Introduction

Despite the exceptional efficiency and parallel scalability of the LBM, the computational cost for the simulation of realistic engineering applications on a uniform mesh with reasonable spatial resolution remains prohibitively large. On the other hand, in many cases, the small scale flow structures are confined in only a small region of the computational domain. This reveals significant optimization potential by either locally embedding refined blocks into the domain or by employing unstructured meshes. In this chapter, both possibilities are explored. In section 4.2 a novel multi-domain block refinement approach is developed and validated for various challenging set-ups. Subsequently, in section 4.3, the entropic LBM is extended to unstructured meshes. Finally, in section 4.4, conclusions are drawn.

4.2 Multi-domain grid refinement

Conceptually, two main approaches to multi-domain grid refinement can be found in the literature. In the first approach, a cell-centered volumetric description is employed for which the populations are continuous over the grid interface and exact conservation of mass and momentum across the grid border may be achieved [53, 297]. However, as reported in [297],

staggering effects on the fine level require additional filtering. The second approach uses a node-centered description, which requires interpolation and rescaling of the population at the grid interface (see, e.g., [82, 96, 184, 343]). Below, the discussion is restricted to the node-centered approach. Note that the accuracy and stability of the entire simulation relies crucially on the two-way coupling between fine and coarse level grids.

In this section, we aim to:

- (i) Propose a novel coupling technique, which avoids the low-order time interpolation commonly used in other approaches by employing the LB space time coupling.
- (ii) Extend the refinement methodology to the entropic thermal and compressible models through a consistent rescaling of the populations.
- (iii) Study the role the entropic stabilizers by analyzing their behavior in multi-grid simulations within and across refinement patches.

To that end, in section 4.2.1, the refinement methodology and the resulting algorithm is presented in detail. Subsequently, extensions to thermal and compressible lattice Boltzmann models are shown in section 4.2.2. Finally, in Sec. 4.2.3, accuracy and range of applicability is studied for various simulations. In the isothermal regime, the turbulent channel flow at Reynolds numbers of $Re_\tau = \{180, 590\}$ is discussed followed by the flow past a sphere at Reynolds number $Re = 3700$. The thermal regime is validated using the Rayleigh-Bénard convection for Rayleigh number $Ra = 10^7$ and the flow past a heated sphere at $Re = 3700$. Finally, in the compressible regime, we focus on the viscous supersonic flow around the NACA0012 airfoil for a free-stream Mach number $Ma_\infty = 1.5$ and Reynolds number of $Re = 10000$. While for all simulations the flow properties are compared to available direct numerical simulations or experiments, we pay special attention to demonstrating the adaptive features of the entropic LBM during multi-grid computations.

4.2.1 Multi-domain coupling

In the multi-domain approach, the fine-level grid patches are inserted into the coarse-level grid and only one level is present for each patch. Thus, the

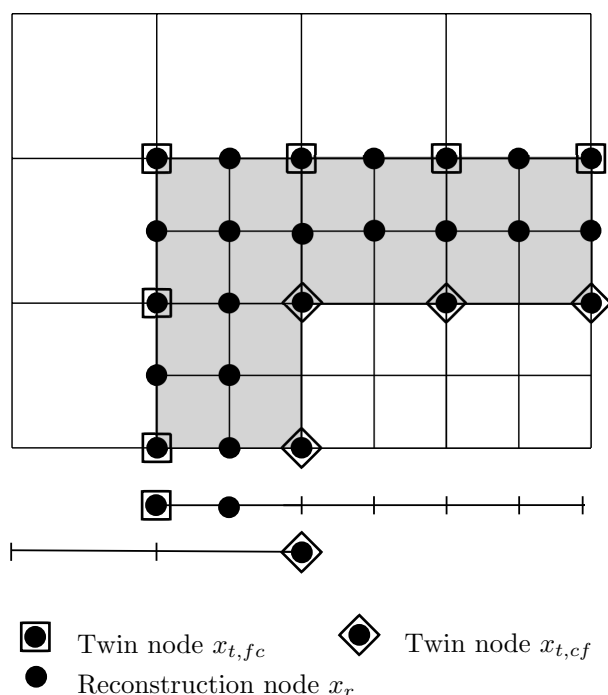


Figure 4.1: Schematic of the overlapping grid interface between two levels in one (bottom) and two (top) dimensions.

most crucial part of the algorithm is the coupling of different grid patches, namely the information transfer from the fine level to the coarse level and vice versa. This two-way coupling is realized through an overlapping region, which extends the nominal domain of the two patches as indicated by the gray shaded region in figure 4.1. In this region both fine and coarse grids are present. The minimal interface width for the proposed coupling mechanism is two and one grid nodes for the fine- and coarse-level grid, respectively. After each time step in the corresponding grid, the information at the boundary needs to be extracted from the available information of the neighboring patch. It is convenient to distinguish two types of nodes, namely twin nodes \mathbf{x}_t and reconstruction nodes \mathbf{x}_r . Twin nodes are nodes within the interface, located in places where both coarse and fine level nodes are overlapping. We write $\mathbf{x}_{t,fc}$ and $\mathbf{x}_{t,cf}$ to indicate twin nodes in the interface of the fine and coarse level grids, respectively. The reconstruction nodes belong to the fine level interface and do not coincide with any coarse level nodes. Thus, the information on those nodes is not readily available and information from the neighboring grid nodes needs to be taken into account in order to complete the information exchange between the grids. The information extraction for the two types of nodes

is conceptually different and will be elaborated below.

4.2.1.1 Twin node coupling and rescaling

The standard LBM is restricted to regular meshes and non-dimensional quantities are usually evaluated with respect to the corresponding lattice units, specific to the chosen grid. Using multiple grids with different spacing yields a set of lattice units which need to be rescaled appropriately in order to assure identical non-dimensional quantities. While the spatial scaling of the grid spacing is straightforwardly defined as

$$r = \frac{\delta x_c}{\delta x_f}, \quad (4.1)$$

more possibilities exist for the time scale. While diffusive scaling relates the time and space scales as $\delta t \sim \delta x^2$, the convective scaling requires $\delta t \sim \delta x$. In this paper, we consider the convective scaling due to its greater numerical efficiency; it follows

$$r = \frac{\delta t_c}{\delta t_f}. \quad (4.2)$$

As a result, the macroscopic quantities such as pressure, velocity and temperature are continuous across the grid border. However, for a continuous Reynolds number $Re = UL/\nu$ the viscosity scales as

$$\nu_f = r\nu_c. \quad (4.3)$$

On the other hand, viscosity is related to the relaxation parameter β by Eq. (2.25) and thus scaling of the relaxation parameter is required as

$$\beta_f = \frac{1}{1 + r(1/\beta_c - 1)}. \quad (4.4)$$

For the rescaling of the populations, we decompose them into $f_i = f_i^{\text{eq}}(M_c) + f_i^{\text{neq}}(M_c, \nabla M_c)$, where the equilibrium distribution is written as a function of the conserved moments M_c and the non-equilibrium part additionally depends on their gradients. Since the conserved fields are continuous across the interface, the equilibrium does not require any rescaling. However, the non-equilibrium part is proportional to the gradients and therefore needs rescaling.

In the case of an external force, we use the exact difference method as proposed in [182], where the post-collision populations are modified according to

$$f'_i = f_i + [f_i^{\text{eq}}(\rho, u_\alpha + \delta u_\alpha) - f_i^{\text{eq}}(\rho, u_\alpha)], \quad (4.5)$$

where δu_α is the change in velocity due to the external force F_α :

$$\delta u_\alpha = \frac{F_\alpha}{\rho} \delta t. \quad (4.6)$$

Due to the convective time scaling employed here, the change in velocity has to be rescaled accordingly; it follows

$$\delta u_f = \frac{\delta u_c}{r}. \quad (4.7)$$

Rescaling In the isothermal case, we may approximate the non-equilibrium part of the population as

$$f_i^{\text{neq}} \approx \frac{W_i}{2c_s^4} P_{\alpha\beta}^{(1)} [c_{i\alpha} c_{i\beta} - c_s^2 \delta_{\alpha\beta}], \quad (4.8)$$

where non-equilibrium part of the pressure tensor is given as

$$P_{\alpha\beta}^{(1)} = \frac{c_s^2 \rho}{2\beta} (\partial_\alpha u_\beta + \partial_\beta u_\alpha). \quad (4.9)$$

Note that strain rate tensor is given in fine and coarse lattice units respectively and therefore requires rescaling to assure continuity of the non-equilibrium fields. Straightforward substitution yields the relation between coarse and fine level non-equilibrium as

$$f_{i,f}^{\text{neq}} = \frac{\beta_c}{r\beta_f} f_{i,c}^{\text{neq}}, \quad (4.10)$$

which identifies the scaling factor [96]. This rescaling is applied to all twin nodes \mathbf{x}_t (see figure 4.1), for the coarse and the fine grids. Note that the adaptive nature of entropy-based LBM does not require additional smoothing or filtering to project the fine-scale solution onto the coarse-level grid (see section 4.2.3 for a more thorough discussion). This is in contrast to, e.g., [184], where a box-filter is required to maintain stability.

4.2.1.2 Reconstruction nodes

The coupling from the coarse to the fine grid requires only the rescaling procedure as outlined above in section 4.2.1.1. The fine level grid however requires an additional reconstruction of the hanging or reconstruction nodes that do not correspond to a coarse level node as indicated in figure 4.1 by \mathbf{x}_r . As no information from the coarse level is available at this location, the information of the neighboring nodes is required to be included through an interpolation scheme. Analogous to [184], we use a centered four point stencil in each spatial dimension of the Lagrange polynomial, which, for a generic quantity λ , reads

$$\lambda(x) = \frac{1}{16} [-\lambda(x - 3\delta x) + 9\lambda(x - \delta x) + 9\lambda(x + \delta x) - \lambda(x + 3\delta x)]. \quad (4.11)$$

Note that in contrast to [184], biased interpolation at the corners is avoided to prevent the anisotropy from influencing the solution. This is particularly important for the thermal and compressible model, where a biased interpolation stencil triggers spurious artifacts at the grid interface. While we did not encounter stability issues caused by these artifacts for all entropic models presented here, instabilities might be triggered for models without a stabilization mechanism such as LBGK. Further, we confirm the observation of [184] that a second-order interpolation is not sufficient.

This interpolation is used for the macroscopic quantities of the flow field needed to compute the equilibrium part of the populations as well as the non-equilibrium part of the populations using their values at the twin nodes on the coarse level grid.

4.2.1.3 Algorithm

In this section, we present the proposed grid refinement algorithm. We aim to avoid the commonly used low-order time interpolation (see, e.g., [184]) and instead replace it by a high-order spatial interpolation using Eq. (4.11) in combination with LB time stepping. After initialization at time $t = t_0$ we assume that all populations and macroscopic fields are specified and available everywhere on all grids. Further, a refinement ratio of $r = 2$ is assumed. Starting at $t = t_0$, the simulation is evolved by the following iterative steps:

1. $t = t_0 + \delta_{t,f}$: Advection and collision on the fine grid. Note that information is missing on the boundary of the fine level interface and collision should be avoided on those nodes.
2. $t = t_0 + \delta_{t,c}$: Advection on both coarse and fine level grids. Information is now missing on two boundary layers in the fine and one in the coarse grid.
3. $t = t_0 + \delta_{t,c}$: Rescaling of populations and macroscopic fields on the twin nodes x_t .
4. $t = t_0 + \delta_{t,c}$: Reconstruction of the populations on \mathbf{x}_r : Interpolation of the macroscopic quantities to compute the equilibrium part of the populations and direct interpolation of the non-equilibrium part of the populations. All information is now available again.
5. $t = t_0 + \delta_{t,c}$: Collision on all grids.

This procedure effectively switches time interpolation with a purely spatial interpolation combined with entropic LB time stepping.

4.2.2 Extensions to thermal and compressible lattice Boltzmann models

In this section, the proposed grid refinement algorithm is extended to thermal and compressible lattice Boltzmann models. This work was done in collaboration with Nicolo Frapolli. In the following, both models and their refinement procedures are presented. Note that the refinement algorithm as outlined above remains identical but the rescaling procedures of the populations differ for each model.

4.2.2.1 Thermal Flows

Two-population KBC model In the two-population KBC model for thermal flows, the kinetic equations, Eq. (2.28), for f -populations are modified in order to account for a variable Prandtl number [7, 155, 265]. The second set of populations, g , is employed to recover the energy equation [155, 265]. The lattice kinetic equations for the f and g populations read

$$f_i(\mathbf{x} + \mathbf{c}_i, t + 1) = (1 - \beta)f_i + \beta f_i^{\text{mirr}} + 2(\beta - \beta_1)[f_i^* - f_i^{\text{eq}}], \quad (4.12)$$

$$g_i(\mathbf{x} + \mathbf{c}_i, t + 1) = g_i(\mathbf{x}, t) + 2\beta(g_i^{\text{eq}} - g_i) + 2(\beta - \beta_1)[g_i^* - g_i^{\text{eq}}], \quad (4.13)$$

where f_i^{mirr} (Eq. (2.40)) and f_i^{eq} (Eq. (2.32)) are the same as for the isothermal model, g_i^{eq} is the equilibrium of g -populations, f_i^* and g_i^* are the quasi-equilibrium states for f - and g -populations, respectively and β_1 is a second, independent, relaxation parameter.

The population, g_i^{eq} , f_i^* and g_i^* are constructed using the general form

$$G_i = W_i \left(M_0 + \frac{M_\alpha c_{i\alpha}}{T_0} + \frac{(M_{\alpha\beta} - M_0 T_0 \delta_{\alpha\beta})(c_{i\alpha} c_{i\beta} - T_0 \delta_{\alpha\beta})}{2T_0^2} \right). \quad (4.14)$$

The moments to be employed for the computation of the equilibrium of g -populations are provided in table 4.1. The choice of moments for the quasi-equilibrium states f^* and g^* depends on the Prandtl number. In table 4.1, the moments for the quasi-equilibrium populations are provided for both regimes ($\text{Pr} \leq 1$ and $\text{Pr} > 1$) [155, 265].

Table 4.1: Moments for equilibrium and quasi-equilibrium construction.

G_i		M_0	M_α	$M_{\alpha\beta}$
g_i^{eq}		$2\rho E$	q_α^{eq}	$R_{\alpha\beta}^{\text{eq}}$
f_i^*	$\text{Pr} \leq 1$	ρ	ρu_α	P^{eq}
f_i^*	$\text{Pr} > 1$	ρ	ρu_α	$P_{\alpha\beta}$
g_i^*	$\text{Pr} \leq 1$	$2\rho E$	$q_\alpha - 2u_\beta \left(P_{\alpha\beta} - P_{\alpha\beta}^{\text{eq}} \right)$	$R_{\alpha\beta}^{\text{eq}}$
g_i^*	$\text{Pr} > 1$	$2\rho E$	$q_\alpha^{\text{eq}} + 2u_\beta \left(P_{\alpha\beta} - P_{\alpha\beta}^{\text{eq}} \right)$	$R_{\alpha\beta}^{\text{eq}}$

In table 4.1, the moments are defined as follows:

$$P_{\alpha\beta}^{\text{eq}} = \sum_i c_{i\alpha} c_{i\beta} f_i^{\text{eq}} = \rho T_0 \delta_{\alpha\beta} + \rho u_\alpha u_\beta, \quad (4.15)$$

$$q_\alpha^{\text{eq}} = \sum_i c_{i\alpha} g_i^{\text{eq}} = 2\rho E u_\alpha + 2\rho T_0 u_\alpha, \quad (4.16)$$

$$\begin{aligned} R_{\alpha\beta}^{\text{eq}} &= \sum_i c_{i\alpha} c_{i\beta} g_i^{\text{eq}} \\ &= 2\rho E (T_0 \delta_{\alpha\beta} + u_\alpha u_\beta) + 2\rho T_0 (T_0 \delta_{\alpha\beta} + 2u_\alpha u_\beta), \end{aligned} \quad (4.17)$$

where the total energy E is defined as

$$E = \frac{D}{2}T + \frac{1}{2}u^2. \quad (4.18)$$

The relaxation parameters β and β_1 are related to the kinematic viscosity and thermal diffusivity depending on the Prandtl number as

$$\nu = \begin{cases} \left(\frac{1}{2\beta} - \frac{1}{2}\right) T_0, & \text{if } \text{Pr} \leq 1, \\ \left(\frac{1}{2\beta_1} - \frac{1}{2}\right) T_0, & \text{if } \text{Pr} > 1, \end{cases}$$

$$\alpha_{th} = \begin{cases} \left(\frac{1}{2\beta_1} - \frac{1}{2}\right) T_0, & \text{if } \text{Pr} \leq 1, \\ \left(\frac{1}{2\beta} - \frac{1}{2}\right) T_0, & \text{if } \text{Pr} > 1, \end{cases}$$

so that the Prandtl number Pr reads

$$\text{Pr} = \frac{\nu}{\alpha_{th}} = \begin{cases} \frac{(1-\beta)\beta_1}{(1-\beta_1)\beta}, & \text{if } \text{Pr} \leq 1, \\ \frac{(1-\beta_1)\beta}{(1-\beta)\beta_1}, & \text{if } \text{Pr} > 1. \end{cases}$$

Rescaling For the thermal two-population model the rescaling of the f - and g -populations cannot be applied in the same way as for the single-population case, Eq. (4.10), because two independent relaxation parameters appear in the kinetic equations. Moreover, we must distinguish between the two cases of $\text{Pr} \leq 1$ and $\text{Pr} > 1$.

For $\text{Pr} \leq 1$ there is no contribution of the quasi-equilibrium state in the kinetic equation for f , so that the same rescaling as Eq. (4.10) can be applied for the f -populations. For the g -populations, however, this is no more valid, since the non-equilibrium part depends on two independent relaxation parameters. This can be verified by deriving an analytical expression for the non-equilibrium g -populations through Chapman-Enskog expansion, as in [265]. The non-equilibrium part of the g -population depends on the higher-order, non-conserved moments as

$$g_i^{\text{neq}} = g_i^{\text{neq}} \left[q_\alpha^{(1)}(\beta, \beta_1), R_{\alpha\beta}^{(1)}(\beta_1) \right], \quad (4.19)$$

where $q_\alpha^{(1)}$ and $R_{\alpha\beta}^{(1)}$ are the first and second order non-equilibrium moments of the g -populations. The $q_\alpha^{(1)}$ moment includes a contribution of β , different from the moment $R_{\alpha\beta}^{(1)}(\beta_1)$ and the higher-order moments, which

need to be excluded before rescaling of the non-equilibrium part. The $q_\alpha^{(1)}$ moment can be written analytically as

$$q_\alpha^{(1)}(\beta, \beta_1) = -\frac{1}{2\beta_1} \rho D T_0 \partial_\alpha T + 2u_\beta P_{\alpha\beta}^{(1)}(\beta), \quad (4.20)$$

so that the contribution in β can be separated from the rest of the contributions to the non-equilibrium part of the g -populations. This contribution can be rescaled separately according to

$$P_{\alpha\beta,f}^{(1)} = \frac{\beta_c}{r\beta_f} P_{\alpha\beta,c}^{(1)}. \quad (4.21)$$

After subtraction of the term dependent on β the rescaling is performed as usual. The final result reads

$$g_{i,f}^{\text{neq}} = \frac{\beta_{1,c}}{r\beta_{1,f}} \left(g_{i,c}^{\text{neq}} - W_i \frac{2u_\beta P_{\alpha\beta,c}^{(1)} c_{i\alpha}}{T_0} \right) + W_i \frac{2u_\beta P_{\alpha\beta,f}^{(1)} c_{i\alpha}}{T_0}. \quad (4.22)$$

Note that the non-equilibrium pressure tensor $P_{\alpha\beta}^{(1)}$ can be computed directly from f -populations by

$$P_{\alpha\beta}^{(1)} = \sum_i c_{i\alpha} c_{i\beta} (f_i - f_i^{\text{eq}}). \quad (4.23)$$

For the case $\text{Pr} > 1$, similar considerations can be applied and the final results are for the f -populations

$$f_{i,f}^{\text{neq}} = \frac{\beta_{1,c}}{r\beta_{1,f}} f_{i,c}^{\text{neq}}, \quad (4.24)$$

while for the g -populations

$$g_{i,f}^{\text{neq}} = \frac{\beta_c}{r\beta_f} \left(g_{i,c}^{\text{neq}} - W_i \frac{2u_\beta P_{\alpha\beta,c}^{(1)} c_{i\alpha}}{T_0} \right) + W_i \frac{2u_\beta P_{\alpha\beta,f}^{(1)} c_{i\alpha}}{T_0}, \quad (4.25)$$

where the non-equilibrium pressure tensor is rescaled as

$$P_{\alpha\beta,f}^{(1)} = \frac{\beta_{1,c}}{r\beta_{1,f}} P_{\alpha\beta,c}^{(1)}. \quad (4.26)$$

4.2.2.2 Compressible Flows

Two-population ELBM for compressible flows Same as for the thermal two-populations ELBM, also for the compressible model [99, 100], we employ two populations. However, in the compressible model a multi-speed lattice, the $DdQ7^d$, is used and the second population is needed to change the adiabatic exponent γ_{ad} . The kinetic equations for the compressible model read [99, 100]

$$f_i(\mathbf{x} + \mathbf{c}_i, t + 1) - f_i(\mathbf{x}, t) = \alpha\beta_2 (f_i^{\text{eq}} - f_i) + 2(\beta_2 - \beta_3) [f_i^* - f_i^{\text{eq}}], \quad (4.27)$$

$$g_i(\mathbf{x} + \mathbf{c}_i, t + 1) - g_i(\mathbf{x}, t) = \alpha\beta_2 (g_i^{\text{eq}} - g_i) + 2(\beta_2 - \beta_3) [g_i^* - g_i^{\text{eq}}]. \quad (4.28)$$

The equilibrium f_i^{eq} for the f -populations is found by minimizing the entropy function under the constraints of conservation laws, Eq. (2.31). The minimization problem is solved with the method of the Lagrange multipliers and leads to the formal expression

$$f_i^{\text{eq}} = \rho W_i \exp(\chi + \zeta_\alpha c_{i\alpha} + \lambda c_i^2), \quad (4.29)$$

where χ , ζ_α and λ are the Lagrange multipliers, which in turn are determined by solving the system of $D + 2$ equations found by inserting Eq. (4.29) into the conservation laws. The system is solved numerically at every node in every time-step. The equilibrium for the g -populations, g_i^{eq} , can be computed directly from f_i^{eq} as

$$g_i^{\text{eq}} = (C_v - D/2)T f_i^{\text{eq}}, \quad (4.30)$$

where C_v is the heat capacity at constant volume. The conservation of total energy becomes

$$2\rho E_{\text{tot}} = 2\rho C_v T + \rho u^2 = \sum_i c_i^2 f_i + \sum_i g_i, \quad (4.31)$$

where E_{tot} is the total energy.

The quasi-equilibrium state needs to be chosen depending on the Prandtl number [103]. For $Pr \leq 1$, the quasi-equilibrium state depends on the centered heat-flux tensor $\overline{Q}_{\alpha\beta\gamma}$, which can be written in a compact form as

$$f_i^* = f_i^{\text{eq}} + W_i \frac{\left(\overline{Q}_{\alpha\beta\gamma} - Q_{\alpha\beta\gamma}^{\text{eq}}\right) [c_{i\alpha} c_{i\beta} c_{i\gamma} - 3T c_{i\gamma} \delta_{\alpha\beta}]}{6T^3}, \quad (4.32)$$

where

$$\bar{Q}_{\alpha\beta\gamma} = \sum_{i=1}^Q f_i (c_{i\alpha} - u_\alpha)(c_{i\beta} - u_\beta)(c_{i\gamma} - u_\gamma). \quad (4.33)$$

The quasi-equilibrium populations g_i^* are written consistently with the f_i^* populations and read

$$g_i^* = g_i^{\text{eq}} + \frac{W_i (\bar{q}_\alpha - q_\alpha^{\text{eq}}) c_{i\alpha}}{T}, \quad (4.34)$$

where \bar{q}_α is the contracted centered heat-flux tensor associated to the internal degrees of freedom of the gas

$$\bar{q}_\alpha = \sum_{i=1}^Q g_i (c_{i\alpha} - u_\alpha). \quad (4.35)$$

In the above expressions $W_i = W_i(T)$ are the temperature-dependent weights [99, 100].

Finally, entropic time stepping as proposed in the original ELBM is employed (see chapter 2.3). The kinematic viscosity and the thermal diffusivity are thus related to the relaxation parameters β_2 and β_3 by

$$\beta_2 = \frac{1}{\frac{2\nu}{T} + 1}, \quad \beta_3 = \frac{1}{\frac{2\alpha_{th}}{T} + 1}, \quad (4.36)$$

and the heat capacity C_v is derived from the desired adiabatic exponent γ_{ad} from

$$C_v = \frac{1}{\gamma_{ad} - 1}. \quad (4.37)$$

The model implies a bulk viscosity ξ of

$$\xi = \left(\frac{1}{C_v} - \frac{2}{D} \right) \mu. \quad (4.38)$$

For further details on the model the reader is referred to [99, 100].

Rescaling As for the thermal model, also in the compressible model the populations can not be rescaled directly, since the non-equilibrium part depends on two relaxation parameters. For both f - and g -populations the non-equilibrium parts can be derived analytically as a function of the higher-order, non-conserved moments [100]. We consider here only the case

$Pr \leq 1$; for the case $Pr > 1$ the relaxation parameters β_2 and β_3 need simply to be interchanged.

For the f -populations, the non-equilibrium part depends on the higher-order, non-conserved moments as

$$f_i^{(1)} = f_i^{(1)} \left[P_{\alpha\beta}^{(1)}(\beta_2), Q_{\alpha\beta\gamma}^{(1)}(\beta_2, \beta_3), R_{\alpha\beta\gamma\mu}^{(1)}(\beta_2) \right], \quad (4.39)$$

where $P_{\alpha\beta}^{(1)}$ is the non-equilibrium pressure tensor and $Q_{\alpha\beta\gamma}^{(1)}$ and $R_{\alpha\beta\gamma\mu}^{(1)}$ are the third- and fourth-order non-equilibrium moments. In this case, the different relaxation shows up only in the $Q_{\alpha\beta\gamma}^{(1)}$ tensor, which can be written analytically as

$$\begin{aligned} Q_{\alpha\beta\gamma}^{(1)}(\beta_2, \beta_3) = & -\frac{1}{2\beta_3} \rho T [\partial_\alpha T \delta_{\beta\gamma} + \partial_\beta T \delta_{\alpha\gamma} + \partial_\gamma T \delta_{\alpha\beta}] \\ & + u_\alpha P_{\beta\gamma}^{(1)}(\beta_2) + u_\beta P_{\alpha\gamma}^{(1)}(\beta_2) + u_\gamma P_{\alpha\beta}^{(1)}(\beta_2). \end{aligned} \quad (4.40)$$

The contribution related to β_3 can be subtracted from the rest of the non-equilibrium part and rescaled separately according to the proper relaxation. The non-equilibrium part without the contribution related to β_3 can be written as

$$\begin{aligned} \bar{f}_i^{\text{neq}} = & f_i^{\text{neq}} \\ & + \frac{W_i Y_{i,\alpha\beta\gamma}}{6T^3} \left(u_\alpha P_{\beta\gamma}^{(1)}(\beta_2) + u_\beta P_{\alpha\gamma}^{(1)}(\beta_2) + u_\gamma P_{\alpha\beta}^{(1)}(\beta_2) \right. \\ & \left. - Q_{\alpha\beta\gamma}^{(1)}(\beta_2, \beta_3) \right), \end{aligned} \quad (4.41)$$

where

$$Y_{i,\alpha\beta\gamma} = c_{i\alpha} c_{i\beta} c_{i\gamma} - 3c_{i\gamma} T \delta_{\alpha\beta}. \quad (4.42)$$

At this point the reduced non-equilibrium part can be rescaled according to

$$\bar{f}_{i,f}^{\text{neq}} = \frac{\beta_{2,c}}{r\beta_{2,f}} \bar{f}_{i,c}^{\text{neq}}, \quad (4.43)$$

and the final non-equilibrium populations become

$$\begin{aligned} f_{i,f}^{\text{neq}} = & \bar{f}_{i,f}^{\text{neq}} \\ & - \frac{\beta_{3,c}}{r\beta_{3,f}} \frac{W_i Y_{i,\alpha\beta\gamma}}{6T^3} \left(u_\alpha P_{\beta\gamma,c}^{(1)}(\beta_2) + u_\beta P_{\alpha\gamma,c}^{(1)}(\beta_2) + u_\gamma P_{\alpha\beta,c}^{(1)}(\beta_2) \right. \\ & \left. - Q_{\alpha\beta\gamma,c}^{(1)}(\beta_2, \beta_3) \right), \end{aligned} \quad (4.44)$$

where $P_{\alpha\beta}^{(1)}$ and $Q_{\alpha\beta\gamma}^{(1)}$ can be computed as

$$P_{\alpha\beta}^{(1)} = \sum_i c_{i\alpha} c_{i\beta} (f_i - f_i^{\text{eq}}), \quad (4.45)$$

and

$$Q_{\alpha\beta\gamma}^{(1)} = \sum_i c_{i\alpha} c_{i\beta} c_{i\gamma} (f_i - f_i^{\text{eq}}). \quad (4.46)$$

For g -populations a similar procedure is applied. The non-equilibrium part can be expressed as

$$g_i^{(1)} = g_i^{(1)} \left[K^{(1)}(\beta_2), q_\alpha^{(1)}(\beta_2, \beta_3), R_{\alpha\beta}^{(1)}(\beta_2) \right], \quad (4.47)$$

where $K^{(1)}$, $q_\alpha^{(1)}$ and $R_{\alpha\beta}^{(1)}$ are the zeroth-, first- and second-order non-equilibrium moments of g -populations. Similar to the f -populations, the different relaxation, β_3 , shows up only in the $q_\alpha^{(1)}$ tensor; this can be expressed analytically as [100]

$$q_\alpha^{(1)} = -\frac{1}{2\beta_3} \rho T (2C_v - D) \partial_\alpha T + u_\alpha K^{(1)}(\beta_2). \quad (4.48)$$

Thus, the contribution related to β_3 can be subtracted from the rest of the non-equilibrium g -populations and thus can be rescaled separately according to the proper relaxation. The non-equilibrium part without the contribution related to β_3 can be written as

$$\bar{g}_i^{\text{neq}} = g_i^{\text{neq}} + W_i \frac{\left(u_\alpha K^{(1)}(\beta_2) - q_\alpha^{(1)}(\beta_2, \beta_3) \right) c_{i\alpha}}{T}. \quad (4.49)$$

The reduced non-equilibrium part can be rescaled as

$$\bar{g}_{i,f}^{\text{neq}} = \frac{\beta_{2,c}}{r\beta_{2,f}} \bar{g}_{i,c}^{\text{neq}}, \quad (4.50)$$

and the final non-equilibrium populations become

$$g_{i,f}^{\text{neq}} = \bar{g}_{i,f}^{\text{neq}} + \frac{\beta_{3,c}}{r\beta_{3,f}} W_i \frac{\left(u_\alpha K^{(1)}(\beta_2) - q_\alpha^{(1)}(\beta_2, \beta_3) \right) c_{i\alpha}}{T}, \quad (4.51)$$

where $K^{(1)}$ and $q_\alpha^{(1)}$ can be computed directly from populations as

$$K^{(1)} = \sum_i (g_i - g_i^{\text{eq}}), \quad (4.52)$$

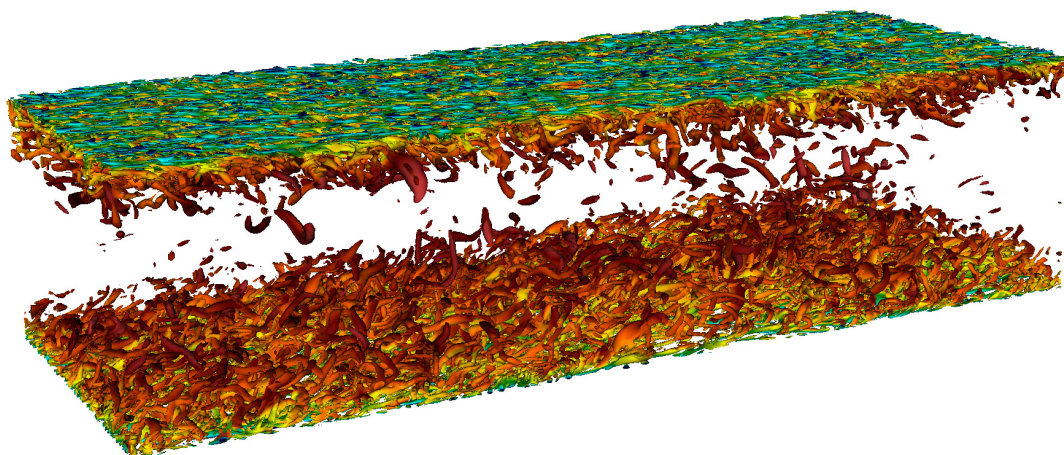


Figure 4.2: Snapshot of the turbulent channel, visualized by isosurfaces of Q -criterion colored by velocity magnitude.

and

$$q_{\alpha}^{(1)} = \sum_i c_{i\alpha} (g_i - g_i^{\text{eq}}). \quad (4.53)$$

4.2.3 Numerical validation

In this section, the proposed grid refinement technique is validated and its range of applicability is assessed in isothermal, thermal and compressible flow regimes.

4.2.3.1 Isothermal flows

In this section, we investigate accuracy and stability of the proposed grid refinement algorithm for turbulent isothermal flows using the examples of the flow past a sphere and the turbulent channel flow, where grid refinement is crucial to obtain accurate results. The boundary conditions used for all wall-boundary nodes is Grad's approximation as presented in chapter 3.

Turbulent channel flow The first validation in the isothermal regime is dedicated to the well-studied problem of the turbulent flow in a rectangular channel for which many experimental and numerical investigations have been conducted (see, e.g., [83, 169, 180, 248]). We compare the performance of the proposed grid refinement technique in combination with KBC models to the DNS data of [248] for a Reynolds number $\text{Re}_{\tau} = u_{\tau}\delta/\nu = 180$ and

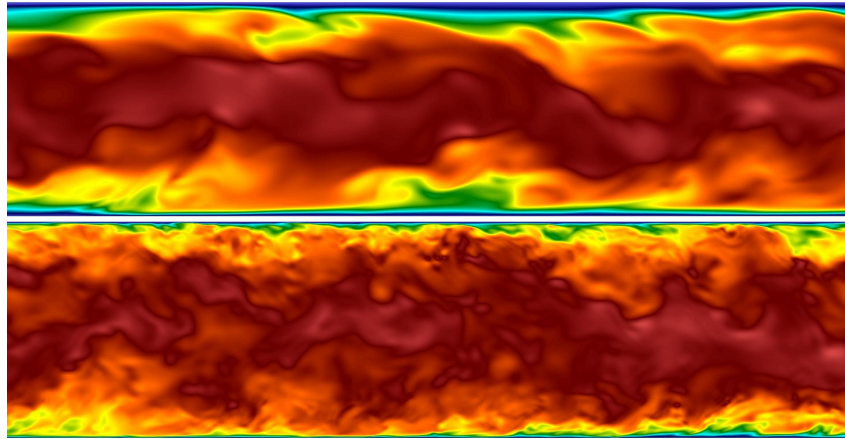


Figure 4.3: Slice through the turbulent channel flow for $Re_\tau = 180$ (top) and $Re_\tau = 590$ (bottom) showing a snapshot of the streamwise velocity.

$Re_\tau = 590$. The friction Reynolds number Re_τ is based on the channel half-width δ and the friction velocity $u_\tau = \sqrt{\tau_w/\rho}$. The flow is driven by a constant body force, which was chosen according to $g = Re_\tau^2 \nu^2 / \delta^3$ to achieve the desired Reynolds number. By computing the wall-shear stress directly from the flow field of the simulation, the friction velocity may be evaluated and the actual Reynolds number measured. The results of our simulations are given in table 4.2. The simulations were conducted for a resolution of the channel half-width of $\delta_c = 50$ lattice points on the coarse level.

The computational domain was chosen as $[4\pi\delta \times 2\delta \times 4/3\pi\delta]$ for $Re_\tau = 180$ and $[8\delta \times 2\delta \times 4\delta]$ for $Re_\tau = 590$, where the x and z coordinates are in streamwise and spanwise direction, respectively. An initial perturbation is introduced into the flow field in order to trigger turbulence. Figure 4.2 shows an instantaneous snapshot of isosurfaces of the Q -criterion

Table 4.2: Turbulent flow in a rectangular channel. The nominal and measured Reynolds numbers are indicated by $Re_{\tau,n}$ and $Re_{\tau,m}$, respectively.

Contribution	$Re_{\tau,n}$	$Re_{\tau,m}$	Δy^+
[248]	180	178.13	~ 0.054
present	180	173.06	~ 1.73
[248]	590	587.19	~ 0.044
present (refined)	590	611.87	~ 3.06
present (uniform)	590	613.19	~ 12.26

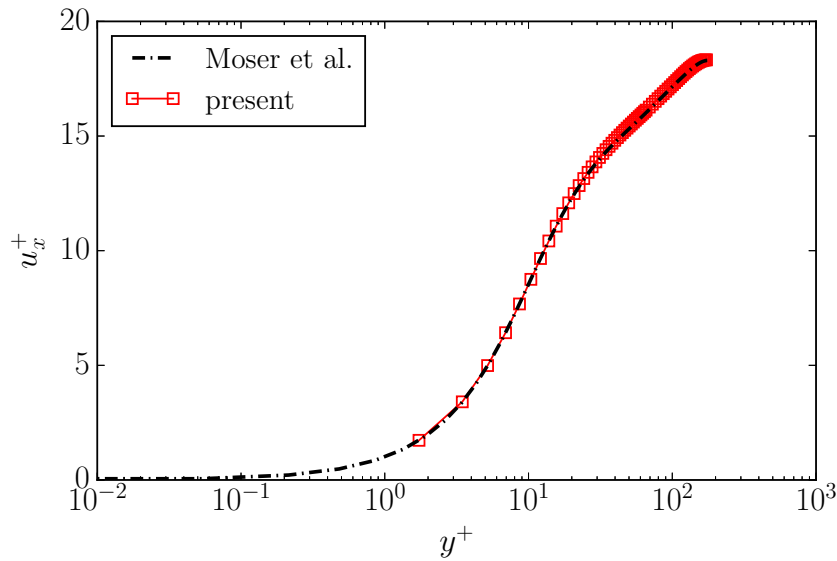


Figure 4.4: Mean velocity profile in a turbulent channel at $Re_\tau = 180$

for the case of $Re_\tau = 590$. In addition, a slice of the instantaneous velocity magnitude for both configurations is plotted in figure 4.3. Most conveniently, all data is expressed in wall-units, where the velocity is defined as $u^+ = u/u_\tau$ and spatial coordinate as $y^+ = yu_\tau/\nu$. Using wall-units, the spatial resolution may be quantified with the non-dimensional grid spacing Δy^+ near the channel wall. The scaling of the average velocity is well understood in a high-Reynolds number turbulent channel by the law of the wall, where one distinguishes between the viscous sublayer ($y^+ < 5$), the buffer layer ($5 < y^+ < 30$) and log-law region ($y^+ \geq 30$) [279]. While the average streamwise velocity u_x^+ is assumed to scale linearly with the wall coordinate y^+ in the viscous sublayer, the log-law suggests a scaling with $u_x^+ = \kappa^{-1} \ln y^+ + C^+$ in the log-law region, where $\kappa \approx 0.41$ denotes the von Kármán constant and the constant C^+ is given by $C^+ \approx 5.5$. While in the $Re_\tau = 180$ case low Reynolds number effects may still be observed, the channel flow at $Re_\tau = 590$ is at a sufficiently high Reynolds number to exhibit all expected features of high Reynolds number wall-bounded flows. Considering the case of $Re_\tau = 180$, we choose one level of refinement near the wall with a spatial extent of 20 coarse-level points, which yields a resolution of $\Delta y_f^+ = 1.73$ near the wall. We compare the average velocity profile in figure 4.4. It is evident that the results match the reference data excellently. Considering the root mean square (rms) velocity profiles, a similarly good agreement is shown in figure 4.5. The marginal overshoot of

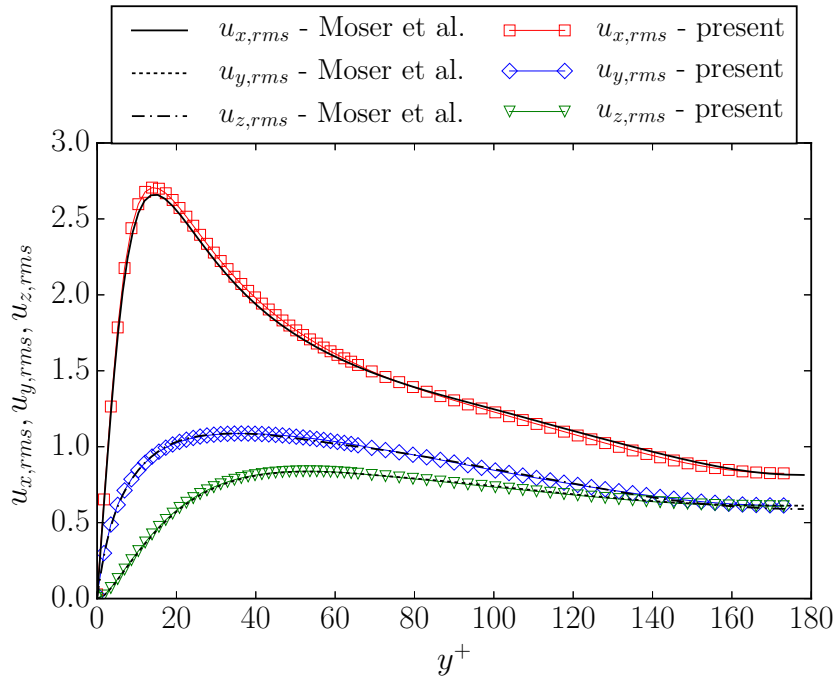


Figure 4.5: Rms velocity profile in a turbulent channel at $Re_\tau = 180$

$u_{x,rms}$ is attributed to a slightly higher Reynolds number in our simulation compared to the reference data. Important to notice is that the transition between the grid levels is smooth for both the mean and rms velocity profiles and no numerical artifacts are present.

With these results, we test the limits of applicability of the proposed grid refinement technique and choose a higher Reynolds number of $Re_\tau = 590$. In this case, we add an additional grid level in the near-wall region to resolve the flow field in the fine level with $\Delta y_f^+ \approx 3.06$ (see figure 4.8). To assess the necessity of grid refinement in the near-wall region, we conduct another simulation for which a uniform mesh with $\Delta y^+ \approx 12.26$ is used. The average velocity profiles are shown in figure 4.6. One can observe that despite of the severe under-resolution in the uniform case, the average profile agree well with the reference data. Note that this is in contrast to various well-established LB models, which are challenged by under-resolved simulations (see, e.g., [111, 255] for comparative studies for the turbulent channel flow set-up). The simulation using the refined mesh matches similarly well and one cannot observe any discontinuities at the level interfaces. Studying this in more detail, we consider the next order of statistics, the rms velocity profiles, for both cases in figure 4.7. In the

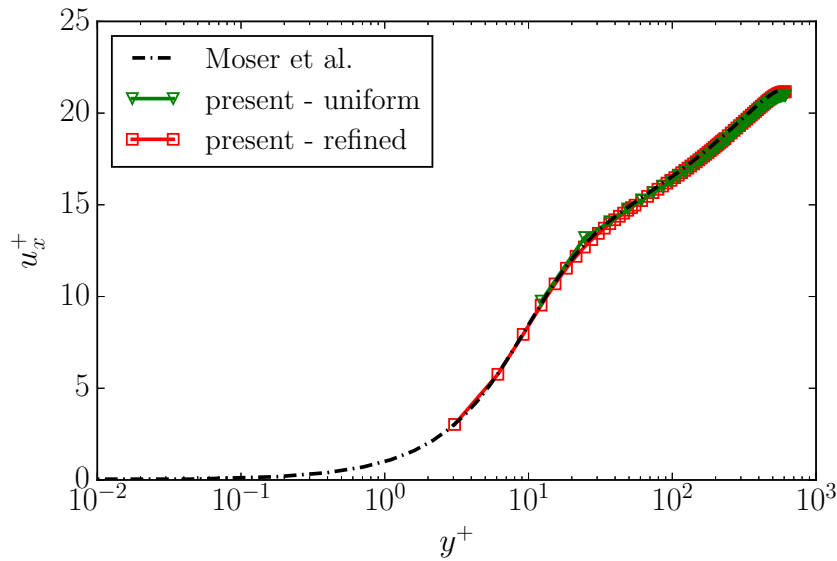


Figure 4.6: Mean velocity profiles in a turbulent channel at $\text{Re}_\tau = 590$

uniform case (figure 4.7, right), it is obvious that the peak $u_{x,rms}$ is severely under-predicted, yielding a rather poor agreement with the reference DNS. This is of course expected as the small-scale structures are not well represented on such a coarse grid. Surprisingly, the periodic and streamwise components of the rms velocities show rather small discrepancies when compared to the DNS. This is attributed to the excellent subgrid features of entropic lattice Boltzmann models for under-resolved simulations as also reported in [40, 74].

The simulation using grid refinement is shown on the left side of figure 4.7, where we zoom in the near-wall region and pay special attention to the level interface. The agreement on the finest level is good, as expected. However, a small but distinct jump may be observed at the interface of level one and level two, which is particularly pronounced for $u_{y,rms}$. This owes to the fact that the severe under-resolution in the coarse level leads to a misrepresentation of the small scale fluctuation on the coarse level. To support this hypothesis, in figure 4.8, we show an instantaneous snapshot of the spatial distribution of the stabilizer γ for the KBC model as computed by Eq. (2.45). As shown in [40], the stabilizer γ tends to the LBGK value $\gamma = 2$ in the resolved case. Thus, its deviation provides a measure of under-resolution. It is apparent that in the refined near-wall region, the stabilizer is indeed very close to $\gamma = 2$, whereas the distribution in the bulk exhibits large deviations. It is interesting to notice that particularly

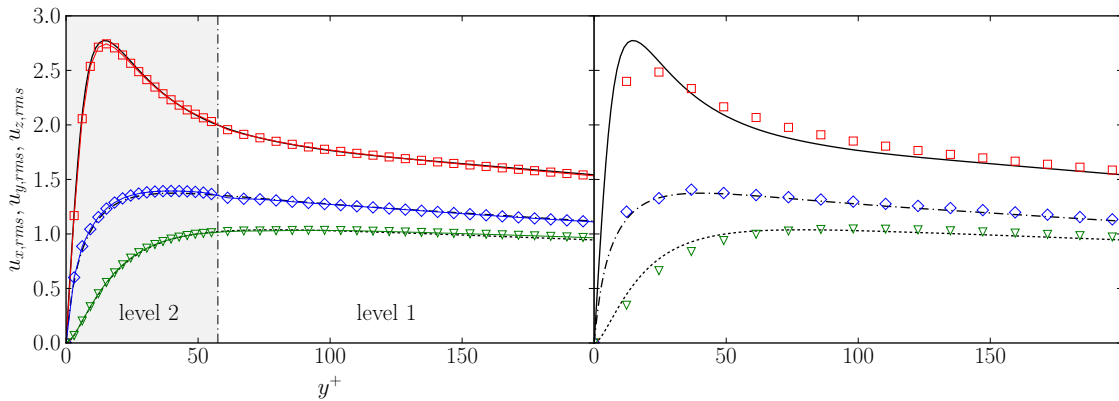


Figure 4.7: Rms velocity profiles in a turbulent channel at $Re_\tau = 590$ with a two-level refinement in the near-wall region (left) and the non-refined case (right). For the legend please refer to figure 4.5.

large deviations arise in the immediate neighborhood of the level interface. It seems that the level interface is detected and compensated by the KBC model, thus rendering explicit projection of the fine level solution onto the coarse mesh by filtering or alike unnecessary [184].

These observations when viewed together with the flow at $Re_\tau = 180$ suggest that despite of the excellent subgrid features of entropic lattice Boltzmann models in matching the average velocity (see uniform mesh at $Re_\tau = 590$), a minimum resolution on the coarse grid is required to reasonably represent the small scale fluctuations on the coarse grid and thus achieve a smooth grid level transition in higher-order statistics. The implicit subgrid model however, alleviates the need for filtering the fine level solution on the coarse level and assures stability in the coarse level. It further needs to be emphasized that due to these excellent subgrid features, the finest patch may itself be under-resolved ($\Delta y_f^+ \approx 3.06$ compared to $\Delta y^+ \approx 0.04$ for the DNS) while accurately capturing the velocity fluctuations near the wall. Thus, the refinement allows to enhance the subgrid features, so that also the higher-order statistics can be captured accurately.

Flow past a sphere After the validation of the grid refinement technique for flat walls in the previous section, we now consider curved walls and choose the well-studied problem of the flow past a sphere. In order

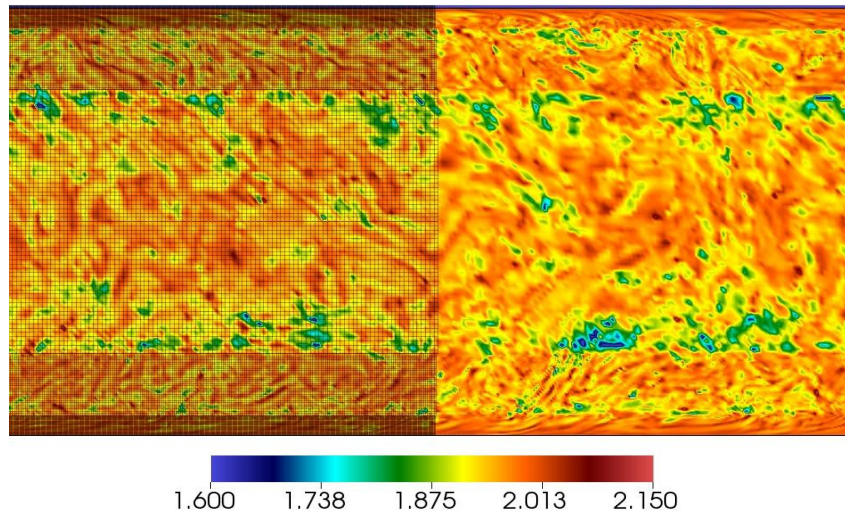


Figure 4.8: Slice through the turbulent channel flow at $\text{Re}_\tau = 590$ showing the spatial distribution of the stabilizer γ for the KBC model and the refinement patches (only left half shown here).

to assess the accuracy of the proposed grid refinement algorithm, we focus on the flow within the subcritical regime, for which the boundary layer remains laminar and the near wake features turbulence. A detailed analysis is conducted for $\text{Re} = 3700$ and an instantaneous snapshot of isosurfaces of the Q -criterion is shown in figure 4.9. The computational domain is chosen as $[-7D, 23D] \times [-10D, 10D] \times [-10D, 10D]$ with the sphere centered at the origin. Four refinement patches are located closely around the sphere, where the finest patch resolves the sphere with $D = 120$. A graphical representation of the refinement patches is shown in figure 4.15a, where the finest level is avoided for $D = 120$. It is worth noting that a simulation for this sphere resolution and without grid refinement would require $N_f \approx 20.7 \cdot 10^9$ grid points, rendering such a simulation unfeasible for practical purposes. With the refinement, the computational grid reduces to a total of $N_r \approx 94.6 \cdot 10^6$ lattice points. By taking into account the time step scaling, the equivalent fine level points in the refined case amount to $39.5 \cdot 10^6$, which is roughly 575 times less than the fully resolved case without refinement. Such an estimate suggests a tremendous optimization potential when employing grid refinement, while still retaining the desired accuracy. This allows for a detailed comparison with the contributions of [296] and their DNS simulation, the LES simulations of [388] and the

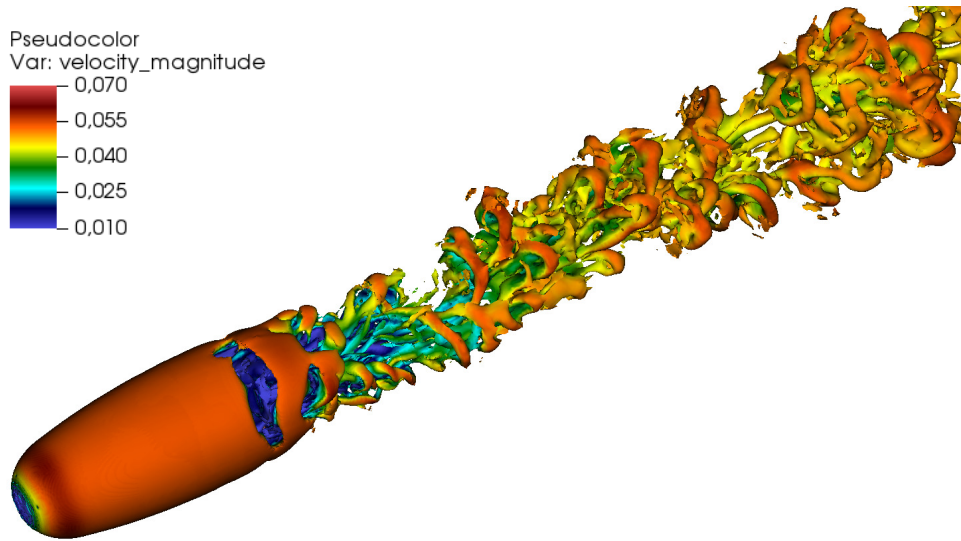


Figure 4.9: Isosurfaces of Q -criterion colored by velocity magnitude for the flow past a sphere at $Re = 3700$.

experimental results of [172, 305].

First, we compare various scalar quantities such as the mean drag coefficient $\overline{C_d} = \overline{F_d}/(1/2\rho_\infty u_\infty^2 D)$, the mean base pressure coefficient $\overline{C_{pb}}$, the recirculation length $\overline{L_r}$ and the separation angle $\overline{\varphi_s}$. Here, the mean drag force is denoted by $\overline{F_d}$ and u_∞ is the uniform inflow velocity. As tabulated in table 4.3, the comparison shows excellent agreement with the literature for all quantities.

For a more thorough analysis, we compare the time-averaged profiles of the streamwise velocity component $\overline{u_x}$ in the near wake to profiles obtained by DNS, LES and experiment, see figure 4.10. Three profiles are measured for a streamwise location of $x/D = 0.2$, $x/D = 1.6$ and further downstream at $x/D = 3$. While for $x/D = 0.2$ all measurements are in almost perfect agreement, the discrepancies increase slightly for all reference data further downstream. Nonetheless, the measurements taken from our simulation appear to be in good agreement with all reference data. Next, in figure 4.11, the azimuthally averaged distribution of the mean pressure coefficient $\overline{C_p} = (\overline{p} - p_\infty)/(1/2\rho_\infty u_\infty^2)$ around the sphere is presented in comparison with the DNS and experimental results. It is apparent that mean pressure distribution matches the two references well. However, it needs to be pointed out that this agreement could only be achieved with an additional layer of refinement, yielding a resolution of $D = 240$ points for the diameter of the sphere. This is in contrast to the velocity profiles,

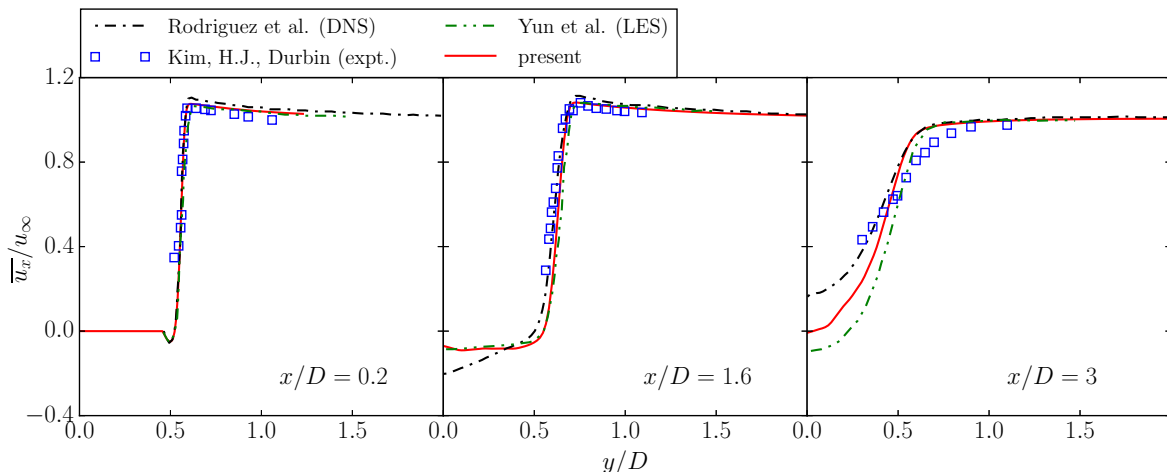


Figure 4.10: Mean streamwise velocity profiles in the wake for the simulation of flow past a sphere at $Re = 3700$.

which were captured already with four levels and a diameter of $D = 120$ points in the finest level.

These results for the turbulent channel flow and the flow past a sphere conclude the validation of the isothermal regime. Our results indicate robustness, high accuracy and compatibility with entropy-based LBM of the proposed grid refinement scheme for high Reynolds number turbulent flows. Although average flow velocity is easily captured using a coarse uniform grid in combination with the KBC model, near-wall features and higher-order statistics do require grid refinement for an accurate representation.

Table 4.3: Turbulent flow past sphere at $Re = 3700$ and the comparison of the mean drag coefficient $\overline{C_d}$, the averaged base pressure coefficient $\overline{C_{pb}}$, the recirculation length $\overline{L_r}$ and the separation angle $\overline{\varphi_s}$ with literature values.

Contribution	$\overline{C_d}$	$\overline{C_{pb}}$	$\overline{L_r}$	$\overline{\varphi_s}$
[296]	0.394	-0.207	2.28	89.4
[388]	0.355	-0.194	2.622	90
[172]	—	-0.224	—	—
[305]	0.39	—	—	—
present	0.383	-0.220	2.51	89.993

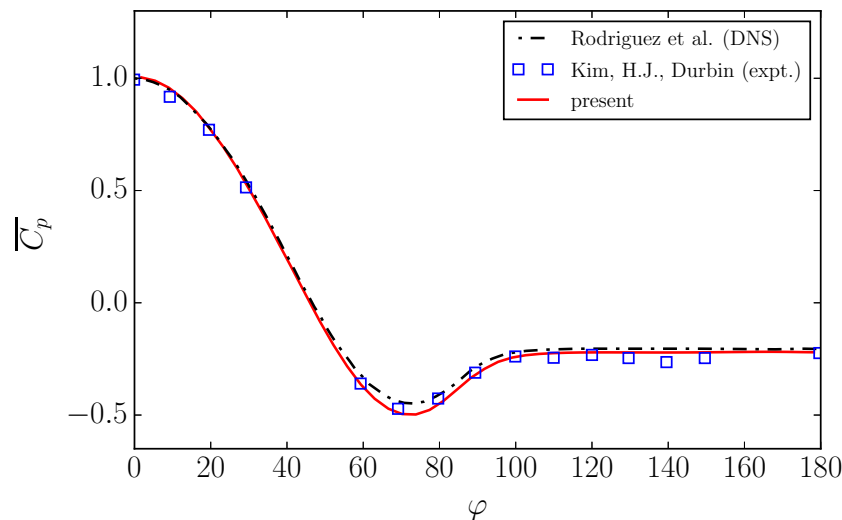


Figure 4.11: Pressure coefficient distribution around the sphere at $\text{Re} = 3700$.

4.2.3.2 Thermal flows

We proceed investigating stability and accuracy of the proposed grid refinement algorithm when applied to thermal flows, simulated with the two-population model [155]. We start with the simulation of Rayleigh-Bénard convection (RBC) in order to validate the model and the grid refinement algorithm for flat walls. As a second step, we revisit the simulation of the flow past a sphere but additionally include the temperature field and compare the mean Nusselt number distribution. The boundary conditions used for all wall-boundary nodes is Grad's approximation as presented in [265].

Rayleigh-Bénard convection The Rayleigh-Bénard set-up consists of a fluid layer which is heated from below and cooled from above. When the temperature difference ΔT between the two walls is sufficiently high, thermal convection is triggered. The non-dimensional parameters governing this problem are the Rayleigh number $\text{Ra} = g\lambda\Delta TH^3/\nu\kappa$ and the Prandtl number $\text{Pr} = \nu/\kappa$, where g represents gravitational acceleration, λ the thermal expansion coefficient, H the height of the fluid layer, ν the kinematic viscosity and κ the thermal conductivity.

In this work, we present the results of the thermal two-population model coupled with the grid refinement algorithm for thermal flows and their comparison with the DNS simulation of [342]. The Rayleigh and Prandtl

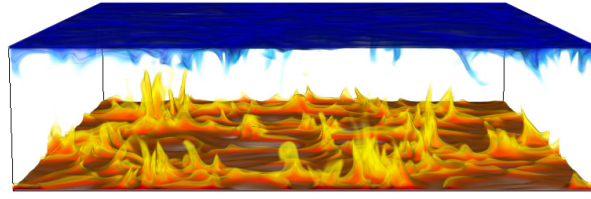
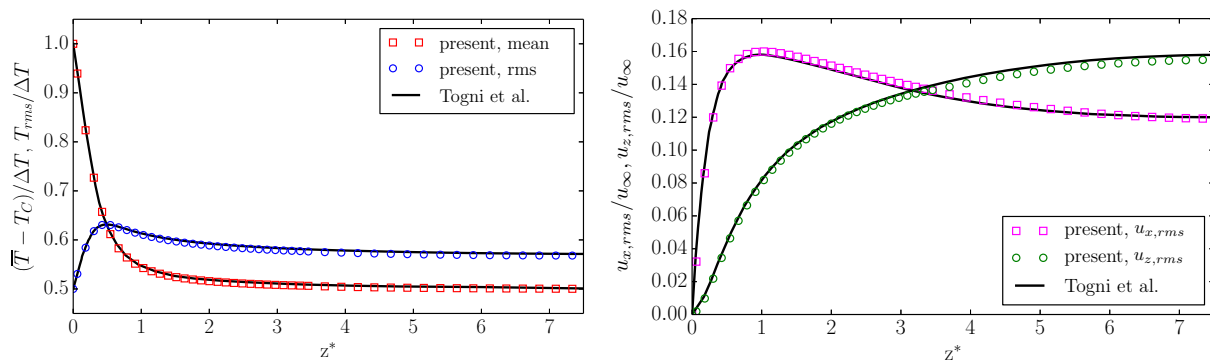


Figure 4.12: Volume rendering of temperature for the Rayleigh-Bénard convection at $Ra = 10^7$.

number are $Ra = 1 \cdot 10^7$ and $Pr = 0.7$. The computational domain is a box with periodicity in the x and y directions and a fixed temperature is imposed at the bottom (hot) and top (cold) walls. The size of the domain is $L_x \times L_y \times L_z = 8H \times 8H \times H$, where $H = 64$ is the resolution in the coarse grid level. On top of the coarse grid, one more refinement patch is added at both hot and cold walls in order to increase the resolution in the boundary layers. To trigger convection an initial random perturbation is imposed on a linear temperature profile. The buoyancy force is computed according to the Boussinesq assumption and implemented as reported in [155].

An instantaneous volume rendering of the temperature in the domain is shown in figure 4.12. One can notice the cold temperature plumes in the upper part of the box and the hot temperature plumes developing from the bottom of the box. Quantitatively, in figure 4.13a, we compare the mean and the rms temperature profiles with the recent DNS data [342] and the agreement is good. All statistics are collected after the initial transient at $40t_L$ and sampled every $2.5t_L$ for a time period of $100t_L$, where $t_L = 2H/U$ denotes the large eddy turnover time with the free fall velocity $U = \sqrt{g\lambda\Delta TH}$. The temperature profiles are plotted as a function of the normalized vertical coordinate (normal to the bottom wall) $z^* = z/(H/\overline{Nu})$, where \overline{Nu} is the mean Nusselt number, defined as $\overline{Nu} = \frac{d\overline{T}/dn}{\Delta T/H}$ and $d\overline{T}/dn$ is the mean temperature gradient at top and bottom walls. In figure 4.13b, the rms velocity profiles for the u and w component are shown and compared to the reference data. Analogous to the temperature profiles, a good agreement is also observed for the velocity fluctuations. To complete the validation for the Rayleigh-Bénard convection we compare the resulting Nusselt number. While in our simulation the Nusselt number at the wall is evaluated as $Nu_{ELBM} = 15.67$, the DNS



(a) Comparison of mean and rms temperature profiles. The rms temperature profile is shifted by 0.5 for visualization. (b) Comparison of u_x and u_z rms velocity components profiles.

Figure 4.13: Rayleigh-Bénard convection at $Ra = 10^7$.

[342] reports $Nu_{DNS} = 15.59$. This amounts to a relative discrepancy of $\epsilon_{Nu} = 5.13 \cdot 10^{-3}$.

Similar to the turbulent channel flow, it is important to notice that the transition at the grid interface is smooth for all quantities presented here, from the mean and rms temperature profiles to the rms x - and z -velocity profiles. This is again attributed to the entropic stabilizer γ for which a snapshot through the domain is shown in figure 4.14. It is evident that larger deviations of γ from the LBGK value $\gamma = 2$ appear in the bulk rather than near the walls where the resolution is higher. Also in this case larger deviations in the γ arise in the immediate neighborhood of the level interface, which seems to be detected and compensated by the KBC model. This is analogous to the observation in the channel flow. Thus demonstrating the self-adaptive nature of the entropic stabilizer γ for all flow situations including grid refinement and complex wall boundary conditions. This self-adaptive nature of γ makes the simulations parameter-free.

Flow past a heated sphere As in the isothermal section, after validation of the scheme for flows involving flat walls, we increase the complexity and consider curved walls next. For this purpose, we consider a heated sphere with the surface at constant temperature. The flow is simulated for a Reynolds number $Re = 3700$ and Prandtl number $Pr = 0.7$. The computational domain is identical to the isothermal case with $D = 240$. A snapshot of the temperature distribution around and in the wake of the

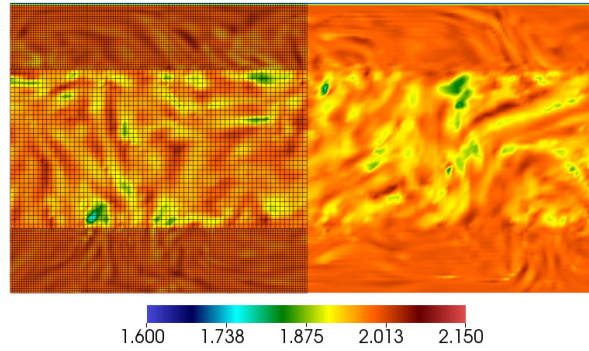


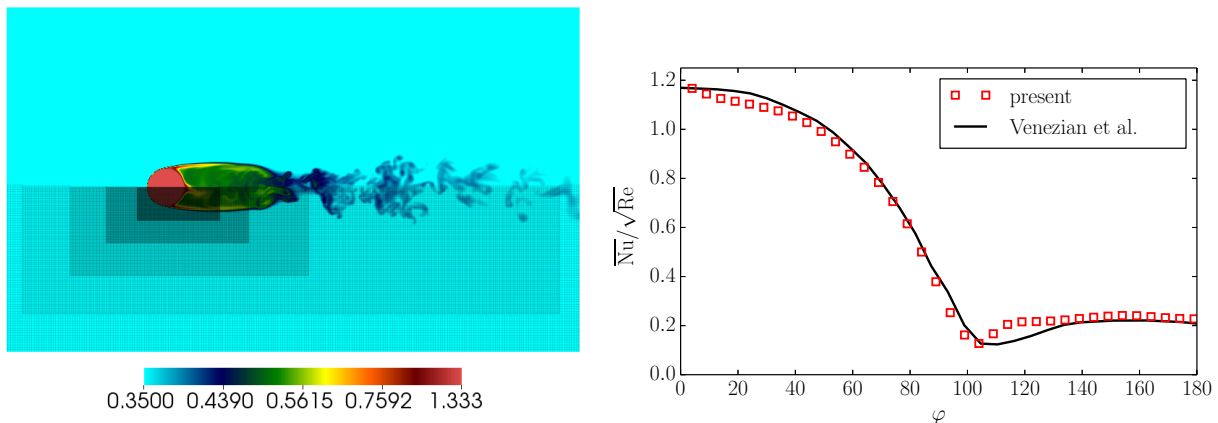
Figure 4.14: Slice through the Rayleigh-Bénard convection at $Ra = 10^7$ showing the spatial distribution of the stabilizer γ for the KBC model and the refinement patch (only left half shown here).

sphere for this simulation along with the refinement patches is shown in figure 4.15a. The figure shows hot temperature streams in the shear layer and the back of the sphere, where the flow recirculates. Further downstream, hot fluid mixes with cold fluid and the temperature becomes diluted. In order to quantitatively validate the heated sphere simulation, the mean reduced Nusselt number distribution $\overline{Nu}/\sqrt{Re} = \frac{dT/dn}{\Delta T/D}/\sqrt{Re}$ around the sphere is shown in comparison to experimental results [355] in figure 4.15b, where n is the normal coordinate with respect to the sphere's surface and ΔT the temperature difference between fluid and sphere surface. The plot shows a good comparison with the experiment.

4.2.3.3 Compressible Flows

We conclude the numerical validation by entering the compressible regime for which we take the simulation of the two-dimensional viscous supersonic flow around a NACA0012 airfoil as an example.

Supersonic NACA0012 airfoil The set-up consists of a two-dimensional simulation of the viscous supersonic flow field around a NACA0012 airfoil, at zero angle of attack $\mathcal{A} = 0^\circ$. The free-stream Mach number is set to $Ma_\infty = u_\infty/a_\infty = 1.5$, where $a_\infty = \sqrt{\gamma_{ad}T_\infty}$ is the speed of sound with $\gamma_{ad} = 1.4$ and $T_\infty = 0.8$, while the Reynolds number, based on the chord C of the airfoil, is $Re = Cu_\infty/\nu = 10000$. The computational domain is prescribed as $[-7.5C, 17.5C] \times [-7C, 7C]$ with the airfoil centered at the origin. Two refinement patches are placed closely around the airfoil, where



(a) Snapshot of the instantaneous temperature distribution around and in the wake along with the refinement patches (only lower half shown here).

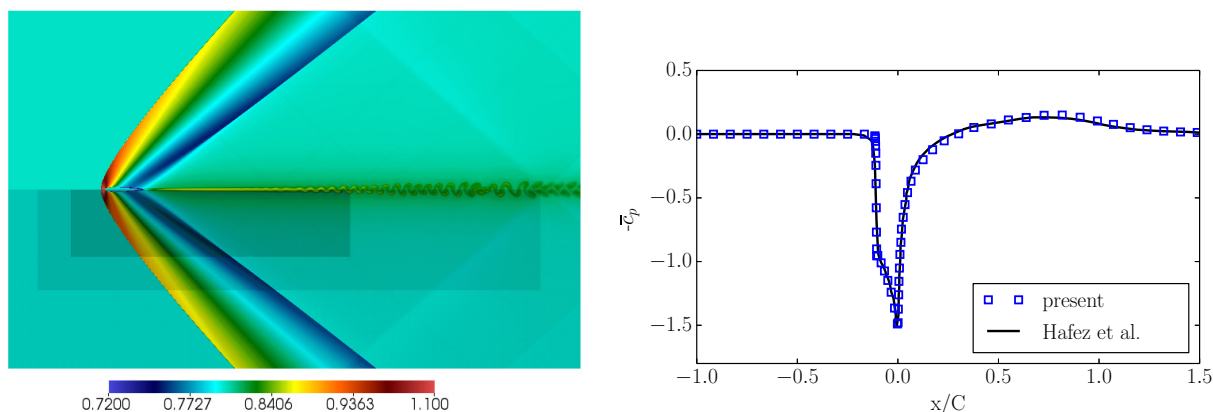
(b) Average Nusselt number distribution around the heated sphere.

Figure 4.15: Flow past a heated sphere at $Re = 3700$.

the finest patch resolves the airfoil chord with $C = 1200$ grid points (see figure 4.16a).

Due to the high Mach number in this simulation, we use a shifted lattice as presented in [101]. In particular, we employ the D2Q49 lattice with a shift in the freestream direction of $U_x = 1$. The advantage of shifted lattices is that the errors in the higher-order moments of the equilibrium populations are also shifted and centered around the shift velocity U_x . This allows us to keep the number of populations of the multi-speed lattice relatively small, while reducing the errors in the high Mach regime. For further details on shifted lattices the reader is referred to [101].

In figure 4.16a, a snapshot of the temperature distribution along with the two refinement patches around the airfoil, indicated by the shadowed regions in the lower half of the domain, is shown. The main features of the viscous supersonic flow field are evident from the temperature distribution: The formation of a bow shock may be observed in front of the airfoil, yielding a jump and drastic increase in temperature. An oblique shock wave develops from the shear layer as a λ shock at the trailing edge of the airfoil. Vortex shedding is initiated further downstream in the shear layer. It is important to notice that the shock waves penetrate through various refinement levels, where special care usually needs to be taken to avoid artificial reflections at the interface. It is apparent that for the proposed refinement



(a) Snapshot of temperature distribution. Grid refinement patches are shown by the shadowed regions around the airfoil in the lower half of the domain. (b) Comparison of the pressure coefficient distribution upstream the airfoil ($x/C \in [-1, 0]$), on the airfoil surface ($x/C \in [0, 1]$) and downstream the airfoil ($x/C \in [1, 1.5]$)

Figure 4.16: Flow around a NACA0012 airfoil at $\mathcal{A} = 0^\circ$, $\text{Ma} = 1.5$ and $\text{Re} = 10000$.

algorithm, no reflections or similar artifacts are observed and thus making it suitable also for compressible flows and the related shock dynamics.

For a quantitative comparison, the mean pressure coefficient distribution upstream the airfoil ($x/C \in [-1, 0]$), on the airfoil surface ($x/C \in [0, 1]$) and downstream the airfoil ($x/C \in [1, 1.5]$) is plotted in figure 4.16b along with the simulation results reported in [126]. Statistics have been collected after $50t^* = 50C/u_\infty$ flow times and at every time step in the coarse level. Evidently, an excellent comparison can be reported.

Before concluding the numerical validation, we present a snapshot of the entropic estimate distribution around the airfoil in figure 4.17. From the plot, two main observations can be made. First, it is apparent that the entropic estimate adapts to the main physical features of the flow. In particular, large deviations from the resolved limit value $\alpha = 2$ may be observed near the bow shock, through the expansion wave preceding the oblique shock at the trailing edge and in the oblique shock itself. A second key observation concerns the interplay of the entropic estimate with the physical feature of the flow and the grid refinement patches. For example, it can be seen that the entropic estimate exhibits larger deviations from the fine to the coarse grid when a shock wave crosses the interface (see interface position in figure 4.16a). These deviations in the entropic estimate arise naturally from the entropy condition Eq. (2.34) and play a central role in

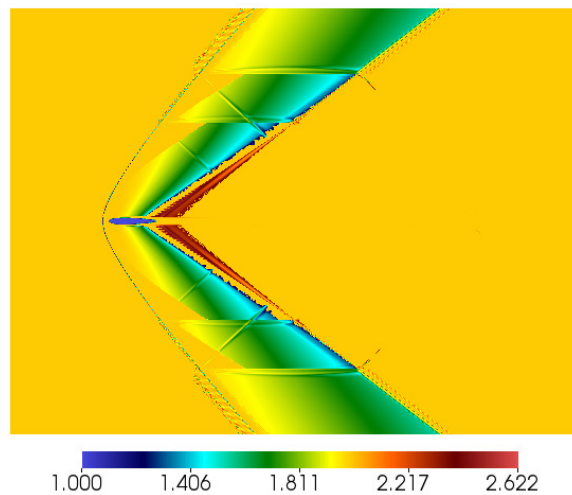


Figure 4.17: Snapshot of the distribution of the entropic estimate α around the NACA0012 airfoil.

sustaining the flow field by damping the spurious oscillations and noise near the shocks, which would otherwise appear near the different grid interfaces.

4.3 Unstructured meshes

The following work was conducted in close collaboration with Giovanni Di Ilio. In the previous section, a block-refinement strategy was developed, where locally, uniformly refined Cartesian have been embedded into the computational domain.

Another approach to reduce the computational costs for complex applications is the use of unstructured meshes. Such schemes attempt to overcome the restrictions of the classical LBM, which is based on regular Cartesian grids, is second-order accurate and imposes a unit Courant-Friedrichs-Lewy (CFL) number. While these properties of the classical LBM lead to crucial advantages such as exact propagation in space and allowing the use efficient data structures, the level of geometrical flexibility of unstructured meshes cannot be matched by Cartesian grids. In particular, for wall-bounded turbulent flows, body-conforming, stretched or unstructured meshes can be used to capture all pertinent small scale structures in vicinity of the body, while keeping the resolution and thus computational cost reasonably low in regions far away from the body, which are mainly dominated by large scale flow structures.

In the realm of LBM a variety of these so-called off-lattice Boltzmann methods (OLBM) have been proposed, which mainly solve the discrete Boltzmann equation using either finite volume (FV) [253, 266, 270, 351, 377], finite difference [90, 129] or discontinuous Galerkin schemes [240, 389]. The first extension of LBM to unstructured meshes was proposed by [270, 271, 377], which is based on FV. The FV approach was further advanced by [266–268, 349–351, 392], enhancing the numerical stability of the scheme. Other notable OLBM are the Discrete Unified Gas Kinetic Scheme (DUGKS) [397] and the general characteristics based off-lattice Boltzmann scheme by [16] (see, e.g., [285] for a comparative study of several explicit OLBM).

While geometrical flexibility can be a tremendous advantage, the computational costs of these high-order OLBM, which explicitly discretize the spatial and temporal derivatives of the discrete Boltzmann equation in an Eulerian frame of reference, are significant compared to traditional LBM. This mainly due to the costly evaluation of the spatial operators [177]. In particular, the advective part of the Boltzmann equation needs to be computed for each discrete particle velocity, i.e. 27 times for the standard $D3Q27$ lattice and the resulting spatial operators are typically evaluated repetitively within each time step, e.g., for explicit Runge-Kutta methods. In addition, the CFL number is restricted by the explicit integration and proportional to the lattice velocities and not the macroscopic flow velocity, which further decreases the allowable time step. These issues limit the applicability of OLBM in terms of attainable complexity and Reynolds number.

A remedy was sought in interpolation-based lattice Boltzmann methods [58, 317]. Most recently, these issues were addressed in work of [177], who proposed a semi-Lagrangian off-lattice Boltzmann approach (SLLBM) based on a finite element reconstruction of the population. The SLLBM has shown promising results for periodic set-ups in two and three dimensions, while keeping the computational costs reasonable. Starting point for the SLLBM is the characteristic equation of the Boltzmann equation and a solution is found by a finite element based interpolation at the departure points of the characteristic lines. This procedure eliminates the need of repetitive evaluation of the spatial operator, while retaining stability at larger CFL numbers. In addition, the SLLBM only solves the streaming

step in a semi-Lagrangian frame and keeps the collision operator local as in the traditional LBM.

For these advantages, we employ the SLLBM, extend it to the entropic multi-relaxation LBM and wall-bounded turbulence with appropriate boundary conditions. The aim of this study is to assess the viability of this approach for three-dimensional turbulent flow simulations.

First, in this section, the general methodology of the SLLBM (following closely [177]) along with appropriate boundary conditions is presented. Subsequently, after a convergence study for laminar flows, results for the turbulent flow past a circular cylinder at $Re = 3900$ are presented.

4.3.1 Semi-Lagrangian LBM

Analog to the traditional LBM, the SLLBM splits algorithm into a streaming and collision step. While the collision remains unchanged, the streaming step is solved by a semi-Lagrangian advection, which follows the characteristics of LBM, $\mathbf{x} + \mathbf{c}_i \delta t$. As in standard LBM, the post-advection population $f_i(\mathbf{x}, t)$ is given by

$$f_i(\mathbf{x}, t) = f_i(\mathbf{x} - \mathbf{c}_i \delta t, t - \delta t), \quad (4.54)$$

where $\mathbf{x} - \mathbf{c}_i \delta t$ is the departure point of the characteristic line. Hence, solving the semi-Lagrangian advection amounts to reconstructing the population at the departure location $\mathbf{x} - \mathbf{c}_i \delta t$ (see also figure 4.18). It is obvious that in the limiting case of a regular Cartesian grid with spacing $c\delta t$, the departure point is also a grid node, which eliminates the need of reconstruction and therefore recovers the classical LBM. However, for unstructured

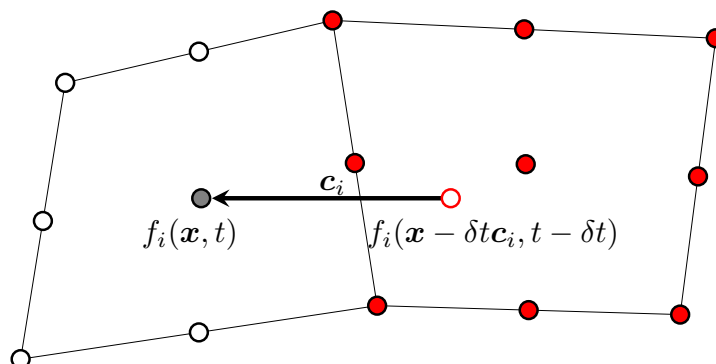


Figure 4.18: Schematic of the semi-Lagrangian streaming step of population $f_i(\mathbf{x}, t)$ along the discrete velocity \mathbf{c}_i .

meshes this is not necessarily the case and an accurate reconstruction is crucial. To that end, the SLLBM represents the population as a finite element instead of the usual point-wise approximation, which decouples the computational grid from the time step and offers high-order accurate reconstruction of the population. In the following, the computational domain is discretized into a shape-regular mesh, which is composed of N_ξ hexahedral elements. The shape functions are the Lagrange polynomials of order p , which are defined on $N_p = (p + 1)^D$ support points (see also chapter 8.2.1 for a detailed definition of the finite element spaces). A bijective trilinear transformation is used to map a physical element to their unit element counterpart.

Thus, the population $f_i(\mathbf{x}, t)$ can be approximated by

$$f_i(\mathbf{x}, t) = \sum_{\xi=1}^{N_\xi} \sum_{j=1}^{N_p} f_{i\xi j}(t) \psi_{\xi j}(\mathbf{x}), \quad (4.55)$$

where $f_{i\xi j}$ and $\psi_{\xi j}$ denote the populations and shape function values at the support points for each cell, respectively. Finally, upon substitution into Eq. (4.54) and evaluation at a support point $\mathbf{x} = \mathbf{x}_{\xi j}$, the semi-Lagrangian advection is given by

$$f_{i\xi j}(\mathbf{x}_{\xi j}, t) = \sum_{\xi=1}^{N_\xi} \sum_{j=1}^{N_p} f_{i\xi j}(t - \delta t) \psi_{\xi j}(\mathbf{x}_{\xi j} - \delta t \mathbf{c}_i). \quad (4.56)$$

In matrix form, the streaming amounts to simple, explicit matrix-vector multiplications, which can be expressed as

$$\mathbf{f}_i(t) = \boldsymbol{\psi}_i \mathbf{f}_i(t - \delta t), \quad (4.57)$$

where $\boldsymbol{\psi}_i$ is the sparse matrix of shape functions and \mathbf{f}_i is the population vector.

For simplicity, we set $p = 2$ in the following but the extension to higher order is straightforward. The time step is set to $\delta t = \delta x_{\min} / \sqrt{3}$, where δx_{\min} is the minimum spacing between any two vertices of the computational mesh. The time step size is chosen such that the departure point remains inside the current cell or in its immediate neighborhood. While the SLLBM remains stable even for larger time steps [177], the limiting case of $\delta t = 2\delta x_{\min}$ and a regular Cartesian grid results in two independent solutions.

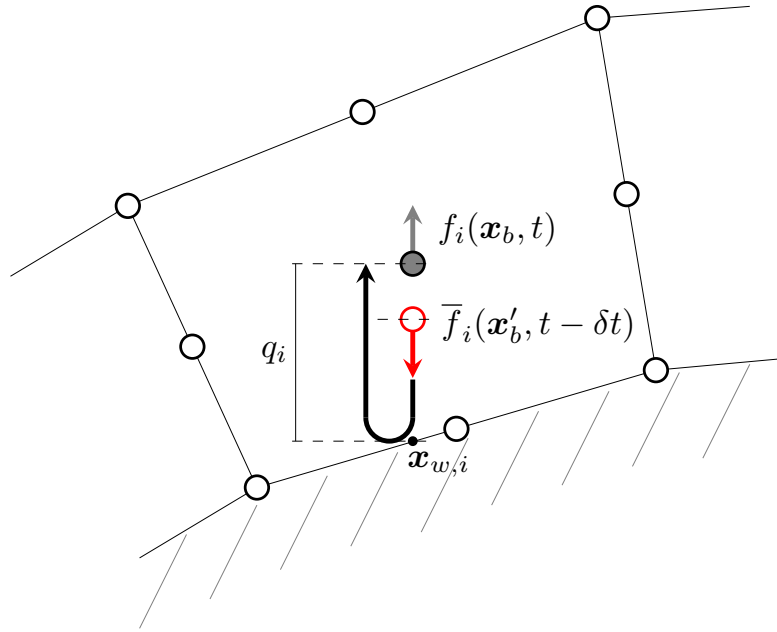


Figure 4.19: Schematic of the boundary condition for the population $f_i(\mathbf{x}_b, t)$.

Such unphysical decoupling is avoided effectively by this choice of the time step size.

The SLLBM was implemented on the basis of the finite element library deal.ii [15] and the linear algebra library Trilinos [131].

4.3.1.1 Boundary conditions

For the SLLBM, it is natural to use a similar interpolation scheme as in the bulk. In particular, a modified version of the interpolated bounce-back boundary condition is employed here. The general problem is depicted in figure 4.19. Analog to chapter 3, populations for which the departure point lies outside the domain need to be reconstructed in order to complete the advection step. Using a bounce-back type boundary condition, which reflects the population at the wall boundary, we define the departure point \mathbf{x}'_b as follows

$$\mathbf{x}'_b = \mathbf{x}_{w,i} + (\delta t - q_i)\mathbf{c}_i, \quad (4.58)$$

where $\mathbf{x}_{w,i} = \mathbf{x}_b + q_i\bar{\mathbf{c}}_i$ is the intersection point between the wall boundary and the velocity vector $\bar{\mathbf{c}}_i = -\mathbf{c}_i$ and the wall distance is given by $q_i = \|\mathbf{x}_b - \mathbf{x}_{w,i}\|/\|\mathbf{c}_i\|$ (see also figure 4.19). The application of the boundary condition at \mathbf{x}_b then reduces to a reconstruction of the population $\bar{f}_i(\mathbf{x}'_b, t - \delta t)$ at the departure point, which is associated with the veloc-

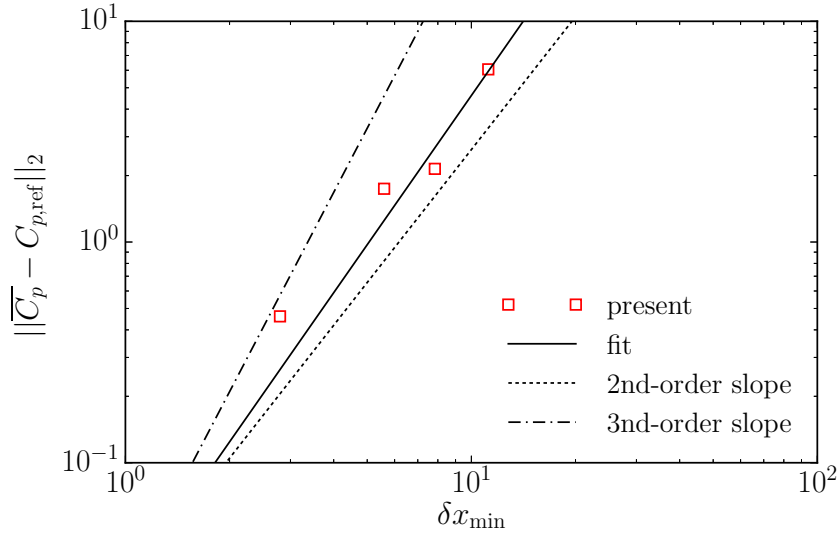


Figure 4.20: Scaling of the L_2 error for the simulation of the flow past a circular cylinder at $Re = 40$.

ity $\bar{\mathbf{c}}_i$. Analogous to the above, the finite element reconstruction for the population $f_{i\xi j}(\mathbf{x}_b, t)$ at the boundary support point \mathbf{x}_b in an arbitrary boundary cell reads

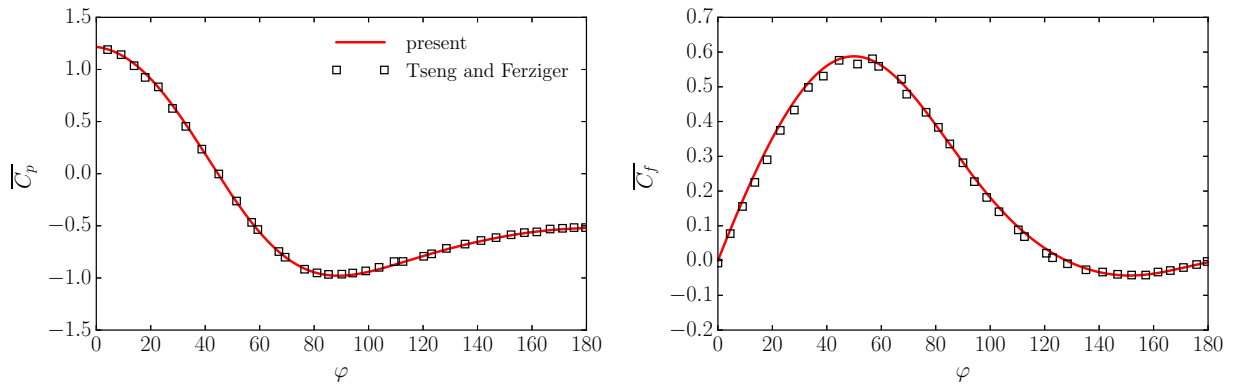
$$f_{i\xi j}(\mathbf{x}_b, t) = \bar{f}_i(\mathbf{x}'_b, t - \delta t) = \sum_{\xi=1}^{N_\xi} \sum_{j=1}^{N_p} \bar{f}_{i\xi j}(t - \delta t) \psi(\mathbf{x}'), \quad (4.59)$$

where $\bar{f}_{i\xi j}$ corresponds to the population associated with the velocity $\bar{\mathbf{c}}_i$.

4.3.2 Validation and convergence study

To validate the SLLBM in combination with the KBC model and the interpolated bounce-back boundary condition, a convergence study for the flow past a circular cylinder is conducted. We start in the laminar regime at a Reynolds number of $Re = u_\infty D / \nu = 40$, where u_∞ and D are the free-stream velocity and the diameter of the cylinder, respectively. In this regime, the wake behind the cylinder is characterized by a steady recirculation region.

Four simulations with varying resolutions are conducted and accuracy is assessed using the L_2 error of the mean pressure and skin friction coefficient compared with the reference solution by [345]. The computational domain is chosen as $[-10D, 30D] \times [-10D, 10D] \times [-0.5D, 0.5D]$ and the centroid



(a) Mean pressure coefficient.

(b) Mean skin friction coefficient.

Figure 4.21: Comparison of the mean pressure and skin friction coefficient distribution around the cylinder at $Re = 40$ with the reference [345].

of the cylinder is located at the origin. A uniform velocity and a zero pressure gradient is imposed at the inlet, while a fixed pressure value and a zero velocity gradient are prescribed at the outlet. In spanwise direction periodic boundary conditions are applied.

In figure 4.20, the L_2 error for the pressure coefficient is plotted as a function of the grid spacing, showing a convergence rate between second and third order. This is in line with the results presented for periodic flows in [177]. Therefore, we can conclude that the presented SLLBM, complemented with appropriate boundary conditions and the KBC collision model, is at least second-order accurate. In figure 4.21, the solution of the pressure and skin friction coefficient as obtained on the finest mesh are plotted against the reference solution of [345]. Here, the mean skin friction coefficient is defined as $\overline{C}_f = \overline{\tau} / (1/2 \rho_\infty u_\infty^2)$, where $\overline{\tau}$ is the mean wall shear stress. As expected from the L_2 error, the agreement is excellent.

This validates the general scheme for curved geometries.

4.3.3 Flow past a circular cylinder at $Re = 3900$

Moving beyond the laminar flows, we increase Reynolds number to $Re = 3900$ and simulate the turbulent flow past a circular cylinder in the lower subcritical regime. In this regime, the flow separation is laminar, while transition to turbulence occurs downstream of the cylinder in the free shear layer. Along the wake, the high instability of the flow causes a periodic vortex shedding process, which in turn leads to a vertical oscillatory motion

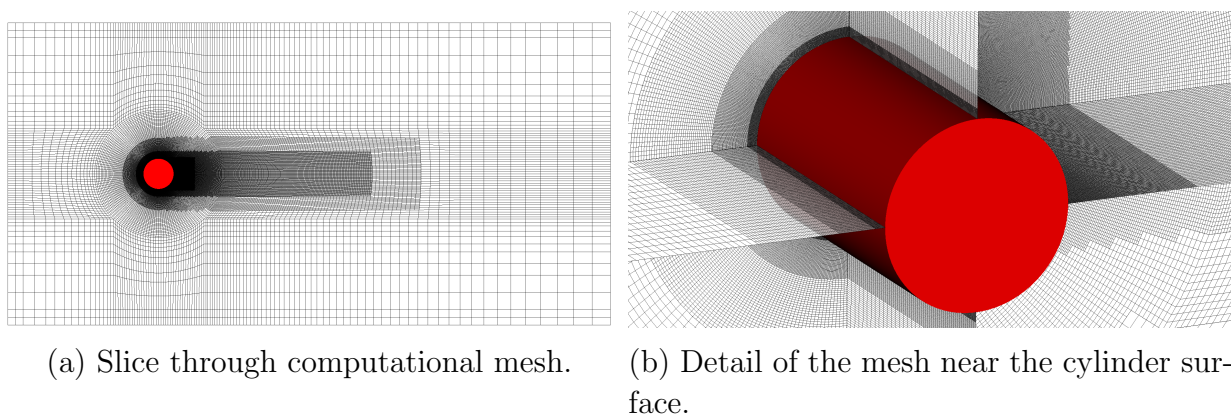


Figure 4.22: Unstructured mesh for the simulation of the flow past a cylinder at $Re = 3900$.

of the free shear layer. These features make the computation of such a flow and the prediction of its unsteady dynamics an interesting as well as a challenging task. Several experimental and numerical investigations exist in literature and, for this reason, has become a canonical benchmark case to assess performance and accuracy of numerical methods.

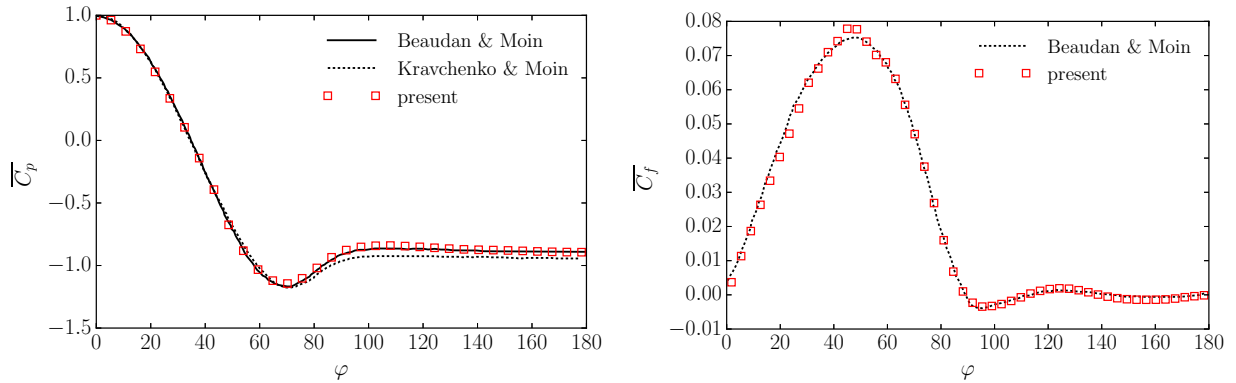
Among the others, the experiments of [212, 257, 262] provide an exhaustive insight on the main features of the turbulent flow under consideration.

As far as numerical simulations are concerned, DNS is most accurate but relatively scarce in literature due to high computational costs. Notable DNS studies include [72, 215, 282, 367]. The majority of numerical studies is conducted using LES and the works of [21, 178, 283, 384] are particularly noteworthy.

The motivation behind the present analysis is to assess the capabilities of the proposed unstructured LBM to capture the main flow features of a turbulent flow past a circular cylinder.

4.3.3.1 Numerical set-up

The simulation is conducted on a computational domain of size $[-5D, 15D] \times [-5D, 5D] \times [-1.5D, 1.5D]$ in streamwise, pitchwise and spanwise direction, respectively (see, e.g., [283] for an overview of the effect of different domain sizes and mesh parameters) and the centroid of the cylinder is placed at the origin. The hexahedral, body-fitted mesh was constructed to minimize the computational cost, while retaining high resolution in close proximity of the cylinder. Hence, we shall focus on the flow field in the near wake,



(a) Comparison of the mean pressure coefficient with Beaudan et al. [21], Kravchenko et al. [178]. (b) Comparison of the mean skin friction coefficient with Beaudan et al. [21].

Figure 4.23: Comparison of the mean pressure and skin friction coefficient distribution around the cylinder at $Re = 3900$ with literature data.

while taking advantage of the favorable implicit sub-grid features of the KBC model in the far field, where the mesh resolution is relatively coarse. Three levels of local refinement patches are placed around the cylinder and in the near wake region. The mesh is highly stretched with a ratio between the largest and smallest cell size of roughly $\delta x_{\max}/\delta x_{\min} \approx 360$. In figure 4.22, a slice through computational mesh as well as a close-up image near the cylinder surface is shown. In the finest level around the cylinder surface, the effective resolution in wall units (based on the maximum wall shear stress) amounts to $\Delta\theta^+ \approx 2.0$ in circumferential direction, $\Delta r^+ \approx 1.20$ in radial direction and $\Delta z^+ \approx 9.2$ in spanwise direction. This yields a total of approximately $36 \cdot 10^6$ degrees of freedom. The boundary conditions are identical to the previous convergence study in section 4.3.2 and a small initial perturbation is introduced to trigger transition to turbulence. Statistics were collected after an initial transient of $t = 35D/u_\infty$ until statistically stationary conditions were reached.

4.3.3.2 Results and discussion

In figure 4.23, the mean pressure and skin friction coefficient distribution along the cylinder surface are displayed. The distributions of the aerodynamic coefficients are compared with the results of [21], who employed a 7th-order upwind-based LES and the study of [178] using a high-order LES based on B-splines. Overall, the results are in excellent agreement.

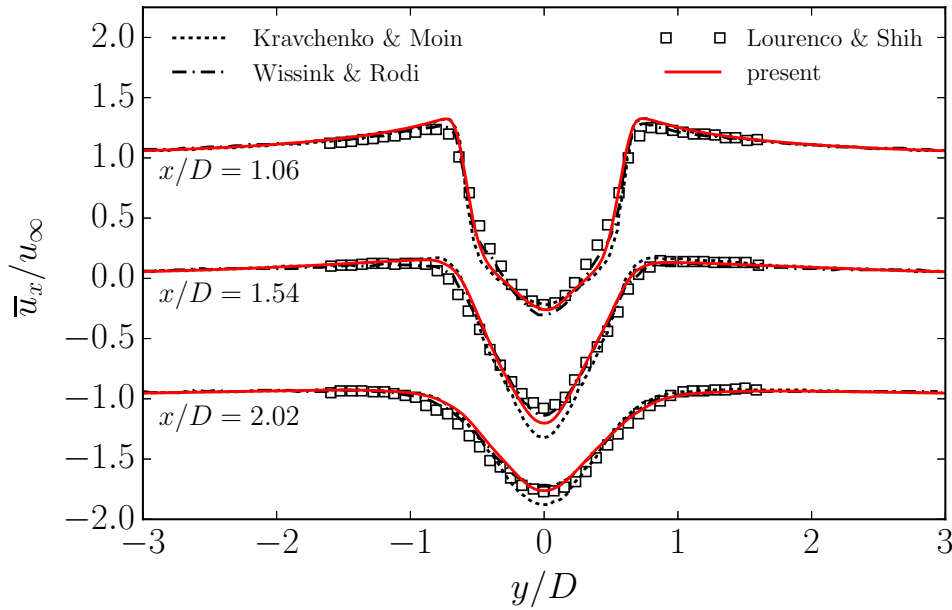


Figure 4.24: Mean streamwise velocity \bar{u}_x/u_∞ profiles in the near wake of a circular cylinder at $Re = 3900$.

Although a slight discrepancy with the reference [178] is noticeable in figure 4.23a, the separation point, i.e. the starting point of the pressure plateau region, seems to be predicted accurately. This is further supported by the skin friction coefficient distribution as shown in figure 4.23b. The separation point corresponds to the location, where the skin-friction is zero and it is obvious that the prediction of the proposed scheme agrees well with the reference [21].

Next, in the figures 4.24 and 4.25, the mean velocity profiles for the streamwise and transverse component at different cross sections in the near wake of the cylinder are presented and compared to the experiment [212], the LES [178] and the DNS [367].

It is apparent that all the computed profiles are in good agreement with reference data. In particular, our simulation seems to predict the mean velocity profile \bar{u}_x/u_∞ , in the near wake region within the experimental accuracy. On the other hand, for the transverse velocity profiles, the overall comparison between numerical methods and experiments shows some discrepancies. However, our results closely follow those of the DNS study [367]. This is also the case for the \bar{u}_x/u_∞ profile.

Finally, in order to provide a qualitative representation of the fully developed flow field, an instantaneous snapshot showing isosurfaces of the Q -

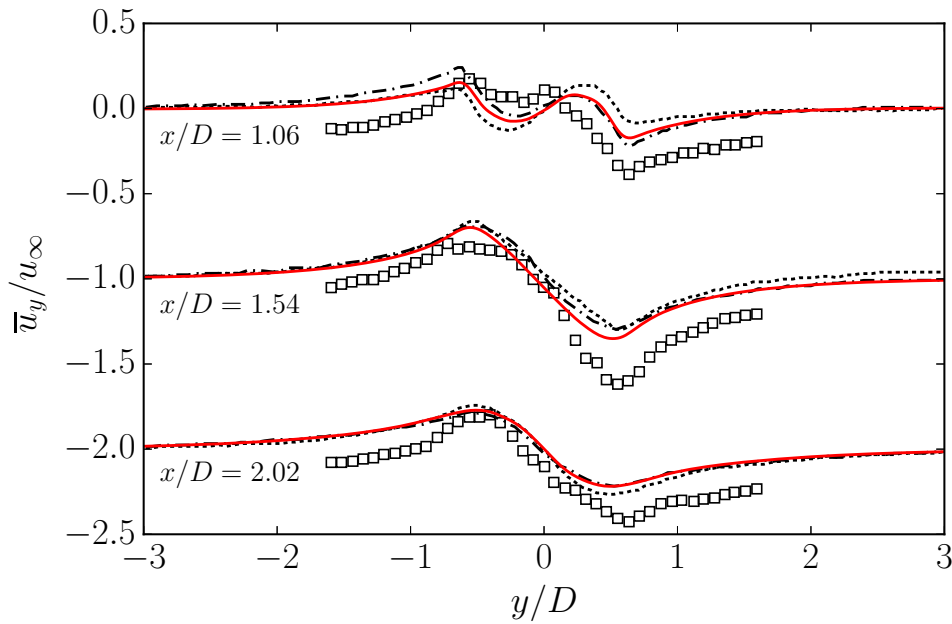


Figure 4.25: Mean transverse velocity \bar{u}_y/u_∞ profiles in the near wake of a circular cylinder at $Re = 3900$. See figure 4.24 for the legend.

criterion, colored by streamwise velocity, is presented in figure 4.26. One can observe laminar separation and subsequently transition to turbulence, which eventually leads to the formation of small-scale structures in the wake of the cylinder.

To conclude, the results from this analysis suggest that the unstructured semi-Lagrangian KBC model is capable of accurately predicting the main flow features of the turbulent flow past a circular cylinder. The current 2nd-order unstructured lattice Boltzmann formulation has been shown to provide accurate results, which are comparable to those obtained by high-order Navier-Stokes solvers. Despite introducing a higher level of complexity in the streaming step, the unstructured semi-Lagrangian KBC model retains a computational efficiency per time step, which is comparable to traditional LBMs.

In addition, the geometrical flexibility of body-fitted mesh allows for an accurate description of the geometry and extremely efficient refinement, which can be optimized to obtain minimal run-times. It also needs to be mentioned that common problems related to hanging nodes do not occur and no particular treatment is needed in the framework of the SLLBM. These aspects are crucial for the simulation of turbulent flows, where un-

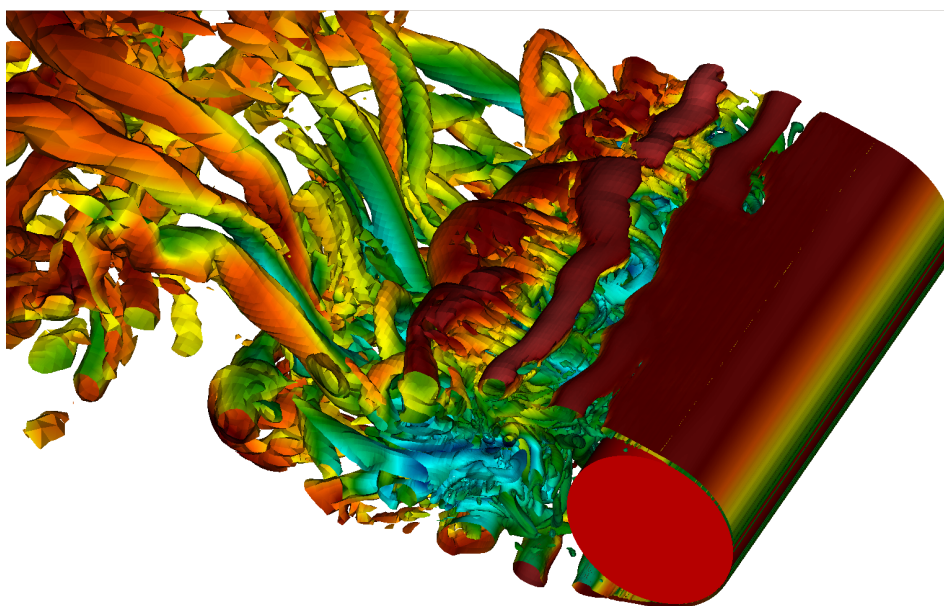


Figure 4.26: Isosurfaces of the Q -criterion, colored by streamwise velocity.

structured, stretched and locally refined meshes can significantly reduce the computational costs.

On the other hand, the semi-Lagrangian approach is limited by two main issues, which need to be addressed in future work. First, despite elements of varying sizes, the time step is constant in the entire computational domain, which negatively affects the overall performance. This is in contrast to multi-domain refinement techniques as presented in the previous section 4.2, but a peculiarity of all the unstructured/non-uniform mesh approaches in the realm of LBM.

Second, the semi-Lagrangian approach as presented above requires an excessive amount of computational memory. In fact, in order to perform the semi-Lagrangian streaming most efficiently, a sparse matrix needs to be stored for each population. This amounts to 27 sparse matrices in three dimensions using the standard $D3Q27$ lattice. This severely limits the attainable number of degrees of freedom and thus Reynolds number for a given amount of resources. A possible solution to both of these issues may be to adopt a hybrid strategy such as the one proposed in [68], where the standard Cartesian, possibly block-refined, LBM is combined with an OLBM. This would allow using multi-domain refinement in the far-field (based on traditional LBM), while retaining an unstructured/non-uniform mesh only in close proximity of the solid body.

4.4 Conclusion

In this chapter we have presented grid refinement strategies for both regular Cartesian as well as unstructured meshes. First, a novel multi-domain refinement technique was proposed, which avoids the low-order time interpolation commonly used in lattice Boltzmann simulations. An extension to thermal and compressible models is achieved by an appropriate rescaling of the populations and thus widening the range of applicability of the proposed grid refinement algorithm. Accuracy and robustness is established through various set-ups in the incompressible, thermal and compressible flow regimes for which local grid refinement is crucial in order to obtain accurate results at a reasonable computational cost. The implicit subgrid features of entropy-based lattice Boltzmann models render the solutions stable and allow for significant under-resolution while retaining accuracy. The entropic stabilizer adapts to the flow features and refinement patches, which enables multi-scale simulations where the fine-to-coarse level projection and vice versa is implicit to the model. These features are particularly important in the simulation of the supersonic airfoil, where shock waves cross the refinement patches without being reflected and destabilizing the flow. With these insights, an extension of entropic LBMs to adaptive grid refinement seems natural, where the deviation of the stabilizer from its resolved value is a measure of under-resolution and can thus serve as a refinement criterion. This is left for future investigations. In conclusion, it has been shown that the proposed multi-domain grid refinement technique in combination with entropy-based lattice Boltzmann models enables accurate and efficient simulations of flows ranging from low Mach number turbulence all the way to supersonic compressible flows.

The second part of this chapter was concerned with off-lattice Boltzmann methods. The SLLBM was combined with the entropic multi-relaxation time model and appropriate boundary conditions, which extends its range applicability to wall-bounded turbulent flows in three dimensions. Simulation of such kind are challenging for existing methods in the realm for OLBMs. The performance of the model was assessed using the classical benchmark of the flow past a circular cylinder in the subcritical regime. It was demonstrated that all relevant flow features are accurately captured by the proposed method. The obtained results are promising for direct numerical simulations of wall-bounded turbulence with body-fitted meshes

and LBM. In addition, the stretched and locally refined meshes can be optimized to retain reasonable computational costs.

Some remarks on the applicability of both strategies are in order. The SLLBM is most effective when a significant amount computational costs can be saved by using stretched grids. This obviously cannot be achieved by the multi-domain refinement strategy. The accuracy of the description of complex geometries and the corresponding boundary condition is slightly diminished for the SLLBM due to the fact that interpolation is still required (albeit using, possibly high-order accurate, finite element interpolation). Thus it is very similar to using a refined Cartesian mesh and interpolation-based curved boundary conditions.

The multi-domain refinement on the other hand, is generally more efficient in terms of lattice node updates per second compared to the SLLBM as the additional complexity of the semi-Lagrangian streaming is omitted and only the grid level coupling adds to the compute time. Fortunately, the costs of coupling are negligible. Furthermore, in contrast to the constant time step in the SLLBM, the multi-domain refinement adapts the time step size in each grid level, which further reduces run-time costs.

Regarding a possible extension to adaptive grid refinement, the multi-domain is trivially extended using, e.g., an octree data structure. For the SLLBM, the construction of the matrices, which are needed to perform the stream step is prohibitively expensive. A remedy would be the development of a matrix-free approach. Conceptually this is straightforward but our preliminary studies could not achieve acceptable performance. As discussed in chapter 3, for moving geometries, body-fitted approaches require sophisticated re-meshing methods. This is also true for the SLLBM and cannot match the flexibility of a multi-domain approach in combination with the appropriate boundary conditions.

For its universality we employ the multi-domain approach in the remainder of this thesis.

Chapter 5

Flow in engine-like geometries

Having introduced the necessary tools in the previous chapters, we can proceed with the first engineering application.

We study in detail the set-up of a simplified internal combustion engine with a valve/piston arrangement. This arrangement allows us to probe the non-trivial interactions between various flow features such as jet breakup, jetwall interaction, and formation and breakup of large vortical structures, among others. A detailed comparison of mean and rms velocity profiles with high-order spectral element DNS and experimental data shows excellent agreement, while computational costs are reduced by an order of magnitude compared to state-of-the-art DNS. Moreover, it is demonstrated that the implicit subgrid features of the entropic lattice Boltzmann method can be utilized to further reduce the grid sizes and computational costs, providing an alternative to modern modeling approaches such as large-eddy simulations for complex flows.

5.1 Introduction

The intrinsic complexity of turbulence arising from the nonlinearity of the governing Navier-Stokes equations eludes an analytical description and requires experimental or advanced numerical tools to gain insight into the fundamental phenomena in such complex flows. Challenges for state-of-the-art numerical and experimental methods become even more apparent

when various distinct flow features are combined and interacting in a single flow field. Unfortunately, this is the case for almost all realistic applications and as a representative of such we consider the turbulent flow field in a valve/piston assembly during multiple cycles in this chapter.

The main driving force of the flow field inside the chamber is given by the periodic motion of the piston inducing an unsteady turbulent flow with cyclic variability. During the intake stroke the piston draws fluid into the chamber, creating a hollow jet as the fluid is pushed through the valve. This results in the formation of large vortex structures, where the interaction with the cylinder walls causes a tumbling and swirling motion at larger scales. The hollow jet has similar flow features as a planar jet for which the turbulent flow field strongly depends on the distance to the nozzle. In first instance, a planar jet exhibits Kelvin-Helmholtz instabilities on both sides of the shear layers, eventually causing jet breakup and the formation of small scale turbulent structures (see, e.g., [123, 216, 323]). Note however, that the situation in the valve/piston arrangement is more intertwined as the large vortical structures, formed by the jet, are deflected by the cylinder walls and interact with the jet itself resulting in a different breakup behaviour. Furthermore, as for the planar jet, the breakup process, the spreading rate and the center-line velocity are strongly influenced by the external flow field corresponding to the residual turbulence in the chamber at the beginning of a new cycle. This, in turn, alters the formation of the vortical structures and their influence on the jet breakup, leading to a cyclic variability [307]. Cyclic variability is the consequence of the non-trivial interaction between small and large scale structures, which differs from most of the classical flows of fully developed turbulence for which the influence of the large scale structures is more significant than vice versa. For the understanding of such complex phenomena numerical or experimental tools need to be applied.

Experimentally, an instantaneous, discrete velocity field may be obtained by techniques such as Laser Doppler Velocimetry (LDV) or more commonly two- and three-dimensional Particle Image Velocimetry (PIV). Despite substantial progress in this field, limitations in terms of temporal and spatial resolution become apparent when considering the smallest scales. Nonetheless, valuable insight and validation data for numerical studies may be obtained from experiment. For instance, the experimental efforts

of [247] using LDV in motored valve/piston assemblies are commonly used for validation of direct numerical simulations and turbulence models in this setup. However, due to the limited access to the chamber, accurate measurements in the near-wall region are particularly challenging. For an overview of available experimental techniques we refer to the work of [362] or [344].

On the numerical side, direct numerical simulations, solving the Navier-Stokes equations directly and accounting for all pertinent scales of the flow, provide an accurate description of the flow field as no turbulence modelling, based on simplifying assumptions, is employed. However, for realistic applications of high-Reynolds number flows involving complex geometries with moving boundaries such as the application considered in this paper, the computational cost becomes prohibitively high and only very few such simulations can be found in the literature. Most notable for this set-up is the recent DNS of [306] employing a high-order spectral element method and an Arbitrary-Lagrangian-Eulerian (ALE) formulation to account for the piston movement. In their work, a detailed analysis of the flow in the chamber with various velocity and stress profiles for different crank angles along with a quantification of cycle-to-cycle variability was presented. This gives us an opportunity to validate our simulations and study its behavior in the case of under-resolution.

On the other hand, turbulence models reduce the computational requirements by not resolving all scales of the flow but by trying to account for the physical effects of the unresolved scales by projection onto the resolved ones. A prominent class, the so-called eddy-viscosity models, provide a closure to the coarse-grained Navier-Stokes equations by relating the Reynolds-stress tensor to a turbulent eddy-viscosity ν_t . The intrinsic assumption behind the eddy-viscosity models is that the anisotropic part of the Reynolds-stress tensor may be linearly related to the local mean rate-of-strain tensor via ν_t , analogous to the relation of the viscous stress in a Newtonian fluid. The analogy to the viscous stress is revealing as the comparison to kinetic theory and a simple time scale analysis show that there is no general basis for neither a local nor linear relationship between the rate-of-strain and the Reynolds-stresses through a scalar quantity, see, e.g., [279] for telling examples. However, for simple cases, whenever the ratio of production to dissipation of turbulent kinetic energy is close to unity,

the eddy-viscosity assumption holds with sufficient accuracy [279]. In that context, various models prescribing the turbulent eddy-viscosity exist and range from algebraic relations to more sophisticated ones, solving a set of transport equations such as the $k - \varepsilon$ or $k - \omega$ models and their variants. Such models may be applied to either Reynolds-averaged Navier-Stokes equation or to the filtered Navier-Stokes equation yielding commonly used RANS and LES formulations, respectively. Despite the known deficiencies of the eddy-viscosity assumption as explained above, such models are often applied to various flows including the flow in the valve/piston assembly with its complex interaction of various base flow types, where the eddy-viscosity assumption is known to fail. In particular, these deficiencies have been assessed for strongly swirling flows, as often encountered in engine-type flows, in the work of [359]. Still, due to their relatively low computational cost these models remain an attractive option to study turbulence phenomena. For the valve/piston assembly, LES has become increasingly popular as it overcomes the shortcomings of RANS, where a time or ensemble average is computed and cycle-specific phenomena as well as cyclic variability cannot be investigated. For an overview of RANS and LES applied to engine flows the reader is referred to the works of [49, 87, 128, 210, 301]. In particular, in [210], various LES models were tested and a reasonable agreement with experimental data was achieved, although it was pointed out that no model was capable of improving the comparison for all relevant quantities. An intrinsic issue of using such modeling approaches is that up to date no universality exists and the model parameter specification is problem dependent, typically only reliably available for simple, homogeneous turbulence with periodic boundaries. Furthermore, as most turbulence is generated in the near-wall region for wall-bounded flows, this issue needs to be addressed for turbulence models. As it was stated in the recent review of [301], the development of wall-models has made no significant progress in the last years. Hence, most LES need either to increase the resolution in the near-wall region [152] or are forced to overcome the stringent resolution requirement by employing wall functions based on the law of the wall (see [277] for a review on this topic in the LES-context). Thus, the range of applicability of those models is limited and requires fine tuning of the model parameters for a specific setup.

To overcome the high computational cost of direct numerical simulations

and to avoid the cumbersome search for the best tuning parameters in turbulence models, much research was focused on the development of accurate alternatives. To that end, the lattice Boltzmann method made significant progress. In the field of internal combustion engines notable modeling approaches on spray formation, breakup and cavitation in the LB realm are given in the works of [91, 92]. On the other hand, the parameter-free KBC model appears particularly suited for this set-up. By employing the Grad boundary conditions as introduced in chapter 3, the implementation of complex geometries with moving boundaries comes at little additional cost and allows us to go beyond periodic set-ups and study the subgrid features of KBC models in the valve/piston assembly. Our results indicate that the KBC model provides a simple and efficient alternative to conventional CFD methods for research and engineering applications.

The outline of the chapter is as follows: Before considering the full complexity of the valve/piston assembly, section 5.2 presents a thorough study of its conceptual building blocks, i.e. periodic turbulence using the Kida vortex as an example as well as the turbulent pipe flow for both resolved and under-resolved simulations. Finally, section 5.3 discusses the valve/piston assembly by a comparison to state-of-the-art DNS and experimental data of [306] and [247], respectively. As in section 5.2, the KBC model's subgrid behavior is tested numerically for various resolutions.

5.2 Model validation for simple flows

The valve/piston assembly reveals a number of hydrodynamic features typical for complex flows. Interactions between large scale coherent structures which are perturbed by residual turbulence characterize the flow in the bulk of the chamber while the complex valve/cylinder geometry adds effects of wall bounded flows. Moreover, the moving piston introduces yet another conceptual dimension to the problem. Not surprisingly, this variety of physically distinct flow patterns and complex nonlinear interactions among them introduce numerical challenges.

In order to show that the KBC model is capable of correctly predicting the physics of the main active flow regimes we consider a number of precursor simulations using the identical KBC model and boundary conditions as described in the previous chapters. By reducing the complexity of the

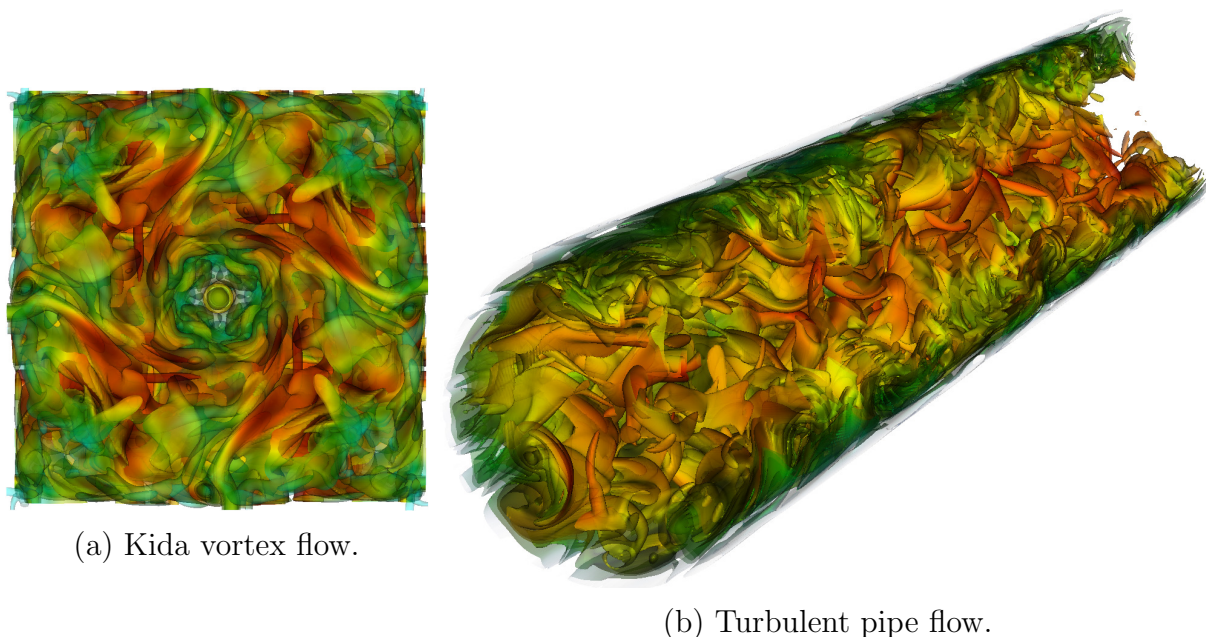


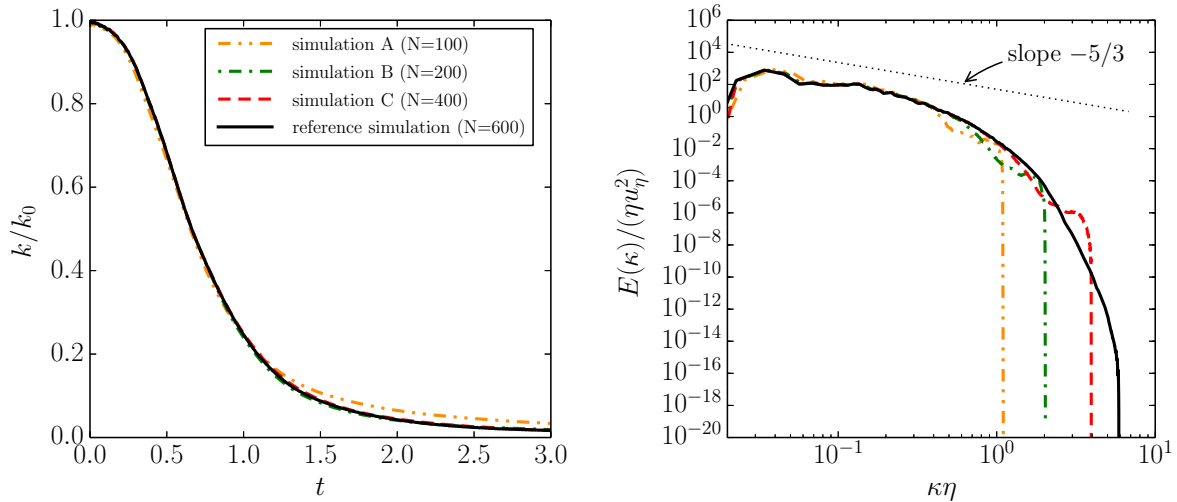
Figure 5.1: (a) Vortex structures for the periodic Kida vortex flow at $Re = 6000$ ($x, y, z \in [0, \pi]$). (b) Turbulent pipe flow at $R^+ = 180$, visualized by isosurfaces of vorticity magnitude and colored with velocity magnitude.

flow and concentrating on a single flow regime we demonstrate that the method is able to accurately capture the main physics at hand individually. Thus, we conceptually decompose the problem into its building blocks while combining them in a last step. The flow in the valve/piston assembly is induced through the moving piston and it is expected that the treatment of the moving boundary has a significant influence on the flow field inside the chamber. This has already been validated in chapter 3 and will be revisited in chapter 7. Thus, we will refrain from further validation in this part of the thesis. In the following we will rather put emphasis on the performance of the model in situations where the simulation cannot resolve all pertinent scales of the flow. Therefore, one can gain insight in the built-in subgrid features which the model exposes.

The work in this section was done in collaboration with Fabian Bösch, who conducted the Kida vortex and pipe flow simulations.

5.2.0.3 Turbulence in a periodic box

As the main flow in the bulk of the engine-like assembly is driven by vortex-vortex interaction and small-scale turbulence, we consider the Kida vortex flow as a classical benchmark simulation (see figure 5.1a). This well studied



(a) Turbulent kinetic energy decay with time. (b) Turbulence kinetic energy spectrum.

Figure 5.2: Statistics for the Kida vortex flow at $\text{Re} = 6000$ and resolutions of $N = \{100, 200, 400\}$ and $N = 600$ for the simulations with KBC and the reference simulation with LBGK, respectively. The theoretical Kolmogorov scaling is indicated by the dotted line.

flow evolves from a deterministic and symmetric initial condition to a state which resembles a fully developed turbulent flow featuring a corresponding energy cascade and has been analyzed extensively using DNS [60, 165, 167, 168]. The initial conditions are given by

$$\begin{aligned}
 u_x(x, y, z) &= U_0 \sin x (\cos 3y \cos z - \cos y \cos 3z) \\
 u_y(x, y, z) &= U_0 \sin y (\cos 3z \cos x - \cos z \cos 3x) \\
 u_z(x, y, z) &= U_0 \sin z (\cos 3x \cos y - \cos x \cos 3y)
 \end{aligned} \tag{5.1}$$

where $x, y, z \in [0, 2\pi]$ and periodic boundary conditions are imposed in all directions. The Reynolds number is defined as $\text{Re} = U_0 N / \nu$ where N is the domain size. While the kinetic energy is decaying, the evolution of enstrophy shows a steep increase in the early stage of the simulation and reaches a maximum value before it starts to decay. Just after the peak of enstrophy the flow reaches the most turbulent state producing large gradients and small scale structures. While large gradients on the one hand may cause numerical instabilities, it is of paramount interest not to over-damp the dynamics on the other hand, which will lead to a corrupted and non-physical result lacking the small scales. Without employing explicit turbulence models one is usually restricted to increase

the resolution such that the smallest eddies are resolved. This is typically satisfied when the grid spacing is smaller than the Kolmogorov scale $\eta = (\nu^3/\epsilon)^{1/4}$ with kinematic viscosity ν and rate of energy dissipation ϵ .

In order to study the accuracy of the KBC model, a detailed investigation was recently conducted by [40]. The Reynolds number here is $\text{Re} = 6000$, which is slightly higher than what can be expected for the valve/piston assembly considering the cylinder diameter and the maximum piston velocity as characteristic scales. A sufficiently resolved reference simulation ($\eta \approx 1.2 \Delta x$) is conducted with a box length of $N = 600$ using the LBGK collision model. Further simulations with $N = \{100, 200, 400\}$ and the same Reynolds number using the KBC model are then carried out and compared to both the reference solution and theoretical limits (see [40]). An important global characteristic is the evolution of the turbulent kinetic energy k as shown in figure 5.2a. For all resolutions in this study the energy decay seems to be captured well despite the rather severe under-resolution in the coarsest simulation ($\eta \approx 0.2 \Delta x$). However, a more meaningful insight is given by the energy distribution across the scales of the flow as shown by means of the normalized energy spectrum along with the theoretical Kolmogorov scaling with a slope of $-5/3$ in the inertial subrange in figure 5.2b. It is apparent that the energy scales with marginal difference for all resolutions with a sharp cut-off at its smallest scale as expected for a well-behaved subgrid model.

A thorough convergence study of various statistical quantities sampled at time points around the peak of enstrophy demonstrates second-order accuracy (see [40]) as is expected for a lattice Boltzmann method.

While convergence towards the reference solution is established, it is of interest to quantify the recovery of the Navier-Stokes equations at small scales. To that end, let us remind the reader that the incompressible Navier-Stokes equation implies the following balance equations for the averaged momentum, vorticity, energy and enstrophy which yield for statistically homogeneous flows [19, 188],

$$\partial_t \langle \mathbf{u} \rangle = 0, \quad (5.2)$$

$$\partial_t \langle \boldsymbol{\omega} \rangle = 0, \quad (5.3)$$

$$\partial_t k = -2\nu\Omega, \quad (5.4)$$

$$\partial_t \Omega = \langle \boldsymbol{\omega} \cdot \mathbf{s} \cdot \boldsymbol{\omega} \rangle - 2\nu P, \quad (5.5)$$

N	100	200	400	600
$\nu_{\text{eff},k}/\nu$	1.5640	1.1356	1.0030	0.9976
$\nu_{\text{eff},\Omega}/\nu$	2.0950	1.4042	1.0912	1.0337

Table 5.1: Effective viscosity ratios at non-dimensional time $t/(N/U_0) = 0.75$ for simulations with different resolutions N .

where

$$\mathbf{s} = \frac{1}{2} (\nabla \mathbf{u} + \nabla \mathbf{u}^\dagger), \quad (5.6)$$

is the rate-of-strain tensor, and P is the palinstrophy,

$$P = \frac{1}{2} \langle \nabla \boldsymbol{\omega} : \nabla \boldsymbol{\omega} \rangle. \quad (5.7)$$

While the global conservation of average momentum (5.2) and vorticity (5.3) are satisfied up to machine precision for all times and all resolutions considered in [40], the balance of various terms in the energy (5.4) and enstrophy (5.5) equations is directly probing the recovery of the Navier-Stokes equation at small scales by the KBC model. To that end, we recast the balance equations (5.4) and (5.5) in terms of the effective viscosity,

$$\nu_{\text{eff},k} = -\frac{\partial_t k}{2\Omega}, \quad (5.8)$$

$$\nu_{\text{eff},\Omega} = \frac{\langle \boldsymbol{\omega} \cdot \mathbf{s} \cdot \boldsymbol{\omega} \rangle - \partial_t \Omega}{2P}. \quad (5.9)$$

In the simulation, the Navier-Stokes equation will be verified at small scales if the ratio $\nu_{\text{eff}}/\nu \approx 1$. Thus, the evaluation of effective viscosities as in Eq. (5.8) and Eq. (5.9) is an important check of the accuracy and is listed in table 5.1. By increasing the resolution, the values are approaching $\nu_{\text{eff},k}/\nu \approx 1$. It is apparent that even for the coarsest run the additional dissipation is rather small, which is consistent with the evolution of turbulence kinetic energy k shown in figure 5.2a. The second effective viscosity $\nu_{\text{eff},\Omega}$ is somewhat larger for simulations for the coarse grids, which is consistent with the under-prediction of the peak in enstrophy. For larger resolutions, however, the values are close to the nominal viscosity. Thus, we conclude that the KBC scheme recovers well the Navier-Stokes equations (in the absence of boundaries) while introducing only small additional dissipation on coarse grids. Further simulations of decaying turbulence are presented

in [40]. Note that due to the temporally and spatially varying parameter γ , a fluctuating bulk viscosity is obtained, which in turn was found to reduce artificial compressibility effects in comparison to LBGK and other KBC models (see [40]).

In general, the family of KBC models has shown outstanding stability allowing for the operating range to be extended by orders of magnitude in terms of the Reynolds number compared to standard MRT- or LBGK-type of models. Further, it has been shown to recover the well-established LBGK model for fully resolved simulations [40]. In the next section, we aim to go beyond the periodic set-up in order to test for the next conceptual building block identified above.

5.2.1 Turbulent flow in a pipe

The chamber of the engine-like geometry is rotationally symmetric and it may be expected that the cylinder walls effect the dynamics of the flow to a large extent. Therefore, the turbulent flow through a round pipe is chosen as a validation of the second building block (see figure 5.1b). This problem has been studied extensively in the literature experimentally, analytically and numerically. While for the flat channel there is consensus about the scaling of the mean velocity profile, it is less clear for the turbulent flow through a pipe and is being discussed in the literature (see, e.g., [17, 234, 246, 273, 360, 368, 374, 390, 391]). Nevertheless, there exists reliable DNS and experimental data. Here, we choose a Reynolds number $\text{Re}_{D_p} = 5300$ based on the pipe diameter D_p and the mean bulk velocity $\overline{u_{\text{bulk}}}$, same as in the DNS of [374]. This number is well in the range of what is expected in the chamber or the valve/piston assembly considered below.

As the problem is axially symmetric, it is conveniently formulated in cylindrical coordinates and one typically uses a corresponding computational mesh. The classical LB method, however, is restricted to a rectilinear Cartesian mesh (which is also employed for the engine-like geometry below). Thus, this benchmark problem is probing the performance of the boundary condition for curved walls to its full extent as the flow is wall bounded.

Three simulations are conducted at diameter $D_p = \{49, 99, 199\}$ lattice units (runs A, B and C). The domain length in stream-wise direction is $L = 16R$, where $R = D_p/2$ is the pipe radius. The flow is initialized

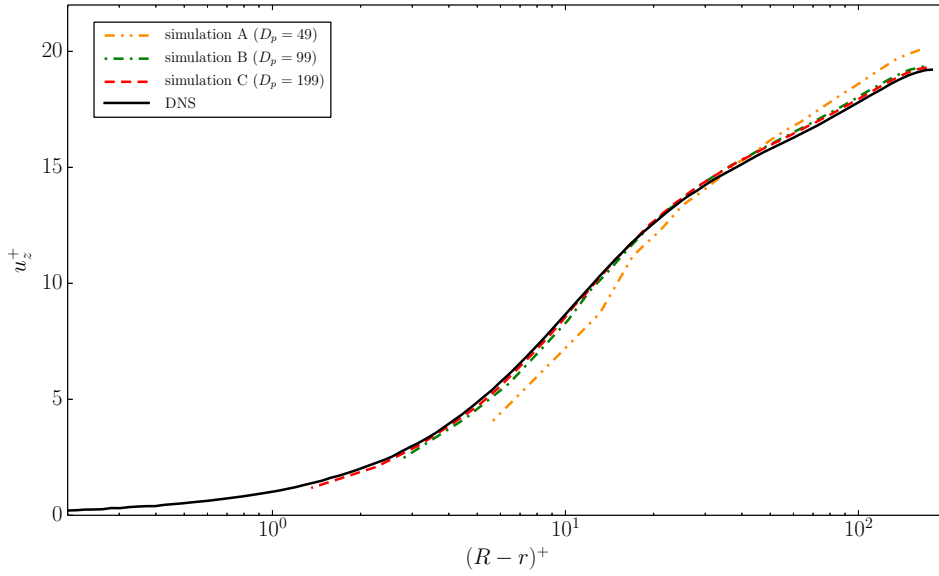


Figure 5.3: Mean velocity component in flow direction for the turbulent pipe flow.

with a random velocity field and evolved for $200T$, where the turnover time is given by $T = R/\overline{u_{\text{bulk}}}$. After this initial transient, statistics are collected for another $200T$, yielding a total run-time of $400T$. The pressure gradient was adjusted during the simulation to reach the desired Reynolds number, which was realized through a body force. The corresponding Kàrmàn number is $R^+ = u_\tau R/\nu = 180$ with the wall friction velocity u_τ and the kinematic viscosity ν .

The distance from the pipe wall is given by $R - r$ with $r = \sqrt{x^2 + y^2}$, where z denotes the spatial coordinate in stream-wise direction. The non-dimensional wall units employed hereafter are defined as $x^+ = xu_\tau/\nu$ and $u^+ = u/u_\tau$ for space and velocity, respectively. Thus, the non-dimensional distance to the wall is $(R - r)^+ = R^+ - r^+$. A natural measure for spatial resolution is the non-dimensional and uniform grid spacing Δx^+ here, while for the DNS of [374] radial (Δr^+), azimuthal ($\Delta(r\theta)^+$) and streamwise (Δz^+) directions are varying non-uniformly. The finest resolution for the DNS is typically found at the wall in the wall-normal direction. In [374] this amounts to $\Delta r^+|_{r=R} = 0.167$ (with a maximum $\Delta r^+|_{r=0.409R} = 1.647$), while in our simulations $\Delta x^+ = 7.3$ (run A), $\Delta x^+ = 3.6$ (run B) and $\Delta x^+ = 1.8$ (run C).

Figure 5.3 shows the comparison of the mean stream-wise velocity component of runs A-C to the reference DNS results. Despite severe under-

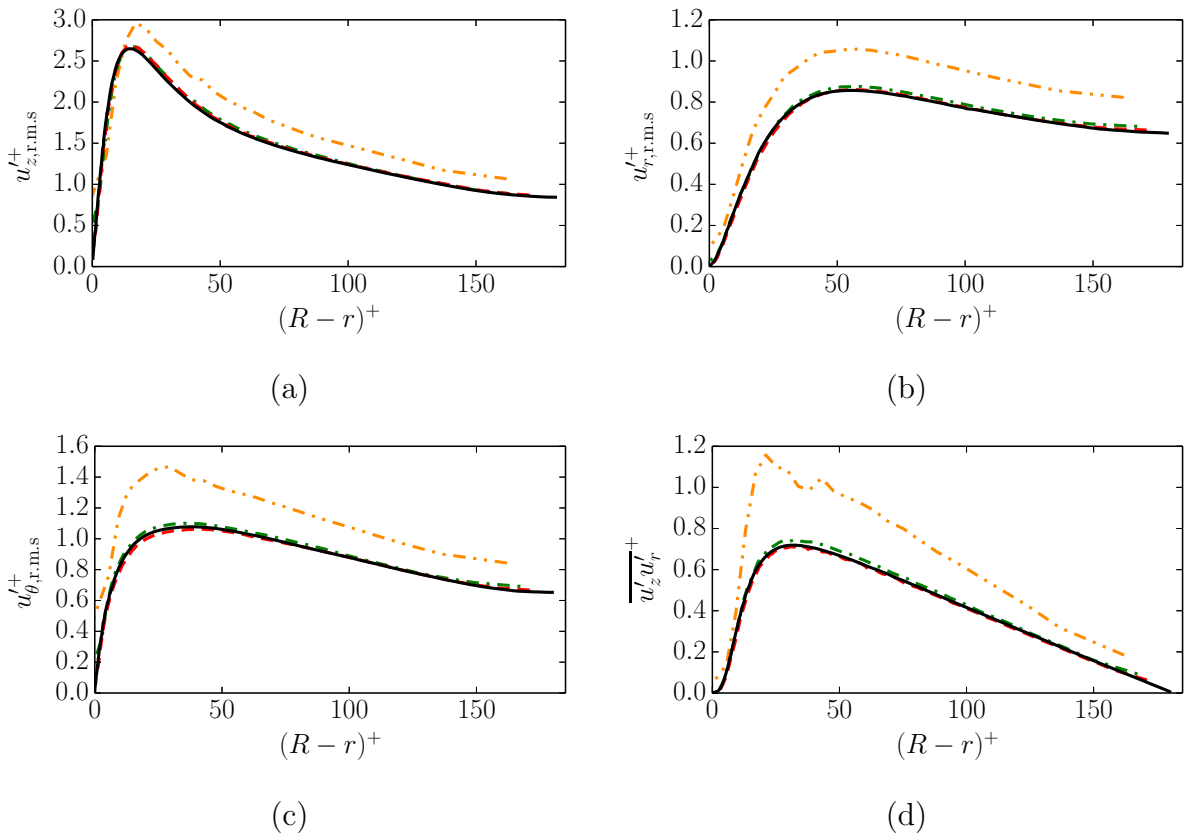


Figure 5.4: Rms velocity profiles for the turbulent pipe flow. The legend is identical to figure 5.3.

resolution, excellent agreement can be observed for runs B and C. Run A obviously employs a mesh which is too coarse to capture the scaling of the mean velocity correctly.

The next order statistical moments are shown in figures 5.4a-5.4d. The rms fluctuations of the axial, radial and azimuthal velocity component show the same trend as seen in figure 5.3; the coarsest simulation does not reproduce the expected values while runs B and C are very close to the DNS results. Moreover, the cross-correlations of the axial and radial fluctuations, figure 5.4d, shows excellent agreement for simulations B and C as well.

5.3 Valve/piston assembly

With the results of the preliminary studies in the previous section, we now consider the flow in a valve/piston assembly. To that end, we shall compare

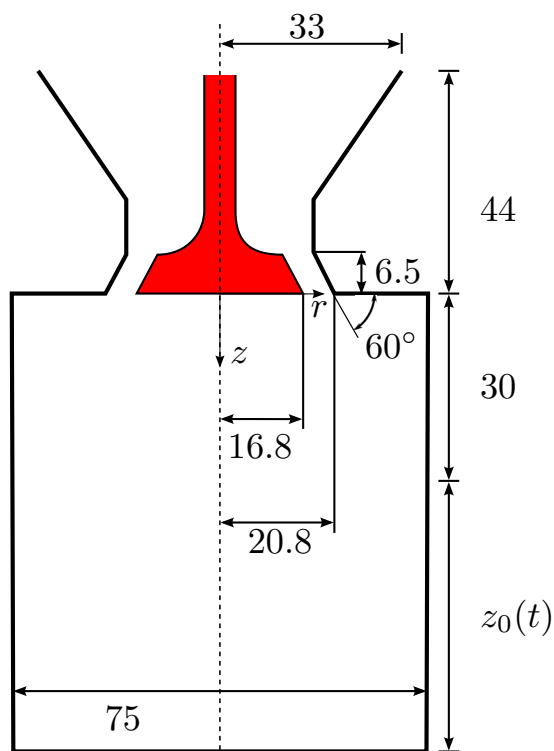


Figure 5.5: Schematic of the valve/piston assembly (all measures are given in mm).

it to the recent DNS simulations of [306] and the experimental data of [247] for different resolutions.

5.3.1 Numerical setup

The numerical setup is identical to the experimental work of [247] and the DNS of [306] for which the schematic and all geometrical specifications are shown in figure 5.5. The axis-symmetric assembly consists of a cylinder with diameter $D_c = 75$ mm, a static centered valve and a flat piston for which a sinusoidal motion corresponding to a speed of 200 rpm, a stroke of $S = 60$ mm and a clearance at Top Dead Center (TDC) of 30 mm is imposed. The maximum piston speed and the viscosity were chosen to obtain a Reynolds number of $Re = u_{p,max} D_c / \nu = 3070$. The valve has the radius $r_v = 16.8$ mm and an angle of 30 degrees, which results in a uniform valve gap of approximately 4 mm. In the experiment, the system is open and was mimicked in our simulation by a large reservoir on top of this assembly (not shown in the schematic) with a volume roughly three times as large as displaced by the cylinder. Due to the open system, compressibility effects

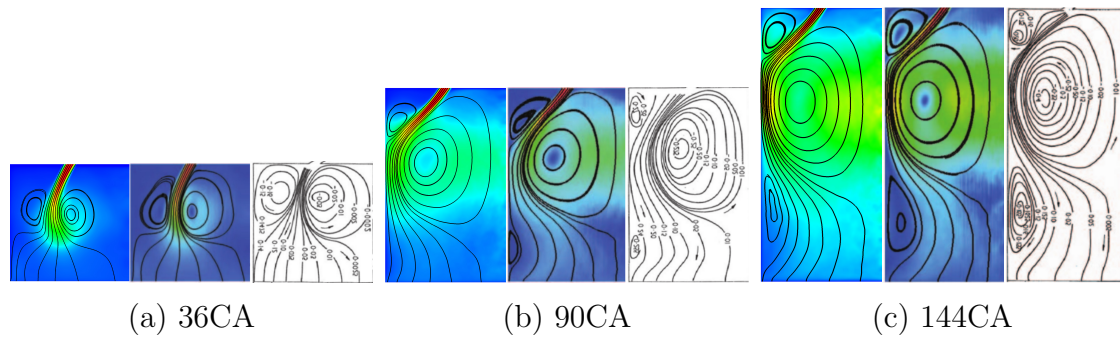


Figure 5.6: Comparison of streamlines of the averaged velocity field. From left to right: Present results, DNS and experimental data are shown for different crank angles, respectively.

are negligible and the flow may be regarded as incompressible. Initially, a quiescent flow field is imposed where the piston is located at TDC. Further, the inlet condition at the top of the reservoir is evaluated instantaneously using the current piston velocity and the ratio of the reservoir and piston area. For all other boundary conditions, the no-slip boundary condition as outlined in section 3.2 is imposed.

In total, eight cycles were simulated and the first two were neglected in the accumulation of statistics to avoid accounting for initialization effects. Statistical quantities were computed using azimuthal and ensemble (across cycles) averaging. To study the nature of the subgrid model, simulations were carried out for a cylinder resolution of $D_{c,lb} = \{100, 150, 300\}$ points, respectively. This yields a total of approximately $N = \{8.5, 28, 228\}$ Mio nodes for each simulation and a uniform cubic mesh, respectively. The resolutions were chosen based on our preliminary studies in section 5.2 for which the flow regimes in terms of Reynolds number are similar to the one exhibited here.

Using a CRAY XC40 system, the computational resources for $D_{c,lb} = 300$ amount to 8.6×10^3 CPUh per cycle, which is roughly 20 times less than the corresponding requirement for the DNS in [306]. The computational cost scales as p^{D+1} for a refinement ratio p and the dimensionality D . Note that since a cubic domain and a regular grid without any local mesh refinement is used, significant optimization options remain. This is focus of subsequent chapters as the scope of the study herein is to validate the implicit subgrid model of KBC for complex flows beyond classical benchmarks.

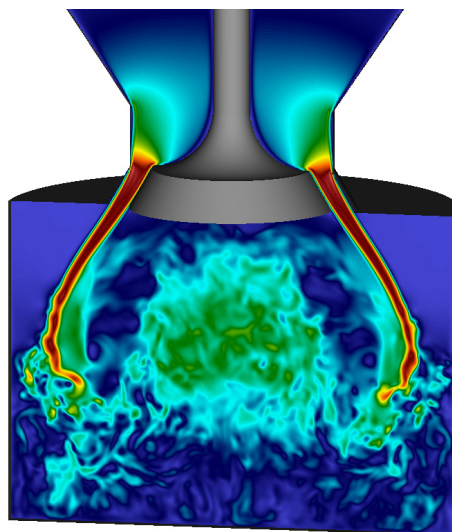


Figure 5.7: Instantaneous velocity magnitude snapshot at 77CA.

5.3.2 Velocity field

Resolved simulation and the DNS-Limit

In this section, we report the radial velocity profiles obtained for the intake stroke at crank angles of 36CA, 90CA and 144CA on different axial planes and a comparison to the DNS and the experimental data. In first instance, the profiles for the highest resolution are compared to establish the correct convergence of KBC models. Later in this section, the influence of under-resolution and its convergence is investigated. The main features of the mean flow field may be identified by the averaged streamlines shown in figure 5.6. In good agreement with both experimental and DNS data, the first phase of the intake stroke consists of fluid drawn into the chamber by the accelerated motion of the piston, forming a hollow cone jet. As a consequence, small vortex rings on both side of the jet are generated, where the inner ring develops into the main feature as the piston moves further down and deflects the jet inwards before it is reflected by the piston. At this stage, one may observe jet breakup processes and the transition to turbulence caused by the interaction with the flow field. For instance, the Kelvin-Helmholtz instabilities in the shear layer are captured in the velocity snapshot of figure 5.7 for the first cycle. Subsequently, the jet is deflected towards the cylinder wall and a third vortex becomes apparent in the averaged flow field (see figure 5.6c).

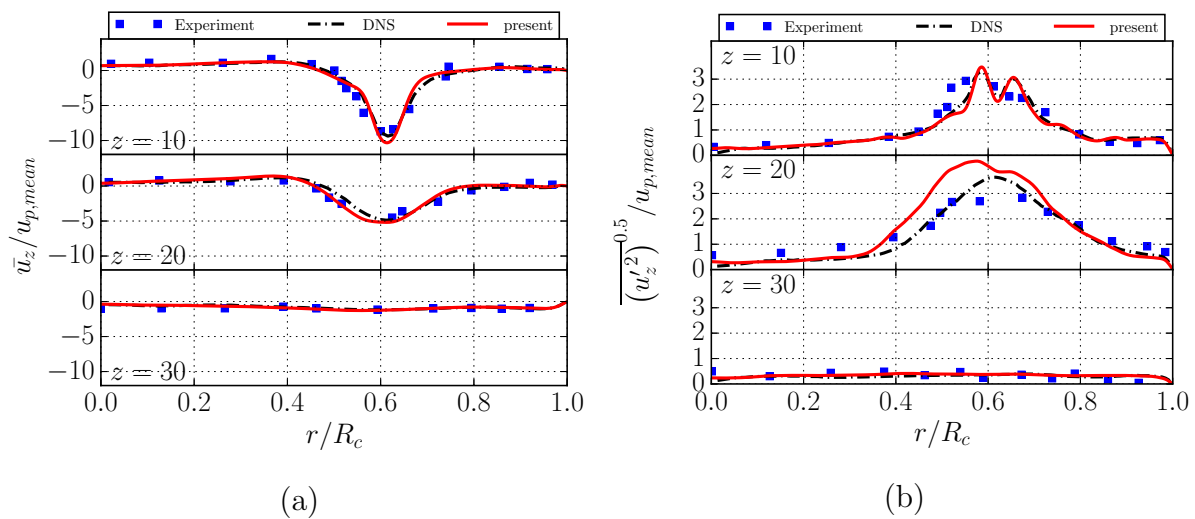


Figure 5.8: Comparison of the ensemble and azimuthally averaged axial mean and rms velocities at 36CA for a resolution of $D_{c,lb} = 300$.

Note that at 90CA the flow undergoes a transition phase as the jet has reached its highest momentum and a fully turbulent flow field, dominated by the large vortical structure, is developed by interaction of the jet with the flow field.

Quantitatively we compare the corresponding mean and rms velocity profiles of the axial velocity component u_z in radial direction on different axial planes with respect to the cylinder head in figure 5.8-5.10. Consistent with the previous observation, the flow at 36CA is mainly dominated by the incoming jet, which results in a peak velocity at $r/R_c \approx 0.6$. The rms velocity profiles indicate that the turbulence generation may be localized to the jet shear layer on both sides. It is clear, that the results predicted by the presented KBC model compare well to both DNS and experiment in terms of mean jet velocities and location. The rms velocities near the cylinder head at $z = 10$ mm are also on top of the DNS data. It is apparent that more turbulence is generated compared to DNS and experiment close to cylinder axis for the $z = 20$ mm-plane, resulting in a broadening of the rms velocity profile towards the center. However, this does not seem to affect the good agreement for different crank angles as shown below.

At 90CA, the deflection of the jet at the cylinder wall leads to an increase of the jet radius, which is manifested by a shift of the average velocity profiles towards the cylinder wall. It should be noted that, as observed in the LES-study of [210], the flow transition at this stage of highest momentum

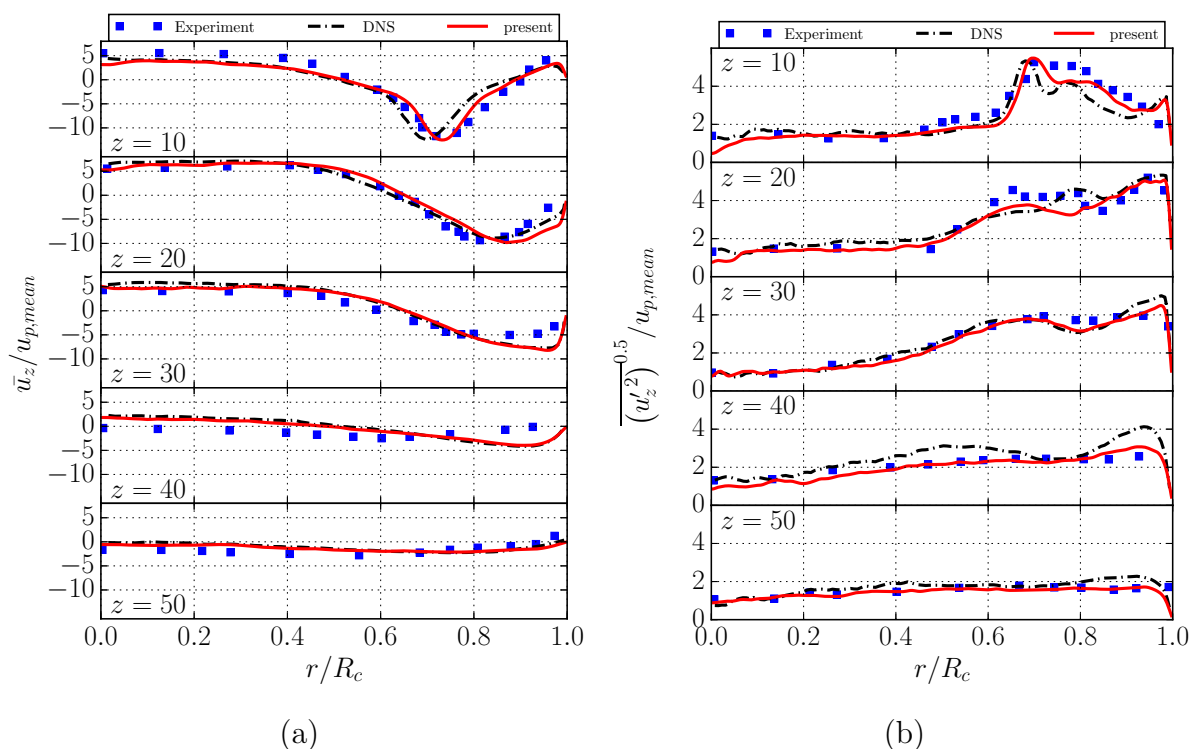


Figure 5.9: Comparison of the ensemble and azimuthally averaged axial mean and rms velocities at 90CA for a resolution of $D_{c,lb} = 300$.

is difficult to capture for various turbulence modeling approaches. In their work, better agreement was achieved by adapting the model parameters but led to more discrepancies for 36CA and 144CA. Despite that figure 5.9 clearly shows excellent agreement for the KBC model for both mean and rms velocity profiles compared with the reference data. A small shift in radial direction compared to the DNS is visible for the upper axial planes and the mean profiles but matches the experimental data. In planes beyond $z = 20$ mm, our simulation is almost indistinguishable from the DNS result. Analogously, this holds for the rms velocity profiles.

At later crank angles, the piston is decelerating and we compare the corresponding profiles for 144CA in figure 5.10. Similarly, the discrepancies are marginal for all data.

Next, let us consider the turbulence statistics of the flow field by means of the Reynolds stress components and the turbulent kinetic energy k as shown in figure 5.11-5.12. As the comparison is very similar during all phases, we choose the most interesting transition phase at 90CA as a representative. It can clearly be seen that the turbulent kinetic energy follows

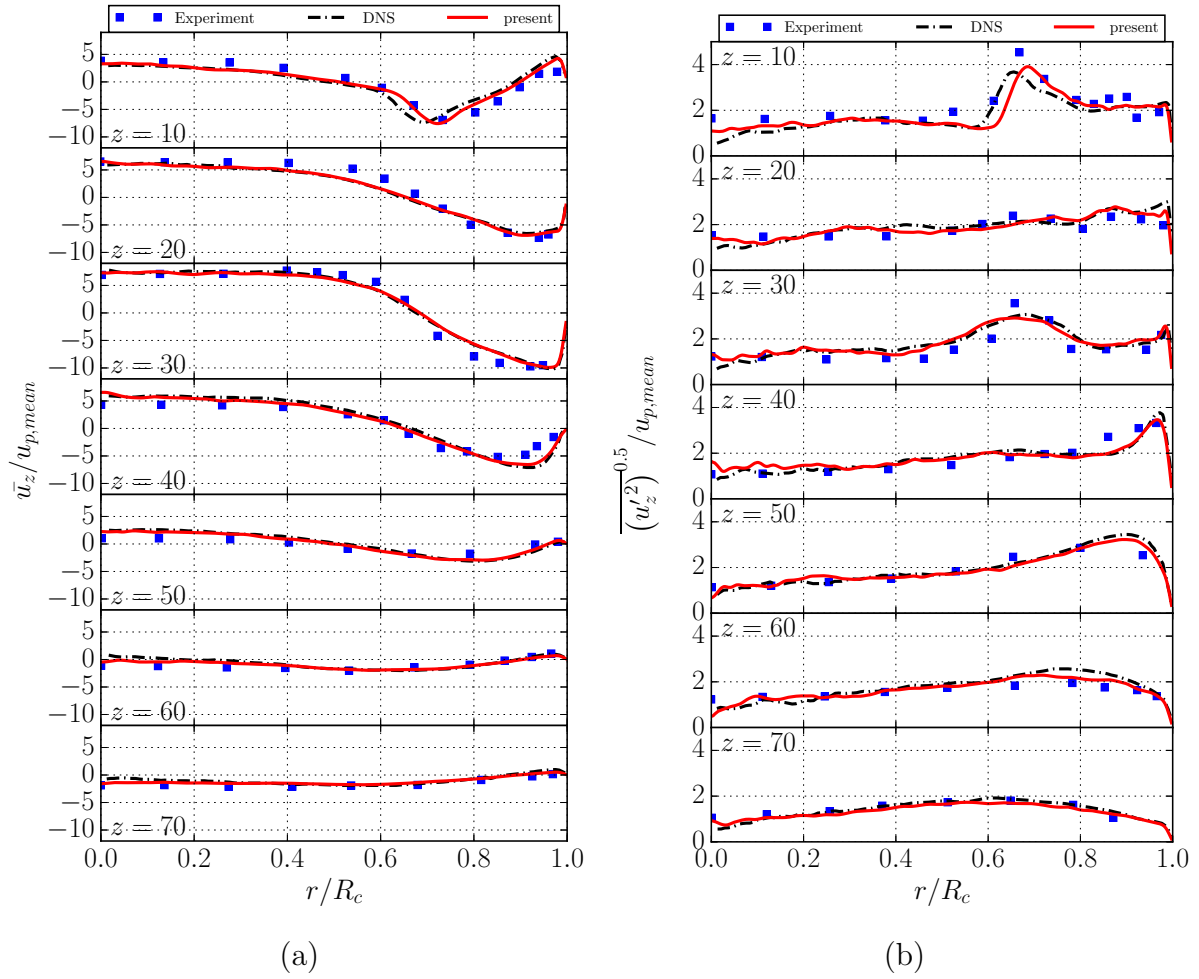


Figure 5.10: Comparison of the ensemble and azimuthally averaged axial mean and rms velocities at 144CA for a resolution of $D_{c,lb} = 300$.

the trend of the reference data. Its shift is analogous to the mean and rms velocities as shown above and minor discrepancies in terms of magnitude are visible. This, however, becomes more pronounced for lower values of the kinetic energy, suggesting that the contribution of the smallest scales are not fully accounted for. Similarly, the radial component $\overline{u'_r u'_r}$ shows a good agreement for the region near the jet entry, but dissipates slightly more. Analogous behavior may be found for the Reynolds stress components $\overline{u'_\varphi u'_\varphi}$ and $\overline{u'_r u'_z}$.

Under-resolved simulations

The above comparison demonstrated an overall excellent agreement between DNS, experimental data and our simulation using the entropic multi-

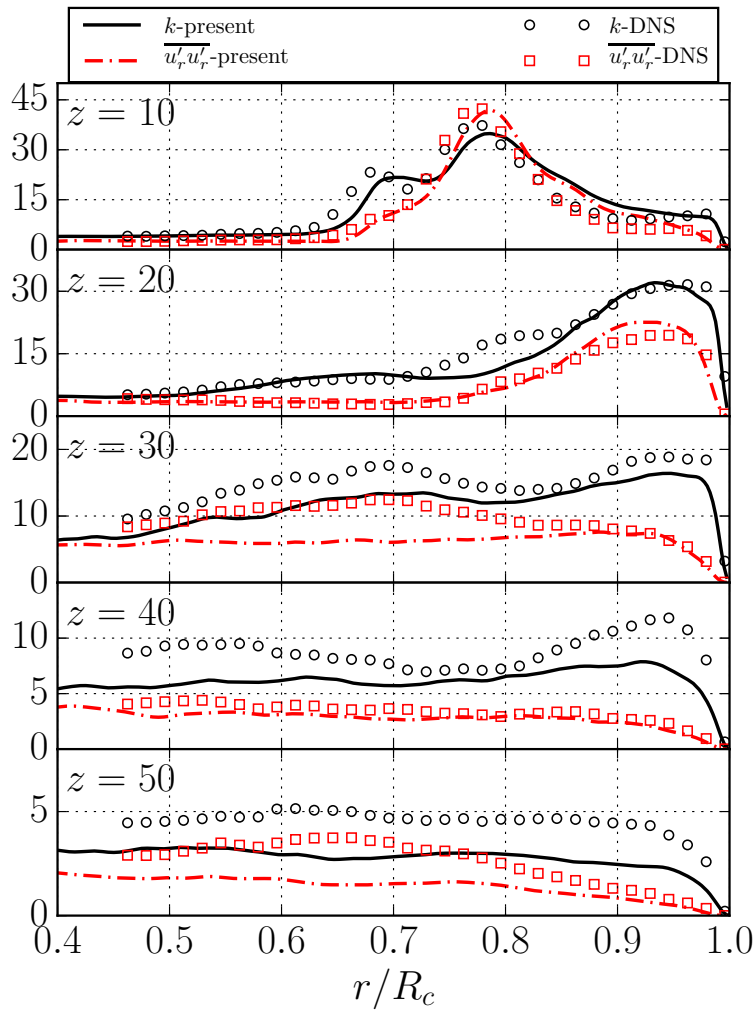


Figure 5.11: Comparison of the ensemble and azimuthally averaged turbulent kinetic energy k and the Reynolds stress component $\overline{u'_r u'_r}$ at 90CA for a resolution of $D_{c,lb} = 300$.

relaxation time lattice Boltzmann model and the highest resolution of $D_{c,lb} = 300$. This provides evidence for the convergence of our simulations to DNS. Having established the correct limit, we can now study the effect of under-resolution.

The discussion is similar for all crank angles and we again choose the most critical phase at 90CA as a representative. In figure 5.13, the mean and rms velocity profiles are shown for cylinder resolutions of $D_{c,lb} = \{100, 150, 300\}$ points. It may be observed that the differences in terms of the average axial velocity profiles between $D_{c,lb} = 150$ and $D_{c,lb} = 300$ are marginal. The rms velocity profiles are very similar as well and only a small over-prediction at the lower resolution may be observed. At first sight, this is not intuitive as one would expect the turbulence production to be smoothed out, which

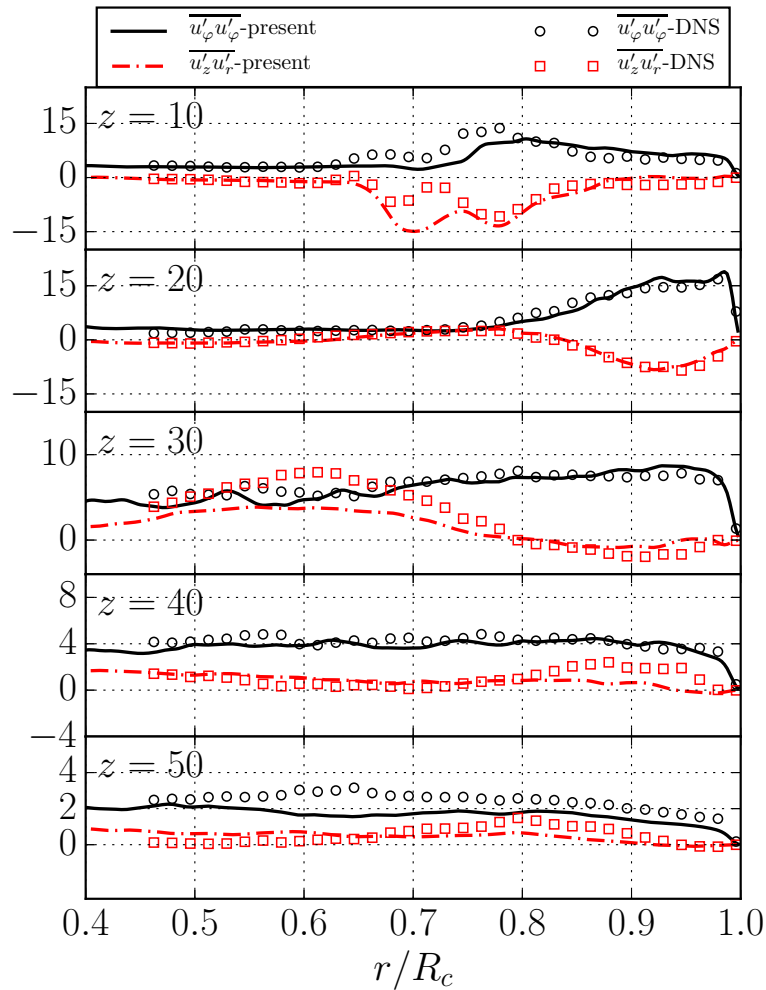


Figure 5.12: Comparison of the ensemble and azimuthally averaged Reynolds stress components $\overline{u'_\varphi u'_\varphi}$ and $\overline{u'_z u'_r}$ at 90CA for a resolution of $D_{c,lb} = 300$.

would lead to lower values of the rms velocities. However, in this case, it may be traced back to very subtle inaccuracies of jet breakup processes, which affect the formation of the large-scale structures of the flow in a nonlinear manner and in turn affect the turbulence production leading to slightly higher rms values. On the other hand, for the case of $D_{c,lb} = 100$, the effect of under-resolution becomes noticeable. The incoming jet is hardly broken up by the surrounding flow field but rather by the confining cylinder walls, which leads to a higher penetration depth and jet radius on average. This may also be seen when considering the corresponding rms profiles, where the consistent under-prediction for $z = 10 - 30$ mm leads to less turbulence production and therefore a delayed jet breakup with an increased diameter. Note that this is well within expectations as the

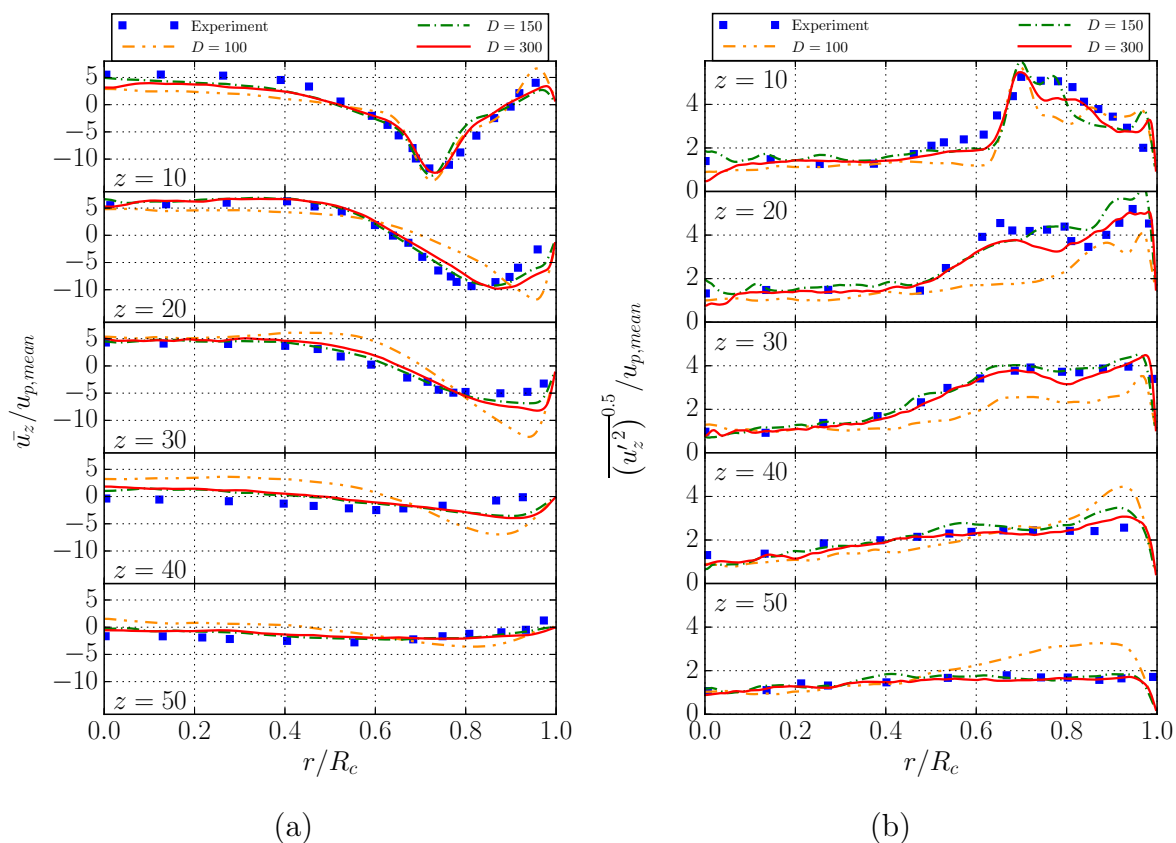


Figure 5.13: Comparison of the ensemble and azimuthally averaged axial mean and rms velocities at 90CA for different resolutions.

valve gap is resolved by only three fluid points for this case. A comparison to our previous simulations of the pipe would suggest that the resolution is sufficient even at $D_{c,lb} = 100$. However, it needs to be kept in mind that due to the impinging jet the Kàrmàn number varies in the range of $R^+ = u_\tau R / \nu \approx 90 - 780$ (measured for $D_{c,lb} = 300$) and that for the local maximum of $R^+ \approx 780$ the effect of the small scale structures cannot be captured accurately at this resolution. On the other hand, the Kida vortex simulation reveals that the small structures in the bulk of the chamber are not correctly represented for a resolution as coarse as $D_{c,lb} = 100$, which further suggests that their contribution to the jet break up is not fully accounted for. Hence, as expected, the complex flow in the cylinder as a combination of distinct flow features requires a higher resolution than the individual building blocks. A slight increase in resolution to $D_{c,lb} = 150$ is necessary. Note that as indicated by the precursor simulations in section 5.2.0.3 and 5.2.1, this is still an under-resolved simulation in which the built-in subgrid model of KBC captures almost all flow features accurately.

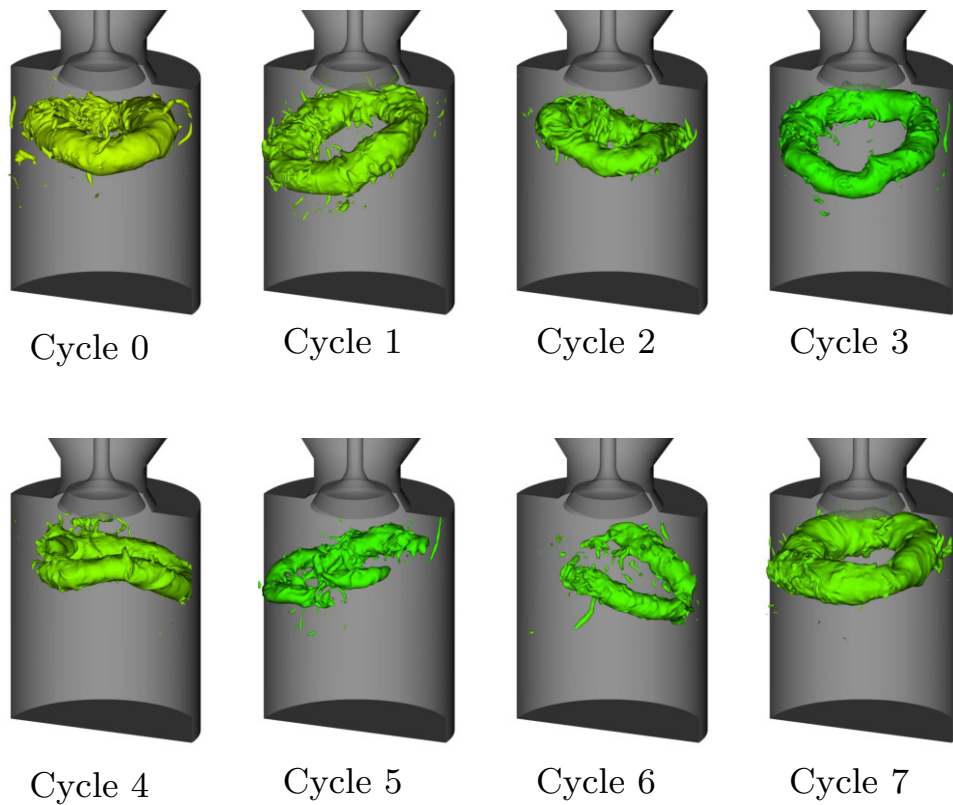


Figure 5.14: Cyclic variation of the vortex ring at BDC visualized by pressure isosurfaces for $D_{c,lb} = 300$.

5.3.3 Cyclic variability

Capturing cyclic variability in internal combustion engine simulations is of crucial importance for its design as it may significantly influence its efficiency and pollutant formation among various other effects. Such variability has also been observed both numerically and experimentally in the valve/piston assembly [128, 301, 306]. Its origin was discussed in the DNS work of [307], where it was mainly attributed to the remaining radial velocity at TDC from the previous cycle, the consequential jet location as well as the vortex ring orientation at bottom dead center (BDC).

The aim of this section is to investigate the predictive capabilities of KBC models concerning the cyclic variability. An indicator of cyclic variability is given by the large vortex ring formed at BDC, which is visualized for all simulated cycles in figure 5.14 by means of the pressure isosurfaces. Variation in shape, size and orientation is observed. Particularly pronounced is the distortion of the vortex ring for the cycles five and six.

Quantitatively, we compare the correlation plot of the normalized, aver-

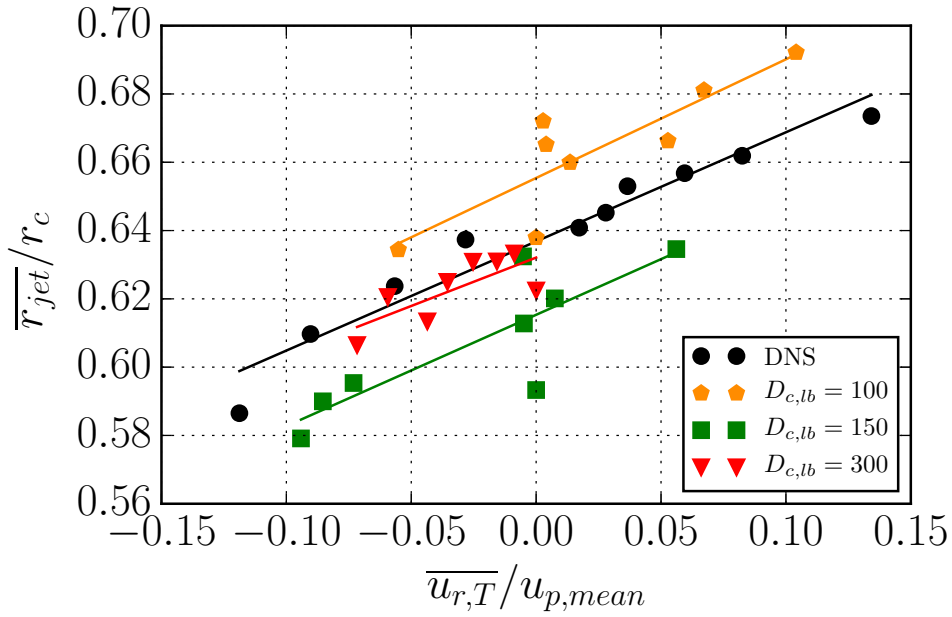


Figure 5.15: Cyclic variation for all resolutions of $D_{c,lb} = \{100, 150, 300\}$ and the DNS results, quantified by mean jet radius $\overline{r_{jet}}/r_c$ at 45CA and correlated to the mean radial velocity $\overline{u_{r,T}}/u_{p,mean}$ at TDC. Lines represent a linear fit through the corresponding data points.

age radial velocity $\overline{u_{r,T}}/u_{p,mean}$ at TDC versus the normalized, average jet radius $\overline{r_{jet}}/r_c$ at 45CA in figure 5.15. Both quantities are evaluated as in [307], where the radial velocity is averaged at TDC azimuthally and radially in an axial window of 11.5 mm starting from the cylinder head. The mean jet radius is defined as the average of the jet radii contained in the isosurface of $u_z = -2.5 \text{ m s}^{-1}$. Our results show that the phenomenon of a cyclic varying jet radius is observed for all resolutions and confirm the result of [307] that it may be correlated to the residual turbulence at TDC from the previous cycle, where an increased averaged radial velocity at TDC results in a increased average jet radius and vice versa. It is notable that even the lowest resolution, for which the average axial velocity profiles have shown effects of under-resolution, is exhibiting pronounced cycle-to-cycle variation with the qualitatively correct cause and effect relation. This is indicated in figure 5.15, where the linear curve fit has an almost identical slope for all resolutions and therefore establishes the correlation of the normalized, average radial velocity $\overline{u_{r,T}}/u_{p,mean}$ at TDC versus the normalized, average jet radius $\overline{r_{jet}}/r_c$. In addition, figure 5.15 reflects the dominant contributions to the subsequent jet breakup and is consistent

with our previous observations in figure 5.13. For the lowest resolution, one can observe the most severe increase of the mean jet radius, which again may be attributed to the fact that the incoming jet is less influenced by the unresolved small scale flow structures but rather is broken up by the interaction with the chamber walls leading to a broader jet with higher penetration depth. This was also observed for mean velocity profiles in figure 5.13. As the resolution is increased, the contributions of the small scale structures become more pronounced and their interaction with the jet do not allow for as large jet radii as in the under-resolved case. On average this yields a lower penetration depth and smaller jet radii, consistent with both DNS and experimental data. As expected, the highest resolution yields the best match in terms of the average jet radius. More simulated cycles will presumably increase the spread on both the jet radius variability as well as the mean radial velocity.

5.4 Concluding remarks

In this chapter, we have presented a detailed study of the entropic multi-relaxation time lattice Boltzmann model for simple and complex flows for both resolved and under-resolved simulations. It was shown that the KBC model rapidly converges towards DNS simulations and experimental results in terms of average velocities, Reynolds stress components and the turbulent kinetic energy for both simple and complex flow setups. For under-resolved cases, the entropy-based, implicit subgrid model shows predictive capabilities already at grids eight times smaller than the resolved case. With further coarsening, the effect of under-resolution becomes noticeable but is expected as only three fluid nodes are used in the valve opening. This can be improved with appropriate grid-refinement in the region of interest and is left for future work. More importantly, this study shows that kinetic methods with built-in subgrid capabilities become reliable without the need for identifying and refining the grid in regions of high spacial gradients (such as near wall regions and jet break-up regions). Also, excellent results were obtained on a static grid as compared to a moving grid, which are commonly used for such valve/piston setups, thus significantly reducing the complexity of the algorithm and realization. The problem of using appropriate grids for each particular flow setup is a

common place for simulation of fluid flows and requires knowledge and expertise on the flow setup at hand. This process is heavily simplified due the built-in subgrid nature of entropic lattice Boltzmann models, which allow the use of simple Cartesian meshes for such complex flow setups and still retain predictive capabilities. Thus, the KBC model may be considered as a robust, parameter-free, efficient and accurate alternative to state-of-the-art modeling techniques such as LES. Apart from simplicity in the choice of grid and implementation, these kinetic methods can significantly reduce the computational costs, especially for complex flow setups with moving walls.

Chapter 6

Transitional flows

In this chapter, we study the class of transitional flows and assess the predictive capabilities of our numerical approach for this challenging regime. A simulation of the flow over a low Reynolds number *SD7003* airfoil at $Re = 6 \cdot 10^4$ and an angle of attack $\alpha = 4^\circ$ is performed and thoroughly validated by comparison to available numerical and experimental data. In order to include blockage and curvature effects, simulations of the flow in a low-pressure turbine passage composed of *T106* blade profiles, at a chord Reynolds number $Re = 6 \cdot 10^4$ and $Re = 1.48 \cdot 10^5$ for different free-stream turbulence intensities are presented.

Using the block-refinement strategy of section 4.2 in combination with Grad's boundary conditions (section 3.2) yields good agreement for all simulations. The results demonstrate that our scheme is a viable, parameter-free alternative to modelling approaches such as large-eddy simulations with similar resolution requirements.

6.1 Introduction

Understanding of boundary layer separation, transition to turbulence and reattachment of the turbulent boundary layer is of great importance for many applications ranging from diffusers, turbine blades to micro air vehicles (MAV) and unmanned air vehicles (UAV). Despite of many experimental and numerical studies, improving the efficiency of engineering designs

remains challenging due to the lack of predictive and controlling capabilities and requires further investigations to complement our current understanding.

Laminar separation typically occurs in the low Reynolds number regime, for example in the flow over an airfoil at incidence or in the flow over a flat plate with a prescribed suction profile as the upper boundary condition. On the upper surface, the boundary layer remains laminar beyond the point of minimum surface pressure and into the pressure recovery region, where the adverse pressure gradient opposes the flow and causes its detachment. Downstream of the separation point, the highly unstable separated shear layer transitions to turbulence. Subsequently, at sufficiently high Reynolds numbers or low angle of attack, the turbulent flow promotes momentum transfer in wall-normal direction and causes reattachment of the boundary layer, thus closing the so-called laminar separation bubble (LSB). The later the reattachment happens, the bigger the LSB and the larger the loss of lift and the increase of drag. In the limit of no reattachment and complete separation, the airfoil is said to be in stall condition with poor aerodynamic performance. Thus, optimizing performance requires understanding and control of these mechanisms.

Recent studies were focused on the transition mechanism with special attention paid to understanding the stability features of LSBs including the role of primary and secondary instability in the transition process. While it was shown theoretically and experimentally by [79, 108] that viscous instabilities, such as Tollmien-Schlichting (T-S) waves (see, e.g., [304], [138]), amplify upstream disturbances in the laminar part of the bubble, inviscid instabilities, e.g. of Kelvin-Helmholtz (K-H) type, play the dominant role in the amplification of disturbances in the free shear layer of the separation bubble and thus in the transition to turbulence [2, 127, 190, 358, 379, 381, 383].

One of the first DNS of transition over a flat plate, induced by a prescribed suction profile as the upper boundary condition, was performed by [3]. Before the transition, a staggered formation of Λ -vortices was observed. Based on linear stability analysis, it was concluded that the transition process was driven by convective instability (disturbances grow in space) rather than by absolute instability (disturbances grow in time and spread everywhere). In a contrast, [321] performed a DNS on the same set-up and

observed transition of an unforced LSB with negligible T-S instabilities and no distinct regions of primary or secondary instabilities, leading to rapid three-dimensionality.

The authors of [222] investigated LSBs over a flat plate by means of experiment and DNS using periodic two-dimensional disturbances upstream of the separation along with a spanwise array of spacers to trigger transition. It was observed that vortices were formed due to the roll-up of the separated shear layer, which eventually broke down to turbulence.

Subsequent investigations in [224] concluded that transition was driven by convective amplification of a two-dimensional T-S wave, and that the dominant mechanism behind transition is an absolute secondary instability as proposed by [225, 227, 291, 292], for which the growth of two-dimensional disturbances via viscous T-S instability upstream the separation point undergoes a gradual transition to inviscid K-H-type amplification. The dominant downstream traveling waves quickly saturate and form large, downstream propagating spanwise vortices. Beside this convective spatial growth, the existence of an additional temporal amplification has been observed experimentally, theoretically and numerically by [3, 107, 109, 226], among others.

In the work of [149] it was shown that although classical linear stability theory of the time-averaged flow fields suggests convective instability [42] with no evidence of absolute instability, removing the forcing still leads to self-sustained turbulence. They concluded, based on three-dimensional simulations resolving the linear response, that transition occurs by absolute instability of two-dimensional vortex shedding within the shear layer in the absence of convectively driven transition. Further studies on flat plates and airfoils have shown the vortex roll-up occurring in the separated shear layer at the frequency of dominant disturbance amplification with downstream vortex pairing for some flow conditions [44, 127, 190, 358, 382, 393]. In the work of [44], time-resolved measurements of the velocity field over the *SD7003* airfoil revealed several types of coherent vortical structures developing during transition. Qualitative differences in these structures compared to the flow over flat plates, such as in [190, 358], were observed and attributed to a dependence of the transition behavior on surface curvature as well as a dependence of the development of the coherent structures on the flow conditions. In [183] it was further demonstrated

that the newly coalesced (due to vortex pairing) shear layer vortices, characterized by an initially high spanwise coherence, undergo rapid spanwise deformations and subsequently break down to smaller structures in the vicinity of the reattachment point.

The flow development near the reattachment point has shown significant variations depending on the surface geometry and the operating conditions. Under certain conditions, the reattachment process appears relatively steady with no shedding of large coherent spanwise vortices [14], while in other cases it was observed to be an unsteady process accompanied by vortex shedding. The unsteady reattachment behavior is called bubble flapping and was observed both experimentally and numerically with a frequency below the one of the primary K-H instabilities (see, e.g., [33, 44, 127, 148, 190, 223, 292, 358]). Among several propositions to explain the cause of bubble flapping, various authors pointed at the absolute secondary instability mechanisms of the shed vortices to three-dimensional disturbances [149], at acoustic feedback mechanisms [148, 150] and at a viscous-inviscid coupling interacting with varying levels of free-stream turbulence [223]. As shown by, e.g., [366], performing a DNS on a flat plate with different free-stream disturbances, a larger disturbance leads to a smaller bubble size, while the reattachment point is moved upstream. Similarly, [149] observed a large decrease of the bubble size when forcing was applied, leading to a significant increase of aerodynamic performance for the NACA0012 airfoil. Due to the lack of a comprehensive picture [41] of the instability mechanisms at play during transition it is inherently difficult to model these phenomena. In the work of [321], the accuracy of various Reynolds-averaged Navier-Stokes turbulence models was assessed. Although the results obtained by the Spalart-Allmaras model showed reasonable agreement with the DNS, large discrepancies between the models and the reference case were observed. In particular, more sensitive quantities such as the skin friction coefficient showed significant deviations. Minor improvements of various RANS models were reported in the works of [125, 141, 264]. In recent years, large-eddy simulations for transitional flows became increasingly popular (see, e.g., [45, 84, 294, 365, 378, 379]). While accurate results were reported for implicit LES, relying on high-order schemes for spatial derivatives to capture transition, combined with filtering for stabilization (see, e.g., [106, 356, 396]), the recent work of [46] highlights the impor-

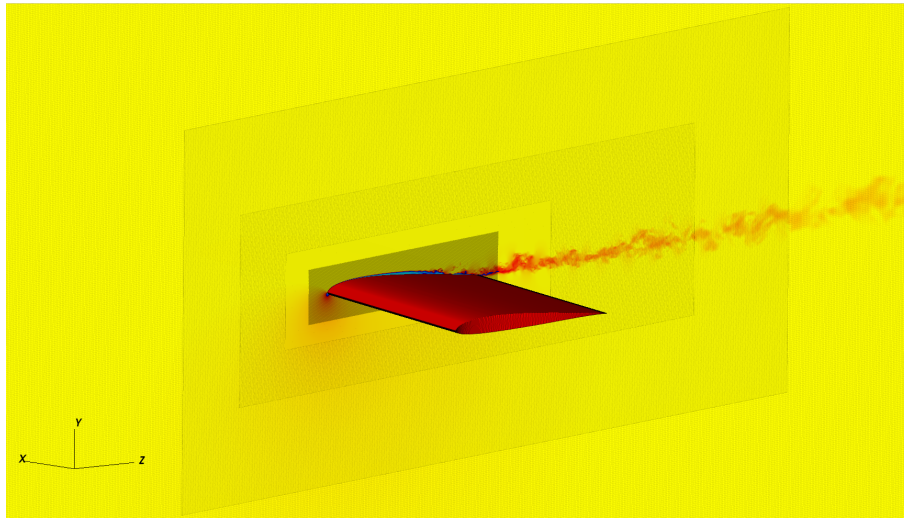


Figure 6.1: Multi-domain block refinement for the flow past the *SD7003* airfoil along with a slice of instantaneous streamwise velocity.

tance of appropriate subgrid-scale modeling by a comparison of dynamic Smagorinsky, truncated Navier-Stokes and no-model under-resolved DNS. The motivation of the present study is to assess if entropy-based LBM can capture the subtle mechanisms of transitional flows. In spite of validation in both laminar and turbulent flow regimes, the transition to turbulence, which not only depends on accurate prediction of the bulk flow but is also highly sensitive to the implementation of the boundary conditions, has received little attention so far in the realm of LBM. However, to establish LBM as a predictive method for engineering applications, it is of great importance to also assess the accuracy of LBM in the transitional flow regime.

This chapter is organized as follows: In section 6.2, we consider the flow past the *SD7003* airfoil at an angle of attack $\alpha = 4^\circ$ and a chord Reynolds number of $Re = 6 \cdot 10^4$. Moreover, in order to test the model's performance for highly curved geometries, simulations of the flow in a low-pressure turbine passage for different Reynolds numbers and free-stream turbulence intensities are performed and, where available, compared to DNS and experimental data. Results are discussed in section 6.3.

6.2 Flow separation and transition to turbulence

In this section, we investigate two cases to test the accuracy of KBC models. In first instance, we consider the flow over the *SD7003* airfoil at angle of attack $\alpha = 4^\circ$ and Reynolds number $Re = 6 \cdot 10^4$ based on the chord length c and the inflow velocity u_∞ . The second test case is regarding the flow in a low-pressure turbine passage composed of *T106A* airfoils at Reynolds numbers of $Re = 6 \cdot 10^4$ and $Re = 1.48 \cdot 10^5$ based on the axial chord and the inflow velocity.

As stated in [46] and also confirmed by our simulations, the key to obtaining accurate results, in agreement with experiment, is to resolve the reverse flow region near the wall and the shear layer which transitions to turbulence. Despite the efficiency of LBM, this is an intractable task for a uniform resolution. To remedy this issue we employ the multi-domain grid refinement technique as introduced in section 4.2.

Finally, we mention that the transitional flows considered in this work are sensitive to the wall-boundary conditions and spurious artifacts can occur for an inappropriate choice. To that end, we employ the Grad boundary condition. Other boundary conditions used in the simulations include inflow, outflow, free-stream and periodic boundary conditions. Unless stated otherwise, we implement these boundary conditions as follows: The inflow is prescribed using equilibrium populations with unit density. For the outflow boundary, we employ the no-boundary condition. The free-stream or free-slip boundary condition reflects the population with respect to the wall normal and is used to mimic an open space. The periodic boundaries are directly applied within the advection step.

6.2.1 Transitional flow past *SD7003* airfoil

6.2.1.1 Numerical set-up

The numerical set-up is identical to the experimental and numerical studies of [106, 260, 396] to allow a direct comparison with the results obtained by the KBC model.

The experimental investigations of [260] were conducted in order to assess the suitability of three different test facilities, namely, a low-turbulence

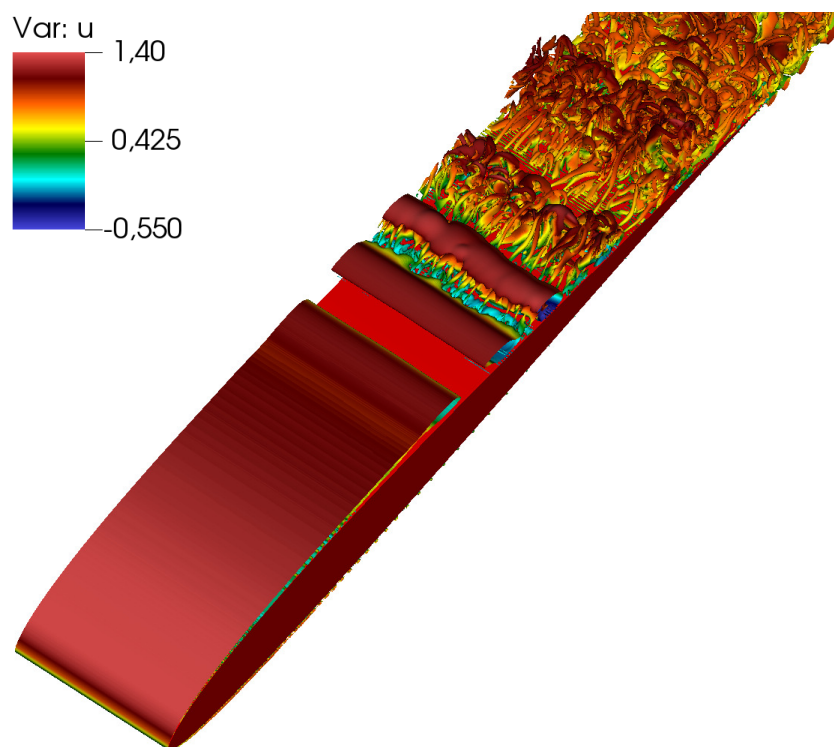


Figure 6.2: Isosurfaces of the Q -criterion ($Q = 4$) colored by normalized streamwise velocity for the simulation of the $SD7003$ airfoil at an angle of attack $\alpha = 4^\circ$ and a Reynolds number $Re = 6 \cdot 10^4$.

wind tunnel (Technical University of Braunschweig (TU-BS) Low-Noise Wind Tunnel), a water tunnel (Air Force Research Laboratory (AFRL) Free-Surface Water Tunnel) and a tow tank (Institute for Aerospace Research (IAR) Tow Tank). While good agreement was found for IAR and TU-BS, the AFRL facility showed significantly earlier separation and reattachment, and was not able to resolve reverse flow in the bubble. The numerical study of [106] was conducted to test the capabilities of implicit large-eddy simulations (ILES) to capture the LSB mechanism accurately. The use of high-order compact schemes for spatial derivatives and a Pade-type low pass filter for stability has shown accurate predictions of LSB for various operating points. In a similar fashion, [396] employed an implicit LES using a high-order spectral difference method to capture the LSB.

In our study and in accordance with [106, 396], we use a uniform inlet velocity with no inflow disturbances. A small perturbation in the beginning of the simulation is introduced to initiate vortex shedding. All statistical quantities are recorded after an initial transient of $t = 15c/u_\infty$ and collected for another $t = 45c/u_\infty$ until statistically stationary conditions

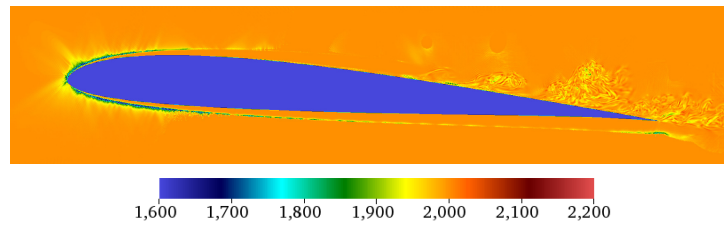


Figure 6.3: Instantaneous snapshot of the spatial distribution of the stabilizer γ .

have been reached. The solutions are obtained on a computational domain of $10c \times 5c \times 0.2c$ for the stream-, pitch- and spanwise direction, respectively. Periodic boundary conditions are applied in the spanwise direction, while free-stream boundary conditions are prescribed in the pitchwise direction. The computational domain is refined with five levels, where the coarsest level resolves the airfoil with $c = 100$ lattice points to ensure enough spatial extent to represent the reverse flow region accurately. As shown in figure 6.1, the refinement patches are located closely around the airfoil to minimize computational cost. Based on the maximum wall shear stress in the reattachment zone, the resolution in wall units amounts to $\Delta y^+ \approx 2.1$ in the finest level, which is similar to the ILES study of [396] with $\Delta y^+ \approx 2.5$ using high-order spectral differences. As an additional verification of sufficient resolution, a snapshot of the spatial distribution of the stabilizer γ is shown in figure 6.3. It has been shown in previous chapters and [39, 40, 77] that the value of γ is directly related to the degree of under-resolution and that γ automatically tends towards the LBGK value $\gamma_{\text{lim}} = 2$ in the limit of a fully resolved simulation. Therefore, the deviation of the stabilizer from its limit value indicates under-resolution. Figure 6.3 shows the expected small deviations from $\gamma_{\text{lim}} = 2$ in the finest grid level, suggesting negligible numerical diffusion. This assertion will be further investigated through comparison to reference data.

6.2.1.2 Results

In order to gain insight into the coherent flow structures in the LSB, we present an instantaneous snapshot of isosurfaces of the Q-criterion colored by streamwise velocity in figure 6.2. As expected, starting from the leading edge, the flow remains laminar and further downstream separates due to the adverse pressure gradient on the suction side of the airfoil. Instabili-

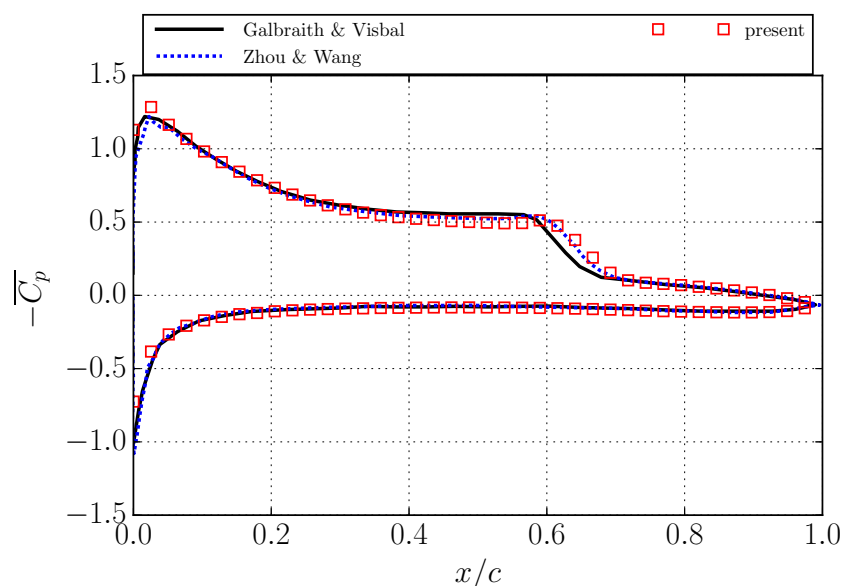


Figure 6.4: Average pressure coefficient \overline{C}_p over the upper and lower surface of the SD7003 airfoil. Here and in the following, the symbols represent sampled values along the chord for clarity.

ties, forming corrugated flow pattern and interaction with the small-scale structures in the recirculation zone, can be observed at the end of the laminar shear layer. Further downstream, spanwise distortion leads to fully three-dimensional structures, indicating the transitional region, followed by fine-scale turbulence.

Beyond the visual inspection, one can quantify separation, transition and reattachment by computing the mean pressure coefficient $\overline{C}_p = (\overline{p} - p_\infty) / (1/2\rho_\infty u_\infty^2)$ and the mean skin friction coefficient $\overline{C}_f = \overline{\tau} / (1/2\rho_\infty u_\infty^2)$ on the airfoil surface as shown in figure 6.4 and figure 6.5, respectively. Here, the mean wall shear stress is denoted by $\overline{\tau}$.

The distribution of the mean pressure coefficient over the suction side of the airfoil surface can be used to extract various characteristics of the LSB. As seen in figure 6.4, the point of minimum pressure is followed by a pressure plateau, which has been shown to occur near the separated flow region [41, 334]. Consequently, the separation point x_s and transition location x_t can be identified as the start and the end of the pressure plateau [261]. Similarly, the reattachment point x_r can be estimated as the point at the end of enhanced rate of pressure recovery downstream of the transition point. These definitions are commonly used to experimentally obtain LSB characteristics by linearly fitting the surface pressure data [41, 114]. A first

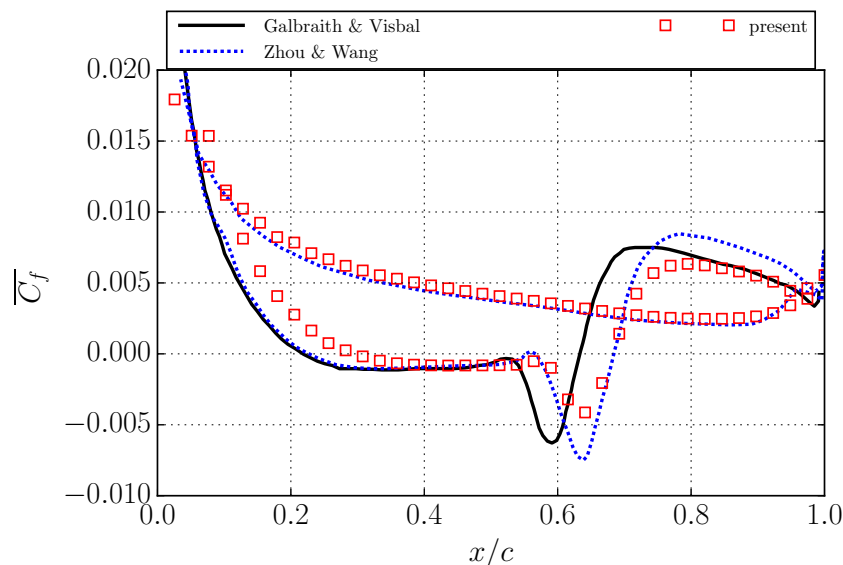


Figure 6.5: Average skin friction coefficient \overline{C}_f over the upper and lower surface of the airfoil of the *SD7003* airfoil.

indication that the KBC model is able to accurately predict the mean bubble size characteristics is given by the excellent match of the \overline{C}_p distribution with the high-order implicit LES of [106, 396].

On the other hand, computing the skin friction on the airfoil surface allows for another meaningful way to determine the average geometrical properties of the LSB. The separation and reattachment points can be inferred from the location of zero skin friction. While the first root with a negative gradient indicates separation, reattachment happens further downstream at zero skin friction and a positive gradient. From this analysis, we report x_s and x_r along with the reference data in table 6.1. It is apparent that excellent agreement with the experimental data is obtained. As was mentioned above, the AFRL facility is an outlier of the experimental studies but is still reported for completeness. Furthermore, the agreement with both ILES simulations is reasonable. From the skin friction plot, a considerably later separation is predicted by the KBC model as compared to the ILES simulations but matches the experimental data. Nonetheless, the location of minimum skin friction and reattachment location agree well with the ILES simulation results from [396].

Finally, in order to identify the mean location of transition, Reynolds shear stresses are considered. In figure 6.6a, the distribution of Reynolds shear stress $-u'_x u'_z / u_\infty^2$ is shown with a threshold of 0.001. The commonly used

Contribution	Tu [%]	x_s/c	x_t/c	x_r/c
[260],IAR (expt.)	0	0.33	0.57	0.63
[260],TU-BS (expt.)	0.1	0.30	0.53	0.62
[260],AFRL (expt.)	~ 0.1	0.18	0.47	0.58
[106] (ILES)	0	0.23	0.55	0.65
[396] (ILES)	0	0.23	0.52	0.69
present	0	0.30	0.55	0.68

Table 6.1: Comparison of the LSB properties for the flow over the *SD7003* airfoil, where Tu denotes the turbulence intensity of the inflow.

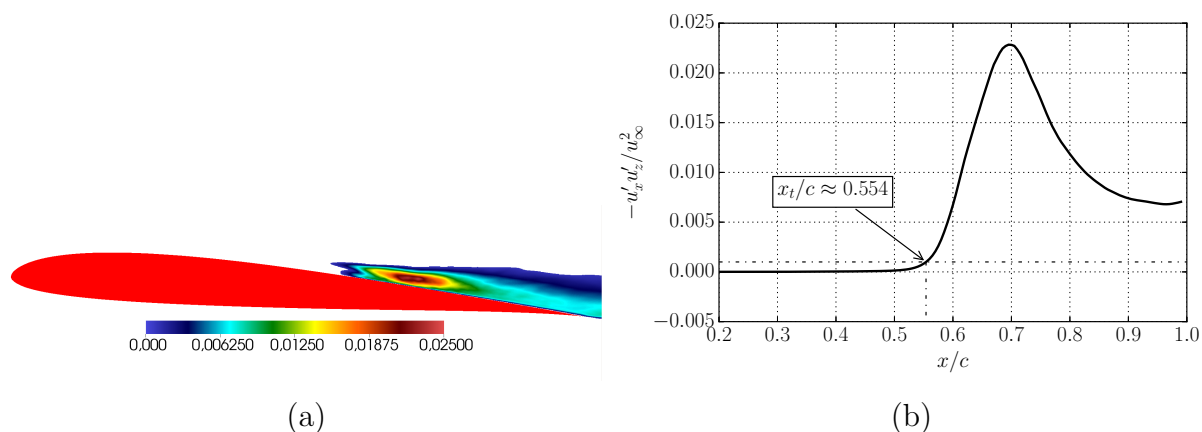


Figure 6.6: Determination of the onset to transition. (a): Distribution of Reynolds shear stress $-u'_x u'_z / u_\infty^2$ with a threshold of 0.001. (b): Reynolds shear stress value plotted along the line of maximum shear stress.

criterion for the transition onset is the region, which exceeds this threshold as these stresses describe the transport of momentum into the boundary layer [44, 260, 387]. Different criteria such as the shape factor H_{12} (defined as the ratio of the displacement thickness and the momentum thickness) or the deviation from exponential growth were identified and are in good agreement among each other [190, 232]. In figure 6.6b, the Reynolds shear stress value is plotted along the line of maximum shear stress, which allows us to accurately extract the transition point as the point exceeding the threshold of 0.001. The comparison with all reference data is excellent (see table 6.1).

The mean velocity profiles along the chord line in wall-normal direction are compared to the ILES by [396] in figure 6.7. The evolution from the attached shear layer to the detachment is clearly visible and the separa-

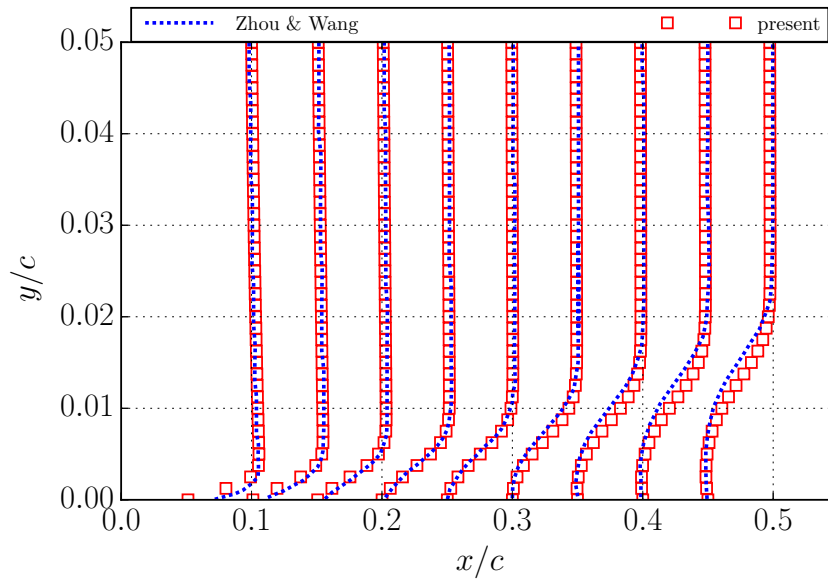


Figure 6.7: Mean velocity profiles at $x/c = 0.1 \sim 0.5$

tion location is in line with its evaluation using the mean skin friction coefficient $\overline{C_f}$. In agreement with the previously observed deviations of the skin friction distribution over the airfoil surface, the ILES predicts earlier separation compared to both experiment and the present simulation. Nonetheless, the agreement between KBC and ILES is reasonable.

Next, we investigate the spanwise flow development. The recent experimental study of the flow over a NACA 0018 airfoil by [183] suggests that newly coalesced shear layer vortices possess a relatively high spanwise coherence and undergo a rapid spanwise deformation, which eventually leads to a break down into small scale structures in the reattachment zone. To quantify this behavior with the present simulation, spanwise wave-length statistics are extracted by computing the spectra of streamwise velocity fluctuations $u'_x u'_x$ along spanwise direction for various chordwise locations within the LSB at a constant wall-normal distance of $y/c = 0.00625$. The corresponding spectra are reported in figure 6.8. Starting beyond the separation point at $x/c = 0.4$, one can observe that the maximum corresponds to the spanwise extent, thereby confirming the two-dimensionality of the main vortices. At the mean transition location at $x/c = 0.55$, a step increase at around $\lambda/c \approx 0.01$ is followed by a plateau of dominant wavelengths ranging from $\lambda/c \approx 0.03$ to $\lambda/c \approx 0.1$. This characteristic behavior is identical to what was observed by [183] and implies three-dimensional

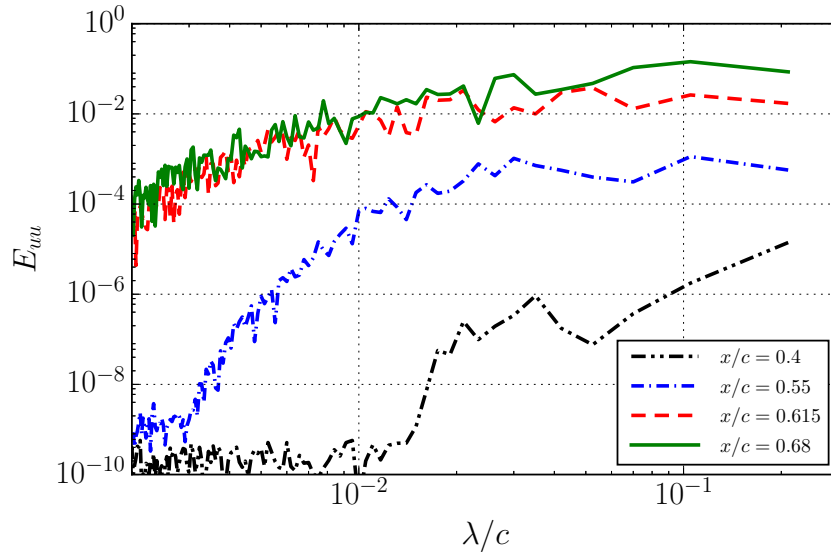
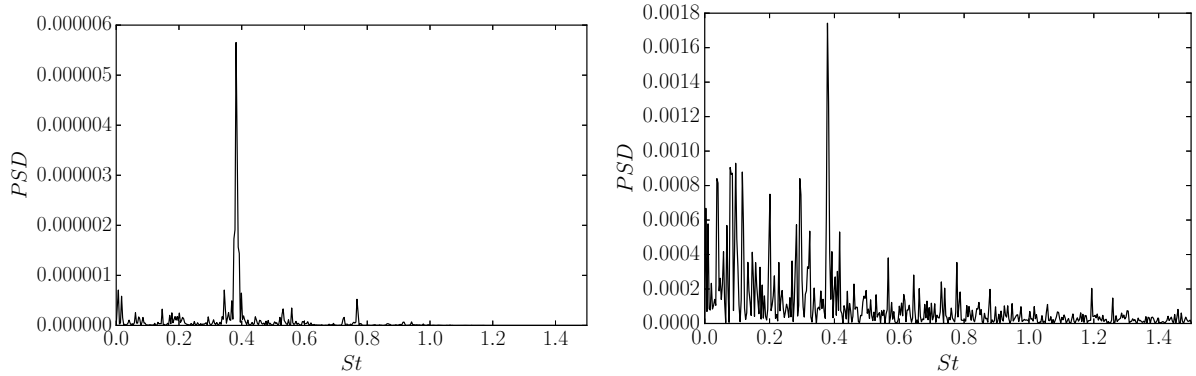


Figure 6.8: Spectra of fluctuating streamwise velocity along the span.

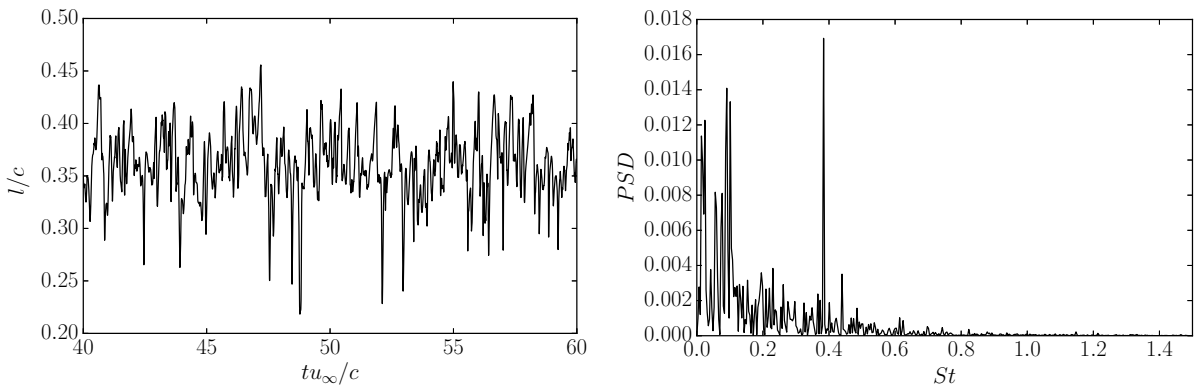
vortex structures and weak spatial periodicity. Beyond transition onset at $x/c = 0.615$, the breakdown into small structures is witnessed by broadening of the aforementioned plateau and an increase of the spectra at lower wave-lengths. At the average reattachment point $x/c = 0.68$, the spectra practically overlap and only a minor increase at higher wave-lengths is observed, suggesting a rather fast breakdown. These results agree well with the experimental study of [183] and therefore confirm that the KBC model is able to capture the spanwise evolution of the flow.

Finally, the time-resolved KBC simulation allows to study the LSB dynamics. The power spectral density of streamwise velocity fluctuations is shown in figure 6.9 for two observer points, one within the LSB at $x/c \approx 0.53$ and the other in the near wake. Despite the fact that more frequencies are present in the near wake, both observer points display a dominant vortex shedding frequency at a Strouhal number $St_{vs} = f \sin(\alpha)c/u_\infty \approx 0.38$. In order to assess if the reattachment behavior is steady or if bubble flapping occurs, the normalized bubble length l/c , which is computed through the instantaneous C_f distribution, is monitored over the course of the simulation (see figure 6.10a). A highly unsteady reattachment behavior with various frequency contributions is evident and the bubble length fluctuates as much as $0.15l/c$ from its mean value. By employing spectral analysis and plotting the power spectral density of the bubble length (see figure 6.10b), various dominant frequencies are revealed. On the one hand, the vortex



(a) Power spectral density in the LSB at $x/c \approx 0.53$. (b) Power spectral density in the near wake.

Figure 6.9: Power spectral density for two observer points, one within the bubble and one in the near wake.



(a) Evolution of the bubble size.

(b) Power spectral density for the bubble size.

Figure 6.10: LSB dynamics.

shedding frequency at St_{vs} is observed as in the analysis above. On the other hand, other dominant frequencies at lower Strouhal numbers, namely $St \approx 0.09$ and $St \approx 0.02$ are superimposed. As mentioned in the introduction, a similar behavior was observed numerically and experimentally (see, e.g., [33, 44, 127, 148, 190, 223, 292, 358]). While the bubble flapping effect is confirmed by the present simulation, the cause of the low frequency contribution is discussed controversially in literature and deserves further investigation in future work.

Summarizing, we have shown that the parameter-free KBC model supplied with the Grad boundary condition is able to accurately predict the boundary layer separation, transition to turbulence and the reattachment of the

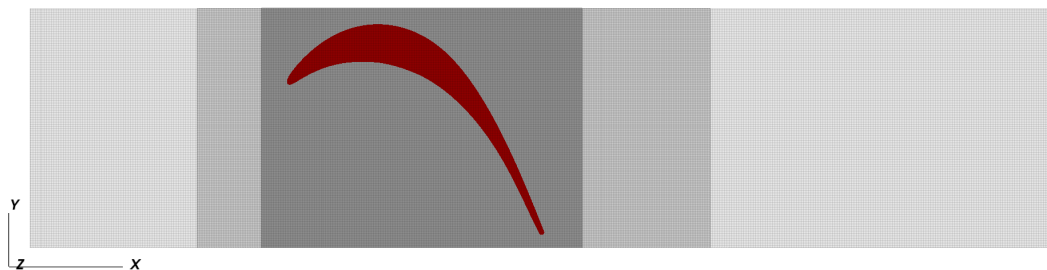


Figure 6.11: Computational set-up for the flow over an *T106* turbine blade.

turbulent boundary layer. Thus, it provides a simple and efficient alternative to conventional modeling approaches such as LES. It also needs to be stressed that to accurately capture the transition phenomena it is necessary to resolve the recirculation region for which grid refinement is crucial to keep the computational costs reasonable.

6.2.2 Flow in a low-pressure turbine passage

In this section, the flow in a low-pressure turbine passage is considered. Similar to the flow past the *SD7003* airfoil in the previous section, low-pressure turbines typically operate at relatively low Reynolds and Mach numbers. Under these conditions, depending on the geometry and the inflow, a LSB might occur. Note that, while in general compressibility effects may not be neglected for industrial applications, insight into LSB dynamics can already be gained in the incompressible flow regime [26, 394]. The present set-up is distinctly different from the previous case of the *SD7003* airfoil as it allows for blockage and curvature effects, as well as the unsteady wake of the blade, which can have a significant influence on the LSB and the onset of transition. In particular, the flow is re-directed by more than 100° and accelerated to roughly double its inflow value, leading to a large streamwise straining, where its principal axes vary spatially, as observed by [375].

Various experimental investigations have been conducted to study LSBs in low-pressure turbines (LPTs) [88, 136, 139, 228, 308, 309, 318, 324]. Considering the full rotor/stator arrangement in real turbine cascades, the incoming flow is highly unsteady, with wakes generated by the preceding row of blades. In the work of [309], a significant effect of a periodically

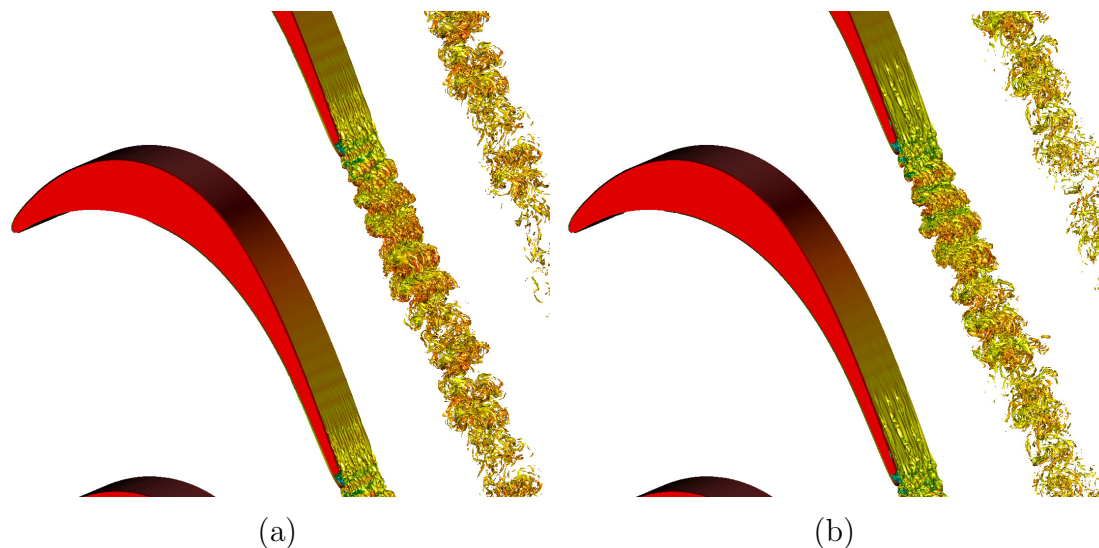


Figure 6.12: Flow in a low-pressure turbine passage at $Re = 1.48 \cdot 10^5$, visualized by vorticity isosurfaces colored by streamwise velocity. (a): Uniform inflow. (b): Turbulent inflow.

passing turbulent inflow wake on the LSB and thus performance was observed. Combined with hot film measurements [308], it was concluded that separation is periodically suppressed by the turbulent incoming wake and the subsequent calmed region with their full velocity profiles (see also [324]).

On the numerical side, the increasing compute power and the relatively low Reynolds and Mach number in LPTs allow for DNS (see, e.g., [375, 376]). Noteworthy is the DNS study of [375], who investigated the bypass transition due to a periodic, turbulent inflow wake, which was used to generate large free-stream disturbances.

On the modeling side, the lack of accuracy of RANS models [286] led to an increasing number of LES simulations to study LSBs in LPTs, focusing again on the boundary layer-wake interference [238, 239, 241, 295]. The results of these LES are encouraging, but uncertainties remain and high resolution is needed to capture all features of transition. In the LES study of [238] for example, significant discrepancies to the reference DNS are observed, where the LES was not capable of fully reproducing the transition location (delayed transition) and skin friction coefficient. These discrepancies are attributed to the resolution near the boundary and also in the bulk, which is not able to account for the fine-scale structures convected by the wake and thus to trigger transition.

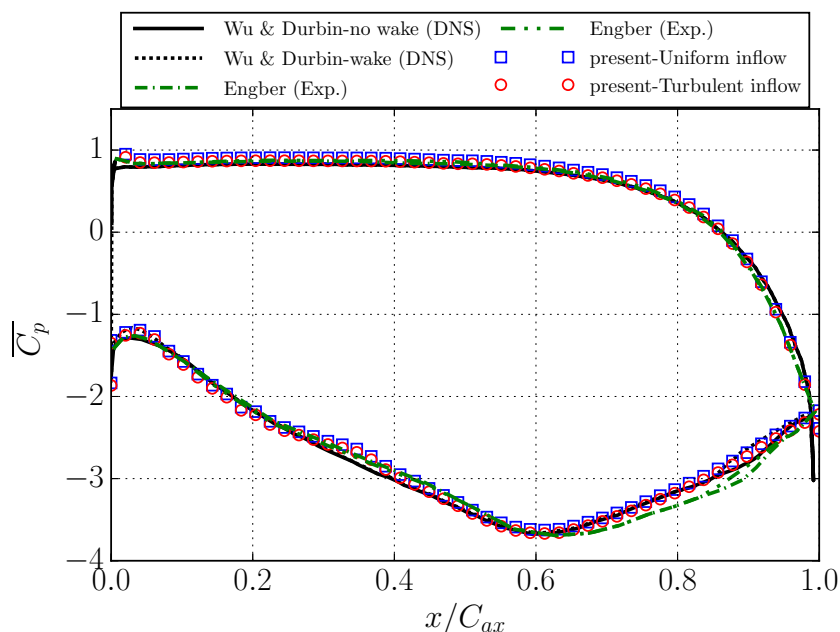


Figure 6.13: Distribution of the mean pressure coefficient over the axial chord of the *T106* turbine blade at $Re = 1.48 \cdot 10^5$.

In this work, analogous to [286], we focus on the flow past the turbine blade without an inflow wake. To analyze the effect of Reynolds number and free-stream turbulence, we conduct simulations at Reynolds numbers of $Re = 6 \cdot 10^4$ and $Re = 1.48 \cdot 10^5$ with imposed free-stream turbulence intensities in the range $Tu = 0 - 10\%$.

6.2.2.1 Numerical set-up

The simulation set-up is identical to the DNS of [375], who conducted incompressible flow simulations with and without a turbulent inflow wake. For comparison with experiment, the study of [88] is considered, who carried out various experiments for different inflow disturbances and Reynolds numbers (but no turbulent wake).

The set-up consists of a single *T106* low-pressure turbine blade, which is periodically repeated to mimic the full turbine passage. The distance between two consecutive blade profiles is given by the normalized pitch $g/C_{ax} = 0.93$, where C_{ax} denotes the axial chord. The Reynolds number is based on the mean inflow velocity and the axial chord. The computational domain is chosen as $[-C_{ax}, 3C_{ax}] \times [-0.5g, 0.5g] \times [-0.1C_{ax}, 0.1C_{ax}]$ for the stream-, pitch- and spanwise direction, where the turbine blade is located

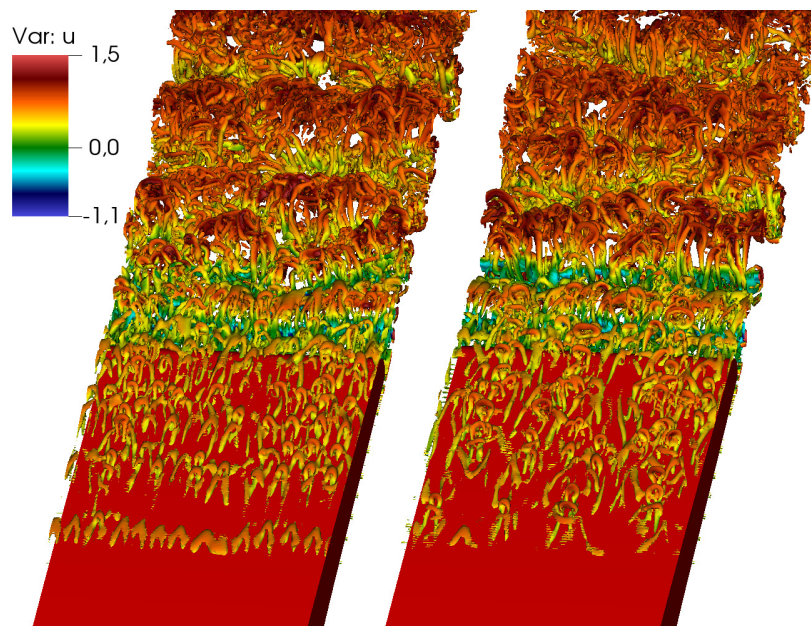


Figure 6.14: Snapshot of isosurfaces of the Q-criterion ($Q = 200$) colored by normalized streamwise velocity at $Re = 1.48 \cdot 10^5$. Left: $Tu = 0\%$. Right: $Tu = 0.2\%$.

at the origin. The computational cost is reduced by using three levels of grid refinement, where the coarsest level resolves the turbine blade with $C_{ax} = 300$ lattice points (see figure 6.11). In the case of full transition, this yields a maximum effective grid spacing of $\Delta y^+ \approx 0.25$ within the separation bubble and $\Delta y^+ \approx 2.1$ in the turbulent boundary layer at the trailing edge.

Periodic boundary conditions are applied in pitch- and spanwise directions. The exit flow has a designed angle of -63.2° with the x -axis and we employ convective boundary conditions at the outlet. Regarding the inflow, simulations with uniform and turbulent inflow conditions at an inlet angle of 37.7° are presented.

In order to generate the inflow turbulence, a methodology similar to [394] was adopted, where a frozen homogeneous isotropic turbulence field within a periodic box of spanwise length is superimposed onto mean flow at the inlet angle. The box is duplicated to fill the entire inflow plane and advected with the inflow velocity to mimic time-varying fluctuations. The initial turbulence field is computed using a synthetic kinematic simulation [105], where the solenoidal velocity field is described as a superposition of a finite number of random Fourier modes according to an energy spectrum of the form $E(k) = Ak^4 \exp(-2k^2/k_0^2)$. The constant A and the wave num-

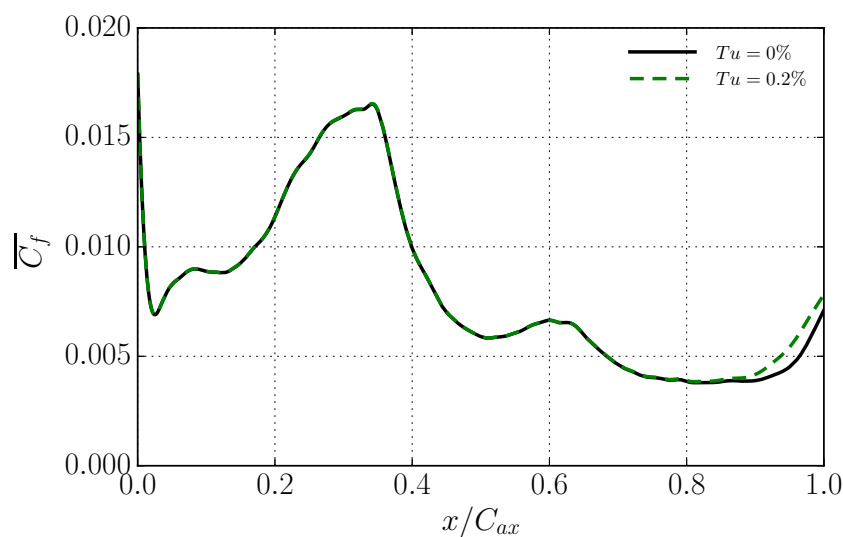


Figure 6.15: Distribution of the mean skin friction coefficient over the axial chord on the suction side of the *T106* turbine blade at $Re = 1.48 \cdot 10^5$.

ber of the spectrum peak k_0 are chosen in accordance with the prescribed turbulence intensity.

6.2.2.2 Results

First, for the purpose of validation, we consider the high Reynolds number case of $Re = 1.48 \cdot 10^5$ with a uniform inflow and a turbulent inflow with $Tu = 0.2\%$. A snapshot of the flow in the periodically completed turbine passage is visualized in figure 6.12 using vorticity isosurfaces, colored by streamwise velocity. The distribution of pressure coefficient over both the suction and the pressure side of the turbine blade is shown in figure 6.13 along with the reference data for the uniform and turbulent inflow. On the suction side, a favorable pressure gradient accelerates the flow until the adverse pressure gradient downstream of $x/C_{ax} \approx 0.6$ causes a deceleration. On the pressure side, the pressure gradient is nearly zero until $x/C_{ax} \approx 0.5$, where a steep pressure gradient accelerates the flow up to the trailing edge.

The comparison of simulated pressure coefficient with the experimental and numerical data in figure 6.13 shows a good agreement. On the pressure side, only marginal discrepancies between all data is observed. On the suction side, due to the different inflow conditions, the discrepancies are larger. The influence of the wake for the DNS data becomes apparent in the

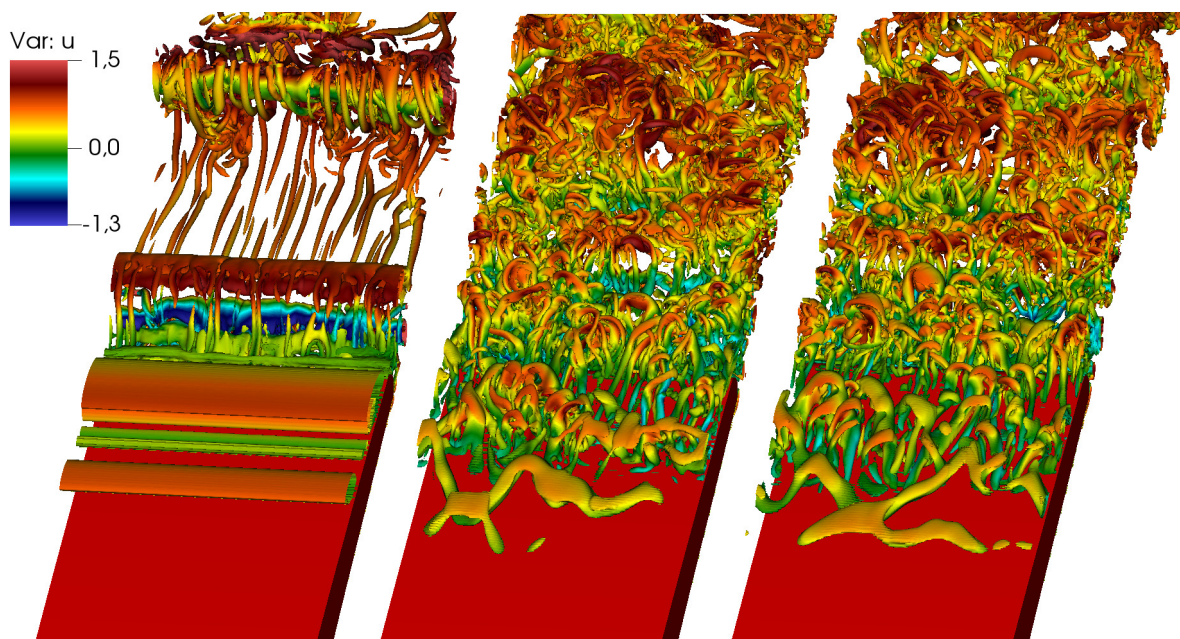


Figure 6.16: Snapshot of isosurfaces of the Q-criterion ($Q = 110$) colored by normalized streamwise velocity at $Re = 6 \cdot 10^4$. Left: $Tu = 0\%$. Middle: $Tu = 5\%$. Right: $Tu = 10\%$.

aft of the blade, where the pressure is increasing at about $x/C_{ax} \approx 0.85$ compared to the uniform inlet. Similarly, minor deviations between the different inflow disturbances can be observed for the experimental data and the present simulation.

To further investigate the effect of the inflow disturbances, a close-up image zoomed in from the top in figure 6.14 shows the isosurfaces of the Q-criterion colored by normalized streamwise velocity. Both simulations exhibit Λ -type vortices at the initial stage, which subsequently develop into hairpin-type vortices. While for the simulation using an uniform inflow, these flow structures are relatively well ordered in staggered formation, the hairpin vortices for the case with turbulent inlet are more pronounced with a higher degree of disorder.

However, as indicated by the distribution of pressure and skin friction coefficient over the airfoil surfaces, the influence of free-stream turbulence is minor regarding the aerodynamic quantities. In fact, the integral effect as manifest by the drag and lift coefficient is insignificant with a deviation of less than 0.25% and 0.01%, respectively. While the rapid increase of the skin friction coefficient as shown in figure 6.15 indicates a starting transition process, full transition, as defined by the Reynolds stress criteria

$Tu[\%]$	x_s/c	x_t/c	x_r/c
0	0.890	NA	0.992
5	0.903	0.973	0.976
10	0.914	0.967	0.968

Table 6.2: Comparison of the LSB properties for the flow over the T106 blade for different free-stream turbulence intensities at $Re = 6 \cdot 10^4$.

used above, is triggered by neither uniform nor turbulent inflow conditions. Moreover, as indicated by the skin friction coefficient and in line with DNS and LES simulations [295, 375] the mean flow does not separate. This is in contrast to the LES by [286], who reported a fully developed LSB, albeit at a lower nominal Reynolds number $Re = 1.1 \cdot 10^5$ and a uniform inflow.

To investigate this discrepancy, another set of simulations was run with the same Reynolds number $Re = 1.1 \cdot 10^5$ as in [286]. However, the change in Reynolds number had only a marginal effect and no transition or mean flow separation was observed, also not under turbulent inflow conditions with $Tu = 0.2\%$. Thus, similar to [394], we decreased the Reynolds number to $Re = 6 \cdot 10^4$, thereby stipulating mean flow separation on the airfoil and studied three cases with varying free stream turbulence intensities, $Tu = \{0\%, 5\%, 10\%\}$. The corresponding instantaneous snapshots showing isosurfaces of the Q-criterion, zoomed in from the top view onto the trailing edge of the blade, are shown in figure 6.16. It is apparent that for uniform inflow in figure (6.16, left), the flow separates as shown by the two-dimensional vortex structures in the aft of the blade. However, turbulent structures are only developing in the wake of the blade and no natural transition occurs on the blade surface. The cases with a free-stream turbulence of $Tu = 5\%$ and $Tu = 10\%$ are shown in figure (6.16, middle) and figure (6.16, right), respectively. It can be seen that transition is triggered for both cases, and is initiated by the formation of Λ -type vortices, similar to the high Reynolds number case. Further downstream these vortices develop into hairpin-type vortices, which eventually break down into fine scale turbulence past the blade. This is in contrast to the high Reynolds number case for which the boundary layer remains attached without transition to turbulence. On the other hand, in the present low Reynolds number cases with free-stream turbulence, separated-flow transition is observed.

The effect of free-stream turbulence on the geometrical properties on

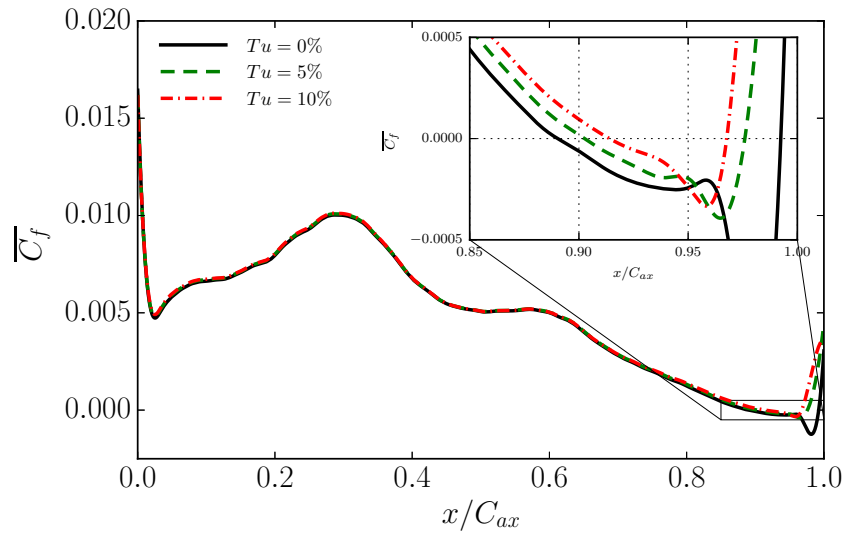


Figure 6.17: Average skin friction coefficient over suction side of the *T106* blade for varying free-stream turbulence intensities at $Re = 6 \cdot 10^4$.

the LSB is investigated next. In figure 6.17 we present the skin friction coefficient for all turbulence intensities. As in [394], we observe that the separation location is affected by the level of free-stream turbulence and moves downstream with increasing Tu . In addition, the reattachment location moves upstream with increasing Tu , thereby reducing the extent of the entire LSB and improving aerodynamic performance. It is worth pointing out that figure 6.17 also shows that the effect of LSB size reduction is nonlinear with respect to Tu . This effect mainly stems from the nonlinear upstream shift of the reattachment location rather than the separation location, which appears to behave more linearly. Similar behavior is shown by the mean pressure coefficient over the suction side of the airfoil in figure 6.18, where the pressure plateau is most pronounced for the uniform inflow case, suggesting the largest LSB. All geometrical quantities of the LSB are tabulated in table 6.2, where we define the onset to transition x_t as above using a threshold of $-u'w'/u_\infty^2 \approx 0.001$. Investigating the flow field in more detail, we report the mean and rms streamwise velocity profiles (tangential to the blade surface on the suction side) for $x/C_{ax} = 0.88 - 0.99$ in steps of $0.1C_{ax}$ as a function of the normal distance n/C_{ax} in figure 6.19. The average velocity profiles in figure 6.19a confirm the visual impression from the instantaneous snapshots of a pronounced separation for the case without free-stream turbulence. For the cases including free-stream turbu-

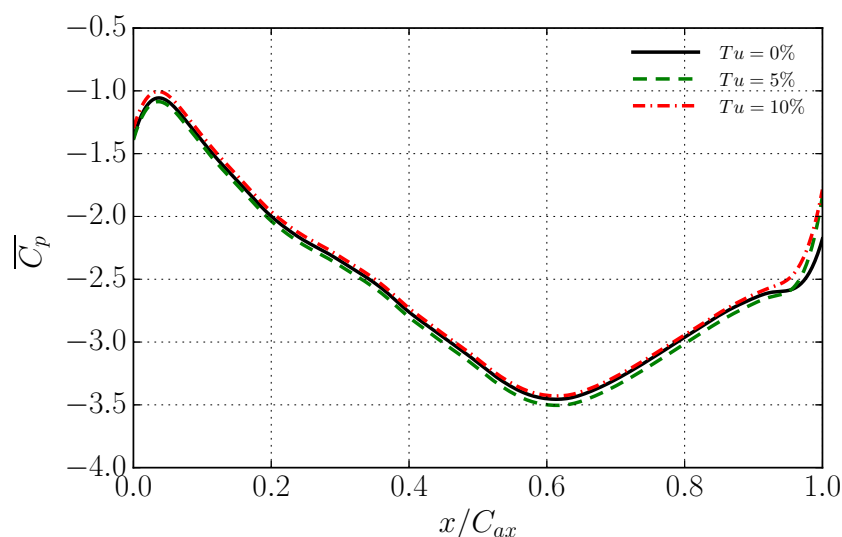


Figure 6.18: Average pressure coefficient over suction side of the *T106* blade for varying free-stream turbulence intensities at $Re = 6 \cdot 10^4$.

lence, separation is less distinct and a smaller shear layer thickness with a clear reattachment zone can be observed. Also for the mean velocity, the trend of earlier reattachment with increasing Tu is obvious. The fluctuations of the streamwise velocity component are presented in figure 6.19b. In the case of uniform inflow, mild fluctuations within separated region indicate the unsteady two-dimensional vortex rolls, whereas relatively sharp peaks of rms-values are measured within the reattachment zone, which are confined to the near wall-region until a normal distance of roughly $n/C_{ax} \approx 0.005$. On the contrary, in the case of free-stream turbulence, no vortex rolls are observed in the separation zone and the reattachment region exhibits a much broader plateau due to transition, as compared to the uniform case. This is in line with what is observed in the literature (see, e.g., [286]).

6.3 Concluding remarks

Due to the lack of a comprehensive understanding of the mechanisms at play during the formation of a LSB, increasing the performance of engineering devices requires simple and efficient predictive tools. In this work, we presented a detailed investigation of entropic multi-relaxation time models and its applications to transitional flows. The simulations show that the

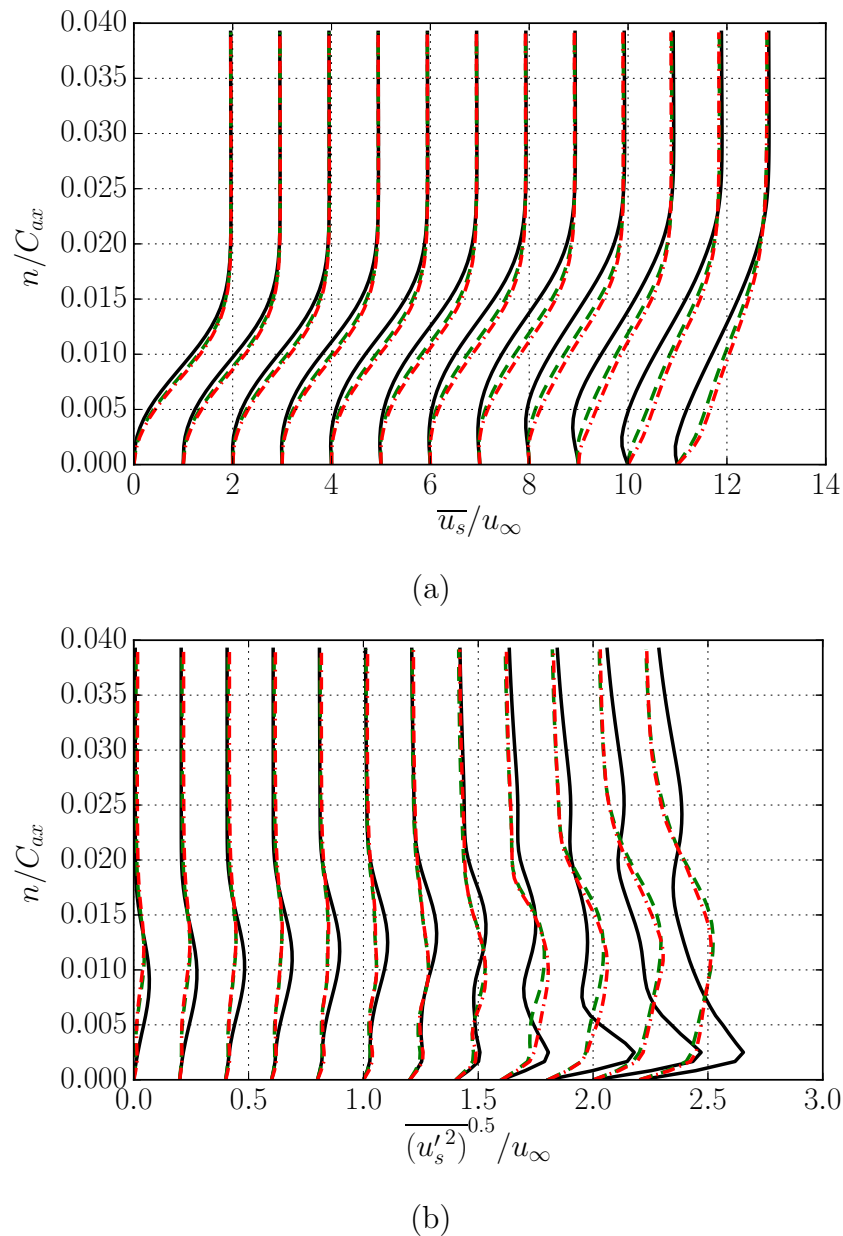


Figure 6.19: Streamwise velocity profiles (tangent to the suction side of the blade surface) as a function of the normal distance for $x/C_{ax} = 0.88 - 0.99$ in steps of $0.1C_{ax}$ at $Re = 6 \cdot 10^4$. (a): Mean streamwise velocity. (b): Rms streamwise velocity. For the legend see figure 6.18.

KBC model together with Grad's boundary conditions is capable of accurately capturing all features of LSB including separation, transition and unsteady reattachment. Although the implicit subgrid features of the KBC allow for a relatively coarse mesh resolution [74], accurate results were only achieved by resolving the reverse flow region on the airfoil surface. To meet these resolution requirements, an appropriate grid refinement technique is

crucial.

Thus, we have shown that the KBC model in combination with appropriate boundary conditions and grid refinement strategies is a robust, parameter-free and accurate alternative to study complex flows of engineering interest, where a simple grid refinement study is sufficient to ensure the validity of the simulation.

Chapter 7

Biocomotion

7.1 Introduction

In recent years, much research effort has been devoted to understanding the propulsion mechanisms of flapping flight and undulatory fish locomotion. The surge of interest originates not only from pure biological curiosity but also serves as a rich source of inspiration to exploit these phenomena in the design of novel robotic devices (see, e.g., [81, 200, 280] and references therein).

In this chapter we extend the class of entropic lattice Boltzmann models to moving and deforming objects in three dimensions with focus on applications relevant to biomimetic fluidmechanics and animal locomotion.

Given the general validation for one and two-way coupled simulation using the classical benchmark of a falling sphere as well as the flow in engine-like geometries in previous chapters, we continue to increase the level of complexity within this chapter. We start by considering the simulation of a plunging airfoil at $Re = 40000$ in the transitional regime, where a detailed comparison with experimental and numerical studies of [233] and [356], respectively, is reported. In addition, the performance for deforming geometries is assessed on the example of a self-propelled anguilliform swimmer.

Finally, in section 7.4 we explore possible extensions by considering examples of flapping flight and multiple anguilliform swimmers.

7.2 Plunging Airfoil

In this section, we focus on the transitional flow past a plunging airfoil at a Reynolds number $Re = 40000$. Motivated to deepen our understanding of the complex physics relevant to small fliers, small unmanned air vehicles, micro air vehicles and alike, this setup was recently investigated experimentally and numerically in the works of [233, 263, 356]. Analogous to small fliers, the flow is mainly characterized by the formation of dynamic-stall vortices on the leading edge due to the large induced angle of attack. As detailed in chapter 6, the transitional flow regime is particularly demanding for turbulence models as a high-Reynolds number analysis may not be valid in the presence of both laminar and turbulent flow. This gives us the opportunity to test the combination of the KBC model and the implementation of moving boundaries to its full extent. Notable is the recent study from [356] using an implicit Large-Eddy simulation (ILES, see, e.g., [219, 220] for details and the rationale of ILES) with high-order compact schemes for the spatial derivatives needed to capture the transitional processes accurately and a Pade-type low-pass filter to gain stability.

In particular and as shown in figure 7.1, the flow past a plunging SD7003 airfoil with a static angle of attack $\alpha_0 = 4$ is considered in the following. The airfoil is resolved by $L = 400$ lattice points using two levels of block-refinement near the airfoil and a domain of $[10L \times 5L \times 0.2c]$ in the streamwise, lateral and spanwise direction, respectively. Same as in [356], a sinusoidal plunging motion of the airfoil is prescribed with a plunging amplitude of $h_D = 0.05c$ and a reduced frequency of $k = \pi fc/u_\infty = 3.93$ as

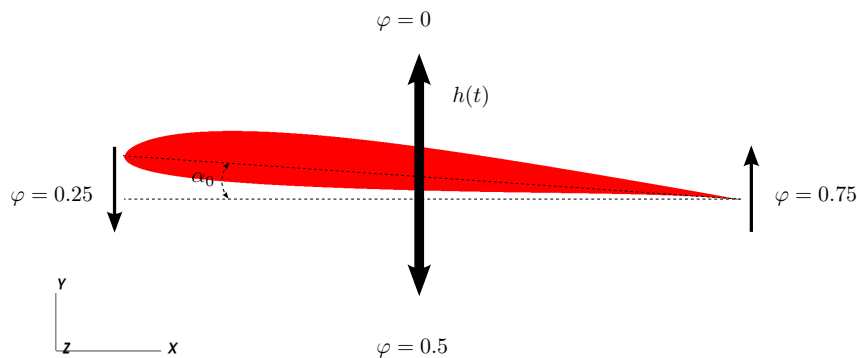


Figure 7.1: Schematic of a plunging airfoil.

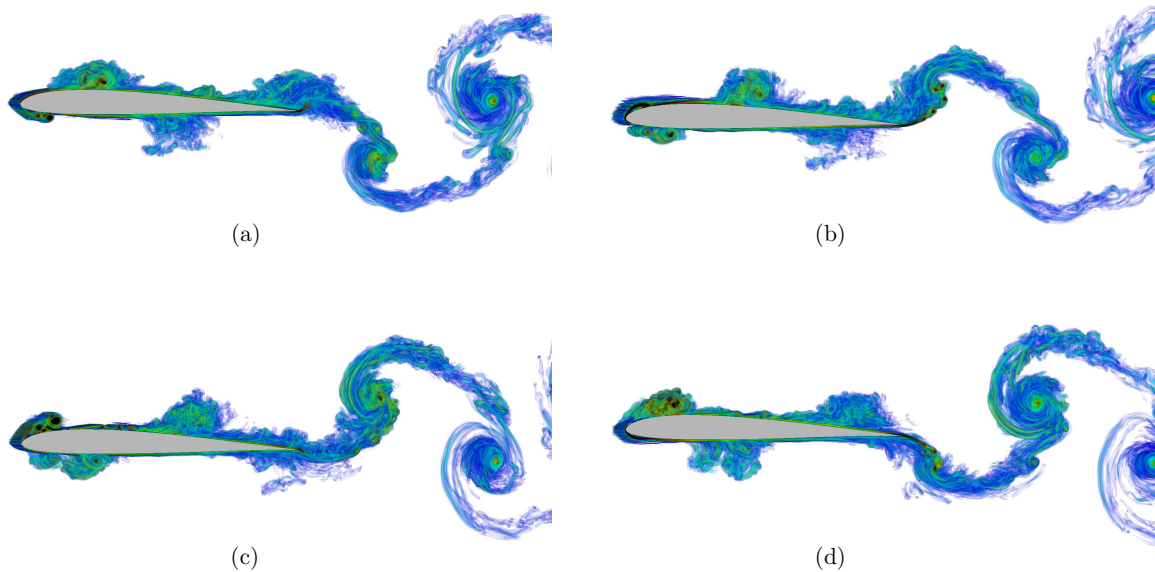


Figure 7.2: Volume rendering of vorticity for various phases of the plunging airfoil. (a): $\varphi = 0$. (b): $\varphi = 0.25$. (c): $\varphi = 0.5$. (d): $\varphi = 0.75$.

$$h(t) = \frac{h_D}{c} \sin(2kF(t)), \quad (7.1)$$

where

$$F(t) = 1 - e^{at}, \quad a = 4.6/2 \quad (7.2)$$

is an initial delay function to achieve a smooth transition from the resting airfoil to the plunging motion and the time t_{lb} in lattice units is non-dimensionalized as $t = t_{lb}u_\infty/c$. This corresponds to an induced angle of attack $\alpha = 21.5$, which is sufficient for the formation of unsteady leading-edge separation and dynamic-stall-like vortices.

Capturing the main flow features occurring during the periodical motion of the airfoil, figure 7.2 shows four volume renderings of the instantaneous vorticity for phase angles of $\varphi = \{0, \frac{1}{4}, \frac{1}{2}, \frac{3}{4}\}$, corresponding to maximum upward displacement, maximum downward velocity, maximum downward displacement and maximum upward velocity, respectively (see also figure 7.1). At the beginning of a new cycle, at a position of maximum upward displacement, the boundary layer near the leading-edge appears laminar and attached to the surface (see figure 7.2a). At later times, caused by the downward acceleration, an emerging flow separation can be observed at the leading-edge (see figure 7.2b). At bottom dead cen-

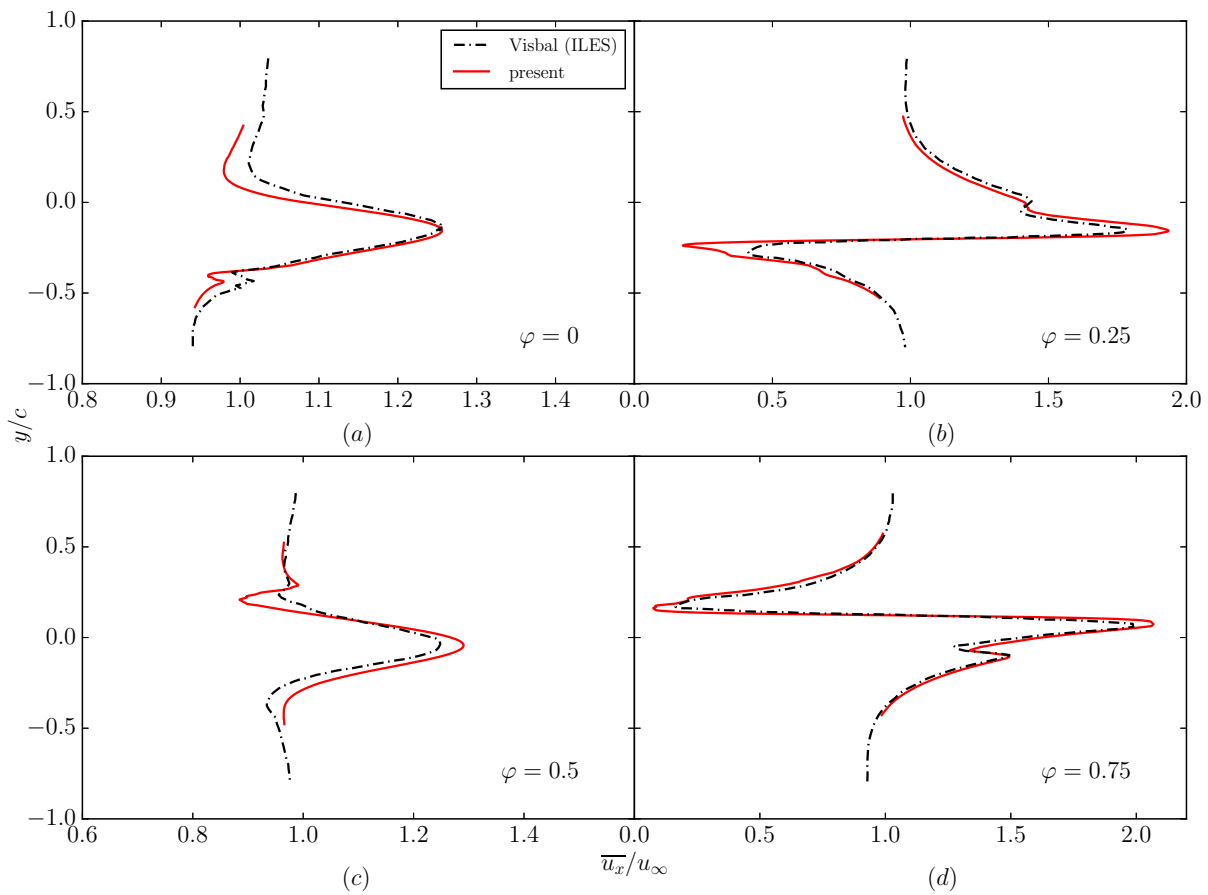


Figure 7.3: Phase-averaged velocity profiles at $x/c = 1.5$.

ter (BDC), the flow is fully separated at the leading-edge on the upper surface of the airfoil, causing the formation of two coherent vortices (see figure 7.2c). However, due to spanwise instabilities, these vortices break down into three dimensional, fine-scale turbulence during the subsequent upward acceleration (see figure 7.2d). While diffusing and annihilating, these vortices propagate close to the airfoil surface during the following cycle. Note that due to the high frequency, a new pair of vortices is formed before the vortex pair of the previous cycle is shed from the trailing edge. Identical but less pronounced is the flow structure on the lower surface of the airfoil, where the large negative motion-induced angle of attack causes the formation of two coherent vortex structures, which subsequently break down into turbulence. Similar observations were reported by [356].

More quantitatively, in figure 7.3, we compare the phase-averaged velocity profiles in the near wake of the airfoil at $x/c = 1.5$ with the study of [356]. In total 25 cycles were computed and the first ten were neglected in the

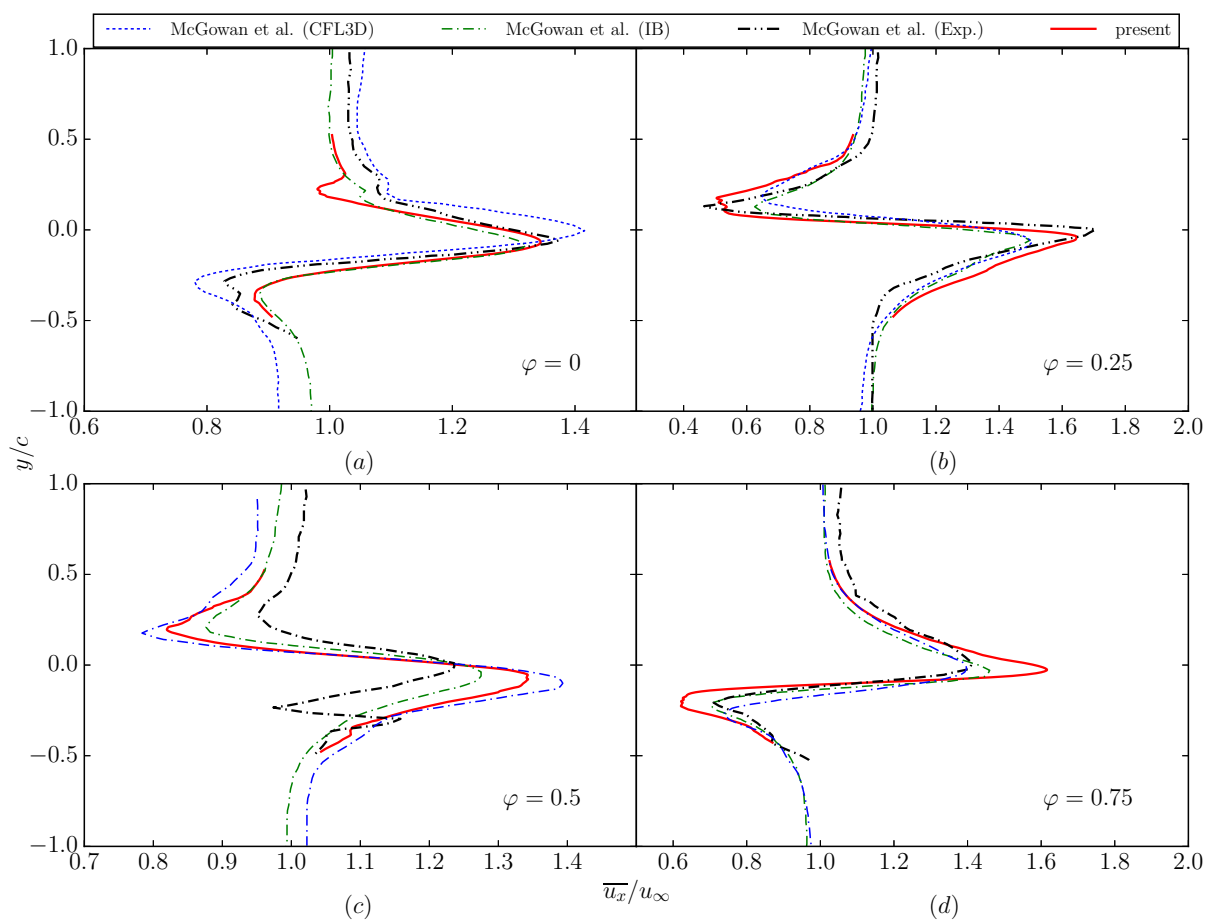


Figure 7.4: Phase-averaged velocity profiles at $x/c = 2$.

accumulation of statistics to avoid accounting for the initial transient. It is apparent that the main flow features are captured for both simulations and the agreement is good. The location of the minimum and maximum of the flow velocity agree well but differ slightly in terms of magnitude. The present simulation exhibits larger velocity magnitudes in comparison with the more smoothed ILES simulation. In addition, a comparison at a location further downstream at $x/c = 2$ with an experimental investigation using Particle Image Velocimetry (PIV), an immersed boundary method and the NASA-CFL3D code from the study of [233] is shown in figure 7.4. It is apparent that due to the complexity of the problem all data have notable discrepancies but the agreement of the present study with the experiment is reasonable.

Finally, we compare the evolution of the aerodynamic forces for three selected cycles with [356] in figure 7.5. The lift coefficient is defined as

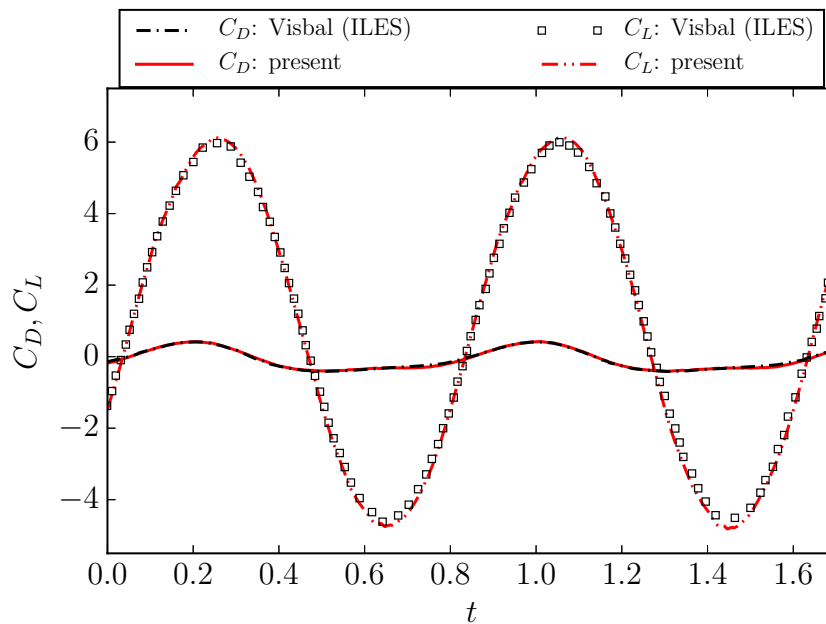


Figure 7.5: Evolution of lift and drag coefficient over three exemplary cycles of a plunging airfoil.

$C_L = F_L / (1/2 \rho u_\infty^2 c L_s)$, where F_L is the total lift force acting on the airfoil and L_s is the extent in spanwise direction. Analogously, the drag coefficient is given by $C_D = F_D / (1/2 \rho u_\infty^2 c L_s)$, where the drag force is denoted by F_D . As shown in figure 7.5, the lift coefficient C_L is dominated by the prescribed motion of the airfoil and has a large amplitude. On the other hand, the amplitude of the drag coefficient is much smaller but notably there is a net mean thrust corresponding to a mainly negative drag coefficient. The comparison with the ILES is excellent.

7.3 Anguilliform Swimmer

In the field of bio-fluidmechanics, the topic of aquatic animal propulsion mechanisms is much discussed among biologists, neuro-scientist as well as engineers trying to mimic these mechanisms to increase efficiency in technical applications (see, e.g., [86, 145, 348]). However, due to the complex interaction between the fluid and the deformable body of the animal, fundamental questions regarding thrust generation and its relation to the kinematics of the swimmer's body, the efficiency and viscous effects remain controversial. In particular, investigations of the undulatory propul-

sion mechanisms of anguilliform fish (e.g.: *Anguilla anguilla*) started with the pioneering work of [120]. In contrast to carangiform fish, anguilliform swimmers generate thrust by passing a transverse wave down their body and therefore utilizing, to a varying degree, the whole body for thrust generation and not just the tail. The hydrodynamics of aquatic locomotion for undulatory swimmers was studied for inviscid flow in the works of [57, 132, 205–208, 373]. Simple algebraic models predict a reverse von Kármán vortex street for optimized swimming performance, where the wake consists of a double row of single vortices when the ratio of the swimming speed and the body wave speed is less than one [206]. On the experimental side, Particle Image Velocimetry (PIV) has proven itself as a valuable tool to quantify the flow field generated by the swimmer. The first visualization using two-dimensional PIV for freely swimming juvenile eel was reported by [249]. They found a linearly increasing flow velocity from head to tail, suggesting continuous thrust generation along the body. In the wake, they observed a double row of double vortices with little backward momentum, which is generated by a start-stop vortex shed from the tail and a separate vortex produced along the body, so-called proto-vortices, for each half tail-beat. They conjectured that the wake morphology is caused by a phase lag between the primary start-stop vortex and the body-generated circulation. Subsequent studies using high-resolution PIV were conducted by [348]. Their results were, in general, similar to [249] but differences were noticed regarding the proto-vortices. Only a negligible phase lag with low vorticity was reported, resulting in a single, combined primary start-stop vortex per half tail-beat. The discrepancies were attributed to the lower PIV resolution and the seemingly accelerating eel in [249] compared to the steadily swimming fish in [348]. In the work of [348], they stated the following mechanism for the generation of the wake: A primary start-stop vortex is shed when the tail changes direction. Due to the acceleration of the tail from one side to the other, a low pressure region develops in the posterior part of the body, drawing fluid in the lateral direction, which is shed off the tail and stretches the primary vortex into an unstable shear layer which rolls up into two separate, co-rotating vortices, which they termed the secondary vortex. Thus, the primary vortex from one half tail beat and the secondary vortex from the subsequent comprise the boundaries of each lateral jet. Notable was the lack of any significant downstream flow

for steady swimming as previously observed for carangiform fish and interpreted as thrust generation mechanism. This was further supported by the observation of only a slight upstream inclination of the lateral jets.

On the numerical front, only a few detailed studies may be found in literature (see , e.g., [34, 35, 47, 166]). The first two-dimensional viscous flow simulations of self-propelled anguilliform fish were reported in the work of [47]. In contrast to the experimentally observed wake morphology, these simulations indicated a single, large vortex ring wrapping around the eel, resulting in an upstream flow, where thrust is almost exclusively produced along the body and not the tail tip. Three dimensional simulations were recently conducted by [166] using the finite volume approach of the commercial software package STAR-CD with a first-order discretization in time and second-order in space. Apart from prescribing a reference motion of the fish, as proposed by [47], an evolutionary algorithm was employed to obtain the body motion as a result of optimizing for burst swimming speed and efficiency. Their results indicate that large amplitude tail undulation in combination with a straight anterior body produce most of the thrust at the tail and are optimal kinematics in the burst swimming mode. On the other hand, optimal kinematics for efficient swimming were obtained for an undulation of the entire body, where thrust is generated with half the body and not just the tail. For all swimming patterns, the wake morphology did not differ qualitatively and is in agreement with the experimental observations of [348], exhibiting a double row of single vortex rings with lateral jets.

Despite the valuable contributions mentioned above, further quantitative analysis is needed for conclusive results. The ease of data extraction, its analysis and the precise control over the body's kinematics make numerical experiments useful for these studies. However, issues related to deforming geometries and the complex fluid-structure interaction are challenging for numerical solvers, thus explaining the sparsity of these simulations in literature. The KBC model on the other hand is a highly efficient approach, which allows for a simple implementation of complex, deforming bodies using the Grad boundary condition on Cartesian meshes and is therefore ideally suited for this type of problem. This, combined with the enhanced stability of KBC models compared to LBGK, the intrinsic parallelizability and efficiency of LBM as well as a suitable block-refinement scheme

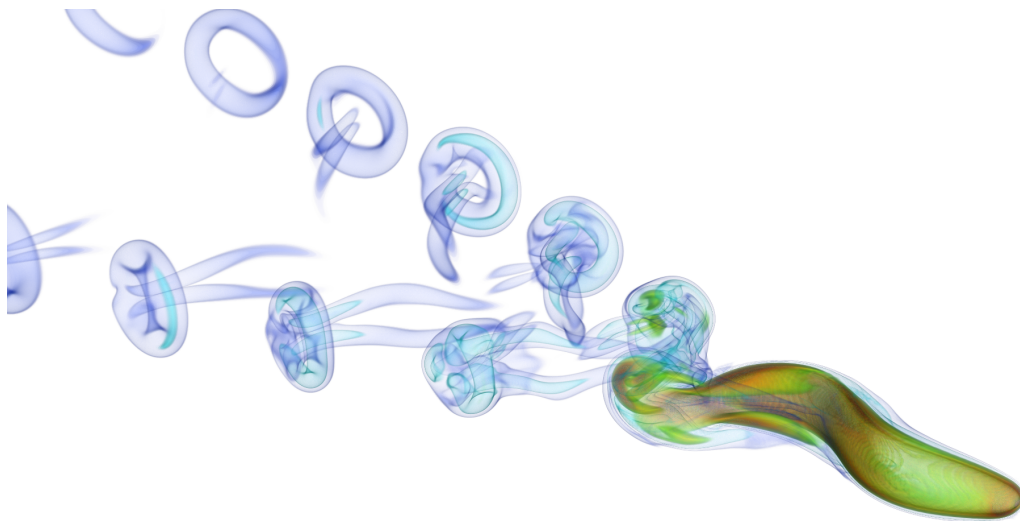


Figure 7.6: Volume rendering of vorticity of the swimmers wake, showing the typical double row vortex street.

make these promising tools for DNS investigations of such complex flows. Therefore, as a first step to assess the predictive capabilities of the proposed scheme, we conduct a simulation of a self-propelled anguilliform swimmer analogous to [166].

Geometrically, the body of the anguilliform swimmer with length L is modeled by spatially varying ellipsoidal cross sections as in [166] for which the half axes $w(s)$ and $h(s)$ are defined as analytical functions of the arc-length s as

$$w(s) = \begin{cases} \sqrt{2w_h s - s^2} & 0 \leq s < s_b, \\ w_h - (w_h - w_t) \left(\frac{s-s_b}{s_t-s_b} \right)^2 & s_b \leq s < s_t, \\ w_t \frac{L-s}{L-s_t} & s_t \leq s \leq L, \end{cases} \quad (7.3)$$

where $w_h = s_b = 0.04L$, $s_t = 0.95L$ and $w_t = 0.01L$. For the height $h(s)$ an elliptical curve is prescribed as

$$h(s) = b \sqrt{1 - \left(\frac{s-a}{a} \right)^2}, \quad (7.4)$$

where the half axes are given as $a = 0.51L$ and $b = 0.08L$. As proposed by [47], the swimmer undergoes a prescribed time-dependent lateral deforma-

tion of the body's center-line as

$$y(s, t) = 0.125\beta L \frac{s/L + 0.03125}{1.03125} \sin \left(2\pi \left(\frac{s}{L} - \frac{t}{T} \right) \right), \quad (7.5)$$

where T is the undulation period and β is an initial ramping function to assure a smooth transition from the initially resting body according to

$$\beta = \begin{cases} \frac{1 - \cos(\pi t/T)}{2} & 0 \leq t \leq T, \\ 1 & t > T. \end{cases} \quad (7.6)$$

The feedback from the fluid onto the body is prescribed by Newton's equations as

$$m_s \ddot{\mathbf{x}}_s = \mathbf{F} \quad (7.7)$$

$$\frac{d\mathbf{I}_s \boldsymbol{\omega}_s}{dt} = \boldsymbol{\omega}_s \dot{\mathbf{I}}_s + \mathbf{I}_s \dot{\boldsymbol{\omega}}_s = \mathbf{M}, \quad (7.8)$$

where m_s , \mathbf{I}_s , \mathbf{x}_s , $\boldsymbol{\omega}_s$ are the mass, the inertia tensor, the center of mass and the angular velocity, respectively. The force and torque acting from the fluid onto the object are denoted by \mathbf{F} and \mathbf{M} , respectively. As in the work of [166], the complexity of the system is reduced by only considering the torque corresponding to the yaw.

In the framework of the LB simulation, the geometrical model is represented as a triangulated surface composed of elliptical disks along the center-line. The center-line was decomposed into 150 segments, which has proven to be sufficient. This allows for a straightforward computation of all geometrical properties including the time derivative of the inertia tensor. The velocity at the intersection points, needed for the boundary conditions, was computed based on a finite-difference scheme and a barycentric interpolation for the given time-dependent deformation. As above, the equations of motion are solved using an Euler integration scheme. Higher-order integration schemes have been tested but marginal differences were observed due to the relatively small time step used. Further, no smoothing or low-pass filtering of the hydrodynamic forces were applied, unlike in [166].

The simulations are carried out in a domain of $[8L \times 4L \times L]$, the swimmer is resolved by $L = 200$ lattice points and the undulation period is taken

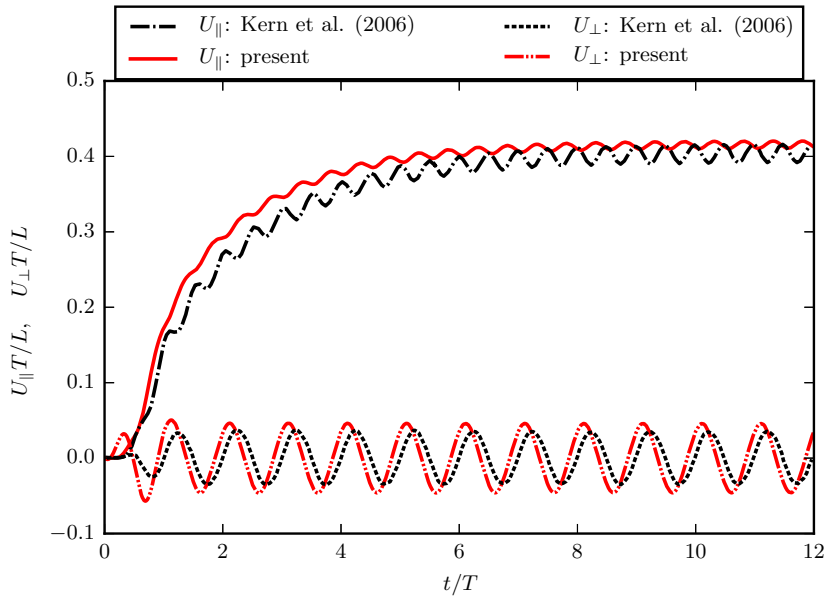


Figure 7.7: Temporal evolution of the forward velocity U_{\parallel} and lateral velocity U_{\perp} .

to be $T = 10^4$ lattice time steps. Same as in the reference, the Reynolds number is taken as $\text{Re} = (L^2/T)/\nu = 7142$.

A volume rendering of vorticity shows the wake of the swimmer in figure 7.6. In agreement with [166, 347, 348], the wake consists of a double row of single vortices. Furthermore, we confirm the measurements from [348] and observe a primary vortex being shed from the tail when it changes direction. The fluid drawn in lateral direction by the accelerating tail and the development of two separate co-rotating vortices as a result of an unstable shear layer roll-up can also be seen in figure 7.6.

Quantitatively, we compare the evolution of the forward and the lateral velocity of the swimmer in figure 7.7. Overall, the agreement is good. Minor discrepancies are observed during acceleration but are attributed to different ramping functions used here, Eq. (7.6), and in [166]. The differences in the asymptotic forward and lateral velocity are within the range of expectation due to the different evolution algorithms. While [166] report an asymptotic forward velocity of $\bar{U}_{\parallel} = 0.4$ with an amplitude of 0.01, the present simulation yields $\bar{U}_{\parallel} = 0.415$ with an amplitude of 0.005. The lateral velocity U_{\perp} has a zero mean for both the reference and the present simulation. An amplitude of 0.046 is measured in the present simulation whereas [166] measure 0.03. All simulations were checked for grid independence.

7.4 Outlook and possible extensions

Robustness and accuracy of the proposed numerical scheme has been demonstrated in previous sections and opens the door for further investigations. In this section we provide a brief overview of possible extensions and directions of future research, which may be pursued with the proposed approach.

7.4.1 Flapping flight

While the plunging airfoil in section 7.2 does exhibit characteristics of small fliers, namely the formation of dynamic-stall vortices on the leading edge, extraordinary stability and maneuverability for flapping flight has been observed for animals ranging from insects such as fruit flies to bats and birds. These properties make flapping flight an interesting candidate for biomimetic robotic devices (see, e.g., [200]). Thus, understanding the aerodynamics, kinematics as well as the sensory system has been focus of much recent research (see, e.g., [27, 70, 293, 299, 328, 385] and [328] for a review). While in-vivo or robotic measurements [71, 201] have been key to understand basic principles of kinematics and force generation, their limitations in terms of controllability or accessibility make numerical simulations a valuable tool to advance this challenging field.

To test our approach in this field of application, some preliminary simulations have been conducted.

First, simulations of a flapping *Drosophila* wing, with the kinematics as given by [28, 115, 303], were performed. Geometrically, a planar wing with an elliptical cross-section of thickness $0.12c$ and the chord length c was

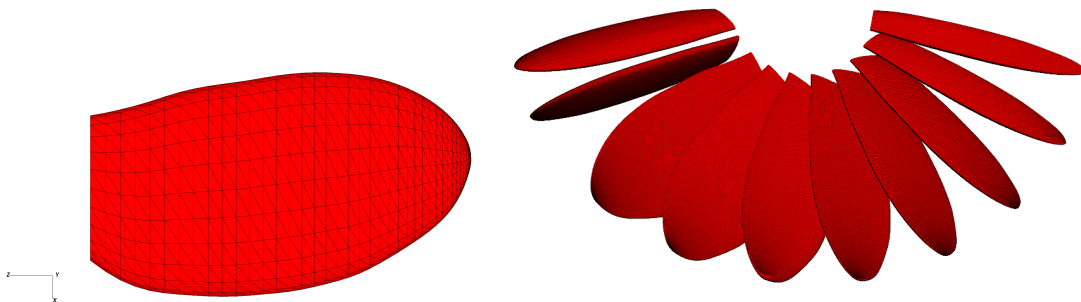


Figure 7.8: Left: Wing planform. Right: Wing kinematics during the upstroke.

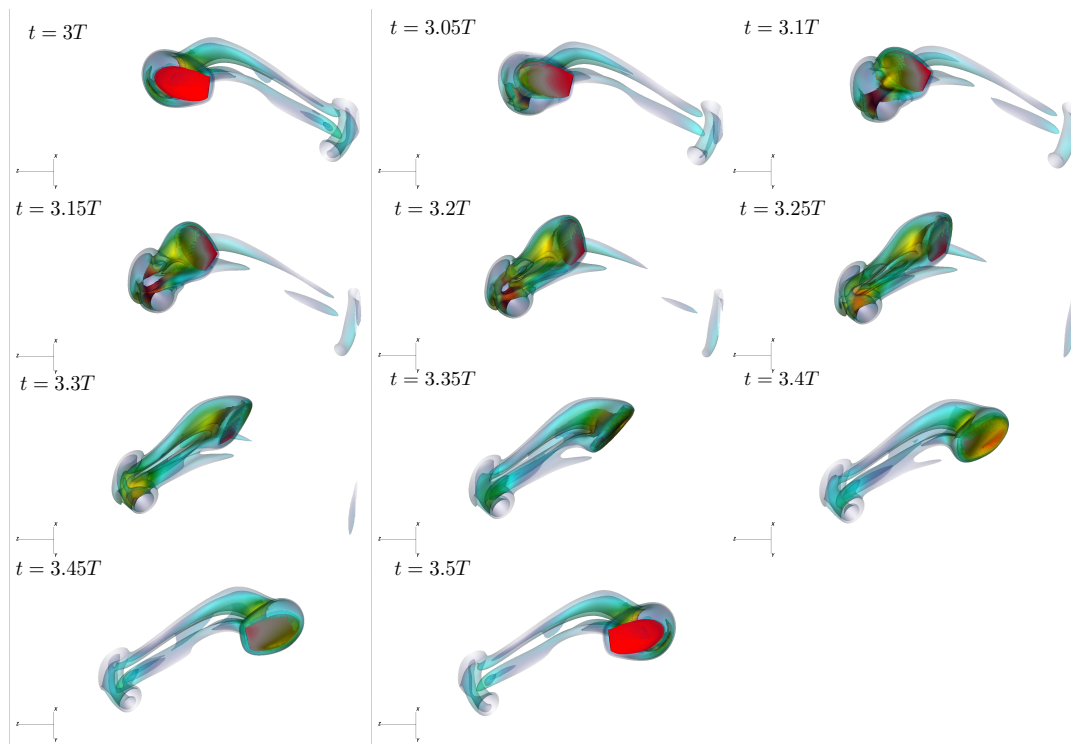


Figure 7.9: Volume rendering of vorticity for a *Drosophila* wing during the upstroke of the third cycle.

employed. As no data of the exact wing geometry was reported, a visually similar planform as in [115] was reproduced (see figure 7.8). The wing undergoes a prescribed flapping motion, which is defined by the evolution of the stroke position $\phi(\tau)$, the angle of attack $\alpha(\tau)$ and the stroke deviation $\theta(\tau)$. While no stroke deviations are considered, i.e. $\theta(\tau) = 0$, the angle of attack is described by a trapezoidal wave function, leading to a constant angle of attack. At stroke reversal, a smooth transition is achieved by prescribing the angular velocity as

$$\dot{\alpha}(\tau) = 0.5\alpha_0(1 - \cos(2\pi(\tau - \tau_0)/\Delta\tau_r)), \quad \tau_0 \leq \tau \leq \tau_0 + \Delta\tau_r, \quad (7.9)$$

where $\tau_0 = 0.26T$ is the flip start, $\Delta\tau_r = 0.24$ the flip duration and $\alpha_0 = 45^\circ$ is the mid-stroke angle of attack.

As in [28, 303], the position of the wing within the stroke plane is described by a smoothed triangular wave form, leading to a constant translational velocity for each half-stroke. The smoothing was realized by prescribing

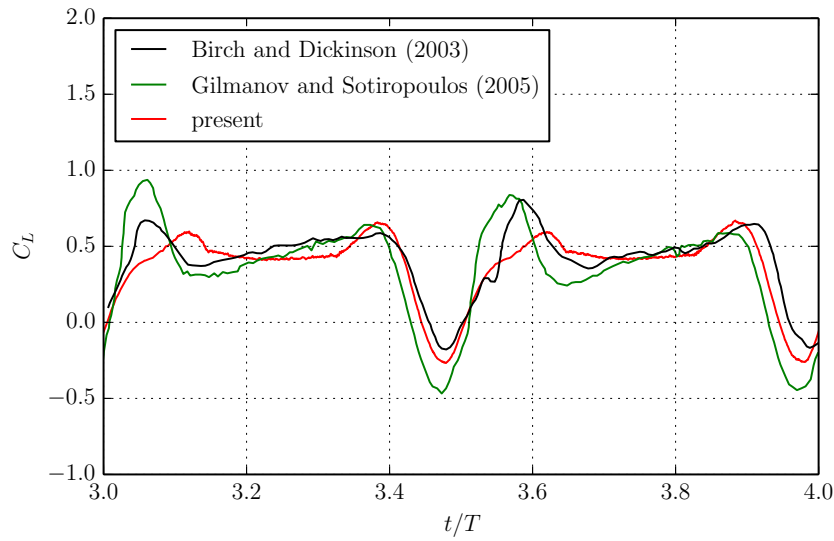


Figure 7.10: Evolution of the lift coefficient and comparison to experimental and numerical data.

an angular velocity as

$$u_t(\tau) = u_{\tau,0} \cos(\pi(\tau - \tau_1)/\Delta\tau_t), \quad \tau_1 \leq \tau \leq \tau_1 + \Delta\tau_t, \quad (7.10)$$

where $\tau_1 = 0.42T$ and $\Delta\tau_t = 0.16T$. The total stroke angle is given by $\phi = 160^\circ$ and T is the stroke period (up- and downstroke). The Reynolds number is taken as $\text{Re} = L_0 U_0 / \nu = 160$, where the wing length is $L_0 = 0.19\text{m}$ and the velocity $U_0 = 0.166\text{m/s}$, which is measured at $0.65L_0$ from the wing base. Further, the distance between the wing tip and the center of rotation is taken to be $L_{Tip} = 0.25\text{m}$. The simulation was evolved for four full stroke cycles during which we measured the lift forces. A visual representation of the wing kinematics during the upstroke and the induced flow field during the third cycle is shown in figure 7.8 and figure 7.9, respectively. As in the references, the lift force is defined in the direction of gravity. For no stroke deviation the radial force is zero. The evolution of the lift force during the third cycle is compared to the numerical and experimental references in figure 7.10.

It is apparent that the main flow features are captured well. Discrepancies compared to the experimental apparatus are observed but are of the same order than the numerical reference. It is conjectured that these deviations originate from the different wing geometries and thus kinematics. It would be interesting to further pursue this set-up in collaboration with an experimental group using the identical wing geometry.

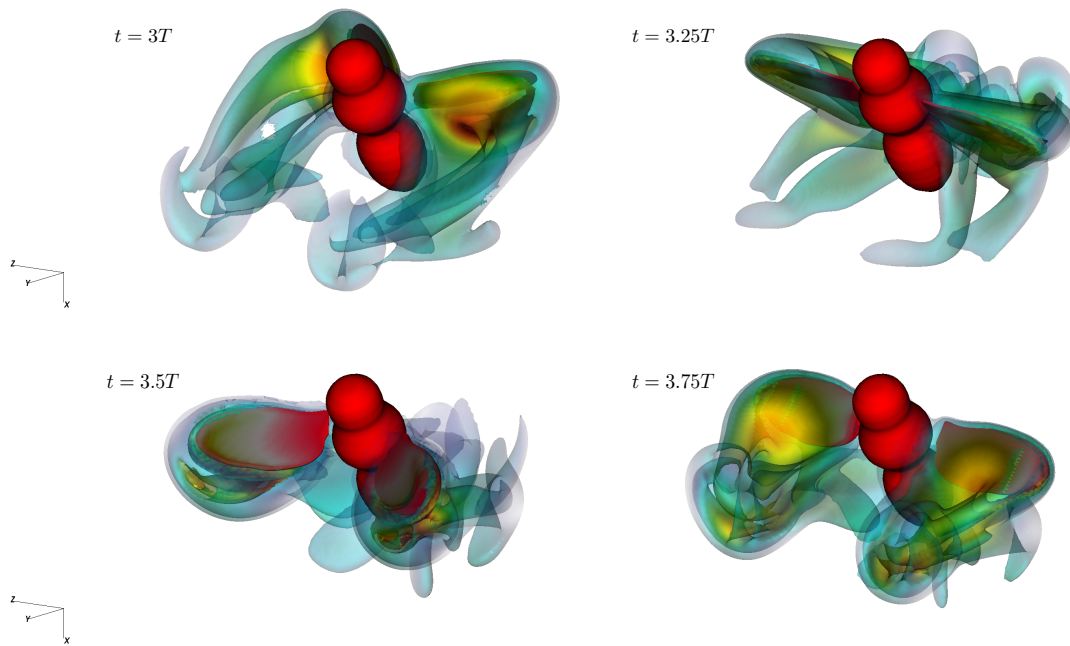


Figure 7.11: Volume rendering of vorticity for a body-wing assembly during the third stroke.

A natural extension of these simulations is to extend the set-up to a full wing-body assembly. A preliminary simulation is shown in figure 7.11 using identical parameters as in the previous case. Possible extensions include modeling elasticity effects of the wings [385] as well as full two-way coupled simulations using a controller or optimization algorithms to study stability and maneuverability properties. As also discussed in the next section for anguilliform swimmers, employing reinforcement learning techniques in combination with deep neural networks might also yield valuable insight into optimal wing kinematics.

7.4.2 Interaction of multiple swimmers

Based on the results of a single anguilliform swimmer in section 7.3, the framework can be extended to multiple individuals in order to investigate the interdependence of swimmers in a swarm. Feasibility of this approach was confirmed by conducting a preliminary simulation with prescribed kinematics for three individuals. An instantaneous snapshot of this set-up, showing a volume rendering of vorticity, is presented in figure 7.12.

This application addresses fundamental questions of fish schooling and its biological advantage. In literature, possible benefits such as reduced

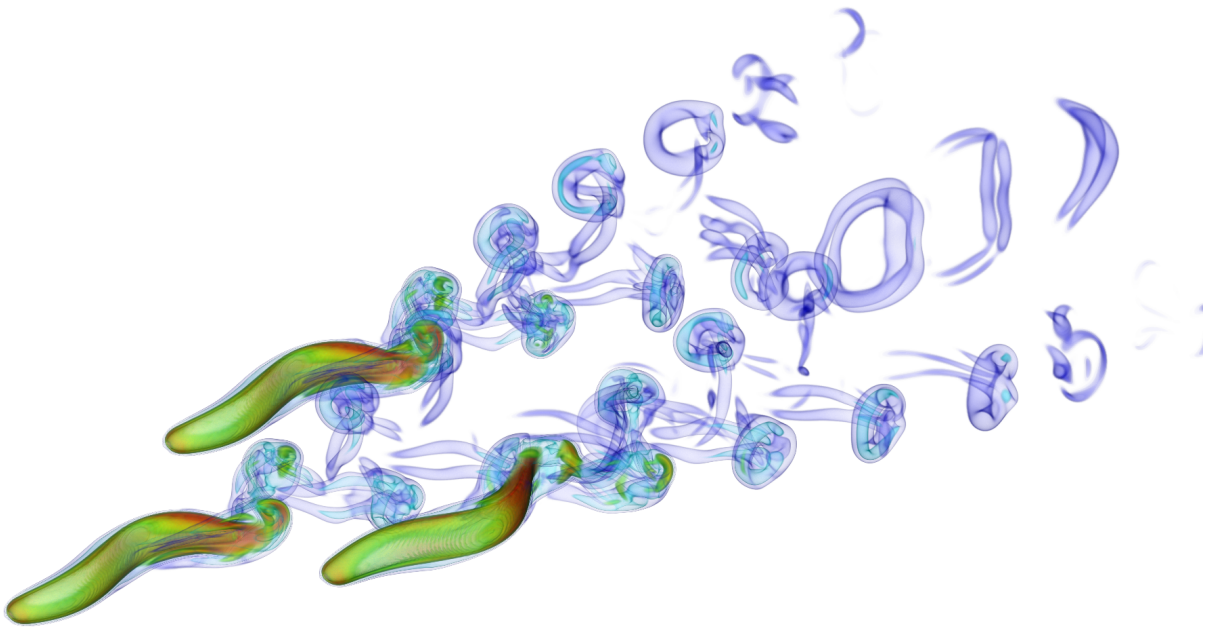


Figure 7.12: Volume rendering of vorticity of three anguilliform swimmers.

vulnerability to predators, enhanced feeding and reproduction possibilities are proposed. On the other hand, a hydrodynamical benefit of swimming in schools, where individuals can extract energy from the vortices shed by others, has been proposed [22, 204, 221, 333]. However, the evidence is by far not conclusive and requires further studies [269]. While schooling can be readily observed with natural swimmers, in simulations it is essential to equip the individuals with an appropriate behavioral model to achieve such group dynamics. Agent-based models [287] that lead to schooling or flocking rely on local interaction rules handcrafted a priori, based on empirical arguments and experimental observations [65, 144]. These models have been a key tool in helping us understand the influence of social traits in the emergence of schooling patterns [12]. However, they do not explicitly account for the flow environment [110].

Along the lines of the work [258], it would be intriguing to take advantage of recent developments in combining deep neural networks and reinforcement learning techniques [244] and incorporate it into our three dimensional simulations of multiple swimmers. This would allow us to obtain the kinematic parameters for optimal performance based on the local flow quantities. The goal here is to determine whether these kinematics, solely based on hydrodynamic and energetic arguments, will indeed yield highly

ordered formations as observed in nature or if non-hydrodynamic factors predominate. In addition, this study could have significant impact on the design of robotic control systems and actuators in a non-steady, perturbed environment.

Another interesting line of research is to investigate the affect of stiffness of body and locomotor on the performance and speed, which to date are not well understood [194, 213, 243]. In particular, recent studies [151, 194–196, 259] on passive and active flexible foils, mimicking undulatory body motion of fish, suggest that a key characteristic of efficient propulsion systems is the use of flexible materials or combinations of them. Notable is the experimental study [151], where actively controlled pneumatic actuators were attached to a flexible foil. A numerical study using the KBC in combination with the fully coupled fluid-structure interaction solver as presented in chapter 8, might shed light on these mechanisms.

7.5 Conclusion

In this chapter we have presented a thorough study of the entropic multi-relaxation time model in combination with the Grad boundary condition for moving and deforming objects in three dimensions. First, accuracy and robustness of the proposed method were assessed in the simulation of a plunging airfoil in the transitional regime. The comparison with literature revealed excellent agreement in all quantities including phase-averaged velocity profiles in the near wake region as well as the evolution of aerodynamic loads, important for realistic two-way coupled simulations. Finally, for deforming objects, the simulation of an anguilliform swimmer was considered and validated by comparison to the numerical investigations of [166].

These simulations, together with previous chapters, establish the predictive capabilities of KBC models for complex, moving and deforming objects, where a simple grid-convergence is sufficient to assert their validity. This opens interesting directions of further research and possible extensions to flapping flight or fish schooling have been outlined in section 7.4.

Having focused on prescribed deformations in this section, we will continue with elastically deforming objects and fully coupled fluid-structure interaction in the following chapter.

Chapter 8

Fluid-structure interaction

8.1 Introduction

Fluid-structure interaction (FSI) is of significant interest in science and engineering applications, where examples include aeroelasticity such as flutter and buffeting [18, 23, 93, 357], or bio-fluidmechanics in order to enhance our understanding of the flow through the cardiovascular system, cell aggregation as well as blood-heart interaction [66, 284]. Insight in these phenomena through experimental and numerical studies has shown tremendous success, for example, in the development of cancer diagnostic devices the size of a chip [181, 302], optimizing wind turbines [18], or in artificial heart valves [37]. Yet, such problems remain a challenge to existing methods due to strong nonlinearity and their multidisciplinary nature [80].

In general, there are two main avenues to numerical FSI simulations, namely, monolithic and partitioned approaches. The monolithic approach describes the fluid and the structural part with the same discretization scheme in one system of equations, which is solved simultaneously with a single solver. This technique implies consistent fluid-structure interface conditions. On the other hand, in most practical applications the partitioned approach is employed, which uses separate solvers for the fluid and structural parts, respectively. The advantage of this approach is its modularity, which allows the use of independently optimized solution strategies in the solid and fluid domain, respectively. Thus partitioned approaches

are most common and therefore are the focus of this chapter. On the other hand, consistent solid-fluid interface conditions are not satisfied implicitly and thus pose the main challenge of partitioned fluid-structure approaches. Most conventional FSI schemes are based on body-fitted grids, where the interface conditions are treated as boundary conditions and the computational mesh conforms to the moving and deforming solid-fluid interface. While the interface conditions are easily imposed, the generation of the moving meshes for complex geometries undergoing large, unprescribed deformations is non-trivial and requires sophisticated procedures to avoid severe mesh distortion to preserve accuracy [130, 251, 338, 340] (see also chapter 3 for a discussion). Viable alternatives are found in non-conforming methods, such as the LBM.

Armed with the encouraging results from previous chapters, the KBC model is employed to solve the fluid part of the FSI algorithm. The structural domain on the other hand is described by a geometrically nonlinear total Lagrangian formulation in the framework of the finite element method (FEM).

Thus, in this chapter, we extend the KBC model, the Grad boundary condition and the block-refinement scheme to fluid-structure interaction problems involving large deformations and assess its predictive capabilities. Apart from thorough validation by comparison to standard benchmarks, the robustness of the scheme allows us to explore its capabilities in multiphysics applications, where we present a novel multiphase formulation of the entropic multi-relaxation time model and its coupling to the structural solver.

The chapter is structured as follows: We begin by introducing the numerical methodology to solve the governing equations of the solid domain. Next, we discuss the coupling methodology between fluid and solid part through the Grad boundary condition. Finally, in section 8.3, we report the numerical results obtained by the proposed scheme. We start by a thorough validation of the model in section 8.3.1 and subsequently present the extension of the FSI scheme to multiphase flows in section 8.3.2.

8.2 Numerical approaches

In the following we briefly describe the numerical methodology of the elastic solid as well as the fluid-solid coupling methodology. The subscripts f and s are used to indicate the fluid and structural quantities, respectively. The time-dependent fluid and solid domains with their common interface are denoted by Ω_f^t , Ω_s^t and $\Gamma_I^t = \partial\Omega_f^t \cap \partial\Omega_s^t$, respectively. The corresponding reference or initial domains and the interface are referred to as Ω_f , Ω_s and $\Gamma_I = \partial\Omega_f \cap \partial\Omega_s$, respectively. Furthermore, Neumann and Dirichlet boundary conditions are indicated by Γ_N and Γ_D , respectively.

8.2.1 Structural modeling

In the Lagrangian frame, the structural part is governed by the momentum equation as

$$\begin{aligned} \rho_s \frac{\partial \mathbf{u}_s}{\partial t} - \nabla \cdot \mathbf{P}_s &= \rho_s \mathbf{b}_s & \text{in } \Omega_s, \\ \mathbf{u}_s &= \bar{\mathbf{u}}_s & \text{on } \Gamma_D, \\ \mathbf{P}_s \mathbf{n}_s &= \bar{\mathbf{t}}_s & \text{on } \Gamma_N, \end{aligned} \quad (8.1)$$

where \mathbf{u}_s , ρ_s and \mathbf{b}_s are the solid velocity, density and body force per unit mass. The outer normal vector of Γ_I or $\Gamma_{s,N}$ is denoted by \mathbf{n}_s . The prescribed velocities and tractions on the Dirichlet and Neumann boundary are indicated by $\bar{\mathbf{v}}_s$ and $\bar{\mathbf{t}}_s$, respectively. The first Piola-Kirchhoff stress is denoted by \mathbf{P}_s and related to the second Piola-Kirchhoff stress \mathbf{S}_s by

$$\mathbf{P}_s = \mathbf{F} \mathbf{S}_s, \quad (8.2)$$

where \mathbf{F} denotes the deformation gradient

$$\mathbf{F} = \mathbf{I} + \nabla \mathbf{d}_s \quad (8.3)$$

and \mathbf{d}_s is the displacement field of the solid. The second Piola-Kirchhoff stress, on the other hand, can be mapped to the Cauchy stress tensor $\boldsymbol{\sigma}_s$ by

$$\mathbf{S}_s = J \mathbf{F}^{-1} \boldsymbol{\sigma}_s \mathbf{F}^{-T}, \quad (8.4)$$

where $J = \det(\mathbf{F})$. Here, we consider the hyperelastic Saint Venant-Kirchhoff constitutive equation, which extends linear elastic models to

the geometrically nonlinear regime and defines the second Piola-Kirchhoff stress as

$$\mathbf{S}_s = \lambda \text{tr}(\mathbf{E}) \mathbf{I} + 2\mu_s \mathbf{E}, \quad (8.5)$$

where

$$\mathbf{E} = \frac{1}{2}(\mathbf{F}^T \mathbf{F} - \mathbf{I}) = \frac{1}{2}(\nabla \mathbf{d}_s + \nabla \mathbf{d}_s^T + \nabla \mathbf{d}_s^T \nabla \mathbf{d}_s) \quad (8.6)$$

is the Green-Lagrangian strain tensor. The first and second Lamé coefficients are indicated by λ_s and μ_s , respectively and are related to Young's modulus E_s and Poisson's ratio ν_s as

$$\nu_s = \frac{\lambda_s}{2(\lambda_s + \mu_s)}, \quad E_s = \frac{\mu_s(3\lambda_s + 2\mu_s)}{\lambda_s + \mu_s}. \quad (8.7)$$

In the present work, we employ a two-field formulation and solve for the displacement field separately using the kinematic compatibility condition

$$\begin{aligned} \frac{\partial \mathbf{d}_s}{\partial t} - \mathbf{u}_s &= 0 \quad \text{in } \Omega_s, \\ \mathbf{d}_s &= \bar{\mathbf{d}}_s \quad \text{on } \Gamma_D, \end{aligned} \quad (8.8)$$

where $\bar{\mathbf{d}}_s$ denotes the prescribed displacement on the Dirichlet boundary. The structural equations are solved using the finite element method (FEM), which we implemented using the open-source library deal.ii [15]. We follow standard FEM procedures, see, e.g., the textbooks [20, 170] or in the context of monolithic FSI with deal.ii [290, 363, 364]. Using the conventional notation for Lebesgue and Sobolev spaces, we define the following functional spaces for trial and weighting functions:

$$\mathcal{L} := \{\mathbf{w}_s \in L^2(\Omega_s)\}, \quad (8.9)$$

$$\mathcal{V}_0 := \{\mathbf{w} \in H^1(\Omega_s) : \mathbf{w} = 0 \text{ on } \Gamma_{s,D} \subset \Omega_s\}, \quad (8.10)$$

$$\mathcal{V}_D := \{\mathbf{w} \in H^1(\Omega_s) : \mathbf{w} = \mathbf{w}_{s,D} \text{ on } \Gamma_{s,D} \subset \Omega_s\}, \quad (8.11)$$

where L^2 and H^1 denote the Lebesgue space of square integrable functions and the first Sobolev space, respectively. Furthermore, the short-hand notations (\cdot, \cdot) and $\langle \cdot, \cdot \rangle$ indicate the scalar product on the L^2 -space and its boundary, respectively. Thus, following standard procedures, we obtain the following variational formulations for $\{\mathbf{u}_s, \mathbf{d}_s\} \in \{\mathcal{L} \times \mathcal{V}_D\}$

$$\begin{aligned} (\rho_s \partial_t \mathbf{u}_s, \boldsymbol{\psi}_{s,u})_{\Omega_s} + (\mathbf{P}_s, \nabla \boldsymbol{\psi}_{s,u})_{\Omega_s} - (\rho_s \mathbf{b}, \boldsymbol{\psi}_{s,u})_{\Omega_s} \\ - \langle \mathbf{t}, \boldsymbol{\psi}_{s,u} \rangle_{\Gamma_I \cup \Gamma_{s,N}} = 0 \quad \forall \boldsymbol{\psi}_{s,u} \in \mathcal{V}_0, \end{aligned} \quad (8.12)$$

$$(\partial_t \mathbf{d}_s, \boldsymbol{\psi}_{s,d})_{\Omega_s} - (\mathbf{u}_s, \boldsymbol{\psi}_{s,d})_{\Omega_s} = 0 \quad \forall \boldsymbol{\psi}_{s,d} \in \mathcal{L}, \quad (8.13)$$

where $\boldsymbol{\psi}_{s,u}$, $\boldsymbol{\psi}_{s,v}$, \mathbf{u}_s and \mathbf{v}_s are the trial and test functions of the solid displacement and velocity, respectively. Note that the traction \mathbf{t} may also be specified in terms of the Cauchy stress tensor $\boldsymbol{\sigma}_s$ as

$$\mathbf{t} = J_s \boldsymbol{\sigma}_s \mathbf{F}_s^{-T} \mathbf{n}_s. \quad (8.14)$$

For simplicity, we use the one-step- θ scheme for the integration in time, which, for a generic quantity g with $\partial_t g(t) = f(t, g(t))$, reads

$$\partial_t g \approx \frac{g^{n+1} - g^n}{\Delta t} = \theta f^{n+1} + (1 - \theta) f^n. \quad (8.15)$$

This allows us to choose implicit/explicit Euler or centered/shifted Crank-Nicolson time integration depending on the choice of θ but can also easily be extended to the fractional-step- θ scheme. Note that the following can be extended in a straightforward manner to other standard time integration schemes such as the Newmark algorithm or alike.

Using the temporal discretization of Eq. (8.15), the variational formulations of Eq. (8.12)-(8.13) may be discretized in time as

$$\begin{aligned} & \rho_s \Delta t^{-1} (\mathbf{u}_s^{n+1}, \boldsymbol{\psi}_{s,u})_{\Omega_s} + \theta (\mathbf{P}_s^{n+1}, \nabla \boldsymbol{\psi}_{s,u})_{\Omega_s} \\ & = \rho_s \Delta t^{-1} (\mathbf{u}_s^n, \boldsymbol{\psi}_{s,u})_{\Omega_s} \\ & \quad + \theta \left[\langle \mathbf{t}^{n+1}, \boldsymbol{\psi}_{s,u} \rangle_{\Gamma_I \cup \Gamma_{s,N}} + (\rho_s \mathbf{b}^{n+1}, \boldsymbol{\psi}_{s,u})_{\Omega_s} \right] \\ & \quad + (1 - \theta) \left[\langle \mathbf{t}^n, \boldsymbol{\psi}_{s,u} \rangle_{\Gamma_I \cup \Gamma_{s,N}} + (\rho_s \mathbf{b}^n, \boldsymbol{\psi}_{s,u})_{\Omega_s} - (\mathbf{P}_s^n, \nabla \boldsymbol{\psi}_{s,u})_{\Omega_s} \right] \\ & \forall \boldsymbol{\psi}_{s,u} \in \mathcal{V}_0, \end{aligned} \quad (8.16)$$

$$\begin{aligned} & \Delta t^{-1} (\mathbf{d}_s^{n+1}, \boldsymbol{\psi}_{s,d})_{\Omega_s} - \theta (\mathbf{u}_s^{n+1}, \boldsymbol{\psi}_{s,d})_{\Omega_s} \\ & = \Delta t^{-1} (\mathbf{d}_s^n, \boldsymbol{\psi}_{s,d})_{\Omega_s} + (1 - \theta) (\mathbf{u}_s^n, \boldsymbol{\psi}_{s,d})_{\Omega_s} \\ & \forall \boldsymbol{\psi}_{s,d} \in \mathcal{L}. \end{aligned} \quad (8.17)$$

With slight rearrangement it should be obvious that Eq. (8.16) and Eq. (8.17) can conveniently be expressed in matrix form as

$$\mathbf{A}(\mathbf{U}^{n+1}, \boldsymbol{\Psi}) = \mathbf{F}(\boldsymbol{\Psi}), \quad (8.18)$$

where $\mathbf{U}^{n+1} = \{\mathbf{u}_s^{n+1}, \mathbf{d}_s^{n+1}\}$ and $\boldsymbol{\Psi} = \{\boldsymbol{\psi}_{s,u}, \boldsymbol{\psi}_{s,d}\}$.

Based on the time-discrete equations shown above, we employ a finite element Galerkin discretization in space. We discretize the undeformed or

reference domain Ω_s in a shape-regular mesh \mathcal{M}_h , which is composed of hexahedral elements \mathcal{E} . The finite element spaces are given by

$$\mathcal{L}_h := \{\mathbf{w}_h \in C(\Omega_h), \mathbf{w}_h|_{\mathcal{E}} \in Q_p(\mathcal{E}) \quad \forall \mathcal{E} \in \mathcal{M}_h\} \subseteq L^2, \quad (8.19)$$

$$\begin{aligned} \mathcal{V}_{0,h} := \{\mathbf{w}_h \in C(\Omega_h), \mathbf{w}_h|_{\mathcal{E}} \in Q_p(\mathcal{E}) \quad \forall \mathcal{E} \in \mathcal{M}_h, \\ \mathbf{w}_h = 0 \text{ on } \Gamma_{s,D,h}\} \subseteq H^1, \end{aligned} \quad (8.20)$$

$$\begin{aligned} \mathcal{V}_{D,h} := \{\mathbf{w}_h \in C(\Omega_h), \mathbf{w}_h|_{\mathcal{E}} \in Q_p(\mathcal{E}) \quad \forall \mathcal{E} \in \mathcal{M}_h, \\ \mathbf{w}_h = \mathbf{w}_{s,D,h} \text{ on } \Gamma_{s,D,h}\} \subseteq H^1, \end{aligned} \quad (8.21)$$

where $Q_p(\mathcal{E})$ is the space of tensor product polynomials of degree p . In the following, we restrict ourselves to the Q_2 element for simplicity, but it can straightforwardly be extended to higher order. Further, a trilinear transformation is used to map the physical elements to the unit element. Finally, the fully time- and space-discrete nonlinear system in matrix notation reads as

$$\mathbf{A}(\mathbf{U}_h^{n+1}, \mathbf{\Psi}_h) = \mathbf{F}(\mathbf{\Psi}_h), \quad (8.22)$$

for $\mathbf{U}_h^{n+1} = \{\mathbf{u}_{s,h}^{n+1}, \mathbf{d}_{s,h}^{n+1}\} \in \{\mathcal{L}_h \times \mathcal{V}_{D,h}\}$ and $\mathbf{\Psi}_h = \{\boldsymbol{\psi}_{s,u,h}, \boldsymbol{\psi}_{s,d,h}\} \in \{\mathcal{V}_{h,0} \times \mathcal{L}_h\}$.

The nonlinear equations arising from the integration procedures and the Saint-Venant Kirchhoff constitutive relation are solved using a Newton-Raphson method in combination with a simple line search algorithm. This yields the incremental updating rule for the k -th iteration as

$$\mathbf{A}'(\mathbf{U}_h^{n,k})(\delta\mathbf{U}_h^{n,k}, \mathbf{\Psi}_h) = -\mathbf{A}(\mathbf{U}_h^{n,k})(\mathbf{\Psi}_h) + \mathbf{F}(\mathbf{\Psi}_h) \quad (8.23)$$

$$\mathbf{U}_h^{n,k+1} = \mathbf{U}_h^{n,k} + \lambda\delta\mathbf{U}_h^{n,k}, \quad (8.24)$$

where $\lambda \in (0, 1]$ is the line search relaxation parameter. For all cases in this chapter $\lambda = 0.7$ has proven to be a good choice. The Gâteaux derivatives $\mathbf{A}'(\mathbf{U}_h^{n,k})(\delta\mathbf{U}_h^{n,k}, \mathbf{\Psi}_h)$ are analytically computed. In particular, the nonlinearity arises due to the Saint-Venant Kirchhoff relation, which only depends on the displacement. Thus, for direction $\delta\mathbf{U}$ the corresponding derivatives with respect to \mathbf{U} may be identified as

$$\partial_{\mathbf{U}}\mathbf{E} = \frac{1}{2} (\nabla\delta\mathbf{U}^T \mathbf{F} + \mathbf{F}^T \nabla\delta\mathbf{U}), \quad (8.25)$$

which yields

$$\begin{aligned} \partial_{\mathbf{U}} \mathbf{S} = & \frac{1}{2} \lambda \text{tr} (\nabla \delta \mathbf{U}^T \mathbf{F} + \mathbf{F}^T \nabla \delta \mathbf{U}) \mathbf{I} + \\ & \mu_s (\nabla \delta \mathbf{U}^T \mathbf{F} + \mathbf{F}^T \nabla \delta \mathbf{U}), \end{aligned} \quad (8.26)$$

and upon substitution

$$\begin{aligned} \partial_{\mathbf{U}} \mathbf{P} = & \nabla \delta \mathbf{U} \mathbf{S} + \mathbf{F} (\mu_s (\nabla \delta \mathbf{U}^T \mathbf{F} + \mathbf{F}^T \nabla \delta \mathbf{U}) \\ & + \lambda \text{tr} (\mathbf{F}^T \nabla \delta \mathbf{U}) \mathbf{I}). \end{aligned} \quad (8.27)$$

8.2.2 Fluid-structure coupling

A consistent coupling of the fluid and structural domain enforces the following interface conditions

$$\mathbf{u}_f = \mathbf{u}_s \quad \text{on } \Gamma_I^t, \quad (8.28)$$

$$\mathbf{P}_s \mathbf{n}_s + J \boldsymbol{\sigma}_f \mathbf{F}^{-T} \mathbf{n}_s = 0 \quad \text{on } \Gamma_I, \quad (8.29)$$

where $\boldsymbol{\sigma}_f = -p_f \mathbf{I} + \rho_f \nu_f (\nabla \mathbf{u}_f + \nabla \mathbf{u}_f^T)$ is the fluid stress tensor.

Within the context of partitioned approaches, one can distinguish between weakly(loose)- and strongly-coupled FSI schemes. While weakly-coupled methods do not enforce the fluid-solid interface constraints, strongly-coupled methods typically utilize subiterative schemes to converge to the solution of the monolithic system. Weakly-coupled methods are computationally less expensive but have shown to generate artificial energy at the interface due to the staggered nature of the evolution of the fluid and structural part [278]. This so-called added-mass effect can cause fatal instabilities for small solid-fluid density ratios and thus may limit their range of applicability [36, 48, 98, 197, 203].

However, the added-mass effect is proportional to the time step size for compressible flows and converges to a non-zero value only in the fully incompressible regime. Thus, for the weakly compressible LBM at the incompressible limit and the corresponding small time step size this effect has only a limited influence [176].

Hence, for simplicity, we chose a weakly-coupled partitioned approach using the conventional serial staggered (CSS) scheme. The fluid is solved by the LBM and the solid by an appropriate finite element discretization, which

accounts for geometric nonlinearity. The coupling between both domains is achieved through appropriate boundary conditions. On one hand, the Grad boundary condition accounts for the coupling from the solid to the fluid. On the other hand, the fluid is coupled to the solid by the traction force as computed through a pressure tensor extrapolation scheme similar to [176].

Thus, in the CSS algorithm, we first perform a fluid step (including boundary conditions) and compute the force (traction) on the solid. Subsequently, the structural solver computes its deformation, where the traction is imposed as a boundary condition. Finally, we transfer velocity and displacement of the solid to the fluid solver, update the solid geometry in the fluid solver and incorporate the boundary velocity in the fluid boundary conditions.

In the following, we briefly summarize the implementation of the corresponding boundary conditions needed to perform full coupling.

8.2.2.1 Fluid boundary conditions

In the FSI simulations, the fluid boundary condition imposes the no-slip condition and accounts for the momentum exerted from the solid to the fluid. We again employ the Grad boundary condition as detailed in chapter 3. However, in contrast to previous applications, we do not prescribe the velocity directly but it is rather computed by the FEM solver.

To that end, we use the FEM mesh to construct a surface mesh, which is passed to the fluid solver. In particular, we partition the quadrilateral surface elements of the FEM solver into triangular elements for an efficient detection of the intersection location and update the vertex locations using the displacements as computed by the FEM solver. Furthermore, the corresponding velocity values are transferred to the fluid solver and used to interpolate the velocity values at the intersection locations $\mathbf{x}_{w,i}$. The remaining target quantities are computed as before, which completes the fluid boundary condition.

8.2.2.2 Solid boundary conditions

For the coupling of the fluid to the solid, we impose a traction boundary condition as

$$\mathbf{t} = J_s \boldsymbol{\sigma}_f \mathbf{F}_s^{-T} \mathbf{n}_s. \quad (8.30)$$

Thus, we need to evaluate $\boldsymbol{\sigma}_f$ at the quadrature points of the FEM mesh. Fortunately, in LBM the fluid stress tensor can conveniently be computed as

$$\boldsymbol{\sigma}_f = -p\mathbf{I} - (1 - \beta)\boldsymbol{\Pi}^{(1)}, \quad (8.31)$$

where $p = \rho c_s^2$ in the athermal case and $\boldsymbol{\Pi}^{(1)} = \sum_i f_i^{(1)} \mathbf{c}_i \otimes \mathbf{c}_i$, which is evaluated using $f_i^{(1)} \approx f_i - f_i^{eq}$. As $\boldsymbol{\sigma}_f$ needs to be evaluated at all quadrature points on the solid surface mesh, we use an extrapolation scheme, similar to [176].

8.3 Numerical results

8.3.1 Validation

8.3.1.1 Turek Benchmark

For the validation of FSI schemes a comprehensive test suite was proposed in [346], which consists of a rigid circular cylinder with a flexible flag attached to its downstream side. The structure is placed asymmetrically in a laminar channel flow and therefore induces an oscillatory motion of the elastic beam as the flow evolves. The setup is schematically shown in

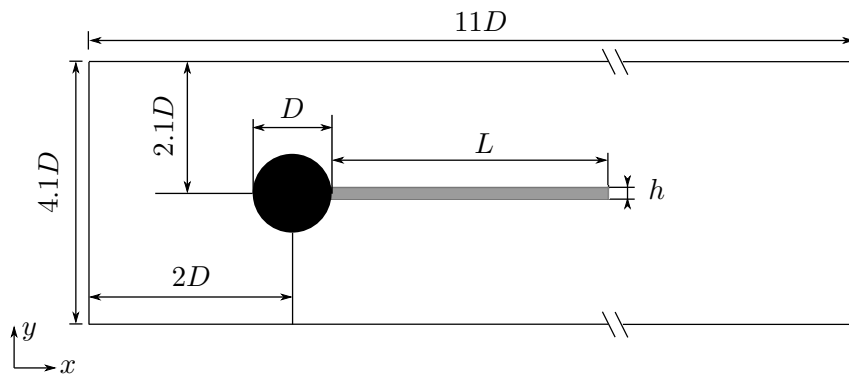


Figure 8.1: Schematic - Turek Benchmark.

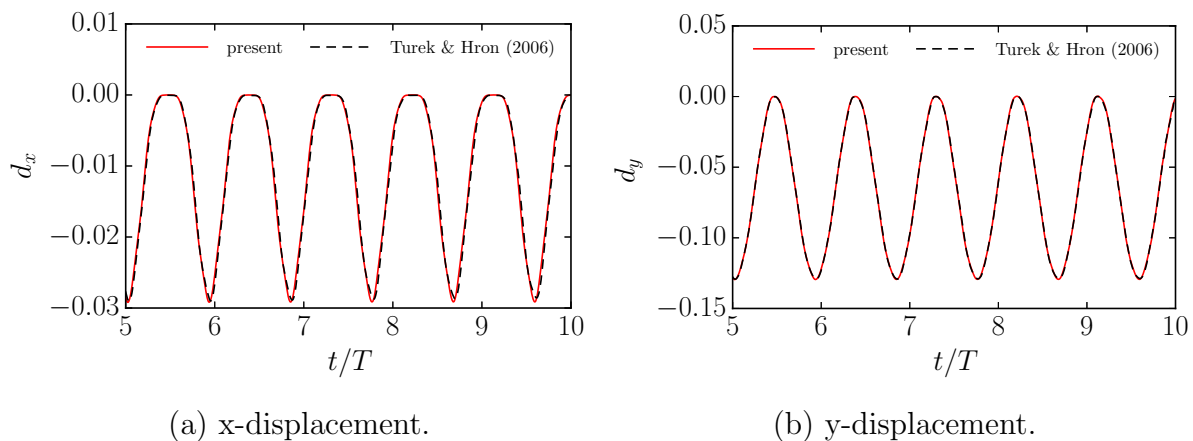


Figure 8.2: CSM3: x - and y -displacement of the beam tip.

figure 8.1. While the boundary conditions in pitchwise directions are no-slip boundaries, the inflow at the left boundary has a prescribed parabolic velocity profile according to

$$u_x(0, y) = 1.5\bar{U}_x \frac{y(H-y)}{(H/2)^2}, \quad (8.32)$$

where the mean inflow velocity is \bar{U}_x and the channel height H . As an initial condition for the unsteady simulation we use a smooth ramping function for the inflow. The cylinder with diameter D is placed asymmetrically at $(2D, 2.1D)$, while the beam has length $L = 3.5D$ and thickness $h = 0.2D$. Note that while in [346] all computations were carried out in two dimensions, we perform a quasi two-dimensional simulation by using only a few points in the spanwise direction and apply periodic and plane strain boundary conditions for the fluid and the solid, respectively. The constitutive law for the solid part is assumed to follow the hyperelastic Saint Venant-Kirchhoff model.

Before attempting to solve the fully coupled FSI system, we first validate the structural solver separately using a time-dependent large deformation test case. Thus, we do not consider the surrounding fluid of the setup in

Contribution	d_x	d_y	f
[346]	-0.01431 ± 0.01431	-0.06361 ± 0.06516	1.0995
present	-0.01460 ± 0.01460	-0.06463 ± 0.06492	1.10

Table 8.1: Results for CSM3.



Figure 8.3: Snapshot of the computational domain, zoomed in on the cylinder-flag assembly.

figure 8.1, but only account for a gravitational force $\mathbf{g} = (0, 2 \cdot 10^3 \text{m/s}^2)$, which is acting on the beam with density $\rho_s = 10^3 \text{kg/m}^3$. The Poisson ratio and the shear modulus are taken as $\nu_s = 0.4$ and $\mu_s = 0.5 \cdot 10^6 \text{kg/ms}^2$, respectively. This corresponds to CSM3 in [346], where the authors report the evolution of the beam tip displacement in the x and y directions. For this setup the beam was discretized by 280 elements and evolved using a time step of $\Delta t = 0.001$. The comparison to [346] is shown in figure 8.2 and table 8.1 and it is obvious that apart from minor artificial damping in the simulations of [346] both results agree well. This validates our implementation of the structural model.

For brevity, we avoid presenting the pure CFD validation as done in [346]. The fluid solver however was thoroughly validated as witnessed by preceding chapters. Thus, having validated the structural solver, we proceed with benchmarks of the fully coupled FSI scheme. To that end, we consider the FSI3 benchmark of [346] for which the density ratio is $\rho_s/\rho_f = 1$ and the Reynolds number $Re = \bar{U}_x D/\nu = 200$. The aeroelastic coefficient was taken as $Ae = E_s/(\rho_f \bar{U}_x^2) = 1.4 \cdot 10^3$, where E_s indicates Young's modulus for the structure and the Poisson ratio was set to $\nu_s = 0.4$. In the fluid domain, we use two levels of refinement as shown in figure 8.3, which effectively resolves the cylinder diameter by $D_{lb} = 40$ lattice points. The elastic beam was discretized using $(140, 10, 1)$ elements.

On one hand, the elastic beam is periodically excited by the vortex street in the wake of the cylinder, which yields strongly nonlinear deflections of

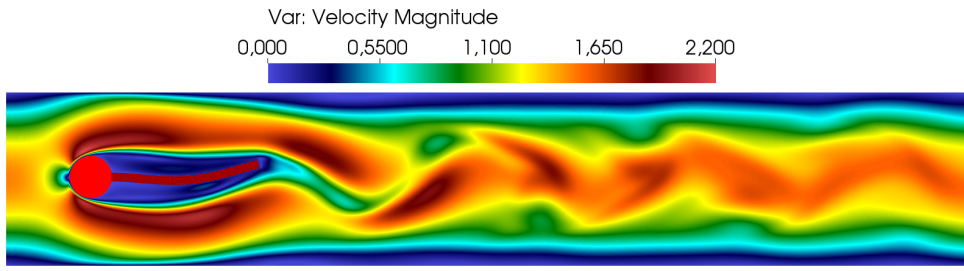
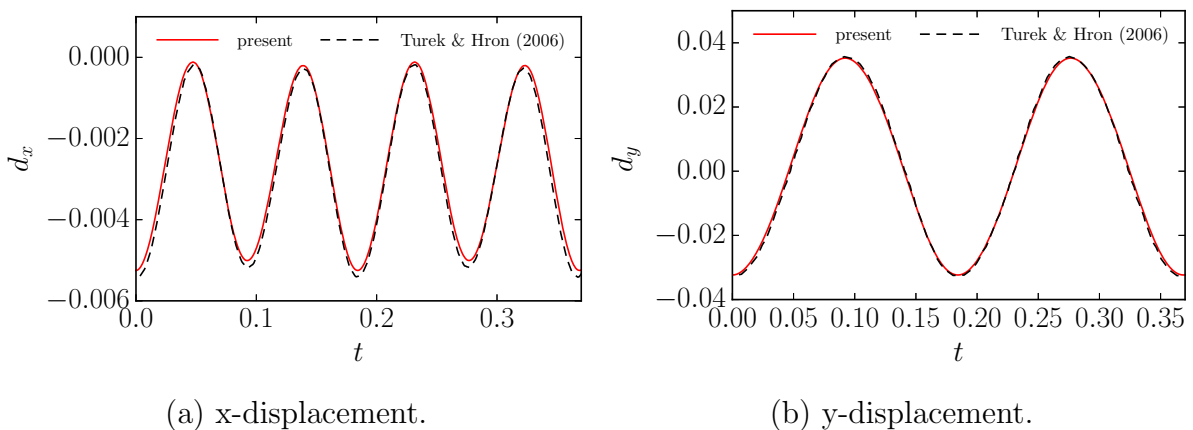


Figure 8.4: FSI3: Snapshot of velocity magnitude.

Contribution	d_x	d_y	f_x	f_y
LB-FEM[176]	-0.00288 ± 0.00271	0.00148 ± 0.0351	11	5.5
ALE-FEM [346]	-0.00269 ± 0.00253	0.00148 ± 0.03438	10.9	5.3
present	-0.00268 ± 0.00257	0.00145 ± 0.03380	11	5.5

Table 8.2: FSI3: Mean and amplitude of the flag tip deflection.

the flag. On the other hand, the momentum transferred from the solid excites the fluid. A slice through the computational domain, showing a snapshot of velocity magnitude is presented in figure 8.4. More quantitatively, we computed the mean and amplitude of the deflection at the free end of the flag along with the corresponding oscillation frequencies. The comparison with literature values is excellent and listed in table 8.2. Finally, the deflection evolution is reported in figure 8.5, which agrees well with the reference data of [346].



(a) x-displacement.

(b) y-displacement.

Figure 8.5: FSI3: Evolution of the flag tip deflection in x - and y -direction.

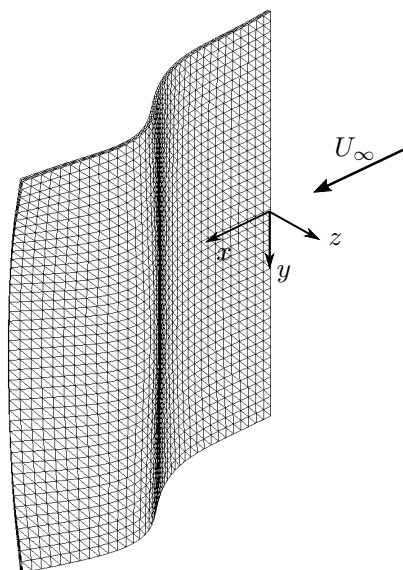
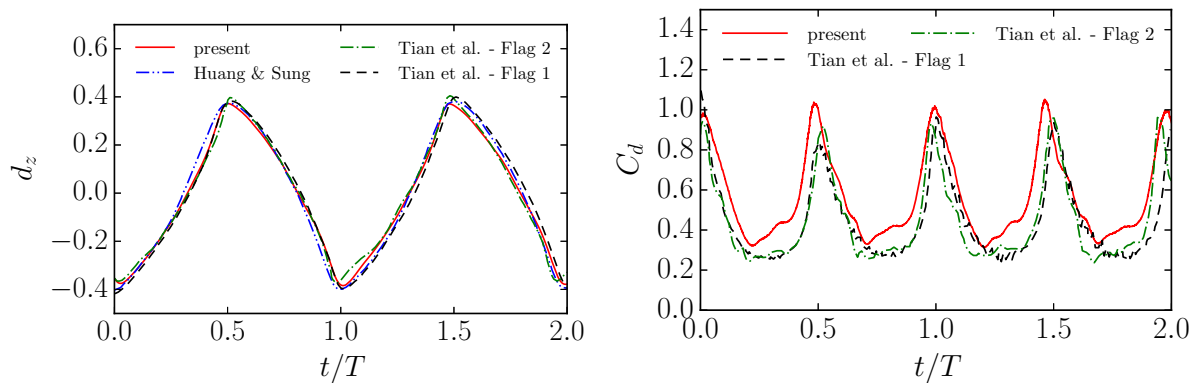


Figure 8.6: Schematic of the flow past a flapping flag

8.3.1.2 Flow past a flapping flag

Having validated the proposed scheme in the quasi two-dimensional setting, we next consider a fully three-dimensional flow. To that end, we investigate the nonlinear dynamics of a flag in a uniform fluid flow. Despite being a classical model problem for FSI, the complex motion of the flag challenges numerical methods and thus only a few cases have been reported in the literature [143, 171, 341]. Here, we use the case as provided in [143, 341] for validation. While in [143] a diffuse-interface immersed boundary method was employed, [341] used an immersed boundary method coupled with a nonlinear FEM solver. As shown in figure 8.6, the leading edge of a square flag of length L and thickness $h = 0.01L$ is placed at the origin of the domain. In addition, zero displacement and velocity boundary conditions are imposed at the leading edge. The rectangular fluid domain spans from $[-2L \times -1L \times -4L]$ to $[8L \times 1L \times 4L]$ in streamwise, spanwise and transverse directions, respectively. Periodic boundary conditions are applied in spanwise direction and free-stream boundaries are imposed in transverse direction. Using two levels of refinement, the flag was resolved by $L = 100$ lattice units in the finest level. The flexible flag is discretized with a uniform mesh of $[50 \times 50 \times 2]$ elements. The Poisson ratio is set to $\nu_s = 0.4$ and the bending rigidity is $Eh^3/(12(1 - \nu_s^2)\rho_f u_\infty^2 L^3) = 10^{-4}$. The density ratio is taken as $\rho_s/\rho_f = L/h$ and the Reynolds number is



(a) Displacement of the point B located at $B = (L, 0, 0)$ in the undeformed configuration.

(b) Evolution of the drag coefficient.

Figure 8.7: Flow past a flapping flag.

$Re = u_\infty L / \nu = 200$. Initially, the flag coincides with the xy -plane and a small perturbation is used to trigger the periodical flapping behavior. During the evolution, we record the displacement of the Point B, which is located at $B = (L, 0, 0)$ in the undeformed configuration and compare it to the reference data of [143, 341] in figure 8.7a. Note that in [341] two flag models were considered, namely, a plate model with infinitesimal thickness (Flag 1) and a three-dimensional model with thickness $h = 0.01L$ (Flag 2). Both cases demonstrate negligible discrepancies due to the low Reynolds number in this case. After the initial transient, the flow quickly converges to a periodic flapping as seen in figure 8.7a. The comparison of the present simulations to the references shows good agreement. Besides the displacement, we compute the evolution of the drag coefficient $C_d = F_x / (1/2 \rho_f u_\infty^2 L^2)$ and compare it to the values reported in [341] in figure 8.7b. Significant noise can be observed for the simulations by [341], which, according to the authors, originates from the noisy prediction of the thin plate. In contrast, the results from the present method appear smooth and do not exhibit oscillations. Overall, both results agree qualitatively but do exhibit small discrepancies, which are most pronounced when the flag goes through the origin. One can conjecture that these discrepancies originate either from the noisy prediction of the reference or from a more pronounced deformation (at locations different from point B) of the present model when passing the origin, which would lead to an increased drag. Unfortunately, no data regarding the drag evolution were

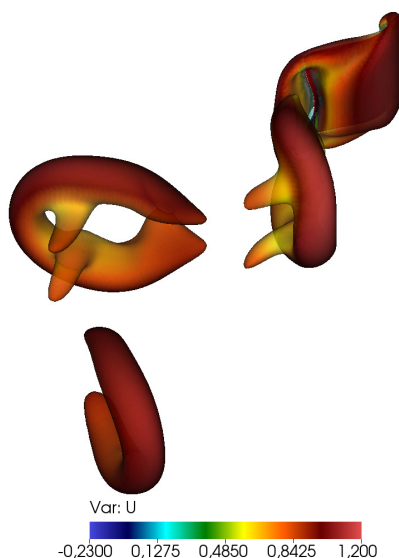


Figure 8.8: Wake of a flapping flag visualized by isosurfaces of Q -criterion and colored by streamwise velocity.

reported in [143], thus eluding a comparison. Finally, in figure 8.8, the vortical structures in the wake of the flag are visualized by isosurfaces of the Q -Criterion, which are colored by streamwise velocity. The vortices shed from the trailing edge connect with the vortices shed from the side edges to form hairpin-type vortices along with two separate co-rotating vortices. Notably, the structure of the wake bears significant resemblance to self-propelled anguilliform swimmers [73]. Analogous vortex structures have been observed in the references [143, 341].

8.3.1.3 Beam in crossflow

So far we have successfully validated the proposed scheme for quasi-two-dimensional and three-dimensional flows. As a final validation, we include a simulation involving turbulence. To that end, we consider a flexible beam in a cross flow. This set-up has been studied both experimentally and numerically in [341] and [214], respectively and aims to model the deformation of aquatic plants caused by the flow. The beam is vertically mounted in a uniform flow and has length L , thickness h and width b . As in the references, the Reynolds number is set to $Re = u_\infty L / \nu = 8000$ and the geometrical properties of the beam are given by $L/b = 5$, $h/b = 0.2$. The solid material has the non-dimensional Young's modulus $\tilde{E}_s = E_s / \rho u_\infty^2$ and the Poisson's ratio $\nu_s = 0.4$. The density ratio is set to $\rho_s / \rho_f =$

Contribution	C_d	d_x/b	d_z/b
IMB-FEM [341]	1.03	2.12	0.54
Exp. [214]	1.15	2.14	0.59
present	1.13	2.14	0.55

Table 8.3: Flexible plate in a cross flow. Comparison of drag coefficient C_d and plate deflection d_x/b and d_y/b in stream- and pitchwise directions, respectively.

0.678 and a buoyancy force $f_b = (\rho_f - \rho_s)gh/(\rho_f u_\infty^2) = 0.2465$ is applied. The rectangular domain ranges from $[-5b, -8b, -8.5b]$ to $[16b, 8b, 8.5b]$ in which the centroid of the beam is placed at the origin of the undeformed configuration. Using one level of refinement, the fluid domain discretizes the beam width with $b = 40$ lattice points and the solid mesh employs $[2 \times 20 \times 140]$ elements to represent to beam.

Using these flow and structural conditions and parameters, the plate converges to a steady deformation. A snapshot of the deformed state is presented in figure 8.9, where the wake behind the deformed beam is visualized by isosurfaces of the Q-Criterion and colored by velocity magnitude. Qualitatively this is in line with the reference. For a more thorough comparison, we computed the drag coefficient $C_d = F_x/(1/2\rho_f u_\infty^2 bL)$ along with the deflection of the beam's free end in the deformed state. Along with the reference values, the results of the present simulation are listed in table 8.3. It is apparent that the results are in good agreement with the reference data. While some discrepancies to the numerical study of [341] may be observed, the present simulation matches the experimental study well [214].

8.3.2 Extensions to fluid-structure interaction in multiphase flow

Two-phase flows are of fundamental interest in science and engineering applications [4], which exhibit various complex phenomena at multiple temporal and spatial event scales [218, 380]. These include droplet breakup, droplet reconnection as well as droplet impact on a surface, where effects such as splash [217, 288], skating [175, 300], rebound [30, 211, 289] or the

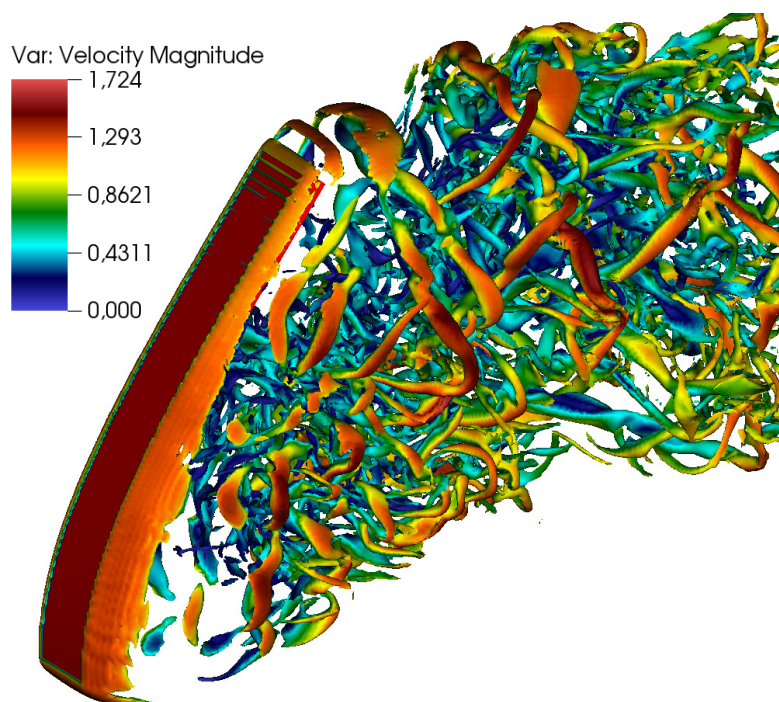


Figure 8.9: Flexible plate in a cross flow: Isosurfaces of Q-criterion, colored by velocity magnitude.

trampoline effect [311] have been observed.

In recent years, much attention has been devoted to droplet impact on so-called superhydrophobic surfaces. Superhydrophobic surfaces exhibit strong repellence of liquid droplets, which can be exploited in for anti-icing, self-cleaning, drag reduction and many other applications [25, 31, 179]. The most known example of a natural superhydrophobic surface is the surface of the lotus leaf, i.e. *Nelumbo nucifera*. Numerous studies suggested that the combination of surface chemistry and roughness on multiple scales on the surface is responsible for its repellence. Thus, modern synthetic designs of superhydrophobic surfaces combine the effects of micro-texturing and chemistry to enhance the hydrophobic effect. To that end, many studies have investigated the underlying physics of droplet impact on superhydrophobic surfaces using different designs and conditions with the ultimate goal to reduce the contact time [173, 310]. Note however that most studies have focused on rigid surfaces and neglected the flexibility of the substrate, which is inherent to most naturally occurring repellent surfaces such as leaves, textiles and butterfly wings. Notable is the recent study of [354], where the effect of elasticity on hydrophobicity was investigated

experimentally.

In this section, we aim to go beyond classical benchmark cases and explore the capabilities of the KBC-FSI solver in the context of multiphase flows by considering droplet impact on flexible superhydrophobic surfaces, similar to [354]. From the numerical point of view, simulations of such a kind are challenging. However, the LBM offers an attractive alternative to conventional schemes, due to the ease of implementing inter-molecular forces and complex boundaries without sacrificing efficiency [230]. While various LB models for multiphase flow exist, restrictions on density ratio, kinematic viscosity and interface thickness remained for long. Among others, a viable alternative was proposed in [230], where combining the notion of a discrete entropy function, the free-energy based formulation (see, e.g., [312] and references herein) and an appropriately regularized equation of state significantly increased the range of applicability of LB models for multiphase flow. This approach has been thoroughly validated by simulations of droplet impact on flat and micro-textured superhydrophobic surfaces for a variety of different bouncing regimes [231, 245]. Here, we build on these results and extend it to the KBC model, the Grad boundary condition and the coupling to the structural solver. The equation of state and the forcing approach are kept the same.

On the fluid side, following [230], the phase separation and wetting properties are implemented through a body force

$$\mathbf{F} = \mathbf{F}_f + \mathbf{F}_s. \quad (8.33)$$

The mean field force

$$F_{f,\alpha} = \partial_\beta (\rho c_s^2 \delta_{\alpha\beta} - P_{\alpha\beta}^K), \quad (8.34)$$

accounts for the phase separation by implementing the Korteweg stress tensor

$$P_{\alpha\beta}^K = \left(p - \kappa \rho \partial_\gamma \partial_\gamma \rho - \frac{\kappa}{2} (\partial_\gamma \rho) (\partial_\gamma \rho) \right) \delta_{\alpha\beta} + \kappa (\partial_\alpha \rho) (\partial_\beta \rho), \quad (8.35)$$

where the pressure p is prescribed through a non-ideal equation of state and κ controls the surface tension. This yields

$$F_{f,\alpha} = 2\varphi \partial_\alpha \varphi + \kappa \rho \partial_\alpha (\partial_\beta \partial_\beta \rho), \quad (8.36)$$

with

$$\varphi = \sqrt{\rho c_s^2 - p}. \quad (8.37)$$

The differential operators are discretized using second-order finite difference approximations and spatially window-averaged to avoid large spurious velocity (see, e.g., [231] for explicit expressions).

The equation of state is a polynomial regularization of Peng-Robinson form [386] as introduced in [230] and reads

$$\begin{aligned} p = & 5.3 \cdot 10^{-2} \rho \\ & - 3.818183621928911 \cdot 10^{-2} \rho^2 \\ & + 4.139745482116095 \cdot 10^{-3} \rho^3 \\ & + 3.748484095210317 \cdot 10^{-4} \rho^4 \\ & - 1.4552652965531227 \cdot 10^{-4} \rho^5 \\ & + 1.2746947442749278 \cdot 10^{-5} \rho^6, \end{aligned} \quad (8.38)$$

which yields an effective density ratio of $\rho_v/\rho_l \approx 100$ with liquid and vapour densities $\rho_l \approx 7.55$ and $\rho_v \approx 0.073$, respectively.

Different wetting states can be modeled by means of the force \mathbf{F}_s , which reads

$$F_{s,\alpha}(x_\alpha, t) = \kappa_w \rho(x_\alpha, t) \sum_i^N w_i s(x_\alpha + c_{i,\alpha} \delta t) c_{i,\alpha}, \quad (8.39)$$

where κ_w allows us to choose the equilibrium contact angle in accordance with the Young-Laplace equation. The term $s(x + c_{i,\alpha} \delta t)$ is an indicator function that is equal to one for the solid domain nodes and is equal to zero otherwise; w_i are appropriately chosen weights [231]. To model superhydrophobic surfaces, the equilibrium contact angle was set to $\theta = 165^\circ$, which corresponds to $\kappa_w = -0.145$.

The total body force \mathbf{F} is imposed through the exact difference method [182] with the velocity increment

$$\delta u_{f,\alpha} = \frac{F_\alpha}{\rho \delta t}. \quad (8.40)$$

Hence, the LB equation can be written as

$$f_i(\mathbf{x} + \mathbf{c}_i, t + 1) = f'_i \equiv (1 - \beta) f_i(\mathbf{x}, t) + \beta f_i^{\text{mirr}}(\mathbf{x}, t) + F_i(\mathbf{x}, t), \quad (8.41)$$

with

$$F_i = f_i^{\text{eq}}(\rho, \mathbf{u}_f + \delta \mathbf{u}_f) - f_i^{\text{eq}}(\rho, \mathbf{u}_f). \quad (8.42)$$

Unlike the entropic LBM of [230], we here use the KBC realization of the LBM, where we incorporate the force term into the KBC model through the shifted entropic scalar product

$$\langle X | Y \rangle' = \sum_i \frac{X_i Y_i}{f^{\text{eq}}(\rho, \mathbf{u}_f + \delta \mathbf{u}_f)}, \quad (8.43)$$

which is used to compute the stabilizer γ from Eq. (2.45).

Also in the multiphase model, we use Grad's boundary condition. Before considering the fully coupled FSI simulation, the KBC model and the boundary condition are validated for the impact of a low viscosity liquid drop on a flat superhydrophobic surface. Experimentally, this set-up was investigated in [64], which suggests that in the low viscosity regime the maximum spreading diameter D_{max} scales with the Weber number $We = (\rho_l u_0^2 D_0) / \sigma$ as

$$D_{\text{max}} / D_0 \sim We^{1/4}, \quad (8.44)$$

where D_0 and u_0 are the initial droplet diameter and the impact velocity, respectively. Our simulations were performed on a $[350 \times 350 \times 250]$ grid, which resolves the droplet with $D = 80$ lattice points and the surface tension is set to $\sigma = 0.295$ ($\kappa = 0.002$). In figure 8.10, the numerical results are compared to both the scaling law and the experiment. The excellent agreement to the reference data validates the multiphase flow solver using KBC and the Grad boundary condition for superhydrophobic surfaces.

For the fluid-structure coupling, we employ the same methodology as outlined above but include the pressure p as prescribed by the equation of state in Eq. (8.38). Note, however, that the diffuse nature of the liquid-vapour interface necessitates a pressure regularization. This arises from the fact that the numerical integration of the pressure over the solid surface is prone to numerical errors, due to sharp pressure gradients and large negative values in the interface region, which are sampled only relatively coarsely on the FEM mesh. This leads to an artificial negative pressure, which is compensated in our simulations by a regularization procedure, where we use a simple linear interpolation between the liquid and vapor density to evaluate the pressure.

Motivated by the experimental study of [354], we investigate the effect of elasticity on the droplet impact on a superhydrophobic, elastic beam for a wide range of Weber numbers.

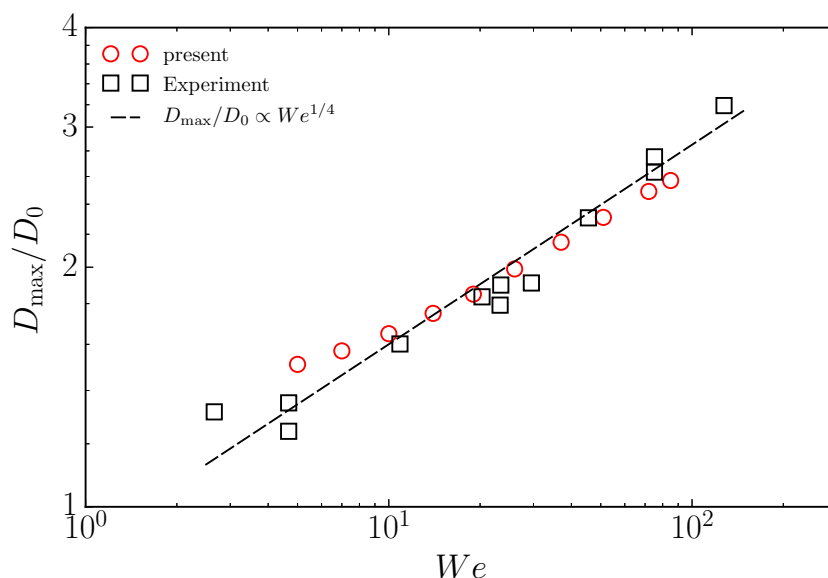


Figure 8.10: Maximum droplet spreading diameter on a flat superhydrophobic surface in the low viscosity limit.

In all simulations, the droplet is resolved by $D = 80$ lattice points, the surface tension is set to $\sigma = 0.295$ ($\kappa = 0.002$) and the computational domain of the fluid is given by $[320 \times 250 \times 320]$. The beam has the dimensions $[300 \times 200 \times 5]$ and the Lamé coefficients are set to $\lambda_s = 1500$ and $\mu_s = 1000$. While one end of the beam is clamped, the other end is only simply supported and the droplet impacts the center of the beam.

We simulated Weber numbers in the range of $We \in [7, 72]$ for both rigid and flexible beams and recorded the maximum spreading diameter D_{max}/D_0 as shown in figure 8.11.

For the entire range of Weber numbers, it is apparent that the maximum spreading diameter decreases when elasticity of the beam is taken into consideration. Analogously, the experimental study conducted in [354] also observed a reduction of the apparent spreading diameter. While a quantitative comparison is out of reach for the current preliminary simulations due to the large dimensions of the beam used in the experiment, the proposed scheme does capture the effect of elasticity qualitatively. A natural explanation for the cause of the reduction of the spreading diameter is that the momentum of the droplet is transferred to the beam, which decreases the effective Weber number perceived by the droplet and thus reduces the maximum spreading of the droplet. It is only long after the droplet has

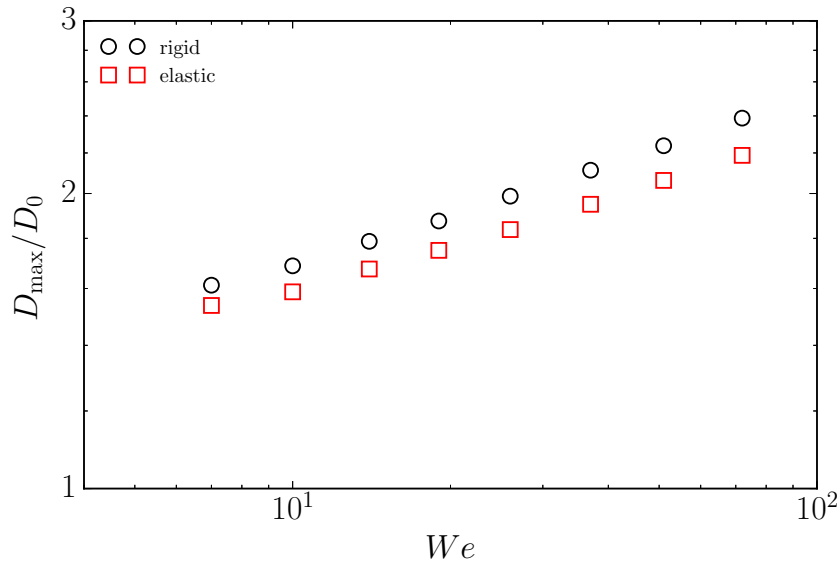


Figure 8.11: Maximum droplet spreading diameter on rigid and elastic superhydrophobic surfaces.

reached its maximum spread that the momentum is transferred back (no damping is applied) to the liquid. A similar explanation was proposed in [354]. A sequence of snapshots of the droplet impact on both the rigid beam and the elastic beam is shown in figure 8.12. It is clear that initially both the rigid beam and the elastic beam behave similar, but the elastic case exhibits faster rebound and takeoff. The reduction of rebound time might be explained by remembering that the rebound time is independent of the Weber number in a wide range and by spring analogy is only influenced by the droplet mass and the surface tension [289]. In the case of an elastic surface, however, the maximum spreading diameter is reduced (due to momentum transfer to the beam), which decreases the distances to be traveled until the recoiling phase is completed. Note that the density ratio between solid and fluid is roughly $\rho_s/\rho_f \approx 100$, which explains the delayed response of the fluid. Further, the observed asymmetry in the elastic case is due to the asymmetric boundary conditions of the beam.

These results are promising and underline the robustness and viability of multi-physics simulations based on the KBC-FSI solver. A detailed investigation of FSI for multiphase flows is left for future work.

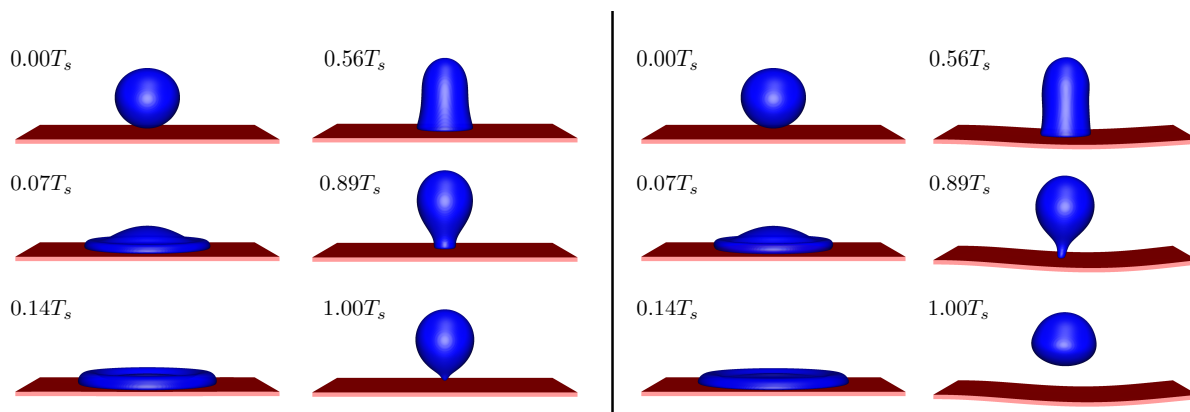


Figure 8.12: Droplet spreading on rigid (left) and elastic (right) superhydrophobic surfaces. Timings are normalized by the contact time T_s of the rigid surface.

8.4 Concluding remarks

In this chapter we have presented a partitioned fluid-structure interaction approach. On one hand, the fluid flow is computed by the entropic multi-relaxation time lattice Boltzmann model in combination with Grad boundary conditions and multi-domain grid refinement. On the other hand, the elastic solid was modeled by the hyperelastic Saint Venant-Kirchhoff model, which accounts for large, geometrically nonlinear deformations and was solved by a corresponding FEM formulation.

The proposed scheme was validated for various challenging set-ups for quasi-two dimensional and fully three dimensional simulations of laminar and turbulent flows. Finally, extensions to multi-physics simulations were explored. An extension of the KBC model to multiphase flows and its coupling to the solid solver was presented. Promising results, in qualitative agreement with recent experiments, were shown for the simulation of droplet impact on elastic superhydrophobic surfaces, which demonstrate the viability of the proposed scheme.

Chapter 9

Conclusions and outlook

In this thesis, we have developed the necessary numerical tools and strategies to enable the simulation of complex, engineering relevant applications of low-dissipative flows using entropic lattice Boltzmann models. In the first section of this chapter, the main results of this thesis will be summarized. In the second section, we will provide a critical comment on the limitations of the method and finally, in the last section, possible directions of further research are outlined.

9.1 Results

In this thesis, we have provided thorough investigation of the entropic multi-relaxation time lattice Boltzmann model and assessed viability for complex flows in both resolved and under-resolved simulations.

To tackle arbitrarily complex geometries, a consistent treatment of fluid-solid interaction was developed. An analog of Grad's moment approximation was utilized to ensure stability and robustness. The Grad boundary condition was shown to be second-order accurate and capable of describing curved, moving and deforming geometries. The scheme was thoroughly validated for both one- and two-way coupled simulations in various set-ups throughout this thesis.

To enable multi-scale simulations at reasonable computational costs two grid refinement strategies were explored. On one hand, a novel multi-

domain block refinement method using Cartesian grids was developed. By allowing entropic time-stepping within the grid level interface, a consistent fine-to-coarse grid level projection was achieved, where the entropic stabilizer adapts to the flow features and refinement patches, rendering explicit filtering or alike unnecessary. This feature also enabled its extension to thermal and compressible flows. The entropic time-stepping within the interface is crucial for compressible flows, where shocks penetrate the grid level interface without being reflected and destabilizing the flow. Validity was assessed for various benchmark simulations.

On the other hand, viability of unstructured meshes within the framework of the LBM was explored. To that end, the semi-Lagrangian LBM was implemented and extended to the KBC model with appropriate boundary conditions. While promising, further developments are required to be competitive with refinement strategies based on Cartesian Grids.

These ingredients, namely the entropic collision model, Grad boundary condition and block-refinement enabled efficient simulations of engineering relevance. The first test case was the flow in engine-like geometries, with focus on resolved and under-resolved simulations. A comparison to a high-order spectral element solver demonstrated accuracy and robustness of the approach, while significantly reducing the computational costs. Subsequently, transition to turbulence was considered. As both laminar and turbulent regions are present within transitional flows, the high Reynolds number assumption on which most turbulence model rely, may not be valid anymore. In addition, a DNS study of such flows might already be too expensive. Thus it is of crucial importance to assess if our approach is capable of accurately capturing this phenomenon. To that end, various simulations of transitional flows over airfoils and turbine blades were conducted, showing excellent agreement with literature values. Also in this case, the resolution requirements were much less stringent than for DNS and rather in the regime of pertinent implicit LES schemes.

In chapter 7, the level of complexity was further increased and three-dimensional simulations in the realm of biolocomotion were presented. Starting with the simulation of a plunging airfoil in the transitional regime and self-propelled anguilliform swimmers, further extensions to flapping flight and fish schools were presented.

In the final chapter, the scheme was extended to incorporate structural

mechanics in order to compute the nonlinear elastic deformation, yielding a fully coupled fluid-structure interaction solver. A CSS algorithm was employed to couple the fluid and the structural domain. After thorough validation for laminar and turbulent cases, the scheme was extended to multiphase flows. Here, viability towards multi-physics simulation was shown by the simulation of droplet impact on elastic, superhydrophobic surfaces for a wide range of Weber numbers.

All schemes presented in this thesis (except the SLLBM) were implemented in a generic, modern C++ framework, which was developed in the scope of this thesis together with Fabian Bösch. The code is dimension agnostic, parallelized using MPI, fully vectorized using SIMD and allows for parallel IO. Furthermore, it is capable of handling arbitrarily complex, moving geometries, mesh refinement and fluid-structure interaction problems. Its generic, modular structure enables the user to choose arbitrary (multi-speed) lattices, models and boundary conditions. For example, extensions to compressible models have been implemented by Nicolò Frapolli. The code has shown excellent scalability up to thousands of cores on the machines of the Swiss National Supercomputing Center (CSCS).

9.2 Limitations

The results presented in this thesis are promising. However, some critical remarks on its limitations are in order.

While the KBC model has shown excellent stability properties for a large range of flows, this does not necessarily imply accuracy. In fact, for severe under-resolution or very large Reynolds numbers, the effective viscosity as measured from the flow field deviates significantly from the nominal viscosity, leading to a misrepresentation of the small scales. The KBC model formally does not alter the viscosity but the effect of higher-order error terms manifest themselves in a measurable macroscopic viscosity for very coarse-grained simulations. While it was shown that accurate results can be obtained despite under-resolutions, a thorough grid convergence study is necessary to ensure its validity. To further advance our understanding of the KBC's subgrid scale behavior, it would be insightful to derive and analyze the error terms beyond second order in the Chapman-Enskog multi-scale expansion. One can conjecture that on the basis of such an analysis

it might be helpful to introduce additional relaxation times to counteract these error terms and thereby enhance the implicit subgrid scale behavior. Another limiting factor is the time step size. The weakly compressible LBM on standard lattices requires a small Mach number and thus time step size to converge to the incompressible solution. The requirements on the time step size become even more stringent when moving geometries are involved. To avoid spurious oscillations in the flow field a reduction of a factor two in the time step is required to ensure accurate results.

Lastly, as also shown in this thesis, the LBM is most powerful on Cartesian grids. While block-refinement strategies are tremendously helpful to reduce the computational cost, the attainable level of flexibility using unstructured grid can reduce computational costs significantly. However, unstructured grids and adaptive time-stepping are not inherent to LBM and require sophisticated techniques such as high-order interpolation schemes as shown in chapter 4. In turn, this results in higher computational cost and loss of some of the key advantages of LBM such as exact propagation in space.

9.3 Future research

The LBM is still an active area of research. Here we list some suggestions of future research, which, based on the results presented in this thesis, could further advance the field.

As mentioned above, the subgrid scale behavior of the KBC model requires further analysis using, e.g, higher-order Chapman-Enskog expansion. Such analysis could also be a possibility to incorporate explicit turbulence models into the KBC model in a consistent manner. This would further increase the range of applicability of the KBC to very large Reynolds numbers.

Regarding grid refinement strategies, further reduction of computational cost could be achieved by using adaptive block-refinement, where the deviation of the entropic stabilizer from its limiting value could serve as a refinement criterion. This has the additional advantage that the criterion is computed locally with no computational overhead.

For unstructured meshes and in particular the SLLBM further work is required to be competitive. As discussed in chapter 4, the memory requirements of SLLBM are excessive and computational cost significant compared to standard LBM. A remedy would be to combine the advantage of

standard LBM on Cartesian grid and the SLLBM using a hybrid formulation. This has already been explored for a finite volume LBM on unstructured grids in [68] and could also be beneficial in the case of SLLBM. Another possible extension could consist of developing an efficient matrix-free version of the SLLBM. This would alleviate the memory issue and also make adaptive refinement possible.

Regarding the FSI solver in chapter 8, it would be instructive to explore iterative, strongly-coupled fluid-structure schemes to minimize the added mass effect. This might further increase its range of applicability.

Finally, various directions of research have been opened up for further applications. For example, in the realm of biolocomotion, it would be intriguing to study the formation of fish schools or bird flocks. Employing recent developments in deep neural networks and reinforcement learning might yield novel insight. Here, the limiting factor of existing approaches is the efficiency of the underlying fully-coupled FSI simulations, as multiple simulations are needed to properly train the network. This renders the proposed scheme an ideal candidate.

Furthermore, extending the investigation of the effect of elasticity for multiphase flow might be key to develop innovative liquid repellent surfaces. This would significantly impact on a vast range of applications in science and engineering .

Appendix

A.1 Moment representation of the populations

For ease of notation, let us introduce the trace of the stress tensor

$$T = M_{200} + M_{020} + M_{002}, \quad (\text{A.1})$$

the normal stress differences

$$\begin{aligned} N_{xz} &= M_{200} - M_{002} \\ N_{yz} &= M_{020} - M_{002} \end{aligned} \quad (\text{A.2})$$

and the off-diagonal components of the stress tensor at unit density

$$\begin{aligned} \Pi_{xy} &= M_{110} \\ \Pi_{xz} &= M_{101} \\ \Pi_{yz} &= M_{011}, \end{aligned} \quad (\text{A.3})$$

which yields the natural moment representation of the population as

	(ρ, \mathbf{u})	$\mathbf{\Pi}'$
	$(0, 0, 0)$	1
	$(\sigma, 0, 0)$	$\sigma u_x/2$
	$(0, \lambda, 0)$	$\lambda u_y/2$
	$(0, 0, \delta)$	$\delta u_z/2$
	$(\sigma, \lambda, 0)$	0
	$(\sigma, 0, \delta)$	0
	$(0, \lambda, \delta)$	0
	$(\sigma, \lambda, \delta)$	0

Table A.1: Contribution of the locally conserved fields and the deviatoric stress tensor to the populations at unit density

$$\begin{aligned}
f_{(0,0,0)} &= \rho (1 - T + M_{022} + M_{202} + M_{220} - M_{222}) \\
f_{(\sigma,0,0)} &= \frac{1}{6}\rho (3\sigma u_x + 2N_{xz} - N_{yz} + T - 3\sigma M_{120} - 3\sigma M_{102} + 3\sigma M_{122} - 3M_{202} - \\
&\quad 3M_{220} + 3M_{222}) \\
f_{(0,\lambda,0)} &= \frac{1}{6}\rho (3\lambda u_y - N_{xz} + 2N_{yz} + T - 3\lambda M_{210} - 3\lambda M_{012} + 3\lambda M_{212} - 3M_{022} - \\
&\quad 3M_{220} + 3M_{222}) \\
f_{(0,0,\delta)} &= \frac{1}{6}\rho (3\delta u_z - N_{xz} - N_{yz} + T - 3\delta M_{201} - 3\delta M_{021} + 3\delta M_{221} - 3M_{022} - \\
&\quad 3M_{202} + 3M_{222}) \\
f_{(\sigma,\lambda,0)} &= \frac{1}{4}\rho (\sigma \lambda \Pi_{xy} + \lambda M_{210} + \sigma M_{120} + M_{220} - \sigma M_{122} - \lambda M_{212} - \sigma \lambda M_{112} - M_{222}) \\
f_{(\sigma,0,\delta)} &= \frac{1}{4}\rho (\sigma \delta \Pi_{xz} + \delta M_{201} + \sigma M_{102} + M_{202} - \sigma M_{122} - \delta M_{221} - \sigma \delta M_{121} - M_{222}) \\
f_{(0,\lambda,\delta)} &= \frac{1}{4}\rho (\lambda \delta \Pi_{yz} + \delta M_{021} + \lambda M_{012} + M_{022} - \lambda M_{212} - \delta M_{221} - \lambda \delta M_{211} - M_{222}) \\
f_{(\sigma,\lambda,\delta)} &= \frac{1}{8}\rho (\sigma \lambda \delta M_{111} + \sigma M_{122} + \lambda M_{212} + \delta M_{221} + \sigma \lambda M_{112} + \sigma \delta M_{121} + \\
&\quad \lambda \delta M_{211} + M_{222}).
\end{aligned} \tag{A.4}$$

where the subscript triple, defined by the indices $\sigma, \lambda, \gamma \in \{-1, 1\}$, denotes the associated discrete velocity vector of the population. The KBC model in the main text utilizes this representation and partitions it into three

parts according to Eq. (2.39), where the shear part only includes the deviatoric stress tensor. The contribution of the locally conserved field (ρ, \mathbf{u}) and the deviatoric stress tensor $\mathbf{\Pi}'$ to the populations at unit density is summarized in Table (A.1). Using this partition allows for the kinematic, the shear and the remaining higher order moments to be relaxed according to Eq. (2.40).

List of Tables

2.1	<i>D3Q27</i> lattice.	14
3.1	Flow past a sphere at $Re = 100$	33
3.2	Terminal settling velocity for a sedimenting sphere at $Re = 100$	35
4.1	Moments for equilibrium and quasi-equilibrium construction.	44
4.2	Turbulent flow in a rectangular channel. The nominal and measured Reynolds numbers are indicated by $Re_{\tau,n}$ and $Re_{\tau,m}$, respectively.	52
4.3	Turbulent flow past sphere at $Re = 3700$ and the comparison of the mean drag coefficient $\overline{C_d}$, the averaged base pressure coefficient $\overline{C_{pb}}$, the recirculation length $\overline{L_r}$ and the separation angle $\overline{\varphi_s}$ with literature values.	59
5.1	Effective viscosity ratios at non-dimensional time $t/(N/U_0) = 0.75$ for simulations with different resolutions N	89
6.1	Comparison of the LSB properties for the flow over the <i>SD7003</i> airfoil, where Tu denotes the turbulence intensity of the inflow.	117
6.2	Comparison of the LSB properties for the flow over the <i>T106</i> blade for different free-stream turbulence intensities at $Re = 6 \cdot 10^4$	127
8.1	Results for CSM3.	160
8.2	FSI3: Mean and amplitude of the flag tip deflection.	162
8.3	Flexible plate in a cross flow. Comparison of drag coefficient C_d and plate deflection d_x/b and d_y/b in stream- and pitchwise directions, respectively.	166

A.1	Contribution of the locally conserved fields and the deviatoric stress tensor to the populations at unit density	182
-----	--	-----

List of Figures

3.1	The unknown populations at the boundary node \mathbf{x}_b are represented by the dashed arrows. \bullet : Solid nodes. \circ : Fluid nodes. \blacksquare : Solid boundary nodes. \square : Fluid boundary nodes.	26
3.2	Scaling of L_2 error for the simulation of channel flow and Couette flow at $Re = 100$	32
3.3	Temporal velocity evolution of a sedimenting sphere. . . .	34
4.1	Schematic of the overlapping grid interface between two levels in one (bottom) and two (top) dimensions.	39
4.2	Snapshot of the turbulent channel, visualized by isosurfaces of Q -criterion colored by velocity magnitude.	51
4.3	Slice through the turbulent channel flow for $Re_\tau = 180$ (top) and $Re_\tau = 590$ (bottom) showing a snapshot of the streamwise velocity.	52
4.4	Mean velocity profile in a turbulent channel at $Re_\tau = 180$.	53
4.5	Rms velocity profile in a turbulent channel at $Re_\tau = 180$.	54
4.6	Mean velocity profiles in a turbulent channel at $Re_\tau = 590$	55
4.7	Rms velocity profiles in a turbulent channel at $Re_\tau = 590$ with a two-level refinement in the near-wall region (left) and the non-refined case (right). For the legend please refer to figure 4.5.	56
4.8	Slice through the turbulent channel flow at $Re_\tau = 590$ showing the spatial distribution of the stabilizer γ for the KBC model and the refinement patches (only left half shown here).	57
4.9	Isosurfaces of Q -criterion colored by velocity magnitude for the flow past a sphere at $Re = 3700$	58
4.10	Mean streamwise velocity profiles in the wake for the simulation of flow past a sphere at $Re = 3700$	59

4.11	Pressure coefficient distribution around the sphere at $Re = 3700$	60
4.12	Volume rendering of temperature for the Rayleigh-Bénard convection at $Ra = 10^7$	61
4.13	Rayleigh-Bénard convection at $Ra = 10^7$	62
4.14	Slice through the Rayleigh-Bénard convection at $Ra = 10^7$ showing the spatial distribution of the stabilizer γ for the KBC model and the refinement patch (only left half shown here).	63
4.15	Flow past a heated sphere at $Re = 3700$	64
4.16	Flow around a NACA0012 airfoil at $\mathcal{A} = 0^\circ$, $Ma = 1.5$ and $Re = 10000$	65
4.17	Snapshot of the distribution of the entropic estimate α around the NACA0012 airfoil.	66
4.18	Schematic of the semi-Lagrangian streaming step of population $f_i(\mathbf{x}, t)$ along the discrete velocity \mathbf{c}_i	68
4.19	Schematic of the boundary condition for the population $f_i(\mathbf{x}_b, t)$	70
4.20	Scaling of the L_2 error for the simulation of the flow past a circular cylinder at $Re = 40$	71
4.21	Comparison of the mean pressure and skin friction coefficient distribution around the cylinder at $Re = 40$ with the reference [345].	72
4.22	Unstructured mesh for the simulation of the flow past a cylinder at $Re = 3900$	73
4.23	Comparison of the mean pressure and skin friction coefficient distribution around the cylinder at $Re = 3900$ with literature data.	74
4.24	Mean streamwise velocity \bar{u}_x/u_∞ profiles in the near wake of a circular cylinder at $Re = 3900$	75
4.25	Mean transverse velocity \bar{u}_y/u_∞ profiles in the near wake of a circular cylinder at $Re = 3900$. See figure 4.24 for the legend.	76
4.26	Isosurfaces of the Q -criterion, colored by streamwise velocity.	77

5.1	(a) Vortex structures for the periodic Kida vortex flow at $\text{Re} = 6000$ ($x, y, z \in [0, \pi]$). (b) Turbulent pipe flow at $\text{Re}^+ = 180$, visualized by isosurfaces of vorticity magnitude and colored with velocity magnitude.	86
5.2	Statistics for the Kida vortex flow at $\text{Re} = 6000$ and resolutions of $N = \{100, 200, 400\}$ and $N = 600$ for the simulations with KBC and the reference simulation with LBGK, respectively. The theoretical Kolmogorov scaling is indicated by the dotted line.	87
5.3	Mean velocity component in flow direction for the turbulent pipe flow.	91
5.4	Rms velocity profiles for the turbulent pipe flow. The legend is identical to figure 5.3.	92
5.5	Schematic of the valve/piston assembly (all measures are given in mm).	93
5.6	Comparison of streamlines of the averaged velocity field. From left to right: Present results, DNS and experimental data are shown for different crank angles, respectively.	94
5.7	Instantaneous velocity magnitude snapshot at 77CA.	95
5.8	Comparison of the ensemble and azimuthally averaged axial mean and rms velocities at 36CA for a resolution of $D_{c,lb} = 300$	96
5.9	Comparison of the ensemble and azimuthally averaged axial mean and rms velocities at 90CA for a resolution of $D_{c,lb} = 300$	97
5.10	Comparison of the ensemble and azimuthally averaged axial mean and rms velocities at 144CA for a resolution of $D_{c,lb} = 300$	98
5.11	Comparison of the ensemble and azimuthally averaged turbulent kinetic energy k and the Reynolds stress component $\overline{u'_r u'_r}$ at 90CA for a resolution of $D_{c,lb} = 300$	99
5.12	Comparison of the ensemble and azimuthally averaged Reynolds stress components $\overline{u'_\varphi u'_\varphi}$ and $\overline{u'_z u'_r}$ at 90CA for a resolution of $D_{c,lb} = 300$	100
5.13	Comparison of the ensemble and azimuthally averaged axial mean and rms velocities at 90CA for different resolutions.	101

5.14	Cyclic variation of the vortex ring at BDC visualized by pressure isosurfaces for $D_{c,lb} = 300$	102
5.15	Cyclic variation for all resolutions of $D_{c,lb} = \{100, 150, 300\}$ and the DNS results, quantified by mean jet radius $\overline{r_{jet}}/r_c$ at 45CA and correlated to the mean radial velocity $\overline{u_{r,T}}/u_{p,mean}$ at TDC. Lines represent a linear fit through the corresponding data points.	103
6.1	Multi-domain block refinement for the flow past the <i>SD7003</i> airfoil along with a slice of instantaneous streamwise velocity.	111
6.2	Isosurfaces of the Q-criterion ($Q = 4$) colored by normalized streamwise velocity for the simulation of the <i>SD7003</i> airfoil at an angle of attack $\alpha = 4^\circ$ and a Reynolds number $Re = 6 \cdot 10^4$	113
6.3	Instantaneous snapshot of the spatial distribution of the stabilizer γ	114
6.4	Average pressure coefficient $\overline{C_p}$ over the upper and lower surface of the <i>SD7003</i> airfoil. Here and in the following, the symbols represent sampled values along the chord for clarity.	115
6.5	Average skin friction coefficient $\overline{C_f}$ over the upper and lower surface of the airfoil of the <i>SD7003</i> airfoil.	116
6.6	Determination of the onset to transition. (a): Distribution of Reynolds shear stress $-u'_x u'_z / u_\infty^2$ with a threshold of 0.001. (b): Reynolds shear stress value plotted along the line of maximum shear stress.	117
6.7	Mean velocity profiles at $x/c = 0.1 \sim 0.5$	118
6.8	Spectra of fluctuating streamwise velocity along the span.	119
6.9	Power spectral density for two observer points, one within the bubble and one in the near wake.	120
6.10	LSB dynamics.	120
6.11	Computational set-up for the flow over an <i>T106</i> turbine blade.	121
6.12	Flow in a low-pressure turbine passage at $Re = 1.48 \cdot 10^5$, visualized by vorticity isosurfaces colored by streamwise velocity. (a): Uniform inflow. (b): Turbulent inflow.	122
6.13	Distribution of the mean pressure coefficient over the axial chord of the <i>T106</i> turbine blade at $Re = 1.48 \cdot 10^5$	123

6.14	Snapshot of isosurfaces of the Q-criterion ($Q = 200$) colored by normalized streamwise velocity at $Re = 1.48 \cdot 10^5$. Left: $Tu = 0\%$. Right: $Tu = 0.2\%$	124
6.15	Distribution of the mean skin friction coefficient over the axial chord on the suction side of the $T106$ turbine blade at $Re = 1.48 \cdot 10^5$	125
6.16	Snapshot of isosurfaces of the Q-criterion ($Q = 110$) colored by normalized streamwise velocity at $Re = 6 \cdot 10^4$. Left: $Tu = 0\%$. Middle: $Tu = 5\%$. Right: $Tu = 10\%$	126
6.17	Average skin friction coefficient over suction side of the $T106$ blade for varying free-stream turbulence intensities at $Re = 6 \cdot 10^4$	128
6.18	Average pressure coefficient over suction side of the $T106$ blade for varying free-stream turbulence intensities at $Re = 6 \cdot 10^4$	129
6.19	Streamwise velocity profiles (tangent to the suction side of the blade surface) as a function of the normal distance for $x/C_{ax} = 0.88 - 0.99$ in steps of $0.1C_{ax}$ at $Re = 6 \cdot 10^4$. (a): Mean streamwise velocity. (b): Rms streamwise velocity. For the legend see figure 6.18.	130
7.1	Schematic of a plunging airfoil.	134
7.2	Volume rendering of vorticity for various phases of the plunging airfoil. (a): $\varphi = 0$. (b): $\varphi = 0.25$. (c): $\varphi = 0.5$. (d): $\varphi = 0.75$	135
7.3	Phase-averaged velocity profiles at $x/c = 1.5$	136
7.4	Phase-averaged velocity profiles at $x/c = 2$	137
7.5	Evolution of lift and drag coefficient over three exemplary cycles of a plunging airfoil.	138
7.6	Volume rendering of vorticity of the swimmers wake, showing the typical double row vortex street.	141
7.7	Temporal evolution of the forward velocity U_{\parallel} and lateral velocity U_{\perp}	143
7.8	Left: Wing planform. Right: Wing kinematics during the upstroke.	144
7.9	Volume rendering of vorticity for a <i>Drosophila</i> wing during the upstroke of the third cycle.	145

7.10	Evolution of the lift coefficient and comparison to experimental and numerical data.	146
7.11	Volume rendering of vorticity for a body-wing assembly during the third stroke.	147
7.12	Volume rendering of vorticity of three anguilliform swimmers.	148
8.1	Schematic - Turek Benchmark.	159
8.2	CSM3: x - and y -displacement of the beam tip.	160
8.3	Snapshot of the computational domain, zoomed in on the cylinder-flag assembly.	161
8.4	FSI3: Snapshot of velocity magnitude.	162
8.5	FSI3: Evolution of the flag tip deflection in x - and y -direction.	162
8.6	Schematic of the flow past a flapping flag	163
8.7	Flow past a flapping flag.	164
8.8	Wake of a flapping flag visualized by isosurfaces of Q-criterion and colored by streamwise velocity.	165
8.9	Flexible plate in a cross flow: Isosurfaces of Q-criterion, colored by velocity magnitude.	167
8.10	Maximum droplet spreading diameter on a flat superhydrophobic surface in the low viscosity limit.	171
8.11	Maximum droplet spreading diameter on rigid and elastic superhydrophobic surfaces.	172
8.12	Droplet spreading on rigid (left) and elastic (right) superhydrophobic surfaces. Timings are normalized by the contact time T_s of the rigid surface.	173

Bibliography

- [1] H. T. Ahn and Y. Kallinderis. “Strongly coupled flow/structure interactions with a geometrically conservative ALE scheme on general hybrid meshes”. In: *Journal of Computational Physics* 219.2 (2006), pp. 671–696.
- [2] K Ahuja and R Burrin. “Control of flow separation by sound”. In: *9th Aeroacoustics Conference*. 1984, p. 2298.
- [3] M Alam and N. D. Sandham. “Direct numerical simulation of ‘short’ laminar separation bubbles with turbulent reattachment”. In: *Journal of Fluid Mechanics* 410 (2000), pp. 1–28.
- [4] N. Amini and Y. a. Hassan. *Fundamentals of Multiphase Flow Fundamentals of Multiphase Flow*. Cambridge university press, 2005, pp. 4–5.
- [5] S. Ansumali, I. V. Karlin, C. E. Frouzakis, and K. B. Boulouchos. “Entropic lattice Boltzmann method for microflows”. In: *Physica A: Statistical Mechanics and its Applications* 359.1-4 (2006), pp. 289–305.
- [6] S. Ansumali, I. V. Karlin, and H. C. Öttinger. “Minimal entropic kinetic models for hydrodynamics”. In: *Europhysics Letters* 63.6 (2003), pp. 798–804.
- [7] S Ansumali, S Arcidiacono, S. Chikatamarla, N. Prasianakis, A. Gorban, and I. Karlin. “Quasi-equilibrium lattice Boltzmann method”. In: *The European Physical Journal B* 56.2 (2007), pp. 135–139.
- [8] S. Ansumali and I. V. Karlin. “Consistent lattice Boltzmann method”. In: *Physical review letters* 95.26 (2005), p. 260605.
- [9] S. Ansumali and I. V. Karlin. “Entropy function approach to the lattice Boltzmann method”. In: *Journal of Statistical Physics* 107.1 (2002), pp. 291–308.

-
- [10] S. Ansumali and I. V. Karlin. “Single relaxation time model for entropic lattice Boltzmann methods”. In: *Physical Review E* 65.5 (2002), p. 056312.
- [11] S. Ansumali and I. V. Karlin. “Stabilization of the lattice Boltzmann method by the H theorem: A numerical test”. In: *Physical Review E* 62.6 (2000), p. 7999.
- [12] I. Aoki. “A Simulation Study on the Schooling Mechanism in Fish”. In: *Bulletin of the Japanese Society of Scientific Fisheries* 48(8) (1982), pp. 1081–1088.
- [13] J. A. Bærentzen and H. Aanaes. “Signed distance computation using the angle weighted pseudonormal”. In: *IEEE Transactions on Visualization and Computer Graphics* 11.3 (2005), pp. 243–253.
- [14] W. Balzer and H. Fasel. “Direct numerical simulation of laminar boundary-layer separation and separation control on the suction side of an airfoil at low Reynolds number conditions”. In: *40th Fluid Dynamics Conference and Exhibit*. 2010, p. 4866.
- [15] W. Bangerth, R. Hartmann, and G. Kanschat. “deal.II—A general-purpose object-oriented finite element library”. In: *ACM Transactions on Mathematical Software* 33.4 (2007), p. 24.
- [16] A. Bardow, I. Karlin, and A. Gusev. “General characteristic-based algorithm for off-lattice Boltzmann simulations”. In: *Europhys. Lett.* 75 (2006), 434440.
- [17] G. Barenblatt, A. Chorin, and V. Prostokishin. “Scaling laws for fully developed turbulent flow in pipes”. In: *Applied Mechanics Reviews* 50.7 (1997), pp. 413–429.
- [18] T. K. Barlas and G. A. van Kuik. “Review of state of the art in smart rotor control research for wind turbines”. In: *Progress in Aerospace Sciences* 46.1 (2010), pp. 1–27.
- [19] G. K. Batchelor. *An Introduction to Fluid Dynamics*. Cambridge University Press, 2000.
- [20] K. K. Bathe. *Finite Element Procedures*. 2006, p. 1073.

- [21] P. Beaudan and P. Moin. “Numerical experiments on the flow past a circular cylinder at sub-critical Reynolds number”. In: *Report No. TF-62, Department of Mechanical Engineering, Stanford University* (1994).
- [22] A. D. Becker, H. Masoud, J. W. Newbolt, M. Shelley, and L. Ristroph. “Hydrodynamic schooling of flapping swimmers”. In: *Nature Communications* 6.May (2015), p. 8514.
- [23] S. Beskhyroun, L. D. Wegner, and B. F. Sparling. “New methodology for the application of vibration-based damage detection techniques”. In: *Structural Control and Health Monitoring* 19.1 (2011), pp. 88–106.
- [24] P. L. Bhatnagar, E. P. Gross, and M. Krook. “A model for collision processes in gases. I. Small amplitude processes in charged and neutral one-component systems”. In: *Physical review* 94.3 (1954), p. 511.
- [25] B. Bhushan and Y. C. Jung. “Natural and biomimetic artificial surfaces for superhydrophobicity, self-cleaning, low adhesion, and drag reduction”. In: *Progress in Materials Science* 56.1 (2011), pp. 1–108.
- [26] F. Bigoni, S. Vagnoli, T. Arts, and T. Verstraete. “Detailed Numerical Characterization of the Suction Side Laminar Separation Bubble for a High-Lift Low Pressure Turbine Blade by Means of RANS and LES”. In: *ASME Turbo Expo 2016: Turbomachinery Technical Conference and Exposition*. American Society of Mechanical Engineers. 2016, V02DT44A015–V02DT44A015.
- [27] J. M. Birch and M. H. Dickinson. “Spanwise flow and the attachment of the leading-edge vortex on insect wings.” In: *Nature* 412.6848 (2001), pp. 729–733.
- [28] J. M. Birch and M. H. Dickinson. “The influence of wing-wake interactions on the production of aerodynamic forces in flapping flight”. In: *Journal of Experimental Biology* 206.13 (2003), pp. 2257–2272.
- [29] G. Bird. “Approach to translational equilibrium in a rigid sphere gas”. In: *Physics of Fluids (1958-1988)* 6.10 (1963), pp. 1518–1519.

-
- [30] J. C. Bird, R. Dhiman, H.-M. Kwon, and K. K. Varanasi. “Reducing the contact time of a bouncing drop.” In: *Nature* 503.7476 (2013), pp. 385–388.
- [31] R. Blossey. “Self-cleaning surfacesvirtual realities”. In: *Nature materials* 2.5 (2003), pp. 301–306.
- [32] B. M. Boghosian, J. Yopez, P. V. Coveney, and A. Wager. “Entropic lattice Boltzmann methods”. In: *Proceedings of the Royal Society of London A: Mathematical, Physical and Engineering Sciences*. Vol. 457. 2007. The Royal Society. 2001, pp. 717–766.
- [33] A. V. Boiko, G. R. Grek, A. V. Dovgal, and V. V. Kozlov. *The origin of turbulence in near-wall flows*. Springer Science & Business Media, 2002.
- [34] I Borazjani and F Sotiropoulos. “Numerical investigation of the hydrodynamics of anguilliform swimming in the transitional and inertial flow regimes”. In: *Journal of Experimental Biology* 212.4 (2009), pp. 576–592.
- [35] I. Borazjani and F. Sotiropoulos. “Numerical investigation of the hydrodynamics of carangiform swimming in the transitional and inertial flow regimes”. In: *Journal of Experimental Biology* 211.10 (2008), pp. 1541–1558.
- [36] I. Borazjani, L. Ge, and F. Sotiropoulos. “Curvilinear immersed boundary method for simulating fluid structure interaction with complex 3D rigid bodies”. In: *Journal of Computational Physics* 227.16 (2008), pp. 7587–7620.
- [37] I. Borazjani, L. Ge, and F. Sotiropoulos. “High-resolution fluid-structure interaction simulations of flow through a bi-leaflet mechanical heart valve in an anatomic aorta”. In: *Annals of Biomedical Engineering* 38.2 (2010), pp. 326–344.
- [38] F Bösch and I. Karlin. “Exact lattice Boltzmann equation”. In: *Physical review letters* 111.9 (2013), p. 090601.
- [39] F. Bösch, S. S. Chikatamarla, and I. Karlin. “Entropic Multi-Relaxation Models for Simulation of Fluid Turbulence”. In: *ESAIM. Proceedings and Surveys* 52 (2015), 1–24.

- [40] F. Bösch, S. S. Chikatamarla, and I. V. Karlin. “Entropic multirelaxation lattice Boltzmann models for turbulent flows”. In: *Phys. Rev. E* 92.4 (2015), p. 43309.
- [41] M. S. H. Boutilier and S. Yarusevych. “Parametric study of separation and transition characteristics over an airfoil at low Reynolds numbers”. In: *Experiments in Fluids* 52.6 (2012), pp. 1491–1506.
- [42] M. S. Boutilier and S. Yarusevych. “Separated shear layer transition over an airfoil at a low Reynolds number”. In: *Physics of Fluids* 24.8 (2012), p. 084105.
- [43] M. Bouzidi, M. Firdaouss, and P. Lallemand. “Momentum transfer of a Boltzmann-lattice fluid with boundaries”. In: *Physics of fluids* 13.11 (2001), pp. 3452–3459.
- [44] S. Burgmann, J. Dannemann, and W. Schröder. “Time-resolved and volumetric PIV measurements of a transitional separation bubble on an SD7003 airfoil”. In: *Experiments in Fluids* 44.4 (2008), pp. 609–622.
- [45] F. Cadieux, J. A. Domaradzki, T. Sayadi, and S. Bose. “Direct Numerical Simulation and Large Eddy Simulation of Laminar Separation Bubbles at Moderate Reynolds Numbers”. In: *Journal of Fluids Engineering* 136.6 (2014), p. 60902.
- [46] F. Cadieux and J. A. Domaradzki. “Performance of subgrid-scale models in coarse large eddy simulations of a laminar separation bubble”. In: *Physics of Fluids* 27.4 (2015), p. 045112.
- [47] J. Carling, T. L. Williams, and G. Bowtell. “Self-propelled anguilliform swimming: Simultaneous solution of the two-dimensional Navier-Stokes equations and Newton’s laws of motion”. In: *Journal of Experimental Biology* 201.23 (1998), pp. 3143–3166.
- [48] P. Causin, J. F. Gerbeau, and F. Nobile. “Added-mass effect in the design of partitioned algorithms for fluid-structure problems”. In: *Computer Methods in Applied Mechanics and Engineering* 194.42-44 (2005), pp. 4506–4527.
- [49] I. Celik, I. Yavuz, and A. Smirnov. “Large eddy simulations of in-cylinder turbulence for internal combustion engines: A review”. In: *International Journal of Engine Research* 2.2 (2001), pp. 119–148.

- [50] C. Cercignani. *Theory and application of the Boltzmann equation*. Scottish Academic Press, 1975.
- [51] C. Cercignani, R. Illner, and M. Pulvirenti. *The mathematical theory of dilute gases*. Vol. 106. Springer Science & Business Media, 2013.
- [52] S. Chapman and T. G. Cowling. *The mathematical theory of non-uniform gases: an account of the kinetic theory of viscosity, thermal conduction and diffusion in gases*. Cambridge university press, 1970.
- [53] H. Chen, O. Filippova, J. Hoch, K. Molvig, R. Shock, C. Teixeira, and R. Zhang. “Grid refinement in lattice Boltzmann methods based on volumetric formulation”. In: *Physica A: Statistical Mechanics and its Applications* 362.1 (2006), pp. 158–167.
- [54] H. Chen, S. Kandasamy, S. Orszag, R. Shock, S. Succi, and V. Yakhot. “Extended Boltzmann Kinetic Equation for Turbulent Flows”. In: *Science* 301.5633 (2003), pp. 633–636.
- [55] H. Chen, S. Chen, and W. H. Matthaeus. “Recovery of the Navier-Stokes equations using a lattice-gas Boltzmann method”. In: *Physical Review A* 45.8 (1992), R5339.
- [56] S. Chen, H. Chen, D. Martnez, and W. Matthaeus. “Lattice Boltzmann model for simulation of magnetohydrodynamics”. In: *Physical Review Letters* 67.27 (1991), p. 3776.
- [57] J.-Y. Cheng, L.-X. Zhuang, and B.-G. Tong. “Analysis of swimming three-dimensional waving plates”. In: *Journal of Fluid Mechanics* 232 (1991), pp. 341–355.
- [58] M Cheng and K. C. Hung. “Lattice Boltzmann method on nonuniform mesh”. In: *International Journal of Computational Engineering Science* 5.02 (2004), pp. 291–302.
- [59] S. S. Chikatamarla and I. Karlin. “Entropic lattice Boltzmann method for turbulent flow simulations: Boundary conditions”. In: *Physica A: Statistical Mechanics and its Applications* 392.9 (2013), pp. 1925–1930.
- [60] S. S. Chikatamarla, C. E. Frouzakis, I. V. Karlin, a. G. Tomboulides, and K. B. Boulouchos. “Lattice Boltzmann method for direct numerical simulation of turbulent flows”. In: *Journal of Fluid Mechanics* 656 (2010), pp. 298–308.

-
- [61] S. S. Chikatamarla and I. V. Karlin. “Entropic lattice Boltzmann method for turbulent flow simulations: Boundary conditions”. In: *Physica A: Statistical Mechanics and its Applications* 392.9 (2013), pp. 1925–1930.
- [62] S. S. Chikatamarla and I. V. Karlin. “Entropy and Galilean Invariance of Lattice Boltzmann Theories”. In: *Phys. Rev. Lett.* 97 (19 2006), p. 190601.
- [63] S. Chikatamarla, C. Frouzakis, I. Karlin, A. Tomboulides, and K. Boulouchos. “Lattice Boltzmann method for direct numerical simulation of turbulent flows”. In: *Journal of Fluid Mechanics* 656 (2010), pp. 298–308.
- [64] C. Clanet, C. Béguin, D. Richard, and D. Quéré. “Maximal deformation of an impacting drop”. In: *Journal of Fluid Mechanics* 517 (2004), pp. 199–208.
- [65] I. D. Couzin, J Krause, N. R. Franks, and S. A. Levin. “Effective leadership and decision-making in animal groups on the move”. In: *Nature* 433.7025 (2005), pp. 513–516.
- [66] M. D. De Tullio, a. Cristallo, E. Balaras, and R. Verzicco. “Direct numerical simulation of the pulsatile flow through an aortic bileaflet mechanical heart valve”. In: *Journal of Fluid Mechanics* 622 (2009), p. 259.
- [67] D. D’Humières. “Generalized Lattice-Boltzmann Equations”. In: *Rarefied Gas Dynamics: Theory and Simulations*. Progress in Astronautics and Aeronautics. American Institute of Aeronautics and Astronautics, 1994, pp. 450–458.
- [68] G Di Ilio, D Chiappini, S Ubertini, G Bella, and S Succi. “Hybrid lattice Boltzmann method on overlapping grids”. In: *Physical Review E* 95.1 (2017), p. 013309.
- [69] G. Di Ilio, B. Dorschner, G. Bella, S. Succi, and I. V. Karlin. “Simulation of turbulent flows with the entropic multirelaxation time lattice Boltzmann method on body-fitted meshes”. In: *Submitted to Journal of Fluid Mechanics* (2018).

-
- [70] M. H. Dickinson, C. T. Farley, R. J. Full, M. Koehl, R. Kram, and S. Lehman. “How animals move: an integrative view”. In: *Science* 288.5463 (2000), pp. 100–106.
- [71] M. H. Dickinson, F.-O. Lehmann, and S. P. Sane. “Wing rotation and the aerodynamic basis of insect flight”. In: *Science* 284.5422 (1999), pp. 1954–1960.
- [72] S. Dong, G. Karniadakis, A. Ekmekci, and D. Rockwell. “A combined direct numerical simulation-particle image velocimetry study of the turbulent near wake”. In: *J. Fluid Mech.* 569 (2006), 185207.
- [73] B. Dorschner, S. S. Chikatamarla, and I. V. Karlin. “Entropic multi-relaxation time lattice Boltzmann method for moving and deforming geometries in three dimensions”. In: *Phys. Rev. E* 95 (6 2017), p. 063306.
- [74] B. Dorschner, F. Bösch, S. Chikatamarla, K. Boulouchos, and I. Karlin. “Entropic Multi-Relaxation Time Lattice Boltzmann Model for Complex Flows”. In: *Journal of Fluid Mechanics* 801 (2016), pp. 623–651.
- [75] B. Dorschner, S. S. Chikatamarla, and I. V. Karlin. “Fluid-structure interaction with the entropic lattice Boltzmann method”. In: *Phys. Rev. E* 97 (2 2018), p. 023305.
- [76] B. Dorschner, S. Chikatamarla, F. Bösch, and I. Karlin. “Grad’s approximation for moving and stationary walls in entropic lattice Boltzmann simulations”. In: *Journal of Computational Physics* 295 (2015), pp. 340–354.
- [77] B. Dorschner, N. Frapolli, S. S. Chikatamarla, and I. V. Karlin. “Grid refinement for entropic lattice Boltzmann models”. In: *Phys. Rev. E* 94 (5 2016), p. 053311.
- [78] B. Dorschner, S. S. Chikatamarla, and I. V. Karlin. “Transitional Flows with the Entropic Lattice Boltzmann Method”. In: *Journal of Fluid Mechanics* 824 (2017), pp. 388–412.
- [79] A. V. Dovgal, V. V. Kozlov, and A. Michalke. “Laminar boundary layer separation: Instability and associated phenomena”. In: *Progress in Aerospace Sciences* 30.1 (1994), pp. 61–94.

- [80] E. H. Dowell and K. C. Hall. “Modeling of Fluid-Structure Interaction”. In: *Annual Review in Fluid Mechanics* 33.1 (2001), pp. 445–490.
- [81] R. Du, Z. Li, K. Youcef-Toumi, and P. Valdivia y Alvarado. *Robot Fish: Bio-inspired Fishlike Underwater Robots*. 2015, p. 377.
- [82] A. Dupuis and B. Chopard. “Theory and applications of an alternative lattice Boltzmann grid refinement algorithm.” In: *Physical Review E* 67.6 Pt 2 (2003), p. 066707.
- [83] H. Eckelmann. “The structure of the viscous sublayer and the adjacent wall region in a turbulent channel flow”. In: *Journal of Fluid Mechanics* 65.03 (1974), p. 439.
- [84] S. Eisenbach and R. Friedrich. “Large-eddy simulation of flow separation on an airfoil at a high angle of attack and $Re = 10^5$ using Cartesian grids”. In: *Theoretical and Computational Fluid Dynamics* 22.3-4 (2008), pp. 213–225.
- [85] G. Eitel-Amor, M. Meinke, and W. Schröder. “A lattice-Boltzmann method with hierarchically refined meshes”. In: *Computers and Fluids* 75 (2013), pp. 127–139.
- [86] O. Ekeberg. “A combined neuronal and mechanical model of fish swimming”. In: *Biological Cybernetics* 69.5-6 (1993), pp. 363–374.
- [87] S. H. El Tahry and D. C. Haworth. “Directions in turbulence modeling for in-cylinder flows in reciprocating engines”. In: *Journal of Propulsion and Power* 8.5 (1992), pp. 1040–1048.
- [88] M Engber and L Fottner. “The effect of incoming wakes on boundary layer transition of a highly loaded turbine cascade”. In: *AGARD Conference Proceedings*. 1996, p. 21.
- [89] E. Fadlun, R Verzicco, P. Orlandi, and J Mohd-Yusof. “Combined immersed-boundary finite-difference methods for three-dimensional complex flow simulations”. In: *Journal of computational physics* 161.1 (2000), pp. 35–60.
- [90] A. Fakhari and T. Lee. “Numerics of the lattice Boltzmann method on nonuniform grids: standard LBM and finite-difference LBM”. In: *Computers & Fluids* 107 (2015), pp. 205–213.

-
- [91] G. Falcucci, E. Jannelli, S. Ubertini, and S. Succi. “Direct numerical evidence of stress-induced cavitation”. In: *Journal of Fluid Mechanics* 728 (Aug. 2013), pp. 362–375.
- [92] G. Falcucci, S. Ubertini, G. Bella, A. De Maio, and S. Palpacelli. “Lattice Boltzmann modeling of Diesel spray formation and break-up”. In: *SAE International Journal of Fuels and Lubricants* 3.1 (2010), pp. 582–593.
- [93] C. Farhat, K. G. van der Zee, and P. Geuzaine. “Provably second-order time-accurate loosely-coupled solution algorithms for transient nonlinear computational aeroelasticity”. In: *Computer Methods in Applied Mechanics and Engineering* 195.17-18 (2006), pp. 1973–2001.
- [94] Z.-G. Feng and E. E. Michaelides. “Proteus: A direct forcing method in the simulations of particulate flows”. In: *Journal of Computational Physics* 202.1 (2005), pp. 20–51.
- [95] Z.-G. Feng and E. E. Michaelides. “Robust treatment of no-slip boundary condition and velocity updating for the lattice-Boltzmann simulation of particulate flows”. In: *Computers & Fluids* 38.2 (2009), pp. 370–381.
- [96] O. Filippova and D. Hänel. “Boundary-Fitting and Local Grid Refinement for Lattice-BGK Models”. In: *International Journal of Modern Physics C* 09.08 (1998), pp. 1271–1279.
- [97] O. Filippova and D. Hänel. “Lattice-Boltzmann simulation of gas-particle flow in filters”. In: *Computers & Fluids* 26.7 (1997), pp. 697–712.
- [98] C. Förster, W. A. Wall, and E. Ramm. “Artificial added mass instabilities in sequential staggered coupling of nonlinear structures and incompressible viscous flows”. In: *Computer Methods in Applied Mechanics and Engineering* 196.7 (2007), pp. 1278–1293.
- [99] N. Frapolli, S. S. Chikatamarla, and I. V. Karlin. “Entropic lattice Boltzmann model for compressible flows”. In: *Physical Review E* 92.6 (2015), p. 061301.

- [100] N Frapolli, S. Chikatamarla, and I. Karlin. “Entropic lattice Boltzmann model for gas dynamics: Theory, boundary conditions, and implementation”. In: *Physical Review E* 93.6 (2016), p. 063302.
- [101] N Frapolli, S. Chikatamarla, and I. Karlin. “Lattice Kinetic Theory in a Comoving Galilean Reference Frame”. In: *Physical Review Letters* 117.1 (2016), p. 010604.
- [102] N. Frapolli, S. S. Chikatamarla, and I. V. Karlin. “Multispeed entropic lattice Boltzmann model for thermal flows”. In: *Physical Review E* 90.4 (2014), p. 043306.
- [103] N. Frapolli, S. S. Chikatamarla, and I. V. Karlin. “Multispeed entropic lattice Boltzmann model for thermal flows”. In: *Physical Review E* 90.4 (2014), p. 043306.
- [104] U. Frisch, B. Hasslacher, and Y. Pomeau. “Lattice-gas automata for the Navier-Stokes equation”. In: *Physical review letters* 56.14 (1986), p. 1505.
- [105] J. C. H. Fung, J. C. Hunt, N. Malik, and R. Perkins. “Kinematic simulation of homogeneous turbulence by unsteady random Fourier modes”. In: *Journal of Fluid Mechanics* 236 (1992), pp. 281–318.
- [106] M. C. Galbraith and M. R. Visbal. “Implicit large eddy simulation of low Reynolds number flow past the SD7003 airfoil”. In: *AIAA paper* 225 (2008), pp. 1–17.
- [107] M. Gaster. “Laminar Separation Bubbles”. In: *Sixth IUTAM Symposium on Laminar-Turbulent Transition* (2006), pp. 1–13.
- [108] M Gaster. “On the stability of parallel flows and the behaviour of separation bubbles”. PhD thesis. Queen Mary, University of London, 1963.
- [109] M Gaster. “Stability of velocity profiles with reverse flow”. In: *Instability, Transition, and Turbulence*. Springer, 1992, pp. 212–215.
- [110] M. Gazzola, A. A. Tchieu, D. Alexeev, A. de Brauer, and P. Koumoutsakos. “Learning to school in the presence of hydrodynamic interactions”. In: *Journal of Fluid Mechanics* 789.1 (2016), pp. 726–749.

- [111] M Gehrke, C. Janßen, and T Rung. “Scrutinizing Lattice Boltzmann methods for direct numerical simulations of turbulent channel flows”. In: *Computers & Fluids* 156 (2017), pp. 247–263.
- [112] M. Geier, A. Greiner, and J. G. Korvink. “Cascaded digital lattice Boltzmann automata for high Reynolds number flow”. In: *Phys. Rev. E* 73 (6 2006), p. 066705.
- [113] M. Geier, M. Schönherr, A. Pasquali, and M. Krafczyk. “The cumulant lattice Boltzmann equation in three dimensions: Theory and validation”. In: *Computers & Mathematics with Applications* 70.4 (2015), pp. 507–547.
- [114] R. Gerakopulos, M. Boutilier, and S. Yarusevych. “Aerodynamic Characterization of a NACA 0018 Airfoil at Low Reynolds Numbers”. In: *40th Fluid dynamics conference and Exhibit. Fluid Dynamics and Co-located Conferences*. American Institute of Aeronautics and Astronautics, 2010, p. 4629.
- [115] A. Gilmanov and F. Sotiropoulos. “A hybrid Cartesian/immersed boundary method for simulating flows with 3D, geometrically complex, moving bodies”. In: *Journal of Computational Physics* 207.2 (2005), pp. 457–492.
- [116] A. N. Gorban and I. V. Karlin. *Invariant Manifolds for Physical and Chemical Kinetics*. Vol. 660. Springer, Lect. Notes Phys, 2004.
- [117] A. N. Gorban and I. V. Karlin. “General approach to constructing models of the Boltzmann equation”. In: *Physica A: Statistical Mechanics and its Applications* 206.3-4 (1994), pp. 401–420.
- [118] H. Grad. “On the kinetic theory of rarefied gases”. In: *Communications on pure and applied mathematics* 2.4 (1949), pp. 331–407.
- [119] H. Grad. “Principles of the kinetic theory of gases”. In: *Thermodynamik der Gase/Thermodynamics of Gases*. Springer, 1958, pp. 205–294.
- [120] B. Y. J. Gray. “Studies in animal locomotion III”. In: *Journal of Experimental Biology* 3 (1933), pp. 386–400.

- [121] B. E. Griffith, R. D. Hornung, D. M. McQueen, and C. S. Peskin. “An adaptive, formally second order accurate version of the immersed boundary method”. In: *Journal of Computational Physics* 223.1 (2007), pp. 10–49.
- [122] Z. Guo, C. Zheng, and B. Shi. “An extrapolation method for boundary conditions in lattice Boltzmann method”. In: *Physics of Fluids* 14.6 (2002), pp. 2007–2010.
- [123] E. Gutmark and I. Wygnanski. “The planar turbulent jet”. In: *Journal of Fluid Mechanics* 73.03 (1976), pp. 465–495.
- [124] R. D. Guy and D. A. Hartenstine. “On the accuracy of direct forcing immersed boundary methods with projection methods”. In: *Journal of Computational Physics* 229.7 (2010), pp. 2479–2496.
- [125] I. Hadzic and K. Hanjalic. “Separation-induced transition to turbulence : second-moment closure modelling”. In: *Flow, Turbulence and Combustion* (2000), pp. 153–173.
- [126] M. Hafez and E. Wahba. “Simulations of viscous transonic flows over lifting airfoils and wings”. In: *Computers & Fluids* 36.1 (2007), pp. 39–52.
- [127] R. Hain, C. J. Kähler, and R. Radespiel. “Dynamics of laminar separation bubbles at low-Reynolds-number aerofoils”. In: *Journal of Fluid Mechanics* 630 (2009), pp. 129–153.
- [128] D. C. Haworth. “Large-eddy simulation of in-cylinder flows”. In: *Oil & Gas Science and Technology* 54.2 (1999), pp. 175–185.
- [129] K. Hejranfar and E. Ezzatneshan. “Implementation of a high-order compact finite-difference lattice Boltzmann method in generalized curvilinear coordinates”. In: *Journal of Computational Physics* 267 (2014), pp. 28–49.
- [130] J. Hermansson and P. Hansbo. “A variable diffusion method for mesh smoothing”. In: *Communications in Numerical Methods in Engineering* 19.11 (2003), pp. 897–908.

- [131] M. A. Heroux, R. A. Bartlett, V. E. Howle, R. J. Hoekstra, J. J. Hu, T. G. Kolda, R. B. Lehoucq, K. R. Long, R. P. Pawlowski, E. T. Phipps, et al. “An overview of the Trilinos project”. In: *ACM Transactions on Mathematical Software (TOMS)* 31.3 (2005), pp. 397–423.
- [132] F. Hess and J. J. Videler. “Fast Continuous Swimming of Saithe (Pollachius Virens): A Dynamic Analysis of Bending Moments and Muscle Power”. In: *Journal of Experimental Biology* 109.1 (1984), pp. 229–251.
- [133] F. Higuera and J Jimenez. “Boltzmann approach to lattice gas simulations”. In: *EPL (Europhysics Letters)* 9.7 (1989), p. 663.
- [134] F. Higuera, S Succi, and R Benzi. “Lattice gas dynamics with enhanced collisions”. In: *EPL (Europhysics Letters)* 9.4 (1989), p. 345.
- [135] F. Higuera and S. Succi. “Simulating the flow around a circular cylinder with a lattice Boltzmann equation”. In: *EPL (Europhysics Letters)* 8.6 (1989), p. 517.
- [136] L. Hilgenfeld, P. Stadtmüller, and L. Fottner. “Experimental Investigation of Turbulence Influence of Wake Passing on the Boundary Layer Development of Highly Loaded Turbine Cascade Blades”. In: *Flow, Turbulence and Combustion* 69.3-4 (2002), pp. 229–247.
- [137] C. W. Hirt, A. A. Amsden, and J. L. Cook. “An arbitrary Lagrangian-Eulerian computing method for all flow speeds”. In: *Journal of Computational Physics* 14.3 (1974), pp. 227–253.
- [138] C.-M. Ho and P. Huerre. “Perturbed free shear layers”. In: *Annual Review of Fluid Mechanics* 16.1 (1984), pp. 365–422.
- [139] H Hodson. “Turbulence modelling for unsteady flows in axial turbine: Turmunsflat”. In: *Brite-Euram Project, Final TR CT96-1043, von Karman Inst* (2000), pp. 85–99.
- [140] G. Hou, J. Wang, and A. Layton. “Numerical methods for fluid-structure interaction - A review”. In: *Communications in Computational Physics* 12.2 (2012), pp. 337–377.
- [141] R. Howard, M. Alam, and N. Sandham. “Two-Equation Turbulence Modelling of a Transitional Separation Bubble”. In: *Flow, Turbulence and Combustion* 63.1 (2000), pp. 175–191.

- [142] R. Howell, N. Qin, J. Edwards, and N. Durrani. “Wind tunnel and numerical study of a small vertical axis wind turbine”. In: *Renewable Energy* 35.2 (2010), pp. 412–422.
- [143] W.-X. Huang and H. J. Sung. “Three-dimensional simulation of a flapping flag in a uniform flow”. In: *Journal of Fluid Mechanics* 653 (2010), pp. 301–336.
- [144] S. Hubbard, P. Babak, S. T. Sigurdsson, and K. G. Magnússon. “A model of the formation of fish schools and migrations of fish”. In: *Ecological Modelling* 174.4 (2004), pp. 359–374.
- [145] A. J. Ijspeert and J. Kodjabachian. “Evolution and Development of a Central Pattern Generator for the Swimming of a Lamprey”. In: *Artificial Life* 5.3 (1999), pp. 247–269.
- [146] T. Inamuro, M. Yoshino, and F. Ogino. “A non-slip boundary condition for lattice Boltzmann simulations”. In: *Physics of fluids* 7.12 (1995), pp. 2928–2930.
- [147] T. A. Johnson and V. C. Patel. “Flow past a sphere up to a Reynolds number of 300”. In: *Journal of Fluid Mechanics* 378 (Jan. 1999), pp. 19–70.
- [148] L. E. Jones, R. Sandberg, and N. D. Sandham. “Stability and receptivity characteristics of a laminar separation bubble on an aerofoil”. In: *Journal of Fluid Mechanics* 48.2 (2010), pp. 414–426.
- [149] L. Jones, R. Sandberg, and N. Sandham. “Direct numerical simulations of forced and unforced separation bubbles on an airfoil at incidence”. In: *Journal of Fluid Mechanics* 602 (2008), pp. 175–207.
- [150] L. E. Jones and R. D. Sandberg. “Numerical analysis of tonal airfoil self-noise and acoustic feedback-loops”. In: *Journal of Sound and Vibration* 330.25 (2011), pp. 6137–6152.
- [151] A. Jusufi, D. Vogt, R. J. Wood, and G. V. Lauder. “Undulatory Swimming in Performance and Body Stiffness Modulation in a Soft Robotic Fish Model”. In: *Soft Robotics* (2016), pp. 0–21.
- [152] C. Kannepalli and U. Piomelli. “Large-eddy simulation of a three-dimensional shear-driven turbulent boundary layer”. In: *Journal of Fluid Mechanics* 423 (2000), pp. 175–203.

-
- [153] I Karlin, N Gorban, S Succi, and V Boffi. “Exact equilibria for lattice kinetic equations”. In: *Phys. Rev. Lett* 81 (1998), pp. 1–6.
- [154] I. V. Karlin, S. Succi, and S. S. Chikatamarla. “Comment on “Numerics of the lattice Boltzmann method: Effects of collision models on the lattice Boltzmann simulations””. In: *Phys. Rev. E* 84.6 (2011), p. 068701.
- [155] I. V. Karlin, D. Sichau, and S. S. Chikatamarla. “Consistent two-population lattice Boltzmann model for thermal flows”. In: *Physical Review E* 88.6 (2013), pp. 1–13.
- [156] I. V. Karlin, S. Ansumali, E. De Angelis, H. C. Öttinger, and S. Succi. “Entropic Lattice Boltzmann Method for Large Scale Turbulence Simulation”. In: *arXiv preprint cond-mat/0306003* (2003), p. 11.
- [157] I. V. Karlin, F. Bösch, and S. S. Chikatamarla. “Gibbs’ principle for the lattice-kinetic theory of fluid dynamics”. In: *Physical Review E* 90.3 (2014), p. 31302.
- [158] I. V Karlin, A Ferrante, and H. C Öttinger. “Perfect entropy functions of the lattice Boltzmann method”. In: *Europhysics Letters* 47.2 (1999), pp. 182–188.
- [159] I. V. Karlin and S Succi. “Equilibria for discrete kinetic equations”. In: *Physical Review E* 58.4 (1998), R4053.
- [160] I. V. Karlin, A. N. Gorban, S Succi, and V Boffi. “Maximum entropy principle for lattice kinetic equations”. In: *Physical Review Letters* 81.1 (1998), p. 6.
- [161] I. V. Karlin, F. Bösch, S. S. Chikatamarla, and S. Succi. “Entropy-Assisted Computing of Low-Dissipative Systems”. In: *Entropy* 17.12 (2015), pp. 8099–8110.
- [162] I. Karlin, S. Ansumali, C. Frouzakis, and S. Chikatamarla. “Elements of the lattice Boltzmann method I: linear advection equation”. In: 1.1 (2006), pp. 1–45.
- [163] I. Karlin, S Succi, and S Orszag. “Lattice Boltzmann method for irregular grids”. In: *Physical Review Letters* 82.26 (1999), p. 5245.

- [164] I. Karlin, A Ferrante, and H. C. Öttinger. “Perfect entropy functions of the lattice Boltzmann method”. In: *EPL (Europhysics Letters)* 47.2 (1999), p. 182.
- [165] B. Keating, G. Vahala, J. Yopez, M. Soe, and L. Vahala. “Entropic lattice Boltzmann representations required to recover Navier-Stokes flows”. In: *Physical Review E* 75.3 (2007), p. 036712.
- [166] S. Kern and P. Koumoutsakos. “Simulations of optimized anguilliform swimming”. In: *Journal of Experimental Biology* 209.24 (2006), pp. 4841–4857.
- [167] S. Kida. “Three-dimensional periodic flows with high-symmetry”. In: *Journal of the Physical Society of Japan* 54.6 (1985), pp. 2132–2136.
- [168] S. Kida and Y. Murakami. “Kolmogorov similarity in freely decaying turbulence”. In: *Physics of Fluids (1958-1988)* 30.7 (1987), pp. 2030–2039.
- [169] J. Kim, P. Moin, and R. Moser. “Turbulence statistics in fully developed channel flow at low Reynolds number”. In: *Journal of Fluid Mechanics* 177.-1 (1987), pp. 133–166.
- [170] N.-H. Kim. *Introduction to Nonlinear Finite Element Analysis*. 2015, p. 482.
- [171] Y. Kim and C. S. Peskin. “Penalty immersed boundary method for an elastic boundary with mass”. In: *Physics of Fluids* 19.5 (2007).
- [172] P. Kim, H.J., Durbin. “Observations of the frequencies in a sphere wake and of drag increase by acoustic excitation”. In: *Physics of Fluids* 31.11 (1988), pp. 3260–3265.
- [173] G. Kockarts. “Transport phenomena”. In: *Journal de Physique IV (Proceedings)* 12.10 (2002), pp. 235–252.
- [174] J. Koelman. “A simple lattice Boltzmann scheme for Navier-Stokes fluid flow”. In: *EPL (Europhysics Letters)* 15.6 (1991), p. 603.
- [175] J. M. Kolinski, S. M. Rubinstein, S. Mandre, M. P. Brenner, D. A. Weitz, and L. Mahadevan. “Skating on a film of air: Drops impacting on a surface”. In: *Physical Review Letters* 108.7 (2012), p. 74503.

- [176] S Kollmannsberger, S Geller, A. Düster, M. Krafczyk, and E. Rank. “Fluid-Structure Interaction based on Lattice Boltzmann and p-FEM: Verification and Validation”. In: *Proceedings of the . . .* (2009), pp. 1–4.
- [177] A. Krämer, K. Küllmer, D. Reith, W. Joppich, and H. Foysi. “Semi-Lagrangian off-lattice Boltzmann method for weakly compressible flows”. In: *Physical Review E* 95.2 (2017), p. 023305.
- [178] A. Kravchenko and P. Moin. “Numerical studies of flow over a circular cylinder at $Re_D = 3900$ ”. In: *Physics of Fluids* 12 (2000), pp. 403–417.
- [179] M. J. Kreder, J. Alvarenga, P. Kim, and J. Aizenberg. “Design of anti-icing surfaces: smooth, textured or slippery?” In: *Nature Reviews Materials* 1.1 (2016), p. 15003.
- [180] H.-P. Kreplin and H. Eckelmann. “Behavior of the three fluctuating velocity components in the wall region of a turbulent channel flow”. In: *Physics of Fluids* 22.7 (1979), pp. 1233–1239.
- [181] T. Krüger, D. Holmes, and P. V. Coveney. “Deformability-based red blood cell separation in deterministic lateral displacement devices-A simulation study”. In: *Biomicrofluidics* 8.5 (2014).
- [182] A. L. Kupershtokh. “New method of incorporating a body force term into the lattice Boltzmann equation”. In: *Proc. 5th International EHD Workshop*. 2004, pp. 241–246.
- [183] J. W. Kurelek, A. R. Lambert, and S. Yarusevych. “Coherent Structures in the Transition Process of a Laminar Separation Bubble”. In: *AIAA Journal* 54.8 (2016), pp. 1–15.
- [184] D. Lagrava, O. Malaspinas, J. Latt, and B. Chopard. “Advances in multi-domain lattice Boltzmann grid refinement”. In: *Journal of Computational Physics* 231.14 (2012), pp. 4808–4822.
- [185] M.-C. Lai and C. S. Peskin. “An immersed boundary method with formal second-order accuracy and reduced numerical viscosity”. In: *Journal of computational Physics* 160.2 (2000), pp. 705–719.
- [186] P. Lallemand and L.-S. Luo. “Lattice Boltzmann method for moving boundaries”. In: *Journal of Computational Physics* (2003).

- [187] P. Lallemand and L.-S. Luo. “Theory of the lattice Boltzmann Method: Dispersion, Dissipation, Isotropy, Galilean Invariance, and Stability”. In: *Physical Review E* 61.6 (2000), pp. 6546–6562.
- [188] H. Lamb. *Hydrodynamics*. Cambridge university press, 1932.
- [189] P Lammers, K. Beronov, R Volkert, G Brenner, and F Durst. “Lattice BGK direct numerical simulation of fully developed turbulence in incompressible plane channel flow”. In: *Computers & fluids* 35.10 (2006), pp. 1137–1153.
- [190] M. Lang, U. Rist, and S. Wagner. “Investigations on controlled transition development in a laminar separation bubble by means of LDA and PIV”. In: *Experiments in Fluids* 36.1 (2004), pp. 43–52.
- [191] J. Latt. “Hydrodynamic limit of lattice Boltzmann equations”. PhD thesis. University of Geneva, 2007.
- [192] J. Latt and B. Chopard. “Lattice Boltzmann method with regularized pre-collision distribution functions”. In: *Mathematics and Computers in Simulation* 72.2-6 (2006), pp. 165–168.
- [193] J. Latt, B. Chopard, O. Malaspinas, M. Deville, and A. Michler. “Straight velocity boundaries in the lattice Boltzmann method”. In: *Physical Review E - Statistical, Nonlinear, and Soft Matter Physics* 77.5 (2008), pp. 1–16.
- [194] G. V. Lauder, P. G. a. Madden, J. L. Tangorra, E Anderson, and T. V. Baker. “Bioinspiration from fish for smart material design and function”. In: *Smart Materials and Structures* 20 (2011), p. 094014.
- [195] G. V. Lauder, E. J. Anderson, J. L. Tangorra, and P. G. A. Madden. “Fish biorobotics: kinematics and hydrodynamics of self-propulsion”. In: *The Journal of Experimental Biology* 210.16 (2007), pp. 2767–2780.
- [196] G. V. Lauder, J. Lim, R. Shelton, C. Witt, E. Anderson, and J. L. Tangorra. “Robotic Models for Studying Undulatory Locomotion in Fishes”. In: *Marine Technology Society Journal* 45.4 (2011), pp. 41–55.
- [197] P Le Tallec. “Fluid structure interaction with large structural displacements”. In: *Computer Methods in Applied Mechanics and Engineering* 190.24-25 (2001), pp. 3039–3067.

- [198] J. Lebowitz, H. Frisch, and E Helfand. “Nonequilibrium distribution functions in a fluid”. In: *The Physics of Fluids* 3.3 (1960), pp. 325–338.
- [199] H. J. Lee, S. Sherrit, L. P. Tosi, P. Walkemeyer, and T. Colonius. “Piezoelectric energy harvesting in internal fluid flow”. In: *Sensors* 15.10 (2015), pp. 26039–26062.
- [200] D. Lentink. “Bioinspired flight control”. In: *Bioinspir. Biomim.* 9 (2014), p. 020301.
- [201] D. Lentink, A. F. Haselsteiner, and R. Ingersoll. “In vivo recording of aerodynamic force with an aerodynamic force platform: from drones to birds”. In: *Journal of The Royal Society Interface* 12.104 (2015), p. 20141283.
- [202] N. Li, H. Liu, and Y. Su. “Numerical study on the hydrodynamics of thunniform bio-inspired swimming under self-propulsion”. In: *PloS one* 12.3 (2017), e0174740.
- [203] Z. Li and J. Favier. “A non-staggered coupling of finite element and lattice Boltzmann methods via an immersed boundary scheme for fluid-structure interaction”. In: *Computers and Fluids* 143 (2017), pp. 90–102.
- [204] J. C. Liao, D. N. Beal, G. V. Lauder, and M. S. Triantafyllou. “Fish Exploiting Vortices Decrease Muscle Activity”. In: *Science* 302.2003 (2003), pp. 1566–1569.
- [205] M. J. Lighthill. “Aquatic animal propulsion of high hydromechanical efficiency”. In: *Journal of Fluid Mechanics* 44.02 (1970), p. 265.
- [206] M. J. Lighthill. “Hydromechanics of aquatic animal propulsion”. In: *Annual Review of Fluid Mechanics* 1.1 (1969), pp. 413–446.
- [207] M. J. Lighthill. “Large-Amplitude Elongated-Body Theory of Fish Locomotion”. In: *Proceedings of the Royal Society of London B: Biological Sciences* 179.1055 (1971), pp. 125–138.
- [208] M. J. Lighthill. “Note on the swimming of slender fish”. In: *Journal of Fluid Mechanics* 9.02 (1960), p. 305.

- [209] S. Liska and T. Colonius. “A fast immersed boundary method for external incompressible viscous flows using lattice Green’s functions”. In: *Journal of Computational Physics* 331 (2017), pp. 257–279.
- [210] K. Liu and D. C. Haworth. “Large-eddy simulation for an axisymmetric piston-cylinder assembly with and without swirl”. In: *Flow, Turbulence and Combustion* 85.3-4 (2010), pp. 279–307.
- [211] Y. Liu, L. Moevius, X. Xu, T. Qian, J. M. Yeomans, and Z. Wang. “Pancake bouncing on superhydrophobic surfaces”. In: *Nature Physics* 10.June (2014), pp. 515–519.
- [212] L. Lourenco and C. Shih. “Characteristics of the plane turbulent near wake of a circular cylinder, a particle image velocimetry study”. In: *Published in Beaudan and Moin(1994), data taken from Kravchenko and Moin(2000)* (1993).
- [213] K. N. Lucas, N. Johnson, W. T. Beaulieu, E. Cathcart, G. Tirrell, S. P. Colin, B. J. Gemmel, J. O. Dabiri, and J. H. Costello. “Bending rules for animal propulsion.” In: *Nature communications* 5.May 2013 (2014), p. 3293.
- [214] M. Luhar and H. M. Nepf. “Flow-induced reconfiguration of buoyant and flexible aquatic vegetation”. In: *Limnology and Oceanography* 56.6 (2011), pp. 2003–2017.
- [215] X. Ma, G. Karamonos, and G. Karniadakis. “Dynamics and low-dimensionality of a turbulent near wake”. In: *J. Fluid Mech.* 410 (2000), pp. 29–65.
- [216] K. Mahesh. “The Interaction of Jets with Crossflow”. In: *Annual Review of Fluid Mechanics* 45 (2013), pp. 379–407.
- [217] S. Mandre and M. P. Brenner. “The mechanism of a splash on a dry solid surface”. In: *Journal of Fluid Mechanics* 690 (2012), pp. 148–172.
- [218] M. Marengo, C. Antonini, I. V. Roisman, and C. Tropea. “Drop collisions with simple and complex surfaces”. In: *Current Opinion in Colloid and Interface Science* 16.4 (2011), pp. 292–302.
- [219] L. G. Margolin, W. J. Rider, and F. F. Grinstein. “Modeling turbulent flow with implicit LES”. In: *Journal of Turbulence* 7.15 (2006), N15.

- [220] L. G. Margolin and W. J. Rider. “A rationale for implicit turbulence modelling”. In: *International Journal for Numerical Methods in Fluids* 39.9 (2002), pp. 821–841.
- [221] S. Marras, S. S. Killen, J. Lindström, D. J. McKenzie, J. F. Stefensen, and P. Domenici. “Fish swimming in schools save energy regardless of their spatial position”. In: *Behavioral Ecology and Sociobiology* 69.2 (2015), pp. 19–226.
- [222] O. Marxen, M. Lang, U. Rist, and S. Wagner. “A combined experimental/numerical study of unsteady phenomena in a laminar separation bubble”. In: *Flow, Turbulence and Combustion* 71.1 (2003), pp. 133–146.
- [223] O. Marxen and U. Rist. “Mean flow deformation in a laminar separation bubble: separation and stability characteristics”. In: *Journal of Fluid Mechanics* 660 (2010), pp. 37–54.
- [224] O. Marxen, U. Rist, and S. Wagner. “Effect of Spanwise-Modulated Disturbances on Transition in a Separated Boundary Layer”. In: *AIAA Journal* 42.5 (2004), pp. 937–944.
- [225] U. Maucher, U. Rist, and S. Wagner. “Transitional structures in a laminar separation bubble”. In: *New Results in Numerical and Experimental Fluid Mechanics II*. Springer, 1999, pp. 307–314.
- [226] U. Maucher. “Numerical investigations on the transition in the laminar separation bubble in an airfoil boundary layer”. PhD thesis. University of Stuttgart, 2002.
- [227] U. Maucher, U. Rist, and S. Wagner. “Secondary instabilities in a laminar separation bubble”. In: 2 (1997), pp. 229–236.
- [228] R. E. Mayle. “The 1991 IGTI Scholar Lecture: The Role of Laminar-Turbulent Transition in Gas Turbine Engines”. In: *Journal of Turbomachinery* 113.4 (1991), pp. 509–536.
- [229] A. M. Mazloomi, S. S. Chikatamarla, and I. V. Karlin. “Entropic Lattice Boltzmann Method for Multiphase Flows”. In: *Physical Review Letters* 114.17 (2015), p. 174502.
- [230] A. Mazloomi M, S. S. Chikatamarla, and I. V. Karlin. “Entropic lattice Boltzmann method for multiphase flows”. In: *Physical Review Letters* 114.17 (2015), p. 174502.

- [231] A. Mazloomi M., S. S. Chikatamarla, and I. V. Karlin. “Entropic lattice Boltzmann method for multiphase flows: Fluid-solid interfaces”. In: *Physical Review E - Statistical, Nonlinear, and Soft Matter Physics* 92.2 (2015).
- [232] B. R. McAuliffe and M. I. Yaras. “Separation-bubble-transition measurements on a low-Re airfoil using particle image velocimetry”. In: *ASME Turbo Expo 2005: Power for Land, Sea, and Air*. American Society of Mechanical Engineers. 2005, pp. 1029–1038.
- [233] G. McGowan, A. Gopalarathnam, M. Ol, J. Edwards, and D. Fredberg. “Computation vs. Experiment for High-Frequency Low-Reynolds Number Airfoil Plunge”. In: *AIAA paper* 653 (2008), p. 2008.
- [234] B. J. McKeon, C. J. Swanson, M. V. Zagarola, R. J. Donnelly, and A. J. Smits. “Friction factors for smooth pipe flow”. In: *Journal of Fluid Mechanics* 511 (2004), pp. 41–44.
- [235] G. R. McNamara and G. Zanetti. “Use of the Boltzmann equation to simulate lattice-gas automata”. In: *Physical review letters* 61.20 (1988), p. 2332.
- [236] R. Mei, L.-S. Luo, and W. Shyy. “An accurate curved boundary treatment in the lattice Boltzmann method”. In: *Journal of computational physics* 155.2 (1999), pp. 307–330.
- [237] M. Mendoza, B. M. Boghosian, H. J. Herrmann, and S. Succi. “Fast Lattice Boltzmann Solver for Relativistic Hydrodynamics”. In: *Physical Review Letters* 105 (2010), p. 014502.
- [238] V. Michelassi, J. G. Wissink, and W. Rodi. “Large-Eddy Simulation of Flow Around Low-Pressure Turbine Blade with Incoming Wakes”. In: *AIAA Journal* 41.11 (2003), pp. 2143–2156.
- [239] V. Michelassi, J. Wissink, and W. Rodi. “Analysis of DNS and LES of Flow in a Low Pressure Turbine Cascade with Incoming Wakes and Comparison with Experiments”. In: *Flow, Turbulence and Combustion* 69.3-4 (2002), pp. 295–330.
- [240] M. Min and T. Lee. “A spectral-element discontinuous Galerkin lattice Boltzmann method for nearly incompressible flows”. In: *Journal of Computational Physics* 230.1 (2011), pp. 245–259.

- [241] R. Mittal, S. Venkatasubramanian, and F. M. Najjar. “Large Eddy Simulation of Flow Through a Low-Pressure Turbine Cascade”. In: *Mechanical Engineering* (2001), pp. 1–9.
- [242] R. Mittal and G. Iaccarino. “Immersed Boundary Methods”. In: *Annual Review of Fluid Mechanics* 37.1 (2005), pp. 239–261.
- [243] R. Mittal, H. Dong, M. Bozkurttas, G. V. Lauder, and P. Madden. “Locomotion with flexible propulsors: II. Computational modeling of pectoral fin swimming in sunfish.” In: *Bioinspiration & biomimetics* 1.4 (2006), S35–S41.
- [244] V. Mnih, K. Kavukcuoglu, D. Silver, A. a. Rusu, J. Veness, M. G. Bellemare, A. Graves, M. Riedmiller, A. K. Fidjeland, G. Ostrovski, S. Petersen, C. Beattie, A. Sadik, I. Antonoglou, H. King, D. Kumaran, D. Wierstra, S. Legg, and D. Hassabis. “Human-level control through deep reinforcement learning”. In: *Nature* 518.7540 (2015), pp. 529–533.
- [245] A. M. Moqaddam, S. S. Chikatamarla, and I. Karlin. “Drops bouncing off macro-textured superhydrophobic surfaces”. In: *Journal of Fluid Mechanics* 824 (2017), pp. 866–885.
- [246] J. F. Morrison, B. J. McKeon, W. Jiang, and A. J. Smits. “Scaling of the streamwise velocity component in turbulent pipe flow”. In: *Journal of Fluid Mechanics* 508 (2004), pp. 99–131.
- [247] a. P. Morse, J. H. Whitelaw, and M. Yianneskis. “Turbulent Flow Measurements by Laser-Doppler Anemometry in Motored Piston-Cylinder Assemblies”. In: *Journal of Fluids Engineering* 101.2 (1979), pp. 208–216.
- [248] R. D. Moser, J. Kim, and N. N. Mansour. “Direct numerical simulation of turbulent channel flow up to $Re_\tau = 590$ ”. In: *Physics of Fluids* 11.4 (1999), pp. 943–945.
- [249] U. K. Müller, J. Smit, E. J. Stamhuis, and J. J. Videler. “How the body contributes to the wake in undulatory fish swimming”. In: *Journal of Experimental Biology* 204.16 (2001), pp. 2751–2762.
- [250] Y. Muzychka and M. Yovanovich. “Unsteady viscous flows and Stokes’s first problem”. In: *International Journal of Thermal Sciences* 49.5 (2010), pp. 820–828.

- [251] T. Nakata and H. Liu. “A fluid-structure interaction model of insect flight with flexible wings”. In: *Journal of Computational Physics* 231.4 (2012), pp. 1822–1847.
- [252] M. Namburi, S. Krithivasan, and S. Ansumali. “Crystallographic Lattice Boltzmann Method”. In: *Scientific reports* 6 (2016), p. 27172.
- [253] F. Nannelli and S. Succi. “The lattice Boltzmann equation on irregular lattices”. In: *Journal of Statistical Physics* 68.3 (1992), pp. 401–407.
- [254] R. W. Nash, H. B. Carver, M. O. Bernabeu, J. Hetherington, D. Groen, T. Krüger, and P. V. Coveney. “Choice of boundary condition for lattice-Boltzmann simulation of moderate-Reynolds-number flow in complex domains”. In: *Physical Review E* 89.2 (2014), p. 023303.
- [255] F. Nathen, D. Gaudlitz, M. Krause, and A. N. “On the stability and Accuracy of the BGK, MRT and RLB Boltzmann schemes for the simulation of turbulent flows”. In: *Journal of Communications in Computational Physics* 23 (2017), pp. 846–876.
- [256] X. Niu, C. Shu, Y. Chew, and Y. Peng. “A momentum exchange-based immersed boundary-lattice Boltzmann method for simulating incompressible viscous flows”. In: *Physics Letters A* 354.3 (2006), pp. 173–182.
- [257] C. Norberg. “An experimental investigation of flow around a circular cylinder: influence of aspect ratio”. In: *J. Fluid Mech.* 258 (1994), 287316.
- [258] G. Novati, S. Verma, D. Alexeev, D. Rossinelli, W. M. V. Rees, and P. Koumoutsakos. “Synchronisation through learning for two self-propelled swimmers”. In: *Bioinspiration & Biomimetics* 12 (2017), p. 036001.
- [259] J. Oeffner and G. V. Lauder. “The hydrodynamic function of shark skin and two biomimetic applications”. In: *Journal of Experimental Biology* 215.5 (2012), pp. 785–795.
- [260] M. Ol, B. McCauliffe, E. Hanff, U. Scholz, and C. Kaehler. “Comparison of laminar separation bubble measurements on a low Reynolds number airfoil in three facilities”. In: *35th AIAA fluid dynamics conference and exhibit*. 2005, p. 5149.

- [261] M. O'meara and T. Mueller. "Laminar separation bubble characteristics on an airfoil at low Reynolds numbers". In: *AIAA journal* 25.8 (1987), pp. 1033–1041.
- [262] L. Ong and J. Wallace. "The velocity field of the turbulent very near wake of a circular cylinder". In: *Exp. Fluids* 20 (1996), pp. 441–453.
- [263] K Ou, P Castonguay, and A Jameson. "3D Flapping Wing Simulation with High Order Spectral Difference Method on Deformable Mesh". In: *49th AIAA Aerospace Sciences Meeting including the New Horizons Forum and Aerospace Exposition* January (2011).
- [264] E. L. Papanicolaou and W. Rodi. "Computation of Separated-Flow Transition Using a Two-Layer Model of Turbulence". In: *Journal of Turbomachinery* 121.January 1999 (1999), pp. 78–87.
- [265] G Pareschi, N Frapolli, S. Chikatamarla, and I. Karlin. "Conjugate heat transfer with the entropic lattice Boltzmann method". In: *Physical Review E* 94.1 (2016), p. 013305.
- [266] D. Patil. "ChapmanEnskog analysis for finite-volume formulation of lattice Boltzmann equation". In: *Physica A* 392 (2013), 27012712.
- [267] D. Patil and K. Lakshmisha. "Finite volume TVD formulation of lattice Boltzmann simulation on unstructured mesh". In: *Journal of Computational Physics* 228 (2009), 52625279.
- [268] D. Patil and K. Lakshmisha. "Two-dimensional flow past circular cylinders using finite volume lattice Boltzmann formulation". In: *Int. J. Numer. Meth. Fluids* 69 (2012), pp. 1149–1164.
- [269] D. Pavlov and A. Kasumyan. "Patterns and mechanisms of schooling behaviour in fish: A review". In: *Journal of Ichthyology* 40.2 (2000), pp. 163–231.
- [270] G. Peng, H. Xi, C. Duncan, and S. Chou. "A finite volume scheme for the Lattice Boltzmann Method on unstructured meshes". In: *Phys. Rev. E* 59 (1999), pp. 4675–4682.
- [271] G. Peng, H. Xi, C. Duncan, and S. Chou. "Lattice Boltzmann method on irregular meshes". In: *Phys. Rev. E* 58 (1998), R4124–R4127.

- [272] Y. Peng and L.-S. Luo. “A comparative study of immersed-boundary and interpolated bounce-back methods in LBE”. In: *Progress in Computational Fluid Dynamics, an International Journal* 8.1 (2008), pp. 156–167.
- [273] A. E. Perry, S. Hafez, and M. S. Chong. “A possible reinterpretation of the Princeton superpipe data”. In: *Journal of Fluid Mechanics* 439 (2001), pp. 395–401.
- [274] C. S. Peskin. “Flow patterns around heart valves: A numerical method”. In: *Journal of Computational Physics* 10.2 (1972), pp. 252–271.
- [275] C. S. Peskin. “Numerical analysis of blood flow in the heart”. In: *Journal of computational physics* 25.3 (1977), pp. 220–252.
- [276] C. C. S. Peskin. “The immersed boundary method”. In: *Acta Numerica* 11 (2002), pp. 479–517.
- [277] U. Piomelli and B. Elias. “Wall-layer Models for Large-Eddy Simulations”. In: *Annual Review of Fluid Mechanics* 34.1 (2002), pp. 349–374.
- [278] S. Piperno and C. Farhat. “Partitioned procedures for the transient solution of coupled aeroelastic problems - part II: Energy transfer analysis and three-dimensional applications”. In: *Computer Methods in Applied Mechanics and Engineering* 190 (2001), pp. 3147–3170.
- [279] S. B. Pope. *Turbulent flows*. Cambridge university press, 2000.
- [280] M. Porfiri. “Special Issue Editorial: Robotics: Mechanics and Control of Locomotion”. In: *Journal of Nonlinear Science* 27.4 (2017), pp. 1–3.
- [281] Y. Qian, D. d’Humières, and P. Lallemand. “Lattice BGK models for Navier-Stokes equation”. In: *EPL (Europhysics Letters)* 17.6 (1992), p. 479.
- [282] M. Rai. “A computational investigation of the instability of the detached shear layer in the wake of a circular cylinder”. In: *J. Fluid Mech.* 659 (2010), 375404.

- [283] B. Rajani, A. Kandasamy, and S. Majumdar. “LES of Flow past Circular Cylinder at $Re = 3900$ ”. In: *Journal of Applied Fluid Mechanics* 9 (2016), pp. 1421–1435.
- [284] A. E. Randles. “Modeling Cardiovascular Hemodynamics Using the Lattice Boltzmann Method on Massively Parallel Supercomputers”. PhD thesis. 2003.
- [285] P. Rao and L. Schaefer. “Numerical stability of explicit off-lattice Boltzmann schemes: A comparative study”. In: *Journal of Computational Physics* 285 (2015), pp. 251–264.
- [286] B. Raverdy, I. Mary, P. Sagaut, and N. Liamis. “High-resolution large-eddy simulation of flow around low-pressure turbine blade”. In: *AIAA journal* 41.3 (2003), pp. 390–397.
- [287] C. W. Reynolds. “Flocks, herds and schools: A distributed behavioral model”. In: *ACM SIGGRAPH Computer Graphics* 21.4 (1987), pp. 25–34.
- [288] G. Riboux and J. M. Gordillo. “Experiments of drops impacting a smooth solid surface: A model of the critical impact speed for drop splashing”. In: *Physical Review Letters* 113.2 (2014), p. 24507.
- [289] D. Richard, C. Clanet, and D. Quéré. “Contact time of a bouncing drop”. In: *Nature* 417.6891 (2002), p. 811.
- [290] T. Richter. “Goal-oriented error estimation for fluid-structure interaction problems”. In: *Computer Methods in Applied Mechanics and Engineering* 223-224 (2012), pp. 28–42.
- [291] U. Rist, U. Maucher, and S. Wagner. “Direct Numerical Simulation of some Fundamental Problems Related to Transition in Laminar Separation Bubbles”. In: *Proceedings of the ECCOMAS Computational Fluid Dynamics Conference* (1996), pp. 319–325.
- [292] U. Rist and U. Maucher. “Investigations of time-growing instabilities in laminar separation bubbles”. In: *European Journal of Mechanics, B/Fluids* 21.5 (2002), pp. 495–509.

- [293] L. Ristroph, A. J. Bergou, G. Ristroph, K. Coumes, G. J. Berman, J. Guckenheimer, Z. J. Wang, and I. Cohen. “Discovering the flight autostabilizer of fruit flies by inducing aerial stumbles”. In: *Proceedings of the National Academy of Sciences* 107.11 (2010), pp. 4820–4824.
- [294] S. K. Roberts and M. I. Yaras. “Large-Eddy Simulation of Transition in a Separation Bubble”. In: *Journal of Fluids Engineering* 128.2 (2006), p. 232.
- [295] W. Rodi. “DNS and LES of some engineering flows”. In: *Fluid Dynamics Research* 38.2-3 (2006), pp. 145–173.
- [296] I. Rodriguez, R. Borell, O. Lehmkuhl, C. D. Perez Segarra, and A. Oliva. “Direct numerical simulation of the flow over a sphere at $Re = 3700$ ”. In: *Journal of Fluid Mechanics* 679 (2011), pp. 263–287.
- [297] M. Rohde, D. Kandhai, J. J. Derksen, and H. E. A. van den Akker. “A generic, mass conservative local grid refinement technique for lattice-Boltzmann schemes”. In: *International Journal for Numerical Methods in Fluids* 51.4 (2006), pp. 439–468.
- [298] a.M. Roma, C. S. Peskin, and M. J. Berger. “An Adaptive Version of the Immersed Boundary Method”. In: *Journal of Computational Physics* 153.2 (1999), pp. 509–534.
- [299] “Rotational accelerations stabilize leading edge vortices on revolving fly wings.” In: *The Journal of experimental biology* 212.Pt 16 (2009), pp. 2705–2719.
- [300] J. D. Ruitter, R. Lagraauw, D. V. D. Ende, and F. Mugele. “Wettability-independent bouncing on flat surfaces mediated by thin air films”. In: *Nature Physics* 11.November (2014), pp. 48–53.
- [301] C. J. Rutland. “Large-eddy simulations for internal combustion engines - A review”. In: *International Journal of Engine Research* 12.5 (2011), pp. 421–451.
- [302] E. K. Sackmann, A. L. Fulton, and D. J. Beebe. “The present and future role of microfluidics in biomedical research”. In: *Nature* 507.7491 (2014), pp. 181–189.

- [303] S. P. Sane and M. H. Dickinson. “The control of flight force by a flapping wing: lift and drag production”. In: *The Journal of experimental biology* 204.15 (2001), pp. 2607–2626.
- [304] H. Schlichting, K. Gersten, E. Krause, H. Oertel, and K. Mayes. *Boundary-Layer Theory*. Vol. 7. Springer, 1960.
- [305] H. Schlichting and K. Gersten. *Boundary-layer theory*. Springer Science & Business Media, 2003.
- [306] M. Schmitt, C. E. Frouzakis, A. G. Tomboulides, Y. M. Wright, and K. Boulouchos. “Direct numerical simulation of multiple cycles in a valve/piston assembly”. In: *Physics of Fluids* 26.3 (2014), p. 035105.
- [307] M. Schmitt, C. E. Frouzakis, Y. M. Wright, A. G. Tomboulides, and K. Boulouchos. “Investigation of cycle-to-cycle variations in an engine-like geometry”. In: *Physics of Fluids* 26.12 (2014), p. 125104.
- [308] V. Schulte and H. P. Hodson. “Unsteady Wake-Induced Boundary Layer Transition in High Lift LP Turbines”. In: *Journal of Turbomachinery* 120.1 (1998), p. 28.
- [309] V. Schulte and H. Hodson. “Wake-separation bubble interaction in low pressure turbines”. In: *30th Joint Propulsion Conference and Exhibit*. Joint Propulsion Conferences. American Institute of Aeronautics and Astronautics, 1994.
- [310] T. M. Schutzius, S. Jung, T. Maitra, P. Eberle, C. Antonini, C. Stamatopoulos, and D. Poulikakos. “Physics of icing and rational design of surfaces with extraordinary icephobicity”. In: *Langmuir* 31.17 (2015), pp. 4807–4821.
- [311] T. M. Schutzius, S. Jung, T. Maitra, G. Graeber, M. Köhme, and D. Poulikakos. “Spontaneous droplet trampolining on rigid superhydrophobic surfaces”. In: *Nature* 527.7576 (2015), pp. 82–85.
- [312] C. Semperebon, T. Krüger, and H. Kusumaatmaja. “Ternary free-energy lattice Boltzmann model with tunable surface tensions and contact angles”. In: *Physical Review E* 93.3 (2016), p. 033305.
- [313] J. H. Seo and R. Mittal. “A sharp-interface immersed boundary method with improved mass conservation and reduced spurious pressure oscillations”. In: *Journal of Computational Physics* 230.19 (2011), pp. 7347–7363.

- [314] X. Shan and X. He. “Discretization of the velocity space in solution of the Boltzmann equation”. In: *Physical Review Letters* 80.1 (1997), pp. 65–68.
- [315] L. Shen, E.-S. Chan, and P. Lin. “Calculation of hydrodynamic forces acting on a submerged moving object using immersed boundary method”. In: *Computers & Fluids* 38.3 (2009), pp. 691–702.
- [316] C. Shu, N. Liu, and Y. Chew. “A novel immersed boundary velocity correction lattice Boltzmann method and its application to simulate flow past a circular cylinder”. In: *Journal of Computational Physics* 226.2 (2007), pp. 1607–1622.
- [317] C. Shu, X. Niu, and Y. Chew. “Taylor-series expansion and least-squares-based lattice Boltzmann method: two-dimensional formulation and its applications”. In: *Physical Review E* 65.3 (2002), p. 036708.
- [318] C. Sieverding. “Brite EURAM project TURMUNSFLAT, CT96-0143, 2000”. In: *Final Report. Simulation of a Wake-Blade Interaction* (2000).
- [319] P. Skordos. “Initial and boundary conditions for the lattice Boltzmann method”. In: *Physical Review E* 48.6 (1993), p. 4823.
- [320] F. Sotiropoulos and X. Yang. “Immersed boundary methods for simulating fluid-structure interaction”. In: *Progress in Aerospace Sciences* 65 (2014), pp. 1–21.
- [321] P. R. Spalart and M. K. Strelets. “Mechanisms of transition and heat transfer in a separation bubble”. In: *Journal of Fluid Mechanics* 403 (2000), pp. 329–349.
- [322] M. Spasov, D. Rempfer, and P. Mokhasi. “Simulation of a turbulent channel flow with an entropic lattice Boltzmann method”. In: *International journal for numerical methods in fluids* 60.11 (2009), pp. 1241–1258.
- [323] S. A. Stanley, S. Sarkar, and J. P. Mellado. “A study of the flow-field evolution and mixing in a planar turbulent jet using direct numerical simulation”. In: *Journal of Fluid Mechanics* 450 (2002), pp. 377–407.

- [324] R. D. Stieger and H. P. Hodson. “The Transition Mechanism of Highly-Loaded LP Turbine Blades”. In: *ASME Conference Proceedings* 2003.36886 (2003), pp. 779–788.
- [325] S. Succi. *The lattice Boltzmann equation: For fluid dynamics and beyond*. Oxford university press, 2001.
- [326] S. Succi. “Lattice Boltzmann 2038”. In: *EPL (Europhysics Letters)* 109.5 (2015), p. 50001.
- [327] S. Succi, I. V. Karlin, and H. Chen. “Colloquium: Role of the H theorem in lattice Boltzmann hydrodynamic simulations”. In: *Reviews of Modern Physics* 74.4 (2002), p. 1203.
- [328] M. Sun. “Insect flight dynamics: Stability and control”. In: *Reviews of Modern Physics* 86.2 (2014), p. 615.
- [329] K. Suzuki and T. Inamuro. “A higher-order immersed boundary-lattice Boltzmann method using a smooth velocity field near boundaries”. In: *Computers & Fluids* 76 (2013), pp. 105–115.
- [330] K. Suzuki and T. Inamuro. “Effect of internal mass in the simulation of a moving body by the immersed boundary method”. In: *Computers and Fluids* 49.1 (2011), pp. 173–187.
- [331] K. Suzuki, K. Minami, and T. Inamuro. “Lift and thrust generation by a butterfly-like flapping wing–body model: immersed boundary–lattice Boltzmann simulations”. In: *Journal of Fluid Mechanics* 767 (2015), pp. 659–695.
- [332] Sven Woop, Carsten Benthin, and Ingo Wald. “Watertight Ray/Triangle Intersection”. In: *Journal of Computer Graphics Techniques (JCGT)* 2.1 (2013), pp. 65–82.
- [333] J. C. Svendsen, J. Skov, M. Bildsoe, and J. F. Steffensen. “Intra-school positional preference and reduced tail beat frequency in trailing positions in schooling roach under experimental conditions”. In: *Journal of Fish Biology* 62.4 (2003), pp. 834–846.
- [334] I. Tani. “Low-speed flows involving bubble separations”. In: *Progress in Aerospace Sciences* 5 (1964), pp. 70–103.

- [335] S. Tao, J. Hu, and Z. Guo. “An investigation on momentum exchange methods and refilling algorithms for lattice Boltzmann simulation of particulate flows”. In: *Computers and Fluids* 133 (2016), pp. 1–14.
- [336] A. Ten Cate, C. Nieuwstadt, J. Derksen, and H. Van den Akker. “Particle imaging velocimetry experiments and lattice-Boltzmann simulations on a single sphere settling under gravity”. In: *Physics of Fluids* 14.11 (2002), pp. 4012–4025.
- [337] T. E. Tezduyar, M. Behr, S. Mittal, and J. Liou. “New strategy for finite element computations involving moving boundaries and interfaces. The deforming-spatial-domain/space-time procedure. II. Computation of free-surface flows, two-liquid flows, and flows with drifting cylinders”. In: *Computer Methods in Applied Mechanics and Engineering* 94.3 (1992), pp. 353–371.
- [338] T. E. Tezduyar, S. Sathe, R. Keedy, and K. Stein. “Space-time finite element techniques for computation of fluid-structure interactions”. In: *Computer Methods in Applied Mechanics and Engineering* 195.17-18 (2006), pp. 2002–2027.
- [339] C. Thantapanally, S. Singh, D. V. Patil, S. Succi, and S. Ansumali. “Quasiequilibrium lattice Boltzmann models with tunable prandtl number for incompressible hydrodynamics”. In: *International Journal of Modern Physics C* 24.12 (2013), p. 1340004.
- [340] J. F. Thompson, B. K. Soni, and N. P. Weatherill. *Handbook of Grid Generation*. CRC press, 1998, p. 1136.
- [341] F.-B. Tian, H. Dai, H. Luo, J. F. Doyle, and B. Rousseau. “Fluid-structure interaction involving large deformations: 3D simulations and applications to biological systems”. In: *Journal of Computational Physics* 258 (2014), pp. 451–469.
- [342] R. Togni, A. Cimarelli, and E. De Angelis. “Physical and scale-by-scale analysis of Rayleigh–Bénard convection”. In: *Journal of Fluid Mechanics* 782 (2015), pp. 380–404.
- [343] J. Tölke and M. Krafczyk. “Second order interpolation of the flow field in the lattice Boltzmann method”. In: *Computers & Mathematics with Applications* 58.5 (2009), pp. 898–902.

- [344] D. Towers and C. Towers. “Particle Image Velocimetry: New Developments and Recent Applications”. In: Berlin, Heidelberg: Springer Berlin Heidelberg, 2008. Chap. High-Speed PIV: Applications in Engines and Future Prospects, pp. 345–361.
- [345] Y. Tseng and J. Ferziger. “A ghost-cell immersed boundary method for flow in complex geometry”. In: *J. Comp. Physics* 192 (2003), pp. 593–623.
- [346] S. Turek and J. Hron. “Proposal for Numerical Benchmarking of Fluid-Structure Interaction between an Elastic Object and Laminar Incompressible Flow”. In: *Lecture Notes in Computational Science and Engineering* 53 (2006), pp. 371–385.
- [347] E. D. Tytell. “The hydrodynamics of eel swimming II. Effect of swimming speed”. In: *Journal of experimental biology* 207.19 (2004), pp. 3265–3279.
- [348] E. D. Tytell and G. V. Lauder. “The hydrodynamics of eel swimming: I. Wake structure”. In: *Journal of Experimental Biology* 207.11 (2004), pp. 1825–1841.
- [349] S. Ubertini, G. Bella, and S. Succi. “Lattice Boltzmann method on unstructured grids: Further developments”. In: *Phys. Rev. E* 68 (2003), p. 016701.
- [350] S. Ubertini, S. Succi, and G. Bella. “Lattice Boltzmann schemes without coordinates”. In: *Phil. Trans. R. Soc. Lond. A* 362 (2004), pp. 1763–1771.
- [351] S. Ubertini, G. Bella, and S. Succi. “Unstructured Lattice Boltzmann equation with memory”. In: *Math. Comp. Sim.* 72 (2006), pp. 237–241.
- [352] M. Uhlmann. “An immersed boundary method with direct forcing for the simulation of particulate flows”. In: *Journal of Computational Physics* 209.2 (2005), pp. 448–476.
- [353] M. Vanella, A. Posa, and E. Balaras. “Adaptive Mesh Refinement for Immersed Boundary Methods”. In: *Journal of Fluids Engineering* 136.4 (2014), p. 040909.

- [354] T. Vasileiou, J. Gerber, J. Prautzsch, T. M. Schutzius, and D. Poulidakos. “Superhydrophobicity enhancement through substrate flexibility”. In: *Proceedings of the National Academy of Sciences* 113.47 (2016), p. 201611631.
- [355] E. Venezian, M. J. Crespo, and B. Sage. “Thermal and material transfer in turbulent gas streams: One-inch spheres”. In: *AIChE Journal* 8.3 (1962), pp. 383–388.
- [356] M. R. Visbal. “High-Fidelity Simulation of Transitional Flows past a Plunging Airfoil”. In: *AIAA Journal* 47.January (2009), pp. 2685–2697.
- [357] T. V. Vu, Y. M. Kim, and H. E. Lee. “Coupled flutter analysis of long-span bridges using full set of flutter derivatives”. In: *KSCE Journal of Civil Engineering* 20.4 (2016), pp. 1501–1513.
- [358] J. H. Watmuff. “Evolution of a wave packet into vortex loops in a laminar separation bubble”. In: *Journal of Fluid Mechanics* 397 (1999), pp. 119–169.
- [359] R. Weber, B. M. Visser, and F. Boysan. “Assessment of turbulence modeling for engineering prediction of swirling vortices in the near burner zone”. In: *International Journal of Heat and Fluid Flow* 11.3 (1990), pp. 225–235.
- [360] T. Wei, P. Fife, J. Klewicki, and P. McMurtry. “Properties of the mean momentum balance in turbulent boundary layer, pipe and channel flows”. In: *Journal of Fluid Mechanics* 522 (2005), pp. 303–327.
- [361] B. Wen, C. Zhang, and H. Fang. “Hydrodynamic Force Evaluation by Momentum Exchange Method in Lattice Boltzmann Simulations”. In: *Entropy* 17.12 (2015), pp. 8240–8266.
- [362] J. Westerweel, G. E. Elsinga, and R. J. Adrian. “Particle Image Velocimetry for Complex and Turbulent Flows”. In: *Annual Review of Fluid Mechanics* 45.1 (2013), pp. 409–436.
- [363] T. Wick. “Adaptive Finite Element Simulation of Fluid-Structure Interaction with Application to Heart-Valve Dynamics”. PhD thesis. 2011, p. 157.

- [364] T. Wick. “Fluid-structure interactions using different mesh motion techniques”. In: *Computers and Structures* 89.13-14 (2011), pp. 1456–1467.
- [365] P. G. Wilson and L. L. Pauley. “Two- and three-dimensional large-eddy simulations of a transitional separation bubble”. In: *Physics of Fluids* 10.11 (1998), p. 2932.
- [366] J. Wissink and W. Rodi. “DNS of a Laminar Separation Bubble Affected by Free-Stream Disturbances”. In: *Direct and Large-Eddy Simulation V* (2004), pp. 213–220.
- [367] J. Wissink and W. Rodi. “Numerical study of the near wake of a circular cylinder”. In: *International Journal of Heat and Fluid Flow* 29 (2008), pp. 1060–1070.
- [368] M. Wosnik, L. Castillo, and W. K George. “A theory for turbulent pipe and channel flows”. In: *Journal of Fluid Mechanics* 421 (2000), pp. 115–145.
- [369] J Wu and C. Shu. “An improved immersed boundary-lattice Boltzmann method for simulating three-dimensional incompressible flows”. In: *Journal of Computational Physics* 229.13 (2010), pp. 5022–5042.
- [370] J Wu and C. Shu. “Implicit velocity correction-based immersed boundary-lattice Boltzmann method and its applications”. In: *Journal of Computational Physics* 228.6 (2009), pp. 1963–1979.
- [371] J Wu, C Shu, and N Zhao. “Numerical investigation of vortex-induced vibration of a circular cylinder with a hinged flat plate”. In: *Physics of Fluids* 26.6 (2014), p. 063601.
- [372] J. Wu, J. Wu, J. Zhan, N. Zhao, and T. Wang. “A Robust Immersed Boundary-Lattice Boltzmann Method for Simulation of Fluid-Structure Interaction Problems”. In: *Communications in Computational Physics* 20.1 (2016), pp. 156–178.
- [373] T. Y.-T. Wu. “Hydromechanics of swimming of fishes and cetaceans”. In: *Advances in Applied Mechanics* 11 (1971), pp. 1–63.
- [374] X. Wu and P. Moin. “A direct numerical simulation study on the mean velocity characteristics in turbulent pipe flow”. In: *Journal of Fluid Mechanics* 608 (2008), pp. 81–112.

- [375] X. Wu and P. A. Durbin. “Evidence of longitudinal vortices evolved from distorted wakes in a turbine passage”. In: *Journal of Fluid Mechanics* 446 (2001), pp. 199–228.
- [376] X. Wu, R. G. Jacobs, J. C. Hunt, and P. A. Durbin. “Simulation of boundary layer transition induced by periodically passing wakes”. In: *Journal of Fluid Mechanics* 398 (1999), pp. 109–153.
- [377] H. Xi, G. Peng, and S. Chou. “Finite-volume lattice Boltzmann method”. In: *Phys. Rev. E* 59 (1999), pp. 6202–6205.
- [378] T. Xu, P. Sullivan, and M. Paraschivoiu. “Fast Large-Eddy Simulation of Low Reynolds Number Flows over a NACA0025”. In: *Journal of Aircraft* 47.1 (2010), pp. 328–333.
- [379] Z. Yang and P. R. Voke. “Large-eddy simulation of boundary-layer separation and transition at a change of surface curvature”. In: *Journal of Fluid Mechanics* 439 (2001), pp. 305–333.
- [380] A. L. Yarin. “Drop impact dynamics: splashing, spreading, receding, bouncing...” In: *Annual review of Fluid Mechanics* 38 (2006), pp. 159–192.
- [381] S. Yarusevych, P. E. Sullivan, and J. G. Kawall. “Coherent structures in an airfoil boundary layer and wake at low Reynolds numbers”. In: *Physics of Fluids* 18.4 (2006).
- [382] S. Yarusevych, P. E. Sullivan, and J. G. Kawall. “On vortex shedding from an airfoil in low-Reynolds-number flows”. In: *Journal of Fluid Mechanics* 632 (2009), p. 245.
- [383] S. Yarusevych, J. G. Kawall, and P. E. Sullivan. “Separated-Shear-Layer Development on an Airfoil at Low Reynolds Numbers”. In: *AIAA Journal* 46.12 (2008), pp. 3060–3069.
- [384] D. You and P. Moin. “A dynamic global-coefficient subgrid-scale eddy-viscosity model for large-eddy simulation in complex geometries”. In: *Annual Research Briefs, Center for Turbulence Research* (2006), pp. 41–53.
- [385] J. Young, S. M. Walker, R. J. Bomphrey, G. K. Taylor, and A. L. Thomas. “Details of insect wing design and deformation enhance aerodynamic function and flight efficiency”. In: *Science* 325.5947 (2009), pp. 1549–1552.

- [386] P. Yuan and L. Schaefer. “Equations of state in a lattice Boltzmann model”. In: *Physics of Fluids* 18.August 2005 (2006), pp. 1–11.
- [387] W. Yuan, M. Khalid, J. Windte, U. Scholz, and R. Radespiel. “An Investigation of Low-Reynolds-number Flows past Airfoils”. In: *23rd AIAA Applied Aerodynamics Conference* July 2015 (2005), pp. 1–19.
- [388] G. Yun, D. Kim, and H. Choi. “Vortical structures behind a sphere at subcritical Reynolds numbers”. In: *Physics of Fluids* 18.1 (2006), p. 5102.
- [389] A Zadehgo, M Ashrafizaadeh, and S. Musavi. “A nodal discontinuous Galerkin lattice Boltzmann method for fluid flow problems”. In: *Computers & Fluids* 105 (2014), pp. 58–65.
- [390] M. V. Zagarola, A. E. Perry, and A. J. Smits. “Log laws or power laws: The scaling in the overlap region”. In: *Physics of Fluids (1994-present)* 9.7 (1997), pp. 2094–2100.
- [391] M. V. Zagarola and A. J. Smits. “Mean-flow scaling of turbulent pipe flow”. In: *Journal of Fluid Mechanics* 373 (1998), pp. 33–79.
- [392] A. Zarghami, M. Maghrebi, J. Ghasemi, and S. Ubertini. “Lattice Boltzmann finite volume formulation with improved stability”. In: *Commun. Comput. Phys.* 12 (2012), pp. 42–64.
- [393] W. Zhang, R. Hain, and C. J. Kähler. “Scanning PIV investigation of the laminar separation bubble on a SD7003 airfoil”. In: *Experiments in Fluids* 45.4 (2008), pp. 725–743.
- [394] W. Zhang, Z. Zou, L. Qi, J. Ye, and L. Wang. “Effects of freestream turbulence on separated boundary layer in a low-re high-lift LP turbine blade”. In: *Computers & Fluids* 109 (2015), pp. 1–12.
- [395] G. Zhao-Li, Z. Chu-Guang, and S. Bao-Chang. “Non-equilibrium extrapolation method for velocity and pressure boundary conditions in the lattice Boltzmann method”. In: *Chinese Physics* 11.4 (2002), p. 366.
- [396] Y. Zhou and Z. J. Wang. “Implicit Large Eddy Simulation of Transitional Flow over a SD7003 Wing Using High-order Spectral Difference Method”. In: *40th Fluid Dynamics Conference and Exhibit*. 2010, p. 4442.

-
- [397] L. Zhu, P. Wang, and Z. Guo. “Performance evaluation of the general characteristics based off-lattice Boltzmann scheme and DUGKS for low speed continuum flows”. In: *Journal of Computational Physics* 333 (2017), 227246.
- [398] Q. Zou and X. He. “On pressure and velocity boundary conditions for the lattice Boltzmann BGK model”. In: *Physics of fluids* 9.6 (1997), pp. 1591–1598.

Copyright disclaimer

- Chapter 3 is partially reprinted from Dorschner et al. [76] and Dorschner et al. [73]
- Chapter 4 is partially reprinted from Dorschner et al. [77] and Di Ilio et al. [69].
- Chapter 5 is partially reprinted from Dorschner et al. [74].
- Chapter 6 is partially reprinted from Dorschner et al. [78].
- Chapter 7 is partially reprinted from Dorschner et al. [73].
- Chapter 8 is partially reprinted from Dorschner et al. [75]

Curriculum Vitae

Personal Data

Name	Benedikt Dorschner
Date of birth	February 3rd, 1989
Place of birth	Karlsruhe, Germany
Citizen of	Germany
Nationality	German

Education

2015 – 2018	Ph.D. Mechanical Engineering, Swiss Federal Institute of Technology Zurich (ETHZ)
2012 – 2014	M.S. Mechanical Engineering, Swiss Federal Institute of Technology Zurich (ETHZ)
2008 – 2012	B.S. Mechanical Engineering, Karlsruher Institute of Technology (KIT)

Publications

Journal Publications

- B. Dorschner, S. Chikatamarla, F. Bösch, and I. Karlin. "Grad's approximation for moving and stationary walls in entropic lattice Boltzmann simulations". In: *Journal of Computational Physics* 295 (2015), pp. 340-354.
- B. Dorschner, F. Bösch, S. Chikatamarla, K. Boulouchos, and I. Karlin. "Entropic Multi-Relaxation Time Lattice Boltzmann Model for

Complex Flows". In: *Journal of Fluid Mechanics* 801 (2016), pp. 623-651.

- B. Dorschner, S. S. Chikatamarla, and I. V. Karlin. "Entropic multi-relaxation time lattice Boltzmann method for moving and deforming geometries in three dimensions". In: *Phys. Rev. E* 95.6 (2017), p. 63306.
- B. Dorschner, N. Frapolli, S. S. Chikatamarla, and I. V. Karlin. "Grid refinement for entropic lattice Boltzmann models". In: *Phys. Rev. E* 94.5 (2016), p. 053311.
- B. Dorschner, S. S. Chikatamarla, and I. V. Karlin. "Transitional Flows with the Entropic Lattice Boltzmann Method". In: *Journal of Fluid Mechanics* 824 (2017), pp. 388-412.
- B. Dorschner, S. S. Chikatamarla, and I. V. Karlin. "Fluid-structure interaction with the entropic lattice Boltzmann method". In: *Phys. Rev. E* 97.2 (2018), p. 023305.
- F. Bösch, B. Dorschner and I.V Karlin. "Entropic multi-relaxation free-energy lattice Boltzmann model for two-phase flows". Submitted to *Euro. Phys. Let.*
- G. Di Ilio, B. Dorschner, G. Bella, S. Succi and I.V. Karlin. "Simulation of turbulent flows with the entropic multirelaxation time lattice Boltzmann method on body-fitted meshes". Submitted to *Journal of Fluid Mechanics*.

